

Spectroscopic, Electronic, and Mechanistic
Studies of Silicon Surfaces Chemically
Modified with Short Alkyl Chains

Thesis by
Noah Thomas Plymale

In Partial Fulfillment of the Requirements for
the degree of
Doctor of Philosophy

The Caltech logo is displayed in a bold, orange, sans-serif font. The word "Caltech" is centered horizontally and vertically within a light gray rectangular background.

CALIFORNIA INSTITUTE OF TECHNOLOGY
Pasadena, California

2017
(Defended 17 October, 2016)

© 2016

Noah Thomas Plymale
ORCID: 0000-0003-2564-8009

ACKNOWLEDGEMENTS

As I am finishing writing this thesis and reflecting on the past ~5 years in graduate school, I am really overwhelmed with the quality of people with whom I have worked. First, I have to acknowledge my advisor Nate Lewis for working with me on some really interesting surface chemistry and giving me the chance to guide my own projects throughout graduate school. Over the years, I have developed a profound appreciation for Nate and the way he runs his research group. We are all lucky to be able to make our own mistakes, forge our own path, and build our own futures under the guidance of one of the world's most well-known and respected chemists. Thank you, Nate, for everything you have done for me!

I have been lucky enough to have one of the most experienced and supportive committees possible in graduate school. Bill Goddard has been supportive and provided valuable advice during committee meetings and exams. Thank you, Bill, for working with me through this process! Harry Gray served as the chair of my committee, and has been incredibly encouraging throughout graduate school. Through the National Science Foundation Center for Chemical Innovation: Solar Fuels program, I have had the fantastic opportunity of working with Harry on outreach programs like Juice from Juice. Thanks to Harry, I was also supported through the CCI for my last year and some months of graduate school. Thank you Harry for supporting me and giving me a place to work on community outreach!

Bruce Brunschwig has been my fourth committee member since my props exam, but he has been my friend and surrogate advisor since I joined the Lewis group. I have

worked with Bruce since I started as a GLA in the MMRC shortly after we purchased the Dimension Icon AFM. After about 6 months with the AFM, I was moved to the much more labor-intensive XPS instruments. While I have been slowly retiring my XPS responsibilities over the last year, this job had a substantial impact, mostly good and some bad, on my experience in graduate school. Bruce always remained an invaluable resource when doing these jobs, and I really valued his support through the times when the instruments were misbehaving. Additionally, Bruce has been incredibly patient with me, particularly when it comes to charge transfer kinetics at interfaces, and I have learned so much from working with him over the years. Thank you, Bruce, for making my experience in the Lewis group better a great one!

As an XPS GLA, I got to work with some of the best Lewis group members. Taking over responsibilities from Joseph Beardslee and Judy Lattimer was quite an initial shock. Thank you to Joseph and Judy for making the transition as painless as possible! I started my GLA responsibilities with Adam Nielander and Amanda Shing, both of who remain my good friends. Thanks, Adam and Amanda! You made it fun to be a GLA and have all the power!!! Now, I'm handing responsibilities to the seasoned Jonathan Thompson, the somewhat less experienced Annelise Thompson, and the brand new Ellen Yan. All of you have helped make being a GLA, even as I drift farther away from the day-to-day responsibilities, a very positive experience. Best of luck to Jonathan, Annelise, and Ellen!

As a first year getting started in the Lewis group, I remember being overwhelmed with the range of different work that the Lewis group was doing. Coming from a

background in Vitamin B₁₂ kinetics, which I studied as an undergraduate, I had to find an area that interested me in a very diverse and large research group. Initially, I worked with Shane Ardo, who has been an inspiration to me since. A few months into working with Shane, Leslie O’Leary, then a graduating 5th year, approached me about taking on some collaborative projects involving Si surface chemistry. I had initially anticipated working with both Leslie and Shane, but the time-sensitive nature of the collaborations took priority and I soon discovered that Si surface chemistry is a full-time project. As Leslie departed for Dow Chemical a couple months after teaching me the ropes, Ron Grimm became an informal mentor in the lab. Anyone who knows Ron knows that he is truly unique and extremely multi-talented. From how to make a temperature-controlled hot plate to how to review manuscripts, Ron taught me so many of the little skills that I am so grateful to have now. Thank you Ron, Shane, and Leslie for guiding my initial few years in graduate school and providing me with the foundation to succeed!

The Lewis group, by my estimation, is by far one of the most cohesive and fun groups at Caltech, despite being spread out over 3 campus buildings. I have made such an enormous group of phenomenal friends over the years! As academia is structured around the constant revolving door of people, particularly postdocs who come and go faster than the graduate students, one has the advantage of constantly meeting new people. The disadvantage, of course, is the slow but constant stream of friends leaving for greener pastures. When I joined the Lewis group, there were 8 of us, which soon reduced to 7 and the 6. Our giant year was only rivaled and surpassed by the year that came 2 after ours. Azhar Carim, Michael Lichterman, Fadi Saadi, Nick Batara, and Victoria Dix are now all my good friends – I couldn’t have done it without you!

I always enjoyed my conversations with James Blakemore, and when we got Adam Nielander, Aaron Sattler, or Wes Sattler involved, something good and possibly crazy was bound to happen. I look back on trips I went on to Las Vegas with Adam, James, Aaron, Wes, Rob Corridan, Mita Dasog, and Sonja Francis with great fondness. I'll never ever forget the trouble we got into at the Paris club the last time we were there. I also will never forget my darling Sonja Francis, who went with me to Italy! We had such an amazing time, and I have the photos to prove it! I would go visit anywhere with you by my side!

I had the good fortune in graduate school of working with two amazing undergraduate students. Allison Lim came from Harvey Mudd College to work with me in Summer of 2014. She came from working with Ron Grimm while he was a temporary faculty member there, and she was very eager to learn all about semiconductor interfaces. Thank you, Allison, for making my experience as a first-time mentor a positive one. Anshul Ramachandran was my second attempt at mentoring an undergraduate, and his project picked up where Allison's left off. I was lucky to work with both Allison and Anshul, and I am so pleased that we got to write a paper together! Good luck with graduate school, Allison, and good luck with your last couple years at Caltech, Anshul. Also, Anshul, keep up the break dancing!

I also had the great pleasure of working with Mita Dasog on the work presented in Chapter 5 of this thesis. Thank you, Mita, for working with me on this project. Without your influence, I wouldn't have made it through that project. I also want to thank Paul Kempler, who spent some time doing a little bit of surface chemistry and looking for ferrocene in Big Bird. I know you'll put the surface chemistry skills to good use with your

microwire project! Miguel Caban-Acevedo is carrying the silicon surface chemistry torch in the Lewis group, with Ellen, Annelise, and Josh Wiensch developing new ways to do chemistry on tricky 2-dimensional materials. Another indispensable person who must be thanked is Barbara Miralles. Barbara, I am so glad to have your support on the administrative end of things! Your understanding and patience have benefited us all in the Lewis group, and you really do make the world go around as far as I'm concerned.

I also want to devote a quick sentence or two to thank Azhar, Kyra Lee, and Dan Torelli + Susie Haubner for consistently serving as fantastic hosts for house parties. I had so much fun hanging out at your respective places! We will definitely be having a few more parties before I am out of here for good! The atmosphere that you created in the Lewis group has helped dull a lot of the stress and tension that is built into Caltech, and your influence on the group has been invaluable. I honestly have a hard time coming to the realization that our parties left together are limited.

Lastly, I want to thank my family, who has always encouraged me to do my best and find the career I love. Dad always provided me with level headed advice and has not steered me wrong yet! Mom always was a great listener whenever I had something that was bothering me or when I just needed to talk about something. I truly adore my parents, and I hope I can be like them someday. My sister, Rachel, is absolutely without a doubt my favorite person in the world. Somehow, she and I have developed a nearly identical sense of humor, and all of our conversations leave me in such a good mood. Thank you, mom, dad, and Rachel, for all of your support over the years and also keeping up with me all the way from Ohio! I love you all!

ABSTRACT

The chemical, structural, and electronic properties of semiconductor surfaces are known to strongly influence the energetics at semiconductor interfaces. Inexpensive and scalable wet chemical modification of semiconductor surfaces provides a means to impart a desired functionality at semiconductor interfaces for the development of new devices based on precise and cost-effective chemistry. This thesis is composed of three studies that focused on identifying the spectroscopic, electronic, and mechanistic properties of reactions at Si surfaces. First, ethynyl- and propynyl-terminated Si(111) surfaces were prepared and characterized by vibrational and photoelectron spectroscopy as well as electrochemical scanning-tunneling microscopy. Ethynyl-terminated Si(111) exhibited $\equiv\text{C-H}$, $\text{C}\equiv\text{C}$, Si-C stretching signals and a fractional monolayer (ML) coverage (Φ) of $\Phi_{\text{Si-CCH}} = 0.63 \pm 0.08$ ML and $\Phi_{\text{Si-OH}} = 0.35 \pm 0.03$ ML. Propynyl-terminated Si(111) showed $(\text{C-H})_{\text{CH}_3}$ bending, Si-C stretching, and $\text{C}\equiv\text{C}$ stretching with $\Phi_{\text{Si-CCCH}_3} = 1.05 \pm 0.06$ ML. Deprotonation of ethynyl-terminated Si(111) surfaces formed a unique surface-bound lithium acetylide that acted as nucleophile. This work provides definitive spectroscopic and microscopic evidence for the covalent attachment of ethynyl and propynyl groups to the Si(111) surface.

Second, Si(111) surfaces were modified with 3,4,5-trifluorophenylacetylene (TFPA) groups to impart a positive dipole at the Si(111) surface. This negative surface dipole provides the necessary band-edge shift at the Si surface to maximize the interface between p-type Si and the proton reduction half reaction. Vibrational and photoelectron spectroscopy provided evidence for the attachment of TFPA groups to the Si(111) surface. Mixed methyl/TFPA monolayers were prepared and characterized using electrochemical

and photoelectrochemical methods to show that the band-edge positions and open-circuit voltages were shifted positive with increasing fractional TFPA coverage on the surface. This work demonstrates that monolayer chemistry can be used to manipulate the band-edge positions of Si surfaces as a function of surface composition.

Finally, mechanistic studies of the reaction of liquid methanol with hydride-terminated Si(111) surfaces in the presence of an oxidant were carried out. Vibrational and photoelectron spectroscopy showed that acetylferrocenium, ferrocenium, and dimethylferrocenium could serve as oxidants to promote an increased rate of methoxylation of the H-Si(111) surface in the dark. Illumination of intrinsic and n-type surfaces resulted in an increased rate of methoxylation, resulting from a positive shift in energy of the electron quasi-Fermi level in the presence of light. The results are described in the context of a kinetic charge transfer formalism that is consistent with the experimentally observed results. This work provides a general framework to describe the kinetics of charge transfer reactions that occur on semiconductor surfaces.

PUBLISHED CONTENT AND CONTRIBUTIONS

Plymale, N. T.; Kim, Y.-G.; Soriaga, M. P.; Brunschwig, B. S.; Lewis, N. S. Synthesis, Characterization, and Reactivity of Ethynyl- and Propynyl-Terminated Si(111) Surfaces. *J. Phys. Chem. C* **2015**, *119*, 19847–19862. DOI: 10.1021/acs.jpcc.5b05028

Plymale, N. T. participated in the conception of the project, performed the sample preparation, collected the majority of the data, performed the data analysis, and participated in writing the manuscript.

Plymale, N. T.; Ramachandran, A. R.; Lim, A. N.; Brunschwig, B. S.; Lewis, N. S. Control of the Band-Edge Positions of Crystalline Si(111) Surfaces by Functionalization with 3,4,5-Trifluorophenylacetylenyl Moieties. *J. Phys. Chem. C* **2016**, *120*, 14157–14169. DOI: 10.1021/acs.jpcc.6b03824

Plymale, N. T. participated in the conception of the project, the sample preparation, the data collection, the data analysis, and the writing of the manuscript.

TABLE OF CONTENTS

Acknowledgements	iii
Abstract	viii
Published Content and Contributions	x
Table of Contents	xi
List of Figures.....	xv
List of Schemes	xx
List of Tables.....	xxi
Chapter 1: Alkyl-Terminated Silicon Surfaces.....	1
1.1 Hydrogen-Terminated Silicon Surfaces	1
1.2 Halogen-Terminated Silicon Surfaces.....	5
1.3 Methyl-Terminated Silicon Surfaces.....	6
1.4 Surface Chemistry Applications	15
1.5 References	22
Chapter 2: Synthesis, Characterization, and Reactivity of Ethynyl- Terminated Si(111) Surfaces.....	33
2.1 Introduction	33
2.2 Experimental Section	36
2.2.1 Materials and Methods	36
2.2.2 Instrumentation	41
2.2.3 Data Analysis	44
2.3 Results	49
2.3.1 Transmission Infrared Spectroscopy	49
2.3.2 High-Resolution Electron Energy-Loss Spectroscopy	52
2.3.3 X-ray Photoelectron Spectroscopy	55
2.3.4 Atomic-Force Microscopy, Electrochemical Scanning- Tunneling Microscopy, and Low Energy Diffraction	60
2.3.5 Surface Recombination Velocity Measurements	63
2.3.6 Reactivity of HCC–Si(111) Surfaces	64

2.4 Discussion	71
2.4.1 Vibrational Spectroscopy of HCC–Si(111) Surfaces.....	71
2.4.2 Surface Ordering, Stability, and Defects of HCC–Si(111) Surfaces.....	73
2.4.3 Reactivity of HCC–Si(111) Surfaces	75
2.4.4 Comparison with Previously Reported Syntheses and Surface Spectroscopy	76
2.5 Conclusions	79
2.6 References	80
Chapter 3: Synthesis and Characterization of Propynyl-Terminated	
Si(111) Surfaces	90
3.1 Introduction	90
3.2 Experimental Section	92
3.2.1 Materials and Methods	92
3.2.2 Instrumentation	94
3.2.3 Data Analysis	94
3.3 Results	96
3.3.1 Transmission Infrared Spectroscopy	96
3.3.2 High-Resolution Electron Energy-Loss Spectroscopy	98
3.3.3 X-ray Photoelectron Spectroscopy	101
3.3.4 Atomic-Force Microscopy, Electrochemical Scanning- Tunneling Microscopy, and Low-Energy Electron Diffraction.....	105
3.3.5 Surface Recombination Velocity Measurements	108
3.4 Discussion	110
3.4.1 Vibrational Spectroscopy of CH ₃ CC–Si(111) Surfaces	110
3.4.2 Surface Ordering, Stability, and Defects of CH ₃ CC– Si(111) Surfaces.....	111
3.4.3 Comparison with Previously Reported Syntheses and Surface Spectroscopy	114

3.5 Conclusions	116
3.6 References	117
Chapter 4: Control of the Band-Edge Positions of Crystalline Si(111)	
by Surface Functionalization with 3,4,5-	
Trifluorophenylacetylene Moieties.....	
4.1 Introduction	125
4.2 Experimental Section	129
4.2.1 Materials and Methods	129
4.2.2 Instrumentation	136
4.2.3 Data Analysis	137
4.3 Results	144
4.3.1 Spectroscopic Characterization and Surface Recombination Velocity of Si(111)–TFPA and Si(111)– MMTFPA Surfaces	144
4.3.2 Hg Contacts to Si(111)–MMTFPA Surfaces	150
4.3.3 Photoelectrochemical Behavior of Si(111)–TFPA and Si(111)–MMTFPA Surfaces in Contact with CH ₃ CN- Cp* ₂ Fe ⁺⁰	154
4.3.4 Photoelectrochemical Behavior of Si(111)–TFPA and Si(111)–MMTFPA Surfaces in Contact with CH ₃ CN- MV ^{2+/+}	157
4.4 Discussion	159
4.4.1 Si(111)–TFPA Surface Characterization.....	159
4.4.2 Hg Contacts to Si(111)–MMTFPA Surfaces	163
4.4.3 Photoelectrochemical Measurements of Si(111)–TFPA and Si(111)–MMTFPA Surfaces in CH ₃ CN.....	165
4.5 Conclusions	168
4.6 References	169
Chapter 5: A Mechanistic Study of the Oxidative Reaction of	
Hydrogen-Terminated Si(111) Surfaces with Liquid Methanol.....	
	179

5.1 Introduction	179
5.2 Experimental Section	182
5.2.1 Materials and Methods	182
5.2.2 Instrumentation	187
5.2.3 Analysis of TIRS and XPS Data	188
5.3 Results	190
5.3.1 Reaction of H-Si(111) with CH ₃ OH Solutions in the Dark	190
5.3.2 Reaction of H-Si(111) with CH ₃ OH Solutions in the Presence of Light	200
5.3.3 Analysis of F Content on H-Si(111) Surfaces Reacted in CH ₃ OH Solutions	202
5.3.4 Potentiostatic reaction of H-Si(111) with CH ₃ OH	202
5.4 Discussion	207
5.4.1 Kinetic Description and Mechanism of Oxidant-Activated Methoxylation of H-Si(111) Surfaces	207
5.4.2 Kinetic Description and Mechanism of the Potentiostatic Methoxylation of H-Si(111) Surfaces	216
5.5 Conclusions	220
5.6 References	222

LIST OF FIGURES

<i>Number</i>	<i>Page</i>
1.1 TIRS data for the H–Si(111) surface.....	3
1.2 TIRS data for CH ₃ –Si(111) surfaces.....	7
1.3 HREELS data for CH ₃ –Si(111) surfaces	8
1.4 High-resolution XP spectra of the C 1s and Si 2p regions for CH ₃ –Si(111) surfaces	11
1.5 Representative topographical AFM image of the CH ₃ –Si(111) Surface	12
1.6 Representative LEED pattern for a CH ₃ –Si(111) surface.....	13
1.7 <i>S</i> behavior as a function of time exposed to air for CH ₃ – Si(111) Surfaces.....	14
1.8 Example of linker chemistry that could be used to integrate catalyst nanoparticles with semiconductors	16
1.9 Example of linker chemistry that could be used to control metal deposition on a Si surface.....	17
1.10 Example of a silicon/polymer junction formed by a covalent bond between the two materials	19
1.11 Example of a silicon/metal oxide junction formed by atomic layer deposition.....	21
2.1 TIRS data for HCC–Si(111) surfaces prepared using DMSO.....	50
2.2 TIRS data for HCC–Si(111) surfaces prepared using DMA.....	51
2.3 TIRS data for CH ₃ –Si(111) and HCC–Si(111) surfaces referenced to the SiO _x surface	52
2.4 HREELS data for HCC–Si(111) surfaces.....	53
2.5 High-resolution XP spectrum of the C 1s region for HCC– Si(111) surfaces	55

2.6	High-resolution XP spectrum of the Si 2p region for HCC–Si(111) Surfaces	56
2.7	Thermal stability in vacuum of HCC–Si(111) surfaces	58
2.8	Topographical AFM image of the HCC–Si(111) surface	60
2.9	EC-STM image of the HCC–Si(111) surface	61
2.10	Representative LEED pattern for the HCC–Si(111) surface	62
2.11	<i>S</i> measured as a function of air exposure for CH ₃ –Si(111) and HCC–Si(111) surfaces	63
2.12	TIRS data for HCC–Si(111) surfaces collected at 74° incidence after treatment with <i>t</i> -BuLi followed by CD ₃ OD	65
2.13	TIRS data for HCC–Si(111) surfaces collected at 30° incidence after treatment with <i>t</i> -BuLi followed by CD ₃ OD	65
2.14	TIRS data collected at 74° incidence angle for HCC–Si(111) surfaces after treatment with strong bases followed by reaction with CD ₃ OD.	66
2.15	TIRS data collected 74° incidence angle referenced to the SiO _x surface before and after treatment with <i>t</i> -BuLi followed by CD ₃ OD	67
2.16	High-resolution F 1s XP spectra of CH ₃ –Si(111) HCC–Si(111), CH ₃ CC–Si(111), and SiO _x surfaces after reaction with <i>t</i> -BuLi followed by 4-fluorobenzyl chloride	70
3.1	TIRS data for CH ₃ CC–Si(111) surfaces	97
3.2	TIRS data for the CH ₃ CC–Si(111) surface referenced to the SiO _x surface	98
3.3	HREELS data for CH ₃ CC–Si(111) surfaces	99
3.4	High-resolution XP spectrum of the C 1s region for CH ₃ CC–Si(111) surfaces	101
3.5	High-resolution XP spectrum of the Si 2p region for CH ₃ CC–Si(111) surfaces	102
3.6	Thermal stability in vacuum of CH ₃ CC–Si(111) surfaces	104

3.7	Topographical AFM image of a CH ₃ CC–Si(111) surface.....	106
3.8	Representative EC-STM image a CH ₃ CC–Si(111) surface.....	107
3.9	Representative LEED pattern for a CH ₃ CC–Si(111) surface	108
3.10	<i>S</i> measured as a function of exposure to air for CH ₃ –Si(111) and CH ₃ CC–Si(111) surfaces	109
4.1	Effect of a surface dipole on the band-edge positions and barrier height, Φ_b , for a p-type semiconductor.....	127
4.2	The Teflon reaction vessels used to isolate the Al-coated side of p-Si electrodes.....	133
4.3	TIRS data for a Si(111)–TFPA surface collected at 74° and 30° with respect to the surface normal	145
4.4	TIRS data for a Si(111)–MMTFPA surface with $\theta_{TFPA} = 0.16$ ML collected at 74° with respect to the surface normal	147
4.5	<i>S</i> values for Si(111)–CH ₃ , Si(111)–MMTFPA, and Si(111)– TFPA surfaces as a function of θ_{TFPA}	147
4.6	XPS data for an n-Si(111)–MMTFPA surface with $\theta_{TFPA} =$ 0.11 ML.....	149
4.7	XPS data for the Si(111)–TFPA surface with $\theta_{TFPA} = 0.35$ ML.....	150
4.8	Representative two-electrode <i>J-V</i> behavior for n-type and p-type Si(111)–MMTFPA/Hg junctions	151
4.9	Correlation between the calculated barrier height for Si(111)– MMTFPA/Hg junctions and the fractional monolayer coverage of TFPA for n-type and p-type samples	153
4.10	Representative <i>J-E</i> data under 100 mW cm ⁻² simulated sunlight illumination for functionalized Si(111) surfaces in contact with Cp* ₂ Fe ⁺⁰	155
4.11	Representative <i>J-E</i> data under 100 mW cm ⁻² illumination for functionalized Si(111) surfaces in contact with MV ^{2+/*}	157
5.1	Time dependence of the reaction of H–Si(111) with neat CH ₃ OH and CH ₃ OH containing Cp ₂ Fe ⁺	191

5.2	Energy diagram showing the relative energy positions of the Si bands and the formal potentials of the oxidants used	192
5.3	TIRS data for intrinsic H-Si(111) surfaces after treatment in neat CH ₃ OH or CH ₃ OH solutions containing oxidant.....	194
5.4	Correlation between $\theta_{\text{Si-OCH}_3}$ and the oxidizing conditions used in the reaction of H-Si(111) surfaces with CH ₃ OH in the dark	196
5.5	XPS data for the C 1s core level of H-Si(111) surfaces after exposure to neat CH ₃ OH or CH ₃ OH solutions containing oxidant.....	197
5.6	Correlation showing the area under the region containing the three $\nu(\text{C-H})_{\text{CH}_3}$ peaks as a function of the oxidizing conditions used in the reaction of H-Si(111) surfaces with CH ₃ OH in the dark.....	198
5.7	Correlation showing the area under the region containing the $\delta_{\text{s}}(\text{C-H})_{\text{CH}_3}$ and $\nu(\text{C-O}) + \rho(\text{CH}_3)$ peaks as a function of the oxidizing conditions used in the reaction of H-Si(111) surfaces with CH ₃ OH in the absence of light.....	200
5.8	Correlation between $\theta_{\text{Si-OCH}_3}$ and the oxidizing conditions used in the reaction of H-Si(111) surfaces with CH ₃ OH in the absence and presence of ambient light	201
5.9	High-resolution XPS data for the F 1s region of a H-Si(111) sample reacted with CH ₃ OH containing 1.0 mM Me ₂ Cp ₂ Fe ⁺ BF ₄ ⁻	203
5.10	Correlation between θ_{F} and the oxidizing conditions used in the reaction of H-Si(111) surfaces with CH ₃ OH in the absence and presence of ambient light.....	204
5.11	<i>J-E</i> behavior of n-type and p-type H-Si(111) samples in contact with CH ₃ OH.....	205

5.12 Schematic representation of charge transfer across a semiconductor/liquid interface for oxidant-activated methoxylation	210
5.13 Schematic representation of charge transfer across a semiconductor/liquid interface for potentiostatic methoxylation ...	217

LIST OF SCHEMES

<i>Number</i>		<i>Page</i>
2.1	Synthesis of CH ₃ -Si(111) and HCC-Si(111) Surfaces	38
2.2	Monolayer Thickness of Surface-Bound -CH ₃ , -CCH, and -OH Groups	47
2.3	Monolayer Thickness of 4-Fluorobenzyl-Modified Surfaces	48
3.1	Synthesis of CH ₃ CC-Si(111) Surfaces.....	94
3.2	Monolayer Thickness of Surface-Bound -CCCH ₃ Groups.....	96
4.1	Synthesis of Si(111)-TFPA and Si(111)-MMTFPA Surfaces.....	132
4.2	Estimated Thickness of -CH ₃ and TFPA Groups	139
5.1	Methoxylation of H-Si(111) Surfaces in the Absence of an Oxidant	181
5.2	Oxidant-Activated Methoxylation of H-Si(111)	181

LIST OF TABLES

<i>Number</i>	<i>Page</i>
2.1 Summary of the Positions and Assigned Modes for the Vibrational Signatures Observed for the HCC–Si(111) Surface.....	54
2.2 Estimated Fractional Monolayer Coverage, Φ , of a HCC–Si(111) Surface as a Function of Annealing Temperature	59
2.3 Summary of the Positions and Assigned Modes for the Vibrational Signatures Observed for the DCC–Si(111) Surface.....	68
2.4 Summary of Prior Reports of Synthesis and Characterization of Ethynyl- Terminated Si Surfaces	78
3.1 Summary of the Positions and Assigned Modes for the Vibrational Signatures Observed for CH ₃ CC–Si(111) Surfaces.....	100
3.2 The Estimated Fractional ML Coverage, Φ , of a CH ₃ CC–Si(111) Surface as a Function of Annealing Temperature	105
3.3 Summary of Prior Reports of Synthesis and Characterization of Propynyl- Terminated Si Surfaces	115
4.1 E_{oc} and Φ_b measurements for functionalized Si surfaces in contact with CH ₃ CN–Cp* ₂ Fe ⁺⁰	155
4.2 E_{oc} and Φ_b measurements for functionalized Si surfaces in contact with CH ₃ CN–MV ^{2+/+•}	158
5.1 Summary of the Quantification for the Potentiostatic Methoxylation of H–Si(111) Surfaces	207

Chapter 1

INTRODUCTION: ALKYL-TERMINATED SILICON SURFACES

Plymale, N. T.; Kim, Y.-G.; Soriaga, M. P.; Brunshwig, B. S.; Lewis, N. S. Synthesis, Characterization, and Reactivity of Ethynyl- and Propynyl-Terminated Si(111) Surfaces. *J. Phys. Chem. C* **2015**, *119*, 19847–19862. DOI: 10.1021/acs.jpcc.5b05028

1.1 HYDROGEN-TERMINATED SILICON SURFACES

Hydrogen-terminated Si (Si–H) is the fundamental surface termination on which the vast majority of surface modification is based.¹⁻⁴ The semiconductor industry relies on the production of Si–H surfaces in order to produce high-quality silicon oxide films with low electrical defect density. Consequently, the Si–H surface has been widely studied and characterized. Si–H surfaces can be prepared by a number of techniques, including cleavage of Si in vacuum followed by exposure to H₂(g),⁵ electrochemical etching,⁶⁻⁹ or wet-chemical etching in aqueous fluoride solutions.¹⁰⁻¹² Wet-chemical etching of Si is the simplest method to produce Si–H surfaces, resulting in widespread use of this technique to produce Si–H surfaces.

Early reports of Si–H surfaces prepared by exposure of oxide-terminated Si to aqueous HF solutions suggested that the surface was terminated by Si–F bonds.¹³ The basis for this initial conclusion is the known strength of the Si–F bond, which was hypothesized to form the dominant surface termination after fluoride etching based on thermodynamic arguments. However, the kinetics of the fluoride etching of Si surfaces dominates the

thermodynamics in this case; as the atop Si atoms are fluorinated, they are removed from the surface quickly because the kinetics of the cleavage of Si–Si bonds by HF drives the removal of fluorinated surface sites. The result is a surface that is free of detectable Si–F containing species. This was first demonstrated by surface infrared (IR) spectroscopy, which was used to show the presence of Si–H stretching and bending peaks on the surface.^{11, 14} Vibrational spectroscopy remains a very powerful surface analytical tool, particularly when used together with other surface sensitive techniques such as X-ray photoelectron spectroscopy, because it can inform functional group assignments as well as the orientation of bonds on the surface.

HF etching of Si can be performed on any crystal face, including amorphous Si, nanocrystalline Si, or microstructured Si substrates to yield H-terminated surfaces. When etched with unbuffered HF(aq) solutions, Si surfaces are terminated by a distribution of monohydride (SiH), dihydride (SiH₂) and trihydride (SiH₃) surface sites. By adjusting the pH of the HF(aq) solution by addition of NH₄F solution, the etch rate can be controlled in order to select for the desired surface termination.¹⁴ Anisotropic etching the (111) crystal face of silicon in 40% NH₄F(aq) solutions allows for exceptional control over the surface hydride composition, yielding primarily the monohydride H–Si(111) surface.¹⁵ H–Si(111) is known to exhibit broad atomic terraces with >100 nm width and nearly every Si–H bond is oriented perpendicular to the surface. H–Si(111) is an extremely convenient starting surface for studying the surface chemistry of silicon because modification of H–Si(111) with halogens or organic groups results in substitution of the Si–H bonds for Si–X (X = Cl, Br, I), Si–C, or Si–O bonds. Spectroscopic methods allow for the loss of Si–H bonds to be

observed, and the nature of the new bonds formed on the surface can be more readily studied because of the inherent nature of the Si(111) surface, which has reactive Si bonds that are oriented perpendicular to the surface.

Transmission infrared spectroscopy (TIRS) was the primary vibrational spectroscopic method used throughout this work. Compared with attenuated total reflectance infrared (ATR-IR) spectroscopy, TIRS is more effective at observing low energy modes ($<1500\text{ cm}^{-1}$), including Si–C stretching and C–H bending modes.¹⁵ TIRS can readily observe the orientation of bonds with respect to the sample surface by modifying the angle of incidence on the surface. Figure 1.1 shows TIRS data for a H–Si(111) surface to demonstrate its utility as a surface analytical tool.

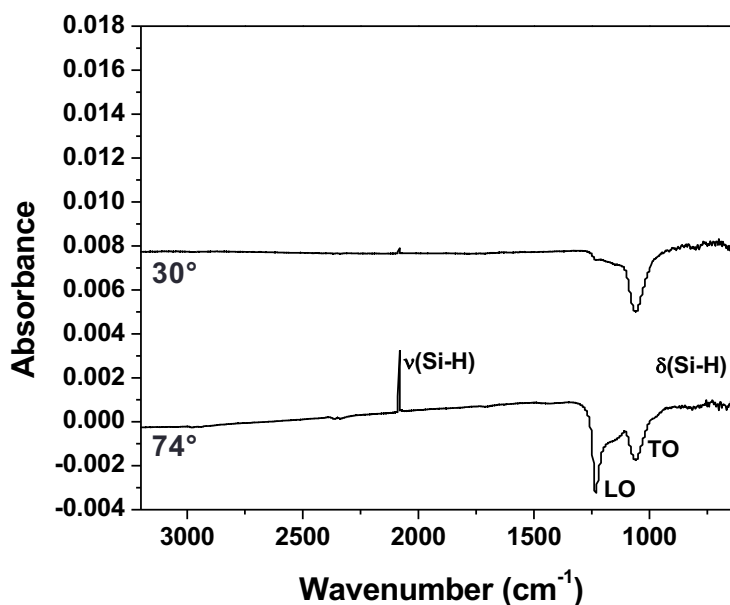


Figure 1.1. TIRS data for the H–Si(111) surface. The bottom spectrum was collected at 74° incidence angle and shows modes that are parallel or perpendicular to the surface. The top spectrum was collected at 30° incidence and primarily shows modes parallel to the surface. Si–H stretching (ν) and Si–H bending (δ) modes are indicated in the plot. The data is referenced to the SiO_x surface, and the negative peaks show the longitudinal optical (LO) and transverse optical (TO) Si–O–Si modes of the SiO_x surface.¹⁵

Si–H surfaces were shown to be capable of undergoing wet-chemical reaction with 1-alkenes and 1-alkynes via a hydrosilylation mechanism in 1995.¹⁶ This discovery spurred a flurry of research aimed at achieving self-assembly of monolayers on Si–H surfaces and a new appreciation for the use of semiconductor surfaces as reactants in wet chemical reactions. Hydrosilylation of 1-alkenes and 1-alkynes on Si–H surfaces remains the most common, and one of the simplest, methods for imparting organic functionality to Si surfaces. Substrates prepared by hydrosilylation have been used to attach reversible redox species to the surface,¹⁷⁻¹⁹ seed the growth of metal oxides by atomic layer deposition (ALD),²⁰⁻²¹ and attach biomolecules, such as DNA, to the surface.²²⁻²³

One of the major drawbacks of hydrosilylation reactions on Si–H surfaces is the mechanism by which it proceeds. The (111) crystal plane has the lowest density of reactive Si–H bonds and is, therefore, the least sterically crowded surface. Still, steric considerations preclude the smallest substrates suitable for undergoing hydrosilylation on H–Si(111) surfaces, such as acetylene or ethylene, from effectively terminating all of the reactive surface sites.²⁴ Incomplete termination of the Si surface with Si–C bonds leaves unreacted Si–H bonds on the surface, which are susceptible to the formation of surface electronic trap states, also known as surface states. Moreover, hydrosilylation has been proposed to occur via a radical mechanism that propagates across the surface, leaving a high density of surface states after the reaction completes.²⁵ The high density of surface states results in a high surface recombination velocity (S), which correlates with current lost to recombination at the interface and negatively impacts the energetics of surfaces prepared by hydrosilylation.

1.2 HALOGENATED SILICON SURFACES

Halogenated Si surfaces are typically used as intermediates in the synthesis of target semiconductor surfaces.²⁶⁻³³ Chlorine-terminated Si (Si-Cl) surfaces, which are the most commonly used halogenated Si surface, have been prepared by methods that include the gas-phase reaction of $\text{Cl}_2(\text{g})$ with Si-H³⁴⁻⁴⁰ or the solution phase reaction of PCl_5 ^{28, 31, 33, 36, 41-43} with Si-H in chlorobenzene. The Si-Cl surface is the least sterically crowded of the halogenated surface, allowing for a greater density of Si-Cl bonds capable of undergoing reaction with an alkylating reagent. While all Si-Cl preparation methods yield Si-Cl bonds on the surface, different methods can yield different surface coverage and etch pit density. Bromine-terminated Si (Si-Br) surfaces can be prepared in similar ways by gas-phase reaction of Si-H surfaces with $\text{Br}_2(\text{g})$, solution phase reaction with $\text{Br}_2(\text{l})$, or solution phase reaction with *N*-bromosuccinamide.⁴⁴⁻⁴⁷ Both Br and Cl are sterically able to terminate all Si atop sites on the (111) crystal plane, allowing for both Cl-Si(111) and Br-Si(111) surfaces to serve as generally interchangeable reactive surfaces in sample preparation.

Iodine terminated silicon (Si-I) surfaces have been prepared by reaction of Si-H surfaces with I_2 in benzene⁴⁸ and by exposure of vacuum-cleaned Si to CH_3I vapor.⁴⁹⁻⁵¹ The van der Waals radius of I is too large to terminate all Si(111) atop sites, and a maximum coverage of ~ 0.33 ML Si-I was observed for reaction of H-Si(111) with $\text{I}_2/\text{benzene}$. The steric bulk of I could be potentially exploited in order to form mixed monolayers on Si surfaces by partial iodination followed by reaction of the Si-I sites with Grignards and reaction of the residual Si-H sites by hydrosilylation. The differences in the reactivity of the Si-Cl, Si-Br, or Si-I surfaces have additionally not been clearly documented.

1.3 METHYL-TERMINATED SILICON SURFACES

Alkyl termination of Si surfaces by a two-step halogenation/alkylation procedure was first reported in 1996.²⁸ Generally, this two-step procedure involves the reaction of a Si-Cl or Si-Br intermediate surface with a Grignard, organolithium, or organosodium reagent.^{15, 24, 26-27, 31-33, 52-53} This method allows for the facile and rapid attachment of short-chain alkyl groups, including methyl, ethyl, and phenyl, which would not be achievable by hydrosilylation chemistry. While long-chain alkyl groups are also readily attached by halogenation/alkylation, the interest in methyl-terminated Si(111) (CH₃-Si(111)) has been the most intense. The novelty of CH₃-Si(111) surfaces is centered around the unique ability of the -CH₃ group to terminate nearly all of the atop Si(111) sites,⁵⁴⁻⁵⁸ affording CH₃-Si(111) surfaces exceptional chemical stability^{26, 31-32} and very low surface recombination velocity.⁵⁹ While CH₃-Si(111) surfaces have been the subject of numerous scientific studies over two decades, my work as a graduate student initially focused on achieving control over the preparation of CH₃-Si(111) surfaces, and I reproduced much of the data that has been reported previously. The following section is a consolidated overview of CH₃-Si(111) surface characterization using the data I collected for control CH₃-Si(111) samples.

TIRS data for CH₃-Si(111) surfaces are given in Figure 1.2.¹⁵ The C-H stretching (ν) region shows modes at 2961, 2926, 2910, and 2856 cm⁻¹ with the signals at 2961 and 2910 cm⁻¹ having been assigned to the asymmetric (ν_a) and symmetric (ν_s) C-H stretching motions of the -CH₃ group, respectively, and the signals at 2926 and 2856 cm⁻¹ having been assigned to -CH₂- groups on adventitious C species. The presence of a signal at 1257

cm^{-1} at 74° with respect to the surface normal but not at 30° indicates the presence of a $(\text{C-H})_{\text{CH}_3}$ symmetric bending (δ_s), or “umbrella,” motion polarized perpendicular to the surface. This signal, in addition to a Si–C stretching peak at 678 cm^{-1} polarized perpendicular to the surface, provides a strong indication that the Si– CH_3 group is oriented normal to the surface. Additionally, a CH_3 rocking (ρ) mode at 753 cm^{-1} is observed at both angles of incidence.

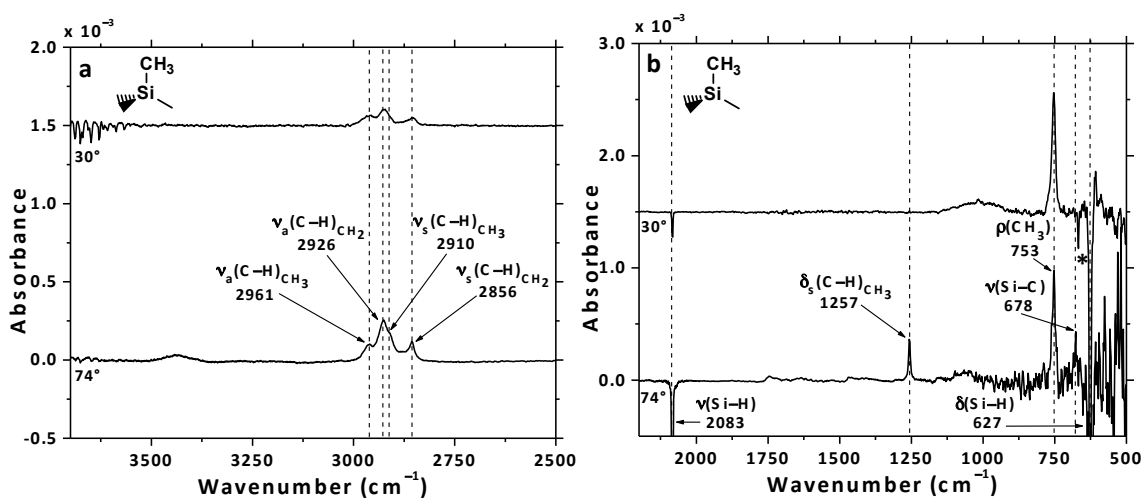


Figure 1.2. TIRS data for $\text{CH}_3\text{-Si}(111)$ surfaces, referenced to the $\text{H-Si}(111)$ surface, collected at 74° (bottom) and 30° (top) from the surface normal. Panel a shows high-energy region, and panel b shows the low-energy region. The negative peaks in panel b resulted from the $\text{H-Si}(111)$ background. A sharp negative peak observed in panel b at 30° incidence marked with * at 667 cm^{-1} resulted from CO_2 in the atmosphere. The subscripts “ CH_3 ” and “ CH_2 ” indicate C–H stretching signals arising from the $-\text{CH}_3$ and $-\text{CH}_2-$ groups, respectively. The peak positions and assignments are indicated. The 30° spectrum is offset vertically for clarity.

HREELS data for $\text{CH}_3\text{-Si}(111)$ surfaces,⁶⁰ shown in Figure 1.3, allows for detection of vibrational signals that could not be readily observed by TIRS. HREELS data for $\text{CH}_3\text{-Si}(111)$ surfaces exhibited peaks centered at 747, 1267, and 2927 cm^{-1} , corresponding to CH_3 rocking, $(\text{C-H})_{\text{CH}_3}$ symmetric bending, and $(\text{C-H})_{\text{CH}_3}$ symmetric and asymmetric stretching motions, respectively, all of which were observed using TIRS. Resolution limitations of the HREELS instrumentation yielded a single C-H stretching peak for the asymmetric and symmetric stretching modes. The use of HREELS allowed for observation of Si-C stretching (665 cm^{-1}) and bending (477 cm^{-1}) signals in addition to the IR-inactive $(\text{C-H})_{\text{CH}_3}$ asymmetric bending (δ_a) motion at 1399 cm^{-1} . A small amount of silicon oxide (SiO_x) gave rise to a signal that was centered at 1066 cm^{-1} . These results compare favorably with previously published spectra of $\text{CH}_3\text{-Si}(111)$ surfaces.

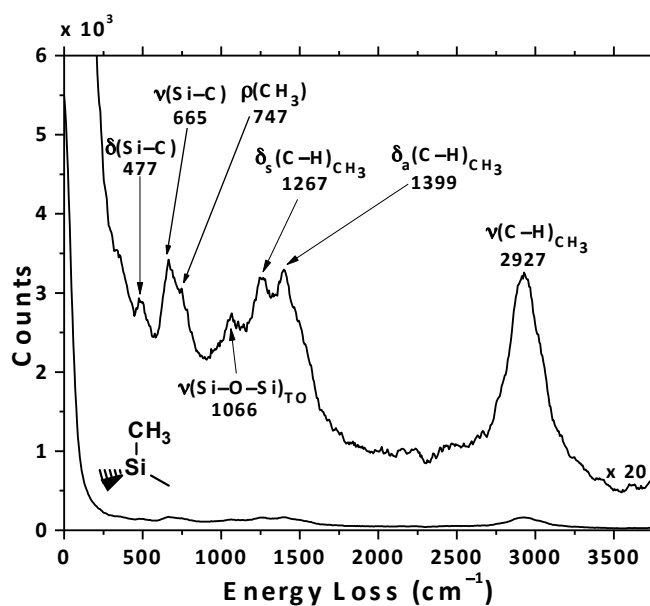


Figure 1.3. HREELS data for $\text{CH}_3\text{-Si}(111)$ surfaces. The data were collected in the specular geometry using an incident beam energy of 5.0 eV, and the fwhm of the elastic peak was 13.3 meV. The raw spectrum (bottom) is shown with the magnified spectrum (top) superimposed for clarity. The peak positions and assignments are indicated in the figure.

Table 1.1 summarizes the vibrational modes detected by TIRS and HREELS for CH₃-Si(111) surfaces along with the orientation of the modes with respect to the surface plane.

Table 1.1. Summary of the Positions and Assigned Modes for the Vibrational Signatures Observed for the CH₃-Si(111) Surface.

TIRS Frequency (cm ⁻¹)	HREELS Frequency (cm ⁻¹) ^a	Assigned Mode ^b	Orientation to Surface ^c
2961	2927	$\nu_a(\text{C-H})_{\text{CH}_3}$	
2926	2927	$\nu_a(\text{C-H})_{\text{CH}_2}$	
2910	2927	$\nu_s(\text{C-H})_{\text{CH}_3}$	
2856	2927	$\nu_s(\text{C-H})_{\text{CH}_2}$	
–	1399	$\delta_a(\text{C-H})_{\text{CH}_3}$	
1257	1267	$\delta_s(\text{C-H})_{\text{CH}_3}$	⊥
weak	1066	$\nu(\text{Si-O-Si})_{\text{TO}}$	not ⊥
753	747	$\rho(\text{CH}_3)$	not ⊥
678	665	$\nu(\text{Si-C})$	⊥
–	477	$\delta(\text{Si-C})$	

^aIn some cases, HREELS signals do not resolve multiple vibrational modes that are observed by TIRS. The HREELS signal with the closest energy to the resolved TIRS signal is paired in the table. ^bThe symbols ν , δ , and ρ signify stretching, bending, and rocking motions, respectively, with subscripts a and s indicating whether the mode is asymmetric or symmetric, respectively. Subscripts “CH₃” and “CH₂” indicate C–H stretching signals arising from –CH₃ and –CH₂– saturated hydrocarbons, respectively. The subscript “TO” indicates a transverse optical Si–O–Si motion. ^cThe orientation of the vibrational mode with respect to the plane of the sample surface determined by TIRS is given.

X-ray photoelectron spectroscopy (XPS) data provides quantitative information about the species present on $\text{CH}_3\text{-Si}(111)$ surfaces. Survey spectra indicate that only signals ascribable to Si, C, and O are observed, and high-resolution spectra are shown for the C 1s and Si 2p core levels in Figure 1.4. $\text{CH}_3\text{-Si}(111)$ surfaces exhibit three distinct C 1s signals, the most prominent of which is centered at 284.3 eV. This photoemission peak is ascribed to C bonded to Si (C_{Si}),⁶¹ while the remaining two signals at 285.2 and 286.4 eV arise from adventitious C species. The fractional monolayer coverage (Φ) of $-\text{CH}_3$ groups on the prepared $\text{CH}_3\text{-Si}(111)$ surfaces can be estimated using a substrate-overlayer model discussed in Chapter 2 (section 2.2.3),⁶²⁻⁶³ to yield $\Phi_{\text{Si-CH}_3} = 1.13 \pm 0.07$ ML, which supports the conclusion that $\text{CH}_3\text{-Si}(111)$ surfaces exhibit nearly full termination of the Si atop sites with Si-C bonds. While the calculated $\Phi_{\text{Si-CH}_3}$ is higher than the maximum 1 ML of $-\text{CH}_3$ groups, the reported value is fairly typical for the magnitude of error expected when quantifying XPS data. Only the photoemission signal at 284.3 eV was used in the estimation of $\Phi_{\text{Si-CH}_3}$ because this signal arises directly from the bound $-\text{CH}_3$ group. Previous work has shown that annealing $\text{CH}_3\text{-Si}(111)$ surfaces to 450 °C in vacuum removes the majority of adventitious species and reveals two additional C 1s photoemission signals resulting from the vibrational fine structure of the $-\text{CH}_3$ group.^{61, 64} However, due to resolution limitations of the instrumentation used in this work, these peaks are omitted from the fitting process for all alkyl-terminated surfaces. No detectable amount of SiO_x was observed by XPS on $\text{CH}_3\text{-Si}(111)$ surfaces.

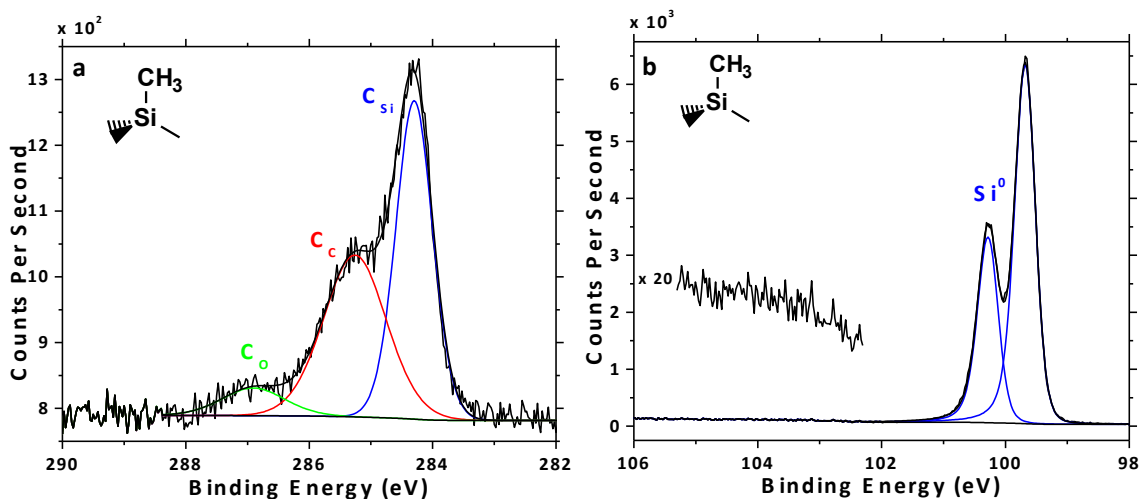


Figure 1.4. High-resolution XPS spectra of the (a) C 1s and (b) Si 2p regions for CH_3 -Si(111) surfaces. The low binding-energy C photoemission signal at 284.3 eV has been ascribed to C bound to Si (blue, C_{Si}), with the C 1s signals at 285.2 and 286.4 eV arising from C bound to C (red, C_C) and C bound to O (green, C_O), respectively. The region from 102–105 eV in the Si 2p spectrum is magnified to show the absence of detectable high-order SiO_x .

Figure 1.5 gives a representative atomic-force microscope (AFM) image of a CH_3 -Si(111) surface. The surface generally exhibits broad atomic terraces with relatively few etch pits. The difference in height observed at terrace step edges is ~ 0.3 nm, which is consistent with the height difference between terraces observed on vacuum cleaved unreconstructed Si(111) surfaces.⁶⁵ The surfaces often exhibit particulates that are shown as raised spots in the AFM images. The size and concentration of these spots tends to vary, and could be correlated with the batch and manufacturer of the Grignard reagent (CH_3MgCl) used in the synthesis process. XPS data shows no detectable metal contaminants, suggesting that these spots are organic in nature and could be the physical manifestation of the adventitious carbon observed in high-resolution C 1s XPS spectra of CH_3 -Si(111) surfaces.

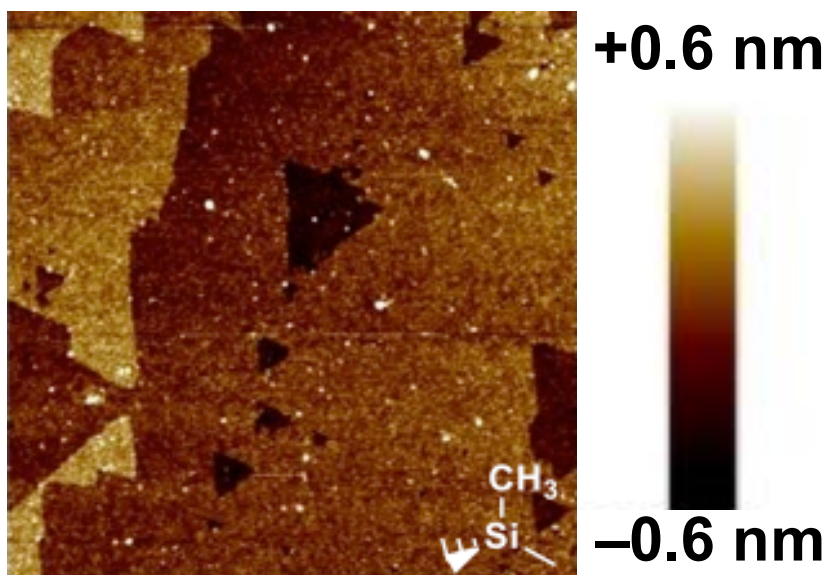


Figure 1.5. Representative topographical AFM image of the CH₃-Si(111) surface. The image is 1 μm \times 1 μm with a z-scale of 1.2 nm (-0.6 to $+0.6$ nm).

Figure 1.6 shows a representative low-energy electron diffraction (LEED) image collected for a CH₃-Si(111) surface.⁶¹ The LEED pattern exhibits 3-fold symmetry, which is indicative of a (1 \times 1) surface unit cell. The image pictured shows 6 bright spots of approximately equal intensity. Adjusting the energy slightly above or below the 43 eV incident beam energy in Figure 1.6 reveals the 3-fold symmetry, as 3 spots remain bright and 3 spots lower in intensity. The spots appear as very bright and sharp relative to the background. This high contrast between the diffraction spots and the background is a strong indication that the CH₃-Si(111) surface exhibits exceptional long-range ordering. Thus, the LEED data supports the conclusion that CH₃-Si(111) surfaces are exceptionally well-ordered and have nearly complete termination of the atop Si sites with Si-C bonds.

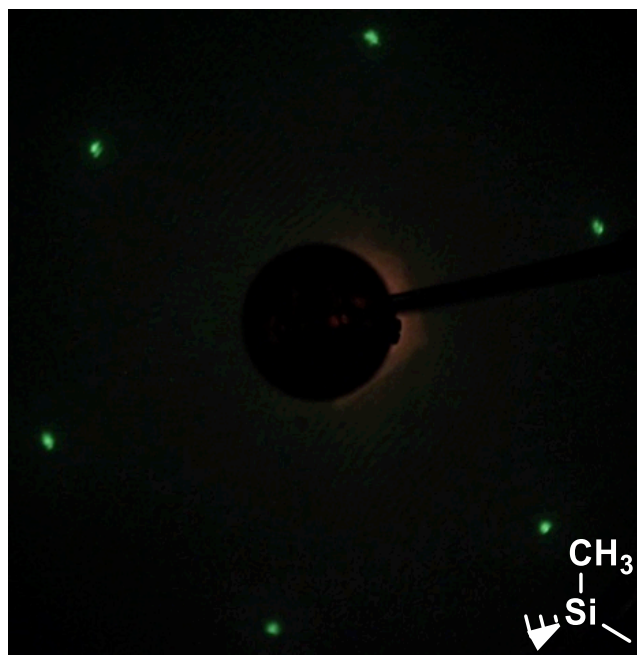


Figure 1.6. Representative LEED pattern for a $\text{CH}_3\text{-Si}(111)$ surface collected at 43 eV incident beam energy.

Surface recombination velocity (S) measurements are typically acquired using a time-resolved microwave conductivity setup, but can also be measured using time-resolved radio frequency conductivity measurements. The microwave conductivity setup used in this work is described in detail in section 2.2.2. The microwave conductivity decay curves can be fitted to an exponential decay to obtain a charge carrier recombination lifetime, τ . Section 2.2.3 describes how to convert τ to a surface recombination velocity in cm s^{-1} . A decrease in S represents a decrease in the electrically active surface state density. Figure 1.7 shows S for a $\text{CH}_3\text{-Si}(111)$ surface as a function of exposure to air. A typical initial S for a $\text{CH}_3\text{-Si}(111)$ surface immediately after preparation and cleaning was 40 cm s^{-1} , which corresponds to an electrical defect density of 1 defect per 2×10^5 surface sites (eq 2.4).⁶⁶ Remarkably, S for $\text{CH}_3\text{-Si}(111)$ surfaces decreases to $\sim 15 \text{ cm s}^{-1}$ after 72 h exposure to air.

This decrease results in a lower surface state density of 1 per 5×10^5 surface sites. Over time, a small increase in S is typically observed, but the increase does not represent a significant increase in the electrically active surface state density. Over the same amount of time, the $\text{CH}_3\text{-Si}(111)$ surface would be expected to form a measurable amount of SiO_x ,³¹ but the formation of SiO_x does not appear to contribute significantly to an increase in S . One hypothesis for the initial decrease in S observed over the first 72 h of air exposure could involve the initial passivation of surface states, such as dangling bonds, by reaction with H_2O and O_2 in the air, with long-term oxidation of the surface in air having little effect on S . This is in contrast to $\text{H-Si}(111)$ surfaces, which undergo comparatively rapid oxidation in air, and exhibit high S after just 15 min air exposure.⁵⁹ Thus, $\text{CH}_3\text{-Si}(111)$ surfaces exhibit improved stability in air relative to $\text{H-Si}(111)$ surfaces and have remarkable electrical properties.

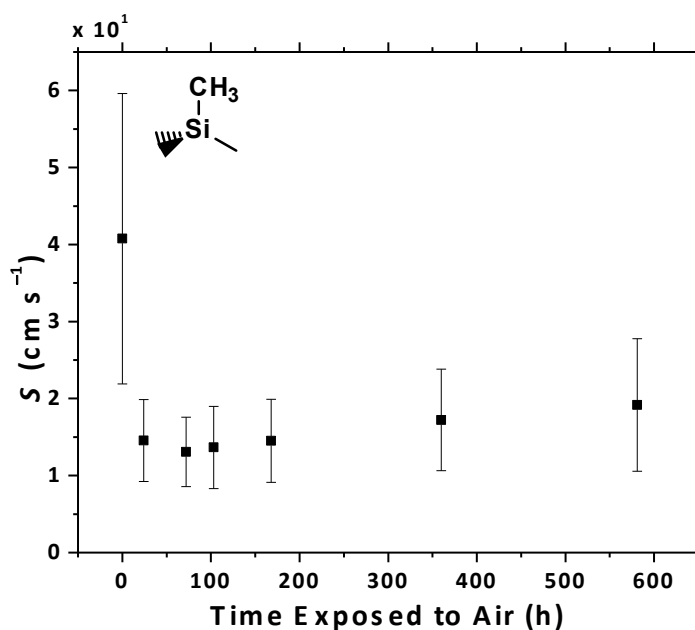


Figure 1.7. S behavior as a function of time exposed to air for $\text{CH}_3\text{-Si}(111)$ surfaces. The error bars represent 1 standard deviation about the mean.

1.4 SURFACE CHEMISTRY APPLICATIONS

Functionalization of semiconductor surfaces is motivated by a variety of applications, often inspired by the conventional uses for semiconductors in transistors, photovoltaics, and photoelectrochemical cells. In particular, surface chemistry offers the opportunity to control the interface between semiconductors and other functional device components, which may include catalysts, metals, conductive polymers, or protecting layers (e.g. metal oxides). Organic scaffolds grafted to semiconductor surfaces can potentially allow for molecular-level control over the interface between the semiconductor and other device components to achieve optimal interactions from a mechanical, physical, and electrical perspective.

As part of the development of efficient and cost-effective photoelectrochemical water splitting cells for fuel generation, the interface between catalysts and semiconductors, depicted in Figure 1.8, is critical to the performance of the device. The catalyst/semiconductor must exhibit favorable mechanical interactions such that the catalyst remains closely associated with the surface, but the energetics at the interface must be favorable to effect the maximum output potential. Surface chemistry provides an exceptional opportunity to control the mechanical properties of the catalyst/semiconductor interface while also allowing for favorable energetics at the interface.

Some of the common catalysts that have been developed for use in photoelectrochemical water splitting cells include Pt, MoSe₂,⁶⁷ CoP,⁶⁸ and Fe₃P⁶⁹ for proton reduction and IrO₂ and NiO_x⁷⁰⁻⁷¹ for water oxidation. These catalysts are all metals,

metal oxides, or alloys that have defined work functions that may not form highly rectifying junctions between Si and the catalyst. Additionally, these catalysts can be deposited by a number of methods, including electrodeposition, drop-cast and sinter, or oxidation of a metallic film. Surface chemistry can be used to (1) tune the semiconductor band edges such that the energetics at the semiconductor/catalyst interface produces the maximum output voltage and (2) to improve the mechanical and physical robustness of the semiconductor/catalyst interaction so the catalyst film or particles remain bound to the semiconductor during long-term device operation. Organic linkers between Si and the catalysts could provide a scalable and robust method of improving Si/catalyst interfaces to achieve the properties required by photoelectrochemical systems.

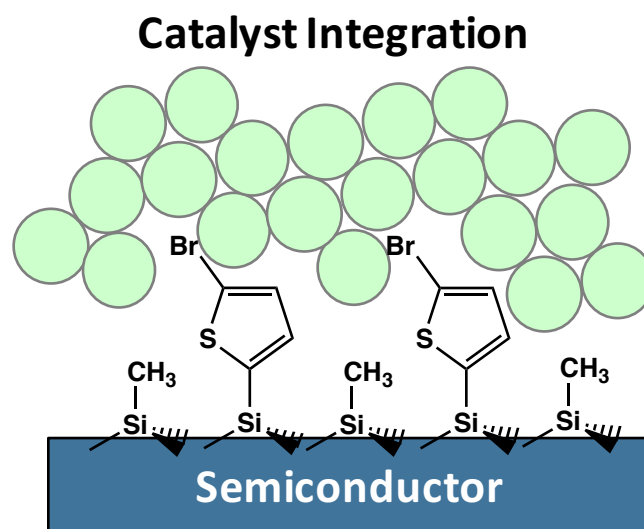


Figure 1.8. Example of linker chemistry that could be used to integrate catalyst nanoparticles (green circles) with semiconductor surfaces. The linker would be designed to impart a favorable surface dipole that positions the semiconductor band edges relative to the catalyst work function to effect the maximum device performance. Additionally, the mechanical interaction between the Si and the catalyst would be improved by the organic linker layer.

Related to Si/catalyst interfaces are Si/metal interfaces (Figure 1.9). The photovoltaic and transistor industries commonly form silicon/metal interfaces in established device manufacturing processes. In some cases, an ohmic Si/metal contact is desired, while other applications require a rectifying Si/metal interaction. Deposition of metals directly on Si–H surfaces by common materials processing methods (e.g. evaporation and sputtering) typically results in the formation of metal silicides that are detrimental to the formation of rectifying contacts. Even soft deposition methods, such as electrodeposition or drop-cast and sinter, can yield high surface recombination velocity because of the propensity of the Si–H surface to oxidize and form surface states.

Organic modification of Si surfaces with molecules that impart a surface dipole that favorably positions the semiconductor band edges to effect the maximum energy out of the

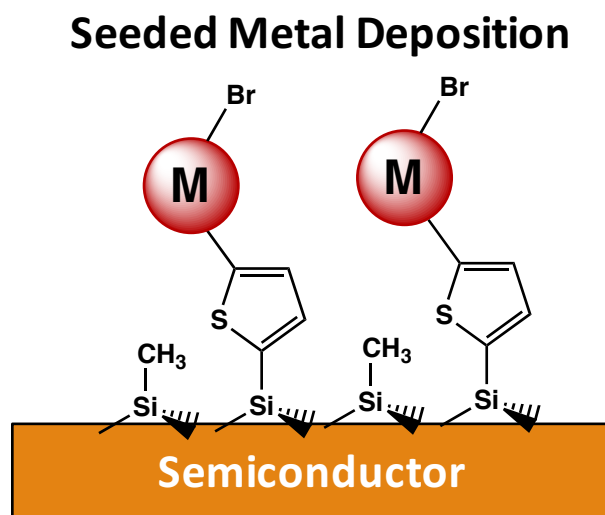


Figure 1.9. Example of linker chemistry that could be used to control metal deposition on a Si surface. The surface chemistry can be used to impart favorable band-edge positions to produce a maximum voltage at the Si/metal interface. Additionally, the reactivity of organic groups on the surface can be exploited to direct metal deposition and form nanopatterns on the surface.

Si/metal interface. Organic modification, such as methyl termination, has been demonstrated to allow for metals that typically form metal silicides, such as Au, to be deposited on CH₃-Si(111) surfaces by soft deposition methods (e.g. electrodeposition or drop-cast and sinter).⁷²⁻⁷³ Additionally, many organic groups, such as the C-Br bond in Figure 1.9, are reactive towards metals in solution and could be used to direct and control the deposition of metals on semiconductor surfaces. By patterning the surface with reactive organic groups, metals can conceivably be deposited in a controlled manner to yield nanopatterned semiconductor/metal contacts. Organic modification of silicon surfaces offers a unique opportunity to achieve unprecedented control over the deposition of metals on semiconductor surfaces.

Hybrid organic/inorganic solar cells have been developed as alternatives to conventional photovoltaics and photoelectrochemical cells. The polymer can serve as a light absorber as well as a conductive medium to direct charge transfer in solid state devices. Additionally, conductive polymers are generally less susceptible to oxidation or corrosion than inorganic semiconductors and thus could potentially be used as protection layers in photoelectrochemical cells. Moreover, polymer layers are typically flexible, and the development of robust semiconductor/polymer interfaces could allow for the development of improved flexible devices that are more cost effective than traditional photovoltaics.

Covalent bonding between silicon and monomer units for polymers, including thiophene and other conductive polymers,^{45, 74-75} has been investigated previously. Figure 1.10 gives an example in which the monomer 3,4-ethylenedioxythiophene is used to

covalently bind poly(3,4-ethylenedioxythiophene) to the Si surface. The electrical properties of the silicon/polymer junction could conceivably be influenced by the nature of the bonding at the Si/polymer interface, with covalent bonds allowing for improved interfacial conductivity and performance. In particular, poly(3,4-ethylenedioxythiophene) (PEDOT)-poly(styrenesulfonate) (PSS) has been proposed for use in photoelectrochemical devices as a means of providing an ohmic electrical contact between the photoanode and photocathode, while allowing for proton transfer through the membrane and flexibility of the device.⁷⁶ Silicon surface chemistry offers a means of providing molecular-level control over the interface between silicon and conductive polymers in order to develop efficient and novel device architectures.

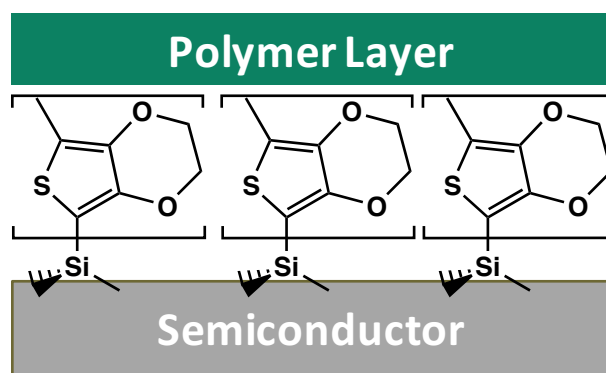


Figure 1.10. Example of a silicon/polymer junction formed by a covalent bond between the two materials. The surface of Si could be modified with monomers, in this case 3,4-ethylenedioxythiophene, and electropolymerization of the corresponding conductive polymer on the surface could allow for improved electrical conductivity and performance.

One of the current most challenging aspects in the development of stable and cost effective photoelectrochemical cells for water splitting is the corrosion or passivation of photoanodes in aqueous electrolyte. Silicon, for example, rapidly oxidizes and passivates, forming an electrically insulating layer on the surface, when used as a photoanode without sufficient protection from oxidation on the surface. Recently, metal oxide layers, such as TiO_2 and NiO_x , deposited on Si substrates by atomic-layer deposition (ALD) or sputtering have been shown to allow for long-term operation of Si and other semiconductors as photoanodes.^{70-71, 77} The interface between the Si and the metal oxide could conceivably be controlled on a molecular level by seeding the metal oxide deposition on the surface using a molecular scaffold that is reactive toward the metal oxide precursor.

Currently, semiconductors are most widely used by the microelectronics industry, which has increasingly relied on semiconductor-based integrated circuit technology to manufacture increasingly powerful computers and other electronic devices. A common motif in integrated circuit technology is the development of increasingly smaller nodes in the pursuit of increased power efficiency and performance. Currently, 14 nm nodes are the smallest commercially available technology, with 10 nm nodes set to be available in the near future. At such small node sizes, the surface of the semiconductor material becomes a significantly larger percentage of the overall node. The deposition of metal oxides, which are commonly used as gate materials in processor nodes, by ALD can be controlled using surface chemistry to direct the metal oxide deposition. Figure 1.11 presents an example of using reactive surface groups, such as aldehydes or alcohols, to direct the assembly of ALD-grown films, like aluminum oxide or titanium dioxide, on silicon surfaces.

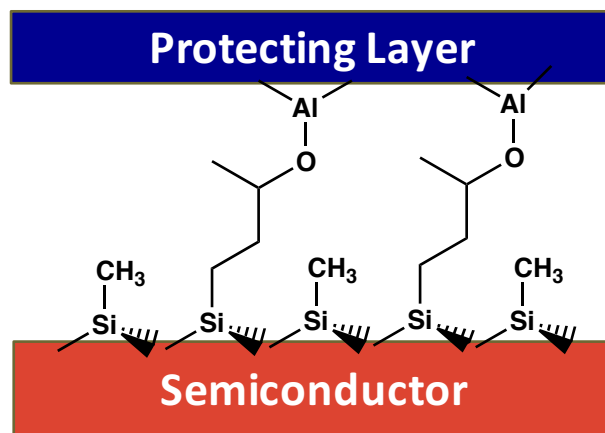


Figure 1.11. Example of a silicon/metal oxide junction formed by atomic layer deposition of trimethylaluminum (TMA) on a mixed methyl/propionaldehyde surface. The aldehyde groups on the surface are reactive toward the TMA precursor, allowing for growth of the TMA to be controlled by the chemical nature of the surface.²¹

This thesis presents a collection of studies that are intended to advance the field of silicon surface chemistry toward achieving the applications described above. Chapters 2 and 3 are focused on the characterization of short-chain unsaturated alkyl groups covalently bound to Si and investigating the reactivity of these groups. This work is broadly applicable to the development of improved interfacial chemistries at Si interfaces. Chapter 4 is focused on achieving control over the molecular surface dipole and band-edge positions through surface functionalization in order to improve the interfaces between silicon and the functional device components described above. Finally, Chapter 5 describes a mechanistic study into the reaction of H-Si(111) surfaces with methanol to improve the understanding of self-limiting, molecular charge transfer reactions at Si surfaces.

1.5 REFERENCES

1. Buriak, J. M. Organometallic Chemistry on Silicon and Germanium Surfaces. *Chem. Rev.* **2002**, *102*, 1271-1308.
2. Wayner, D. D. M.; Wolkow, R. A. Organic Modification of Hydrogen Terminated Silicon Surfaces. *Journal of the Chemical Society, Perkin Transactions 2* **2002**, 23-34.
3. Bent, S. F. Organic Functionalization of Group IV Semiconductor Surfaces: Principles, Examples, Applications, and Prospects. *Surf. Sci.* **2002**, *500*, 879-903.
4. Neergaard Waltenburg, H.; Yates, J. T. Surface Chemistry of Silicon. *Chem. Rev.* **1995**, *95*, 1589-1673.
5. Ibach, H.; Rowe, J. E. Hydrogen Adsorption and Surface Structures of Silicon. *Surf. Sci.* **1974**, *43*, 481-492.
6. Rappich, J.; Lewerenz, H. J. In Situ Fourier Transform Infrared Investigation on the Electrolytic Hydrogenation of n-Silicon (111). *J. Electrochem. Soc.* **1995**, *142*, 1233-1237.
7. Dittrich, T.; Rauscher, S.; Bitzer, T.; Aggour, M.; Flietner, H.; Lewerenz, H. J. Electronic Properties of n-Si(111) during Electrochemical Surface Transformation toward H-Termination. *J. Electrochem. Soc.* **1995**, *142*, 2411-2413.
8. Rappich, J.; Jungblut, H.; Aggour, M.; Lewerenz, H. J. Electrochemical Smoothing of Silicon (111). *J. Electrochem. Soc.* **1994**, *141*, L99-L102.
9. Bitzer, T.; Gruyters, M.; Lewerenz, H. J.; Jacobi, K. Electrochemically Prepared Si(111) 1×1 -H Surface. *Appl. Phys. Lett.* **1993**, *63*, 397-399.

10. Burrows, V. A.; Chabal, Y. J.; Higashi, G. S.; Raghavachari, K.; Christman, S. B. Infrared Spectroscopy of Si(111) Surfaces after HF Treatment: Hydrogen Termination and Surface Morphology. *Appl. Phys. Lett.* **1988**, *53*, 998-1000.
11. Chabal, Y. J.; Higashi, G. S.; Raghavachari, K.; Burrows, V. A. Infrared Spectroscopy of Si(111) and Si(100) Surfaces after HF Treatment: Hydrogen Termination and Surface Morphology. *J. Vac. Sci. Technol. A* **1989**, *7*, 2104-2109.
12. Clark, I. T.; Aldinger, B. S.; Gupta, A.; Hines, M. A. Aqueous Etching Produces Si(100) Surfaces of Near-Atomic Flatness: Strain Minimization Does Not Predict Surface Morphology. *J. Phys. Chem. C* **2010**, *114*, 423-428.
13. Weinberger, B. R.; Peterson, G. G.; Eschrich, T. C.; Krasinski, H. A. Surface Chemistry of HF Passivated Silicon: X-ray Photoelectron and Ion Scattering Spectroscopy Results. *J. Appl. Phys.* **1986**, *60*, 3232-3234.
14. Higashi, G. S.; Chabal, Y. J.; Trucks, G. W.; Raghavachari, K. Ideal Hydrogen Termination of the Si (111) Surface. *Appl. Phys. Lett.* **1990**, *56*, 656-658.
15. Webb, L. J.; Rivillon, S.; Michalak, D. J.; Chabal, Y. J.; Lewis, N. S. Transmission Infrared Spectroscopy of Methyl- and Ethyl-Terminated Silicon(111) Surfaces. *J. Phys. Chem. B* **2006**, *110*, 7349-7356.
16. Linford, M. R.; Fenter, P.; Eisenberger, P. M.; Chidsey, C. E. D. Alkyl Monolayers on Silicon Prepared from 1-Alkenes and Hydrogen-Terminated Silicon. *J. Am. Chem. Soc.* **1995**, *117*, 3145-3155.
17. Lattimer, J. R. C.; Blakemore, J. D.; Sattler, W.; Gul, S.; Chatterjee, R.; Yachandra, V. K.; Yano, J.; Brunshwig, B. S.; Lewis, N. S.; Gray, H. B. Assembly, Characterization,

- and Electrochemical Properties of Immobilized Metal Bipyridyl Complexes on Silicon(111) Surfaces. *Dalton Trans.* **2014**, *43*, 15004-15012.
18. Lattimer, J. R. C.; Brunswig, B. S.; Lewis, N. S.; Gray, H. B. Redox Properties of Mixed Methyl/Vinylferrocenyl Monolayers on Si(111) Surfaces. *J. Phys. Chem. C* **2013**, *117*, 27012-27022.
19. O'Leary, L. E.; Rose, M. J.; Ding, T. X.; Johansson, E.; Brunswig, B. S.; Lewis, N. S. Heck Coupling of Olefins to Mixed Methyl/Thienyl Monolayers on Si(111) Surfaces. *J. Am. Chem. Soc.* **2013**, *135*, 10081-10090.
20. Li, M.; Dai, M.; Chabal, Y. J. Atomic Layer Deposition of Aluminum Oxide on Carboxylic Acid-Terminated Self-Assembled Monolayers. *Langmuir* **2009**, *25*, 1911-1914.
21. O'Leary, L. E.; Strandwitz, N. C.; Roske, C. W.; Pyo, S.; Brunswig, B. S.; Lewis, N. S. Use of Mixed CH₃-/HC(O)CH₂CH₂-Si(111) Functionality to Control Interfacial Chemical and Electronic Properties During the Atomic-Layer Deposition of Ultrathin Oxides on Si(111). *J. Phys. Chem. Lett.* **2015**, *6*, 722-726.
22. Strother, T.; Cai, W.; Zhao, X.; Hamers, R. J.; Smith, L. M. Synthesis and Characterization of DNA-Modified Silicon (111) Surfaces. *J. Am. Chem. Soc.* **2000**, *122*, 1205-1209.
23. Strother, T.; Hamers, R. J.; Smith, L. M. Covalent Attachment of Oligodeoxyribonucleotides to Amine-Modified Si (001) Surfaces. *Nucleic Acids Res.* **2000**, *28*, 3535-3541.

24. Nemanick, E. J.; Solares, S. D.; Goddard, W. A.; Lewis, N. S. Quantum Mechanics Calculations of the Thermodynamically Controlled Coverage and Structure of Alkyl Monolayers on Si(111) Surfaces. *J. Phys. Chem. B* **2006**, *110*, 14842-14848.
25. Lehner, A.; Kohl, F.; Franzke, S. A.; Graf, T.; Brandt, M. S.; Stutzmann, M. Photoconductivity and Spin-Dependent Photoconductivity of Hydrosilylated (111) Silicon Surfaces. *Appl. Phys. Lett.* **2003**, *82*, 565-567.
26. Bansal, A.; Lewis, N. S. Stabilization of Si Photoanodes in Aqueous Electrolytes through Surface Alkylation. *J. Phys. Chem. B* **1998**, *102*, 4058-4060.
27. Bansal, A.; Lewis, N. S. Electrochemical Properties of (111)-Oriented n-Si Surfaces Derivatized with Covalently-Attached Alkyl Chains. *J. Phys. Chem. B* **1998**, *102*, 1067-1070.
28. Bansal, A.; Li, X.; Lauermann, I.; Lewis, N. S.; Yi, S. I.; Weinberg, W. H. Alkylation of Si Surfaces Using a Two-Step Halogenation/Grignard Route. *J. Am. Chem. Soc.* **1996**, *118*, 7225-7226.
29. Tian, F.; Taber, D. F.; Teplyakov, A. V. -NH- Termination of the Si(111) Surface by Wet Chemistry. *J. Am. Chem. Soc.* **2011**, *133*, 20769-20777.
30. Tian, F.; Teplyakov, A. V. Silicon Surface Functionalization Targeting Si-N Linkages. *Langmuir* **2013**, *29*, 13-28.
31. Webb, L. J.; Lewis, N. S. Comparison of the Electrical Properties and Chemical Stability of Crystalline Silicon(111) Surfaces Alkylated Using Grignard Reagents or Olefins with Lewis Acid Catalysts. *J. Phys. Chem. B* **2003**, *107*, 5404-5412.
32. Webb, L. J.; Michalak, D. J.; Biteen, J. S.; Brunschwig, B. S.; Chan, A. S. Y.; Knapp, D. W.; Meyer, H. M.; Nemanick, E. J.; Traub, M. C.; Lewis, N. S. High-Resolution

- Soft X-ray Photoelectron Spectroscopic Studies and Scanning Auger Microscopy Studies of the Air Oxidation of Alkylated Silicon(111) Surfaces. *J. Phys. Chem. B* **2006**, *110*, 23450-23459.
33. Webb, L. J.; Nemanick, E. J.; Biteen, J. S.; Knapp, D. W.; Michalak, D. J.; Traub, M. C.; Chan, A. S. Y.; Brunschwig, B. S.; Lewis, N. S. High-Resolution X-ray Photoelectron Spectroscopic Studies of Alkylated Silicon(111) Surfaces. *J. Phys. Chem. B* **2005**, *109*, 3930-3937.
34. Zhu, X. Y.; Boiadjev, V.; Mulder, J. A.; Hsung, R. P.; Major, R. C. Molecular Assemblies on Silicon Surfaces via Si-O Linkages. *Langmuir* **2000**, *16*, 6766-6772.
35. Terry, J.; Mo, R.; Wigren, C.; Cao, R.; Mount, G.; Pianetta, P.; Linford, M. R.; Chidsey, C. E. D. Reactivity of the H-Si(111) Surface. *Nuclear Instruments and Methods in Physics Research Section B: Beam Interactions with Materials and Atoms* **1997**, *133*, 94-101.
36. Rivillon, S.; Chabal, Y. J.; Webb, L. J.; Michalak, D. J.; Lewis, N. S.; Halls, M. D.; Raghavachari, K. Chlorination of Hydrogen-Terminated Silicon (111) Surfaces. *J. Vac. Sci. Technol. A* **2005**, *23*, 1100-1106.
37. Florio, J. V.; Robertson, W. D. Chlorine Reactions on the Si(111) Surface. *Surf. Sci.* **1969**, *18*, 398-427.
38. Li, Z.; Kamins, T. I.; Li, X.; Williams, R. S. Chlorination of Si Surfaces with Gaseous Hydrogen Chloride at Elevated Temperatures. *Surf. Sci.* **2004**, *554*, L81-L86.
39. Rivillon, S.; Amy, F.; Chabal, Y. J.; Frank, M. M. Gas Phase Chlorination of Hydrogen-Passivated Silicon Surfaces. *Appl. Phys. Lett.* **2004**, *85*, 2583-2585.

40. Eves, B. J.; Lopinski, G. P. Formation and Reactivity of High Quality Halogen Terminated Si(111) Surfaces. *Surf. Sci.* **2005**, *579*, 89-96.
41. Bansal, A.; Li, X.; Yi, S. I.; Weinberg, W. H.; Lewis, N. S. Spectroscopic Studies of the Modification of Crystalline Si(111) Surfaces with Covalently-Attached Alkyl Chains Using a Chlorination/Alkylation Method. *J. Phys. Chem. B* **2001**, *105*, 10266-10277.
42. Cao, P.; Xu, K.; Heath, J. R. Azidation of Silicon(111) Surfaces. *J. Am. Chem. Soc.* **2008**, *130*, 14910-14911.
43. Yu, H.; Webb, L. J.; Heath, J. R.; Lewis, N. S. Scanning Tunneling Spectroscopy of Methyl- and Ethyl-Terminated Si(111) Surfaces. *Appl. Phys. Lett.* **2006**, *88*, -.
44. Gleason-Rohrer, D. C.; Brunshwig, B. S.; Lewis, N. S. Measurement of the Band Bending and Surface Dipole at Chemically Functionalized Si(111)/Vacuum Interfaces. *J. Phys. Chem. C* **2013**, *117*, 18031-18042.
45. He, J.; Patitsas, S. N.; Preston, K. F.; Wolkow, R. A.; Wayner, D. D. M. Covalent Bonding of Thiophenes to Si(111) by a Halogenation/Thienylation Route. *Chem. Phys. Lett.* **1998**, *286*, 508-514.
46. Li, Y.; O'Leary, L. E.; Lewis, N. S.; Galli, G. Combined Theoretical and Experimental Study of Band-Edge Control of Si through Surface Functionalization. *J. Phys. Chem. C* **2013**, *117*, 5188-5194.
47. Plymale, N. T.; Kim, Y.-G.; Soriaga, M. P.; Brunshwig, B. S.; Lewis, N. S. Synthesis, Characterization, and Reactivity of Ethynyl- and Propynyl-Terminated Si(111) Surfaces. *J. Phys. Chem. C* **2015**, *119*, 19847-19862.

48. Cai, W.; Lin, Z.; Strother, T.; Smith, L. M.; Hamers, R. J. Chemical Modification and Patterning of Iodine-Terminated Silicon Surfaces Using Visible Light. *J. Phys. Chem. B* **2002**, *106*, 2656-2664.
49. Gutleben, H.; Lucas, S. R.; Cheng, C. C.; Choyke, W. J.; Yates, J. T. Thermal Stability of the Methyl Group Adsorbed on Si(100): CH₃I Surface Chemistry. *Surf. Sci.* **1991**, *257*, 146-156.
50. Colaianni, M. L.; Chen, P. J.; Gutleben, H.; Yates, J. T. Vibrational Studies of CH₃I on Si(100)-(2×1): Adsorption and Decomposition of the Methyl Species. *Chem. Phys. Lett.* **1992**, *191*, 561-568.
51. Kong, M. J.; Lee, S. S.; Lyubovitsky, J.; Bent, S. F. Infrared Spectroscopy of Methyl Groups on Silicon. *Chem. Phys. Lett.* **1996**, *263*, 1-7.
52. Nemanick, E. J.; Hurley, P. T.; Brunshwig, B. S.; Lewis, N. S. Chemical and Electrical Passivation of Silicon (111) Surfaces through Functionalization with Sterically Hindered Alkyl Groups. *J. Phys. Chem. B* **2006**, *110*, 14800-14808.
53. Nemanick, E. J.; Hurley, P. T.; Webb, L. J.; Knapp, D. W.; Michalak, D. J.; Brunshwig, B. S.; Lewis, N. S. Chemical and Electrical Passivation of Single-Crystal Silicon(100) Surfaces through a Two-Step Chlorination/Alkylation Process. *J. Phys. Chem. B* **2006**, *110*, 14770-14778.
54. Becker, J. S.; Brown, R. D.; Johansson, E.; Lewis, N. S.; Sibener, S. J. Helium Atom Diffraction Measurements of the Surface Structure and Vibrational Dynamics of CH₃--Si(111) and CD₃--Si(111) Surfaces. *J. Chem. Phys.* **2010**, *133*, 104705.
55. Brown, R. D.; Hund, Z. M.; Campi, D.; O'Leary, L. E.; Lewis, N. S.; Bernasconi, M.; Benedek, G.; Sibener, S. J. Hybridization of Surface Waves with Organic Adlayer

- Librations: A Helium Atom Scattering and Density Functional Perturbation Theory Study of Methyl-Si(111). *Phys. Rev. Lett.* **2013**, *110*, 156102.
56. Brown, R. D.; Hund, Z. M.; Campi, D.; O'Leary, L. E.; Lewis, N. S.; Bernasconi, M.; Benedek, G.; Sibener, S. J. The Interaction of Organic Adsorbate Vibrations with Substrate Lattice Waves in Methyl-Si(111)-(1 × 1). *J. Chem. Phys.* **2014**, *141*, 024702.
57. Nihill, K. J.; Hund, Z. M.; Muzas, A.; Díaz, C.; del Cueto, M.; Frankcombe, T.; Plymale, N. T.; Lewis, N. S.; Martín, F.; Sibener, S. J. Experimental and Theoretical Study of Rotationally Inelastic Diffraction of H₂(D₂) from Methyl-Terminated Si(111). *J. Chem. Phys.* **2016**, *145*, 084705.
58. Yu, H.; Webb, L. J.; Ries, R. S.; Solares, S. D.; Goddard, W. A.; Heath, J. R.; Lewis, N. S. Low-Temperature STM Images of Methyl-Terminated Si(111) Surfaces. *J. Phys. Chem. B* **2004**, *109*, 671-674.
59. Royea, W. J.; Juang, A.; Lewis, N. S. Preparation of Air-Stable, Low Recombination Velocity Si(111) Surfaces through Alkyl Termination. *Appl. Phys. Lett.* **2000**, *77*, 1988-1990.
60. Yamada, T.; Kawai, M.; Wawro, A.; Suto, S.; Kasuya, A. HREELS, STM, and STS study of CH₃-Terminated Si(111)-(1 × 1) Surface. *J. Chem. Phys.* **2004**, *121*, 10660-10667.
61. Hunger, R.; Fritsche, R.; Jaeckel, B.; Jaegermann, W.; Webb, L. J.; Lewis, N. S. Chemical and Electronic Characterization of Methyl-Terminated Si(111) Surfaces by High-Resolution Synchrotron Photoelectron Spectroscopy. *Phys. Rev. B* **2005**, *72*, 045317.

62. Briggs, D.; Seah, M. P. *Practical Surface Analysis: Auger and X-ray Photoelectron Spectroscopy*, 2nd ed.; John Wiley & Sons, Inc.: New York, 1990; Vol. 1.
63. Haber, J. A.; Lewis, N. S. Infrared and X-ray Photoelectron Spectroscopic Studies of the Reactions of Hydrogen-Terminated Crystalline Si(111) and Si(100) Surfaces with Br₂, I₂, and Ferrocenium in Alcohol Solvents. *J. Phys. Chem. B* **2002**, *106*, 3639-3656.
64. Jaeckel, B.; Hunger, R.; Webb, L. J.; Jaegermann, W.; Lewis, N. S. High-Resolution Synchrotron Photoemission Studies of the Electronic Structure and Thermal Stability of CH₃- and C₂H₅-Functionalized Si(111) Surfaces. *J. Phys. Chem. C* **2007**, *111*, 18204-18213.
65. Becker, R. S.; Golovchenko, J. A.; McRae, E. G.; Swartzentruber, B. S. Tunneling Images of Atomic Steps on the Si(111)7x7 Surface. *Phys. Rev. Lett.* **1985**, *55*, 2028-2031.
66. Yablonovitch, E.; Allara, D. L.; Chang, C. C.; Gmitter, T.; Bright, T. B. Unusually Low Surface-Recombination Velocity on Silicon and Germanium Surfaces. *Phys. Rev. Lett.* **1986**, *57*, 249-252.
67. Saadi, F. H.; Carim, A. I.; Velazquez, J. M.; Baricuatro, J. H.; McCrory, C. C. L.; Soriaga, M. P.; Lewis, N. S. Operando Synthesis of Macroporous Molybdenum Diselenide Films for Electrocatalysis of the Hydrogen-Evolution Reaction. *ACS Catalysis* **2014**, *4*, 2866-2873.
68. Roske, C. W.; Popczun, E. J.; Seger, B.; Read, C. G.; Pedersen, T.; Hansen, O.; Vesborg, P. C. K.; Brunschwig, B. S.; Schaak, R. E.; Chorkendorff, I.; Gray, H. B.; Lewis, N. S. Comparison of the Performance of CoP-Coated and Pt-Coated Radial

- Junction n⁺p-Silicon Microwire-Array Photocathodes for the Sunlight-Driven Reduction of Water to H₂(g). *J. Phys. Chem. Lett.* **2015**, *6*, 1679-1683.
69. Callejas, J. F.; McEnaney, J. M.; Read, C. G.; Crompton, J. C.; Biacchi, A. J.; Popczun, E. J.; Gordon, T. R.; Lewis, N. S.; Schaak, R. E. Electrocatalytic and Photocatalytic Hydrogen Production from Acidic and Neutral-pH Aqueous Solutions Using Iron Phosphide Nanoparticles. *ACS Nano* **2014**, *8*, 11101-11107.
70. Sun, K.; McDowell, M. T.; Nielander, A. C.; Hu, S.; Shaner, M. R.; Yang, F.; Brunschwig, B. S.; Lewis, N. S. Stable Solar-Driven Water Oxidation to O₂(g) by Ni-Oxide-Coated Silicon Photoanodes. *J. Phys. Chem. Lett.* **2015**, *6*, 592-598.
71. Sun, K.; Saadi, F. H.; Lichterman, M. F.; Hale, W. G.; Wang, H.-P.; Zhou, X.; Plymale, N. T.; Omelchenko, S. T.; He, J.-H.; Papadantonakis, K. M.; Brunschwig, B. S.; Lewis, N. S. Stable Solar-Driven Oxidation of Water by Semiconducting Photoanodes Protected by Transparent Catalytic Nickel Oxide Films. *Proc. Natl. Acad. Sci. U.S.A.* **2015**, *112*, 3612-3617.
72. Maldonado, S.; Knapp, D.; Lewis, N. S. Near-Ideal Photodiodes from Sintered Gold Nanoparticle Films on Methyl-Terminated Si(111) Surfaces. *J. Am. Chem. Soc.* **2008**, *130*, 3300-3301.
73. Maldonado, S.; Lewis, N. S. Behavior of Electrodeposited Cd and Pb Schottky Junctions on CH₃-Terminated n-Si(111) Surfaces. *J. Electrochem. Soc.* **2009**, *156*, H123-H128.
74. Fabre, B.; Lopinski, G. P.; Wayner, D. D. M. Photoelectrochemical Generation of Electronically Conducting Polymer-Based Hybrid Junctions on Modified Si(111) Surfaces. *J. Phys. Chem. B* **2003**, *107*, 14326-14335.

75. Juang, A.; Scherman, O. A.; Grubbs, R. H.; Lewis, N. S. Formation of Covalently Attached Polymer Overlayers on Si(111) Surfaces Using Ring-Opening Metathesis Polymerization Methods. *Langmuir* **2001**, *17*, 1321-1323.
76. Walter, M. G.; Liu, X.; O'Leary, L. E.; Brunshwig, B. S.; Lewis, N. S. Electrical Junction Behavior of Poly(3,4-ethylenedioxythiophene) (PEDOT) Contacts to H-Terminated and CH₃-Terminated p-, n-, and n⁺-Si(111) Surfaces. *J. Phys. Chem. C* **2013**, *117*, 14485-14492.
77. Hu, S.; Shaner, M. R.; Beardslee, J. A.; Lichterman, M.; Brunshwig, B. S.; Lewis, N. S. Amorphous TiO₂ coatings stabilize Si, GaAs, and GaP photoanodes for efficient water oxidation. *Science* **2014**, *344*, 1005-1009.

*Chapter 2*SYNTHESIS, CHARACTERIZATION, AND REACTIVITY OF
ETHYNYL-TERMINATED Si(111) SURFACES

Plymale, N. T.; Kim, Y.-G.; Soriaga, M. P.; Brunschwig, B. S.; Lewis, N. S. Synthesis, Characterization, and Reactivity of Ethynyl- and Propynyl-Terminated Si(111) Surfaces. *J. Phys. Chem. C* **2015**, *119*, 19847–19862. DOI: 10.1021/acs.jpcc.5b05028

2.1 INTRODUCTION

The chemical structure at the surface of crystalline Si determines the susceptibility of the surface to oxidation or corrosion¹⁻³ and strongly influences electronic properties, such as the lifetimes of photogenerated charge carriers⁴⁻⁵ and the positions of the semiconductor band edges.⁶⁻⁷ Accordingly, chemical functionalization of the Si surface is a powerful tool for controlling the physical and chemical properties of interfaces between Si and other materials⁸⁻¹⁰ and is important for numerous applications, such as improving the efficiency of Si-based photovoltaic and photoelectrochemical cells,¹¹⁻¹³ interfacing molecular electronics with Si-based circuitry,¹⁴⁻¹⁶ improving semiconductor device electronics,¹⁷⁻¹⁸ and interfacing molecular catalysts with electrode surfaces.¹⁹⁻²⁰

Wet chemical methods offer a low-cost, scalable approach to functionalization of Si surfaces relative to methods that require vacuum or high temperatures. Covalent attachment of alkyl groups to the Si surface has been shown to impart beneficial

properties, including resistance to oxidation¹⁻³ and low surface recombination velocity.^{4, 21-22} However, correlation of the modified state of the surface with the changes to the chemical and physical properties that accompany the modification requires knowledge of the chemical structure of the functionalized surface. Of the alkyl-terminated surfaces studied, the CH₃-Si(111) surface has been characterized most extensively by methods including vibrational spectroscopy,²³⁻²⁷ high-resolution X-ray photoelectron spectroscopy (XPS),²⁸⁻³¹ low-energy electron diffraction,²⁷⁻²⁸ helium-atom scattering (HAS),³²⁻³⁴ sum-frequency generation (SFG),³⁵ low-temperature scanning tunneling microscopy (STM),³⁶ and surface recombination velocity (*S*) measurements.⁴ This extensive characterization of the CH₃-Si(111) surface has supported the conclusion that nearly full termination of the atop Si(111) sites by Si-C bonds can be achieved, resulting in exceptional surface ordering and stability. The -CH₃ group is unique among saturated hydrocarbons in this respect, whereas termination of Si(111) sites with ethyl (-C₂H₅) groups results in 60-90% termination in Si-C bonds with the remainder of the Si(111) atop sites terminated by Si-H.^{7, 23-24, 37-38} Formation of Si-H at sites not terminated by Si-C leaves the surface susceptible to oxidation and concomitant formation of surface states.²⁹

Despite their favorable properties, CH₃-Si(111) surfaces offer few opportunities for controlled secondary functionalization. Such opportunities have attracted considerable attention for use in solar cells,³⁹⁻⁴⁰ transistors,⁴¹ and molecular sensors.⁴²⁻⁴³ Mixed monolayers have been developed for Si surfaces to impart functionality for facile secondary chemistry while maintaining high Si-C termination and low *S*.²¹ For example,

Heck coupling has been developed for mixed methyl/thienyl monolayers,²² molecular proton-reduction catalysts have been assembled on mixed methyl/bipyridyl monolayers,¹⁹ and growth of Al₂O₃ by atomic-layer deposition (ALD) has been seeded by mixed methyl/propionaldehyde surfaces.¹⁷

Covalent attachment to the Si surface of groups that are similar in size to methyl groups, but that contain versatile functional groups, offers an alternative approach to imparting opportunities for secondary functionalization to Si surfaces that maintain high Si–C termination and low *S*. Ethynyl (–CCH) groups have radial diameters and structures comparable to –CH₃ groups, making them geometrically suitable for nearly full termination of Si(111) atop sites with Si–CCH groups. Moreover, deprotonation of the HCC–Si(111) functional group should, in principle, allow facile chemical reactivity by a variety of synthetic routes and should change the surface functionalization chemistry from electrophilic attack chemistry, such as Cl–Si(111) reacting with RLi or RMgX, to nucleophilic attack chemistry performed by the acetylide-functionalized Si surface. Complete termination of Si(111) atop sites by Si–CCH groups would thus provide an organic scaffold for secondary functionalization of Si surfaces with molecular redox couples and catalysts, heterogeneous catalysts, metal films, ALD-grown protecting films, and conducting polymers, while preserving full termination of the Si atop sites by Si–C bonds.

The synthesis of HCC–Si(111) surfaces has been reported previously and extensively cited.⁴⁴⁻⁴⁸ However, little structural characterization of the HCC–Si(111) surface has been reported, and notable inconsistencies exist between the reported

syntheses and spectroscopic characterization of these surfaces. Further characterization of these surfaces is therefore needed to fully define the functionalization chemistry and to describe the properties of the modified Si(111) surfaces. We describe herein the synthesis of the HCC–Si(111) surfaces and provide extensive characterization of the modified surfaces by transmission infrared spectroscopy (TIRS), high-resolution electron energy-loss spectroscopy (HREELS), X-ray photoelectron spectroscopy (XPS), atomic-force microscopy (AFM), electrochemical scanning-tunneling microscopy (EC-STM), low-energy electron diffraction (LEED), and surface recombination velocity (S) measurements. We also describe an investigation of the reactivity of the terminal alkyne moiety in HCC–Si(111) surfaces. Furthermore, we have compared that reactivity with the reactivity of CH₃–Si(111) and propynyl-terminated Si(111) (CH₃CC–Si(111)) (see Chapter 3) surfaces. Additionally, we have compared the results of the surface analysis presented herein with previously reported data for ethynyl-terminated Si surfaces.

2.2 EXPERIMENTAL SECTION

2.2.1 Materials and Methods

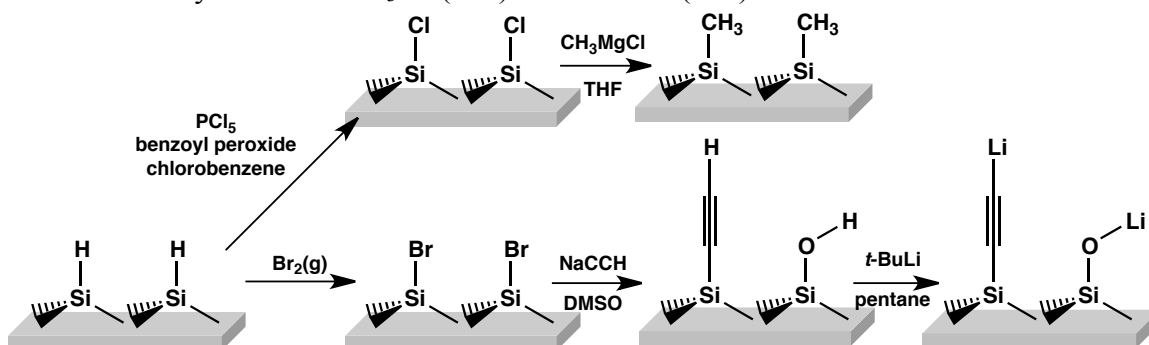
Water (≥ 18.2 M Ω cm resistivity) was obtained from a Barnstead E-Pure system. Ammonium fluoride (NH₄F(aq), 40%, semiconductor grade, Transene Co., Inc., Danvers, MA) was purged with Ar(g) (99.999%, Air Liquide) for 1 h prior to use. Bromine ($\geq 99.99\%$ metal basis, Sigma-Aldrich) was purified by four freeze-pump-thaw cycles and dried over activated 3 Å molecular sieves (Sigma-Aldrich) prior to use. 4-fluorobenzyl chloride (99%, Sigma-Aldrich) was purified by four freeze-pump-thaw cycles and stored

in a $N_2(g)$ -purged glovebox prior to use. Dimethyl sulfoxide (DMSO, anhydrous, $\geq 99.9\%$, Sigma-Aldrich) and *N,N*-dimethylacetamide (DMA, anhydrous, 99.8%, Sigma-Aldrich) were dried over activated 3 Å molecular sieves prior to use. Sodium acetylide (NaCCH, $\geq 95\%$, 17.3% (w/w) in xylenes, Alfa Aesar) was filtered and washed with hexanes (anhydrous, mixture of isomers, $\geq 99\%$, Sigma-Aldrich) under an inert atmosphere. Dry NaCCH powder was stored in sealed glass containers under an inert atmosphere at 22 °C. All other chemicals were used as received.

Czochralski-grown n-Si wafers (Virginia Semiconductor, Fredericksburg, VA) used for the collection of XPS, AFM, EC-STM, LEED, and HREELS data were double-side polished, doped with phosphorus to a resistivity of 1 Ω cm, 381 ± 25 μm thick, and oriented to within 0.1° of the (111) crystal plane. Collection of TIRS data was performed using wafers with one of the following specifications: float-zone-grown n-Si wafers (Silicon Quest International, Santa Clara, CA), double-side polished, doped with phosphorus to a resistivity of 63–77 Ω cm, 435 ± 10 μm thick, and oriented to within 0.5° of the (111) crystal plane; or float-zone-grown Si wafers (Addison Engineering Inc., San Jose, CA), double-side polished, undoped with a resistivity of >20 kΩ cm, 500 ± 20 μm thick, and oriented to within 0.5° of the (111) crystal plane. Undoped, float-zone-grown Si wafers (FZWafers.com, Ridgefield Park, NJ) with a resistivity of 20–40 kΩ cm used for *S* measurements were double-side polished, 300 ± 25 μm thick, and oriented to within 0.5° of the (111) crystal plane. The wafer thickness was determined using calipers prior to performing *S* measurements.

Scheme 2.1 summarizes the methods used for the synthesis of $\text{CH}_3\text{-Si}(111)$ and $\text{HCC-Si}(111)$ surfaces.

Scheme 2.1. Synthesis of $\text{CH}_3\text{-Si}(111)$ and $\text{HCC-Si}(111)$ Surfaces



1. *Preparation of Atomically Flat H-Si(111) Surfaces.* Wafers were cut with a diamond-tipped scribe to the desired size and then rinsed sequentially with water, methanol ($\geq 99.8\%$, EMD), acetone ($\geq 99.5\%$, EMD), methanol, and water. Organic contaminants were removed and the surfaces were oxidized by immersing the wafers in a freshly prepared piranha solution (1:3 v/v of 30% $\text{H}_2\text{O}_2(\text{aq})$ (EMD): 18 M H_2SO_4 (EMD)) at 90–95 °C for 10–15 min. The wafers were rinsed with copious amounts of water and immersed in buffered $\text{HF}(\text{aq})$ (semiconductor grade, Transene Co., Inc.) for 18 s followed by another water rinse. Atomically flat H-Si(111) surfaces were prepared by immersing the wafers in an $\text{Ar}(\text{g})$ -purged solution of $\text{NH}_4\text{F}(\text{aq})$.^{22, 49} Wafers with a miscut angle of 0.5° were etched for 5.5 min, while wafers with a miscut angle of 0.1° were etched for 9.0 min to obtain optimal terrace size. The solution was purged throughout the etching process and the wafers were agitated after each minute of etching to remove bubbles that formed on the surface. After etching, the wafers were rinsed with water and dried under a stream of $\text{Ar}(\text{g})$.

2. *Preparation of Cl-Si(111) Surfaces.* Cl-Si(111) surfaces were prepared for the synthesis of CH₃-Si(111) surfaces (see Chapter 1). Cl-Si(111) surfaces were prepared inside a N₂(g)-purged glovebox with <10 ppm O₂(g). A saturated solution of PCl₅ (≥99.998% metal basis, Alfa Aesar) in chlorobenzene (anhydrous, ≥99.8%, Sigma-Aldrich) was preheated with an initiating amount (<1 mg mL⁻¹) of benzoyl peroxide (≥98%, Sigma-Aldrich) for 1–2 min. The H-Si(111) wafers were rinsed with chlorobenzene and then reacted in the PCl₅ solution at 90 ± 2 °C for 45 min.^{22, 50} Upon completion of the reaction, the solution was drained and the wafers were rinsed with copious amounts of chlorobenzene, followed by tetrahydrofuran (THF, anhydrous, inhibitor-free, ≥99.9%, Sigma-Aldrich).

3. *Preparation of Br-Si(111) Surfaces.* Br-Si(111) surfaces were prepared for the formation of HCC-Si(111) surfaces. Br-Si(111) surfaces were prepared by reaction under ambient light at 22 °C of H-Si(111) with Br₂(g) in a drying chamber connected to a vacuum line as well as to a reservoir of Br₂(l). Immediately after anisotropic etching, H-Si(111) samples were placed inside the drying chamber, which was then evacuated to <20 mTorr. The sample was sealed under vacuum and the Br₂(l) reservoir was quickly opened and closed to allow a visible amount of Br₂(g) into the evacuated drying chamber. The reaction was allowed to proceed for 10 s, after which the Br₂(g) was removed by vacuum to a pressure of <20 mTorr.^{7, 49} The sample was sealed under vacuum and transferred to a N₂(g)-purged glovebox.

4. *Alkylation of Halogenated Si(111) Surfaces.* CH₃-Si(111) surfaces were formed by the reaction of Cl-Si(111) surfaces with CH₃MgCl (1.0–3.0 M in THF, Sigma-

Aldrich or Acros Organics) at $(45\text{--}60) \pm 2$ °C for 3–24 h.²² HCC–Si(111) surfaces were formed by the reaction of Br–Si(111) surfaces with NaCCH in DMSO (allowed to saturate at 22 °C for 12–24 h) at 45 ± 2 °C for 4–8 h. The reaction of Br–Si(111) surfaces with NaCCH was performed in foil-covered test tubes to limit exposure of the NaCCH to ambient light. In several cases, HCC–Si(111) surfaces were also prepared using NaCCH in DMA (allowed to saturate at 22 °C for 12–24 h) at 45 ± 2 °C for 4–8 h. However, HCC–Si(111) surfaces prepared using DMA were not chemically well-defined, so HCC–Si(111) surfaces were prepared using DMSO unless otherwise stated. Upon completion of the reaction, CH₃–Si(111) samples were rinsed with and submerged in THF, removed from the glovebox, and sonicated for 10 min in each of THF, methanol, and water, respectively; HCC–Si(111) samples were rinsed with DMSO or DMA, then rinsed with and submerged in methanol ($\geq 99.8\%$, anhydrous, Sigma-Aldrich), removed from the glovebox, sonicated for 10 min in methanol, and rinsed with water. Samples were dried under a stream of Ar(g) or N₂(g).

5. Deprotonation of HCC–Si(111) Surfaces and Subsequent Reactivity.

Deprotonation of HCC–Si(111) surfaces was achieved by soaking the wafers in *tert*-butyllithium (*t*-BuLi, 1.7 M in pentane, Sigma-Aldrich) for 1 h at room temperature inside a N₂(g)-purged glovebox and subsequently rinsing with hexanes. Deprotonation was also performed for 1 h at room temperature using *n*-butyllithium (*n*-BuLi, 1.6 M in hexane, Sigma-Aldrich), lithium 2,2,6,6-tetramethylpiperidide (LiTMP, 1.0 M in THF, Sigma-Aldrich), lithium hexamethyldisilazide (LiHMDS, 1.0 M in hexane, Sigma-Aldrich) or lithium diisopropylamide (LDA, 1.0 M in THF/hexanes, Sigma-Aldrich) and

yielded similar results to those reported herein with *t*-BuLi used as the deprotonating agent. The deprotonated wafers were then submerged for 1 h at room temperature in neat CD₃OD (99.6 atom % D, Sigma-Aldrich) to yield DCC–Si(111) surfaces or for 4 h at 50 ± 2 °C in neat 4-fluorobenzyl chloride to attach 4-fluorobenzyl groups to the surface. DCC–Si(111) surfaces were allowed to dry inside the glovebox and were sealed inside a centrifuge tube for transport to the IR spectrometer. Surfaces functionalized with 4-fluorobenzyl groups were rinsed with THF, submerged in THF, and removed from the glovebox. The wafers were then rinsed with water, dried under Ar(g), and transported to the XPS for analysis.

2.2.2 Instrumentation

1. Transmission Infrared Spectroscopy. TIRS data were collected using a Thermo Scientific Nicolet 6700 Fourier-transform infrared (FTIR) spectrometer equipped with an electronically temperature-controlled (ETC) EverGlo mid-IR source, a thermoelectric-cooled deuterated L-alanine doped triglycine sulfate (DLaTGS) detector, a KBr beam splitter, and a N₂(g) purge. A custom attachment allowed Si samples (1.3 × 3.2 cm) to be mounted such that the incident IR beam was either 74° or 30° with respect to the sample surface normal. At 74° (Brewster's angle for Si), IR modes parallel and perpendicular to the surface are observed, and at 30°, parallel modes remain visible, while perpendicular modes are greatly diminished in intensity.²³ Reported spectra are averages of 1500 consecutive scans collected at a resolution of 4 cm⁻¹. The baseline was flattened and peaks resulting from water absorption were subtracted in the reported spectra. Background SiO_x and H–Si(111) spectra were recorded separately for each sample prior

to subsequent functionalization. Data were collected and processed using OMNIC software v. 9.2.41.

2. *High-Resolution Electron Energy-Loss Spectroscopy.* HREELS data were collected at pressures of $<5 \times 10^{-10}$ Torr using an LK Technologies ELS5000 model spectrometer equipped with a multichannel analyzer (MCA). Spectra were collected in the specular geometry for the instrument, with the electron impact and scattering angle both at 55° with respect to the sample surface plane. The monochromatic electron beam had an energy of 5.0 eV for $\text{CH}_3\text{-Si}(111)$ surfaces and 2.8 eV for $\text{HCC-Si}(111)$ surfaces. Prior to acquiring data, $\text{CH}_3\text{-Si}(111)$ samples were annealed to 350°C for 1 h in a separate vacuum chamber, while spectra of $\text{HCC-Si}(111)$ samples were acquired without annealing. The y-axis value of each data point was averaged with the eight nearest-neighbor points to smooth the spectra.

3. *Low-Energy Electron Diffraction.* LEED patterns were collected at pressures $<5 \times 10^{-9}$ Torr using an LK Technologies RVL2000 instrument equipped with reverse-view optics, allowing images to be collected from behind the electron-gun assembly. The patterns were collected using a filament current of 3.05 A, a CAN voltage of 6.0 V, a screen voltage of 3.0 kV, and a retarding voltage of 100 V. The incident electron-beam energy was varied from 30–60 eV, and images exhibiting sharp patterns were obtained using a Canon EOS Rebel Tli camera with a 10 s exposure.

4. *X-ray Photoelectron Spectroscopy and Thermal Stability Measurements.* XPS data were collected at pressures $<5 \times 10^{-9}$ Torr using a Kratos AXIS Ultra spectrometer

described previously and equipped with a monochromatic Al K α X-ray source (1486.7 eV), a hybrid electrostatic and magnetic lens system, and a delay-line detector.^{7, 49} Photoelectrons were collected at 90° with respect to the surface plane of the sample, with the lens aperture set to sample a 700 × 300 μm spot. The instrument was operated by Vision Manager software v. 2.2.10 revision 5. Survey and high-resolution scans were collected with analyzer pass energies of 80 eV and 10 eV, respectively. No signals from Cl, Br, Mg, Na, or Li impurities were detected on alkylated samples prepared as described. When HCC–Si(111) surfaces were prepared using DMA as the solvent, however, residual Br and N were often observed by XPS.

Thermal stability in vacuum was studied by collecting XP spectra as a function of annealing temperature. Samples were mounted on a resistive heating stage that consisted of a molybdenum puck heated with a tungsten wire. Stainless-steel clips affixed the sample to the molybdenum stage. The temperature was monitored by a type E thermocouple gauge affixed on the molybdenum stage immediately below the sample. Samples were heated to the desired temperature at a ramp rate of 10 °C min⁻¹ and were held at the indicated temperature for 30 min. The samples were allowed to cool to 22–30 °C prior to collection of XPS data.

5. *Surface Recombination Velocity Measurements.* *S* measurements were performed by use of a contactless microwave conductivity decay apparatus described previously.²⁰⁻²² Electron-hole pairs were formed by a 20 ns, 905 nm laser pulse from an OSRAM diode laser with an ETX-10A-93 driver. For each laser pulse, the decay in reflected microwave intensity was monitored by a PIN diode connected to an

oscilloscope. All recorded decay curves were averages of 64 consecutive decays. Between measurements, samples were stored in air-filled centrifuge tubes in the dark.

6. *Atomic-Force Microscopy.* AFM images were collected using a Bruker Dimension Icon AFM operated by Nanoscope software v. 8.15. Images were collected in ScanAsyst mode using Bruker ScanAsyst-Air probes. The scanner z-range was set to 2 μm and a ScanAsyst noise threshold of 50–100 pm was used. Surface topography data were collected at a scan rate of 0.5–1.0 Hz for 1 μm^2 images. Data were processed using Nanoscope Analysis software v. 1.40.

7. *Electrochemical Scanning-Tunneling Microscopy.* In situ EC-STM studies were performed with a Nanoscope E (Digital Instruments, Santa Barbara, CA) equipped with a three-electrode potentiostat. The electrochemical cell was custom-crafted from Kel-F (Emco Industrial Plastics, Inc.) and fitted with a Pt counter and a Pt pseudoreference electrode calibrated against a Ag/AgCl reference cell. Tungsten tips were prepared by electrochemical etching of 0.25 mm diameter tungsten wire in 1.0 M KOH(aq) at a 15 V AC applied potential. All images were obtained under potential control in 0.1 M HClO₄(aq) with a high-resolution scanner in constant-current mode without post-scan processing.

2.2.3 Data Analysis

1. *Fitting and Quantification of XPS Data.* High-resolution XP spectra were analyzed using CasaXPS software v. 2.3.16. The peak positions for XP spectra were calibrated using the Si 2p_{3/2} peak, which was set to be centered at 99.68 eV.²⁸ For bulk

Si⁰ and Si¹⁺ doublets, the ratio of the peak area of the Si 2p_{1/2}:2p_{3/2} was set to 0.51 and the width of the two peaks was set equal.²⁸ Shirley backgrounds were used for all high-resolution data except when analyzing small amounts of SiO_x in the 102–104 eV range, for which a linear background was applied. C 1s and F 1s high-resolution spectra were fitted using the Voigt function GL(30), which consists of 70% Gaussian and 30% Lorentzian character. Si 2p photoemission signals for bulk Si⁰ and Si¹⁺ species were fitted using asymmetric Lorentzian line shapes convoluted with a Gaussian of the form LA(*a*, *b*, *n*), where *a* and *b* determine the asymmetry of the line shape and *n* specifies the Gaussian width of the function. LA(1.2, 1.4, 200) was found to fit consistently. Contributions from high-order SiO_x in the range of 102–104 eV were fit to a single peak using the GL(30) function.

The thickness (*d*_A) of the overlayer species A was estimated by XPS for HCC–Si(111) surfaces using the substrate-overlayer model⁵¹⁻⁵²

$$\left(\frac{I_A}{I_{Si}}\right)\left(\frac{SF_{Si}}{SF_A}\right)\left(\frac{\rho_{Si}}{\rho_A}\right) = \left(\frac{1 - e^{-\frac{d_A}{\lambda_A \sin\theta}}}{e^{-\frac{d_A}{\lambda_{Si} \sin\theta}}}\right) \quad (2.1)$$

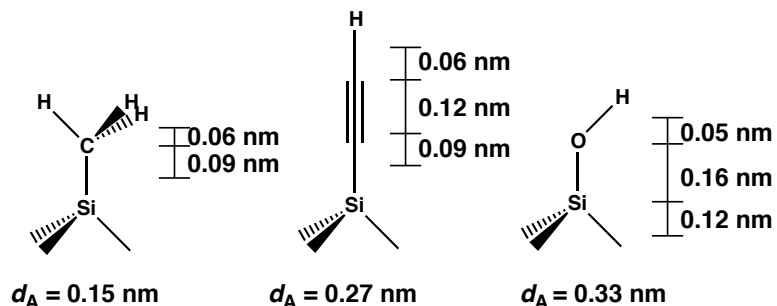
where *I*_A is the area under the photoemission peak arising from the overlayer species A, *I*_{Si} is the area under the Si 2p photoemission signal, *SF*_{Si} is the instrument sensitivity factor for Si 2p (0.328), and *SF*_A is the instrument sensitivity factor for the overlayer species A, which is 0.278 for C 1s photoelectrons in hydrocarbon overlayers. For the hydrocarbon overlayers, *I*_A is the total area under the C 1s photoemission signal corresponding to all C atoms in the overlayer, which is the signal at 284.3 eV for CH₃–Si(111) surfaces and 284.5 eV for HCC–Si(111) surfaces. For Si–OH, *I*_A is the sum of the

area under the Si 2p photoemission signal at 100.5 eV and 101.1 eV. For SiO_x, I_A is the area under the Si 2p photoemission signal appearing from 102–104 eV. The density of Si (ρ_{Si}) is 2.3 g cm⁻³, and the density of the overlayer species A (ρ_A) is 3.0 g cm⁻³ for hydrocarbon overlayers.³⁰ HCC–Si(111) surfaces exhibited a fractional monolayer (ML) coverage of ~0.63 ML, so the assumed density of the overlayer was adjusted to model an overlayer with 63% of the density of a full monolayer (1.9 g cm⁻³). When estimating the thickness of Si–OH or SiO_x overlayers, the quantity $(SF_{\text{Si}}/SF_A)(\rho_{\text{Si}}/\rho_A)$ reduces to a normalizing constant of 1.3 to account for the difference in Si 2p photoelectron signal intensity for Si–OH or SiO_x relative to bulk Si.⁵² The attenuation length for the overlayer species (λ_A) has been estimated to be 3.6 nm for C 1s photoelectrons moving through hydrocarbon overlayers⁵³⁻⁵⁴ or 3.4 nm for Si 2p photoelectrons moving through Si–OH or SiO_x overlayers.⁵³⁻⁵⁴ The attenuation length for Si 2p photoelectrons (λ_{Si}) moving through hydrocarbon overlayers has been estimated to be 4.0 nm.⁵³⁻⁵⁴ For Si–OH or SiO_x overlayers, the value of $\lambda_A = \lambda_{\text{Si}} = 3.4$ nm. The angle between the surface plane and the photoelectron ejection vector (θ) is 90°. The thickness of the overlayer species A was calculated using an iterative process.

The fractional monolayer coverage for the overlayer species A (Φ_A) was estimated by dividing the measured thickness, d_A , by the calculated thickness of 1 ML of overlayer species A, depicted in Scheme 2.2. The thickness of 1 ML of each hydrocarbon overlayer was estimated by summing the bond lengths for the species containing C, but excluding Si and H. For Si–OH overlayers, the thickness of 1 ML was estimated to be the distance from the bottom of the atop Si atom to the top of the O atom. The thickness of 1

ML of SiO_x was estimated to be 0.35 nm.^{3, 52} Assuming uniform overlayers, the value of Φ_A represents the fraction of surface Si(111) sites that were modified with the overlayer species of interest.

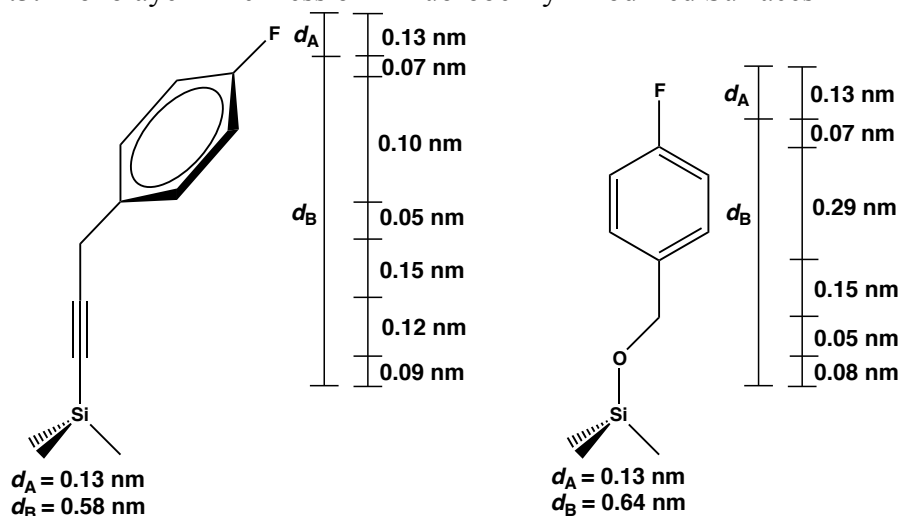
Scheme 2.2. Monolayer Thickness of Surface-Bound $-\text{CH}_3$, $-\text{CCH}$, and $-\text{OH}$ Groups



The fractional monolayer coverage for 4-fluorobenzyl-modified HCC-Si(111) and SiO_x surfaces was estimated using a three-layer model⁵⁵⁻⁵⁶

$$\left(\frac{I_A}{I_{\text{Si}}}\right)\left(\frac{SF_{\text{Si}}}{SF_A}\right)\left(\frac{\rho_{\text{Si}}}{\rho_A}\right) = \left(\frac{1 - e^{-\frac{d_A}{\lambda_{\text{Si}} \sin \theta}}}{e^{-\frac{-(d_A + d_B)}{\lambda_{\text{Si}} \sin \theta}}}\right) \quad (2.2)$$

where d_A is the thickness of the bound F atom and d_B is the thickness of the hydrocarbon layer between the Si crystal and the F atom. The value of SF_A for F 1s photoelectrons is 1.00 and the density of the overlayer was assumed to be the same as for HCC-Si(111) surfaces, 1.9 g cm^{-3} . For F 1s photoelectrons, the value of λ_A is 1.6 nm.⁵² Scheme 2.3 shows the two proposed structures for 4-fluorobenzyl-modified HCC-Si(111) and SiO_x surfaces along with the calculated thickness for d_A and d_B . Since the ratio d_A/d_B is known from Scheme 2.3, eq 2.2 can be expressed in terms of d_A and solved using an iterative process. The measured thickness d_A was divided by the calculated thickness of 1 ML of F atoms, 0.13 nm, to give the fractional monolayer coverage of 4-fluorobenzyl groups.

Scheme 2.3. Monolayer Thickness of 4-Fluorobenzyl-Modified Surfaces

2. Calculation of Surface Recombination Velocity and Surface Trap-State Density.

The minority-carrier lifetime (τ) was estimated by fitting the microwave conductivity decay versus time curve to an exponential decay, as described previously.²⁰⁻²¹ The calculated values of τ were converted to surface recombination velocities (S) for wafers of thickness d using^{4-5, 21}

$$S = \frac{d}{2\tau} \quad (2.3)$$

The surface recombination velocity was converted to an effective trap-state density, N_t , using^{5, 22}

$$N_t = \frac{S}{\sigma v_{th}} \quad (2.4)$$

where the trap-state capture cross section, σ , was 10^{-15} cm^2 and the thermal velocity of charge carriers, v_{th} , was 10^7 cm s^{-1} .⁵ N_t can be used to estimate the absolute number of electrically active defects per surface Si(111) sites by use of the number density of atop Si sites for an unreconstructed Si(111) surface, $\Gamma_{\text{Si}(111)}$, which is $7.83 \times 10^{14} \text{ atoms cm}^{-2}$.

Thus, a wafer with surface recombination velocity S has 1 electrically active defect for every $\Gamma_{\text{Si}(111)}/N_t$ surface sites.

2.3 RESULTS

2.3.1 Transmission Infrared Spectroscopy

Figure 2.1 shows the TIRS data of HCC–Si(111) surfaces prepared in DMSO. The spectra exhibited two closely spaced signals at 3307 and 3296 cm^{-1} , corresponding to ethynyl $\equiv\text{C–H}$ stretching. The close spacing of these peaks resulted from asymmetric (3307 cm^{-1}) and symmetric (3296 cm^{-1}) stretching of the Si–C \equiv C–H unit as a whole. An additional sharp absorbance was observed at 2019 cm^{-1} and was indicative of C \equiv C stretching. These peaks were present at 74° incidence but absent at 30° incidence, which indicated that the stretching modes were oriented perpendicular to the sample surface. A weak but broad peak was observed from 950–1150 cm^{-1} at both angles of incidence and corresponded to transverse optical (Si–O–Si)_{TO} stretching.²³ The appearance of this peak at both angles of incidence suggested that the oxide was primarily subsurface. The spectra collected at 74° incidence also exhibited peaks at 3620, 1294, 920, and 836 cm^{-1} . The signal at 3620 cm^{-1} indicated O–H stretching,⁵⁷ while the signals at 920 and 836 cm^{-1} were characteristic of O–H bending and Si–O stretching, respectively.⁵⁸⁻⁶⁰ The signal at 1294 cm^{-1} was tentatively assigned to O–H stretching coupled with O–H bending, following the analogous signal observed at 1080 cm^{-1} for methoxylated Si(111) surfaces that arises from O–C stretching rocking.⁶¹ The observed signals suggested that a significant portion of the surface was hydroxylated and contained Si–OH functionality.

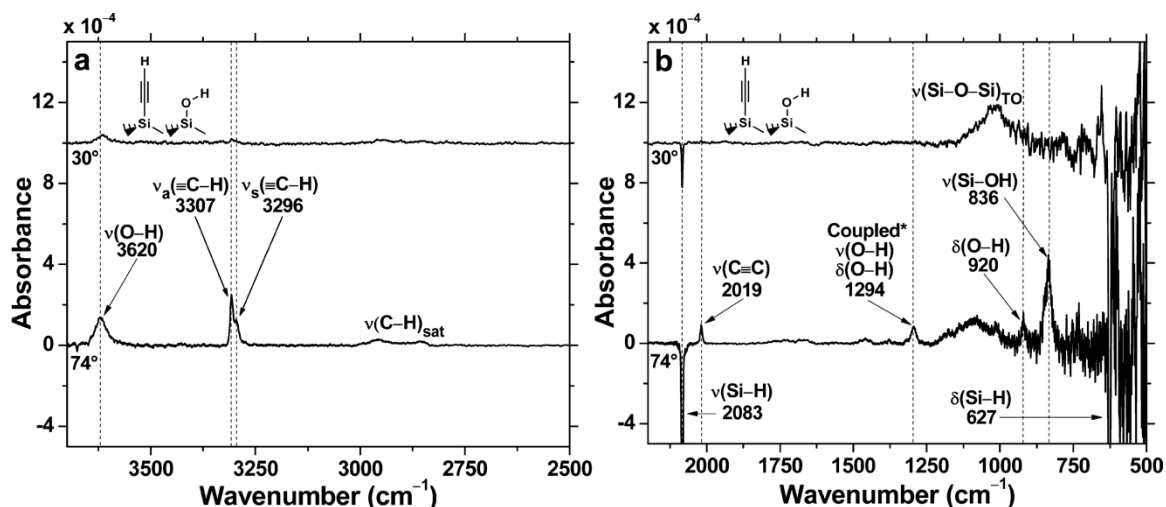


Figure 2.1. TIRS data for HCC-Si(111) surfaces prepared using DMSO, referenced to the H-Si(111) surface, and collected at incidence angles of 74° (bottom) and 30° (top) from the surface normal. Panel a shows the high-energy region, and panel b shows the low-energy region. The negative peaks in panel b resulted from the H-Si(111) background. The peak positions and assignments (* denotes tentative) are indicated in the figure. The subscript “sat” is used to denote C-H stretching signals arising from saturated hydrocarbons. The 30° spectrum is offset vertically for clarity.

TIRS data for HCC-Si(111) surfaces prepared using DMA as the solvent (Figure 2.2) exhibited peaks at 3307, 3292, and 2023 cm^{-1} , consistent with the $\equiv\text{C-H}$ and $\text{C}\equiv\text{C}$ stretching signals observed for the surfaces prepared using DMSO. However, the modes at 3620, 1294, and 920 cm^{-1} were notably absent from surfaces prepared using DMA, and an absorbance at 828 cm^{-1} was lower in energy and intensity compared with the absorbance at 836 cm^{-1} for surfaces that were prepared using DMSO. Thus, surfaces prepared using DMA as the solvent did not exhibit the characteristic peaks for Si-OH sites on the surface. Additionally, surfaces prepared using DMA exhibited significantly stronger saturated hydrocarbon C-H stretching signals at 2947 and 2847 cm^{-1} in addition to several broad peaks between 1250 and 1700 cm^{-1} , which possibly arose from C-H

bending and C–O or C=O stretching. Surfaces prepared using DMA also exhibited a significantly elevated intensity of the (Si–O–Si)_{TO} mode centered at 1058 cm⁻¹.

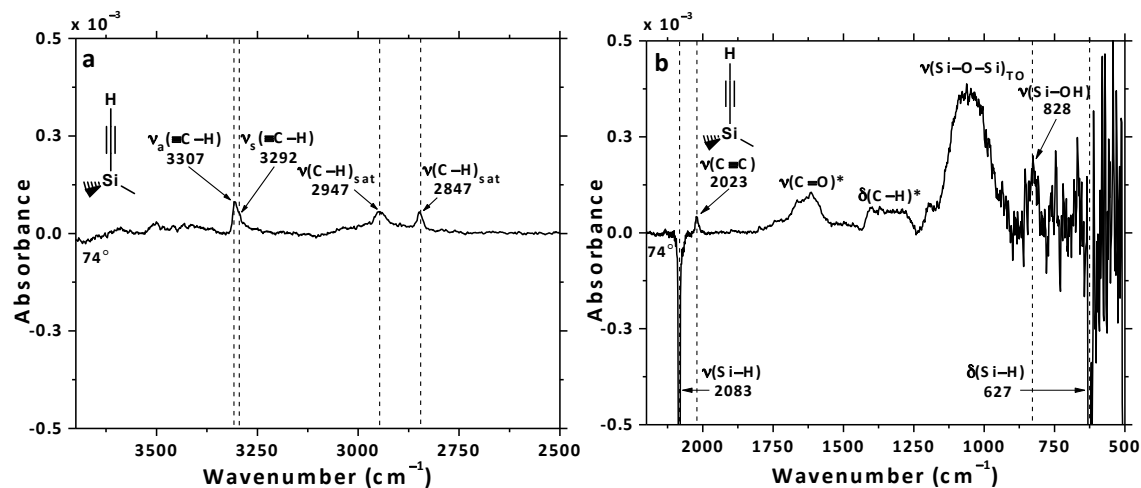


Figure 2.2. TIRS data for HCC–Si(111) surfaces prepared using DMA, referenced to the H–Si(111) surface and collected at 74° incidence. Panel a shows the high-energy region, and panel b shows the low-energy region. The negative peaks in panel b resulted from the H–Si(111) background. The subscript “sat” is used to denote C–H stretching signals arising from saturated hydrocarbons. The peak positions and assignments (* denotes tentative) are indicated in the figure.

Figure 2.3 shows the absence of detectable Si–H stretching for CH₃–Si(111) and HCC–Si(111) surfaces.

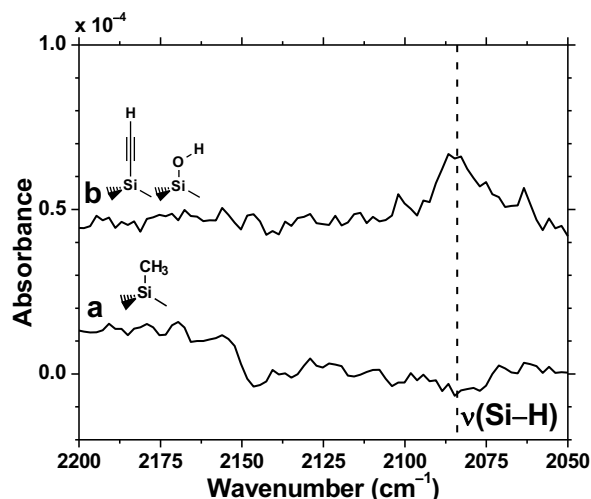


Figure 2.3. TIRS data for (a) CH₃–Si(111) and (b) HCC–Si(111) surfaces referenced to the SiO_x surface. The position of the Si–H stretching peak is indicated by the dotted line.

2.3.2 High-Resolution Electron Energy-Loss Spectroscopy

HREELS data were obtained for HCC–Si(111) surfaces to detect vibrational signals that could not be readily observed by TIRS. The HREELS data for HCC–Si(111) surfaces (Figure 2.4) showed signals centered at 2032 and 3307 cm⁻¹, corresponding to C≡C stretching and ethynyl ≡C–H stretching motions, respectively. A peak centered at 648 cm⁻¹ is assignable to Si–C stretching, indicating that the ethynyl units had been covalently attached to the Si(111) surface. The presence of a peak at 2954 cm⁻¹ arose from adventitious hydrocarbon species adsorbed to the sample surface, and a signal centered at 1072 cm⁻¹ corresponded to the (Si–O–Si)_{TO} mode observed by TIRS. A strong signal centered at 842 cm⁻¹ resulted from surface Si–O stretching convoluted with

O–H bending derived from Si–OH surface sites. This assignment is supported by the presence of a peak centered at 3625 cm^{-1} , corresponding to O–H stretching. Thus, the presence of surface Si–CCH and Si–OH groups was confirmed by the HREELS data.

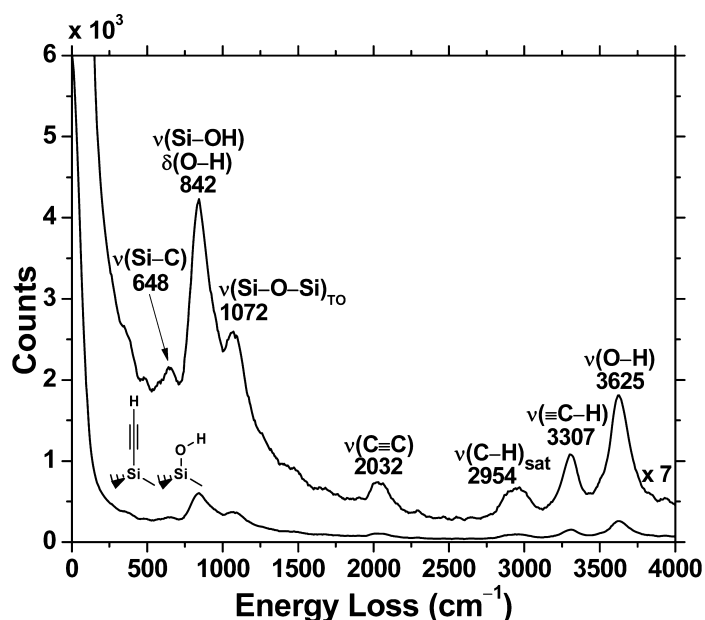


Figure 2.4. HREELS data for HCC–Si(111) surfaces. Data were collected in the specular geometry using an incident beam energy of 2.8 eV, and the fwhm of the elastic peak was 17.3 meV. The subscript “sat” is used to denote C–H stretching signals arising from saturated hydrocarbons. The raw spectrum (bottom) is shown with the magnified spectrum (top) superimposed for clarity. The peak positions and assignments are indicated in the figure.

The vibrational spectroscopy data for HCC–Si(111) surfaces is summarized in

Table 2.1.

Table 2.1. Summary of the Positions and Assigned Modes for the Vibrational Signatures Observed for the HCC–Si(111) Surface

TIRS Frequency (cm⁻¹)	HREELS Frequency (cm⁻¹)^a	Assigned Mode^b	Orientation to Surface^c
3620	3625	$\nu(\text{O-H})$	
3307	3307	$\nu_a(\equiv\text{C-H})$	\perp
3296	3307	$\nu_s(\equiv\text{C-H})$	\perp
weak	2954	$\nu(\text{C-H})_{\text{sat}}$	
2019	2032	$\nu(\text{C}\equiv\text{C})$	\perp
1294	1072	$\nu(\text{O-H})$ and $\delta(\text{O-H})^*$	\perp
~1050	1072	$\nu(\text{Si-O-Si})_{\text{TO}}$	not \perp
920	842	$\delta(\text{O-H})$	\perp
836	842	$\nu(\text{Si-OH})$	\perp
–	648	$\nu(\text{Si-C})$	

^aIn some cases, HREELS signals do not resolve multiple vibrational modes that are observed by TIRS. The HREELS signal with the closest energy to the resolved TIRS signal is paired in the table. ^bThe symbols ν and δ signify stretching and bending motions, respectively, with subscripts a and s indicating whether the mode is asymmetric or symmetric, respectively. The subscript “TO” indicates a transverse optical Si–O–Si motion. The subscript “sat” indicates a C–H stretching signal arising from unidentified saturated hydrocarbons. The subscript “CCH” indicates C≡C stretching peaks arising from –CCH groups. The assignments marked with * are tentative. ^cThe orientation of the vibrational mode with respect to the plane of the sample surface determined by TIRS is given.

2.3.3 X-ray Photoelectron Spectroscopy.

XPS data were collected to provide quantitative information about the species present on HCC–Si(111) surfaces. Survey spectra showed only signals ascribable to Si, C and O, and high-resolution spectra were acquired for the C 1s and Si 2p core levels. Figure 2.5 shows the C 1s high-resolution XP spectrum for HCC–Si(111) surfaces. The C 1s spectrum showed a prominent photoemission signal at 284.5 eV in addition to two signals of lower intensity centered at 285.4 and 287.1 eV. The signals at 285.4 and 287.1 eV exhibited considerable variation in intensity and fwhm between samples and fell within the typical binding energy range for adventitious C on alkyl-terminated Si surfaces.²⁸ The signals arising from adventitious C species exhibited a broad fwhm relative to the signal from the –CCH group at 284.5 eV. The adventitious species exhibited an undefined chemical structure, and thus multiple C species contributed to the

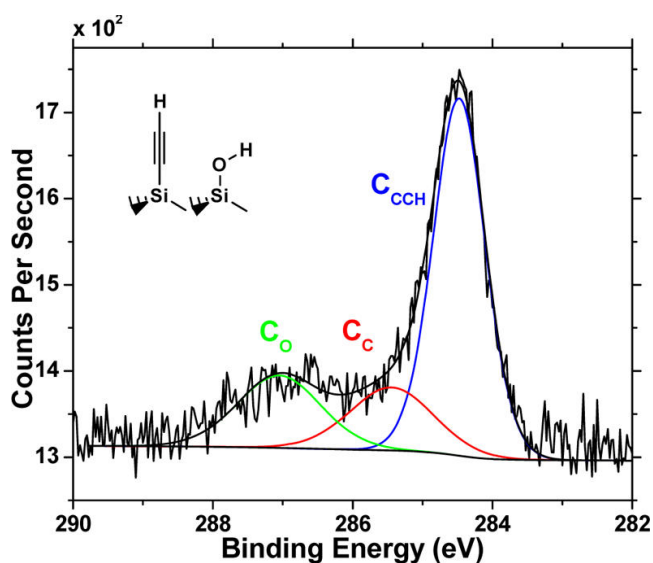


Figure 2.5. High-resolution XP spectrum of the C 1s region for HCC–Si(111) surfaces. The low binding energy C photoemission signal at 284.5 eV (blue, C_{CCH}) arises from both C atoms in the bound –CCH group. The peaks at 285.4 (red, C_C) and 287.1 eV (green, C_O) arise from adventitious C bound to C and C bound to O, respectively.

observed signals and led to broadening. The observed photoemission signal at 284.5 eV was centered at slightly higher binding energy than the photoemission signal ascribed to C bound to Si for CH₃-Si(111) surfaces.^{21, 28} The fwhm of this signal was larger than was typically observed for the C bound to Si signal on CH₃-Si(111) surfaces at 284.3 eV, suggesting multiple contributions to the peak. Additionally, the absence of two fully resolved signals of comparable intensity suggests that the signal centered at 284.5 eV derives from two closely spaced photoemission signals with contributions from both C atoms in the -C≡CH group (C_{CCH}).

Figure 2.6 shows the high-resolution Si 2p spectrum for HCC-Si(111) surfaces. The spectra exhibited a shoulder on the high binding-energy side of the bulk Si 2p_{1/2} peak. This shoulder was fit to two peaks centered at 100.5 and 101.1 eV and was ascribed to

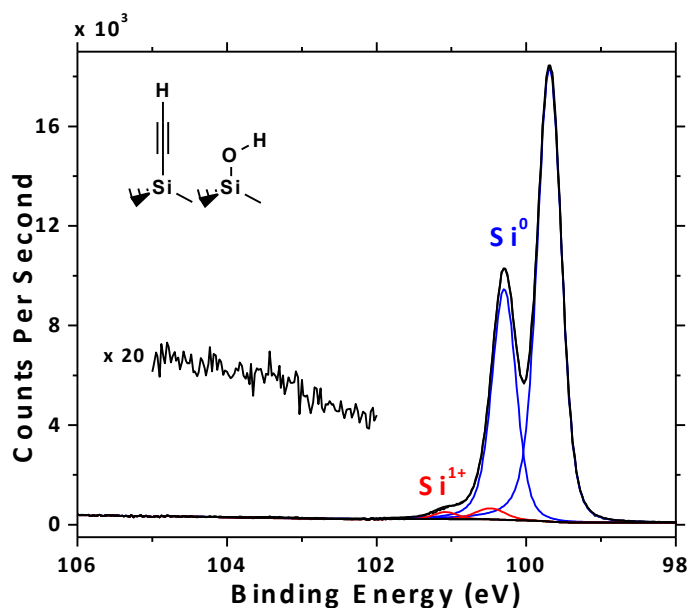


Figure 2.6. High-resolution XPS spectrum of the Si 2p region for HCC-Si(111) surfaces. Contributions from the bulk Si (blue, Si⁰) and Si¹⁺ (red) species are indicated. The region from 102–105 eV in the Si 2p spectrum is magnified to show the absence of detectable high-order SiO_x.

Si–OH groups, in which the surficial Si is bound to a single O atom, consistent with results observed in the vibrational spectra. Some HCC–Si(111) samples showed the presence of a small, broad signal in the range of 102–104 eV, which was ascribed to SiO_x.

The fractional monolayer coverage for HCC–Si(111) surfaces was estimated by XPS, by use of eq 2.1,⁵¹⁻⁵² to yield $\Phi_{\text{Si-CCH}} = 0.63 \pm 0.08$ ML. Only the area under the C 1s photoemission signal at 284.5 eV was used in the quantification of $\Phi_{\text{Si-CCH}}$ because it arises directly from the –CCH group. Vibrational spectroscopic signatures also indicated the presence of Si–OH groups, and XPS was also used to estimate the fractional ML coverage of Si–OH on HCC–Si(111) surfaces by use of eq 2.1⁵¹⁻⁵² to yield $\Phi_{\text{Si-OH}} = 0.35 \pm 0.03$ ML. In addition to Si–OH, high-order oxide signals, between 102 and 104 eV, were observed in limited quantities in the Si 2p spectrum on some HCC–Si(111) surfaces with a fractional ML coverage estimated by eq 2.1⁵¹⁻⁵² of $\Phi_{\text{SiO}_x} = 0.03 \pm 0.02$ ML. The content of high-order SiO_x was near the detection limit for the instrument for most samples, and several samples showed the absence of detectable high-order SiO_x.

The thermal stability of HCC–Si(111) surfaces was investigated in vacuum. Figure 2.7 presents the behavior of HCC–Si(111) surfaces as a function of annealing temperature. Minimal changes to the C 1s and Si 2p high-resolution spectra were observed for HCC–Si(111) surfaces upon annealing to 200 °C. However, heating to 300 °C produced significant broadening of the strongest photoemission signal in the C 1s spectrum, and a shoulder appeared at ~285.1 eV. The C 1s signal further broadened upon heating to 400 and 500 °C, respectively, which suggested that, at elevated temperature, the ethynyl group reacted with adventitious carbon species on the sample and in the

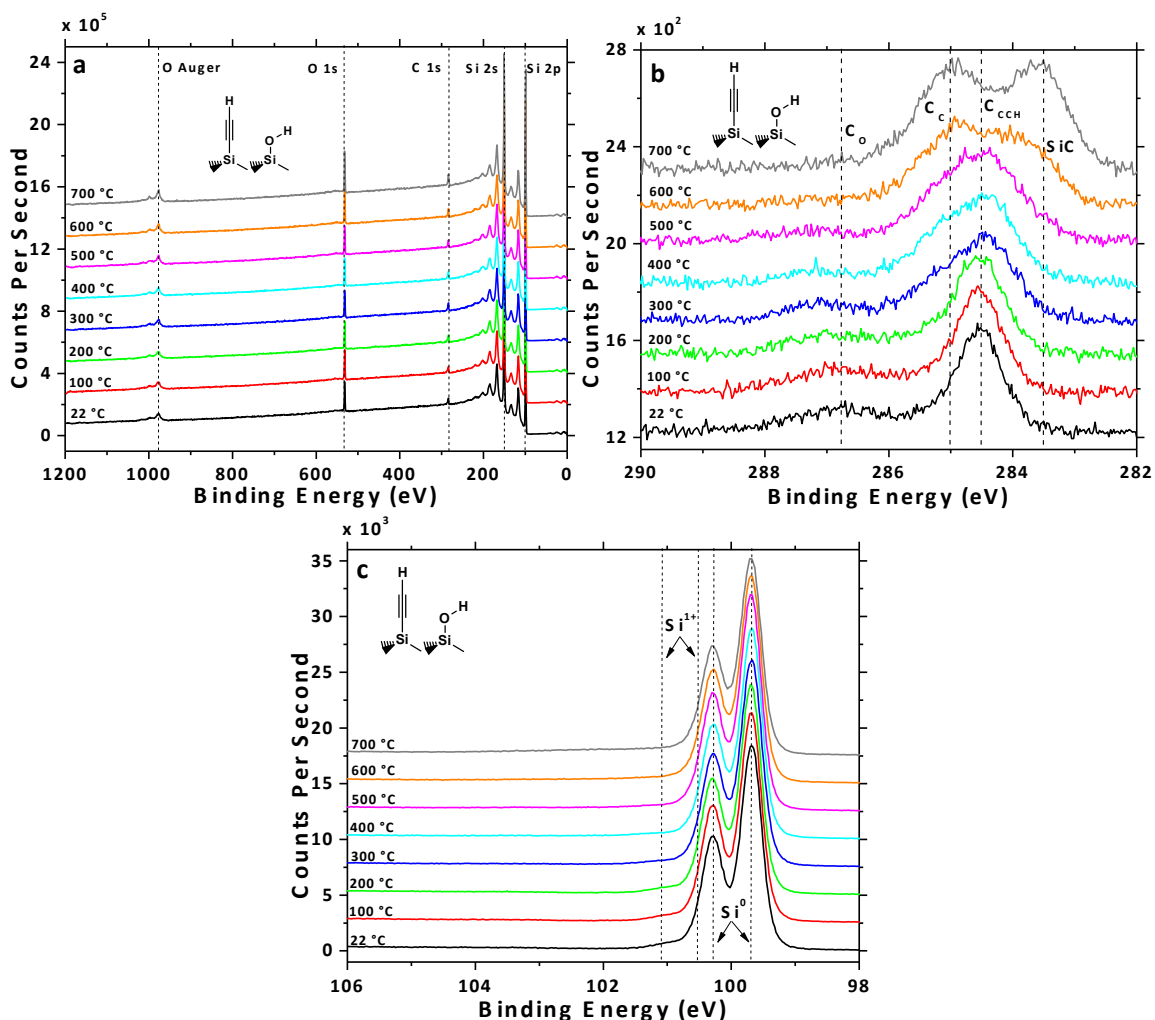


Figure 2.7. Thermal stability in vacuum of HCC-Si(111) surfaces. The annealing temperature is indicated above each spectrum, and the spectra are offset vertically for clarity. The survey spectra (a) showed the presence of only the Si 2p, Si 2s, C 1s, and O 1s core-level peaks along with the O Auger signal and Si plasmon-loss features. The high-resolution C 1s spectra (b) exhibited the peaks arising from C in the ethynyl group (C_{CCH}) and adventitious C (C_C and C_O). Minimal change in the C 1s spectra was observed upon annealing to 200 °C. Broadening was observed as the C 1s peak at ~285.1 eV (C_C) greatly increased in intensity upon heating to 300–500 °C. Heating to 600–700 °C resulted in the appearance of a new C 1s peak at ~283.5 eV (SiC). Si 2p spectra (c) showed gradual smoothing of the shoulder indicated as Si¹⁺ with increased annealing temperature, indicating the loss of surficial Si–OH and formation of Si–O–Si.

vacuum chamber. Heating from 300 to 500 °C reduced the intensity of the signal at 284.5 eV, which indicated that the coverage of the Si(111) surface with chemically defined

ethynyl groups decreased upon heating to this temperature range. Table 2.2 provides the estimated fractional monolayer coverage of the Si(111) surface with chemically defined –CCH groups as a function of annealing temperature. Heating to 600 and 700 °C, respectively, resulted in an increase in intensity and broadening of the overall C 1s signal. A signal at ~283.5 eV, which has been ascribed to silicon carbide (SiC),^{31, 62-63} was observed after annealing to 600 °C and became more prominent after heating the sample to 700 °C. An increase in overall intensity of the C 1s photoemission signal after annealing to 700 °C indicated that additional C species were formed on the surface, though their chemical structure was not readily determined by the XPS measurements performed. The shoulder in the Si 2p photoemission signal on the high binding-energy side of the Si 2p_{1/2} peak became less prominent upon heating past 300 °C, suggesting the removal of surficial Si–OH groups. The survey spectra showed no reduction in O 1s peak intensity as a function of annealing temperature, so the detected O likely inserted between the Si backbonds to produce Si–O–Si. Additionally, a small reduction in the bulk Si 2p

Table 2.2. Estimated Fractional ML Coverage, Φ , of a HCC–Si(111) Surface as a Function of Annealing Temperature

Annealing Temperature (°C)	$\Phi_{\text{Si-CCH}}^a$
22	0.62
100	0.60
200	0.53
300	0.34
400	0.28
500	0.10

^aThe values of Φ were determined using eq (2.1).⁵¹⁻⁵² The appearance of SiC on HCC–Si(111) surfaces upon annealing to 600 °C precluded accurate determination of Φ beyond 500 °C.

signal intensity was observed after heating to 600 and 700 °C, respectively, as a result of the increase in C species on the surface.

2.3.4 Atomic-Force Microscopy, Electrochemical Scanning-Tunneling Microscopy, and Low-Energy Electron Diffraction

Figure 2.8 presents a representative topographical AFM image of an HCC–Si(111) surface. The HCC–Si(111) surface exhibited broad atomic terraces with step edges ~ 0.3 nm in height, consistent with terraces observed on reconstructed Si(111) surfaces in vacuum.⁶⁴ Generally, the surfaces exhibited a low density of particulates adsorbed to the surface, and the density of etch pits observed by AFM was low. The observation of atomic terraces after alkylation was consistent with the grafting of an overlayer with uniform thickness onto the surface of the Si(111) substrate.

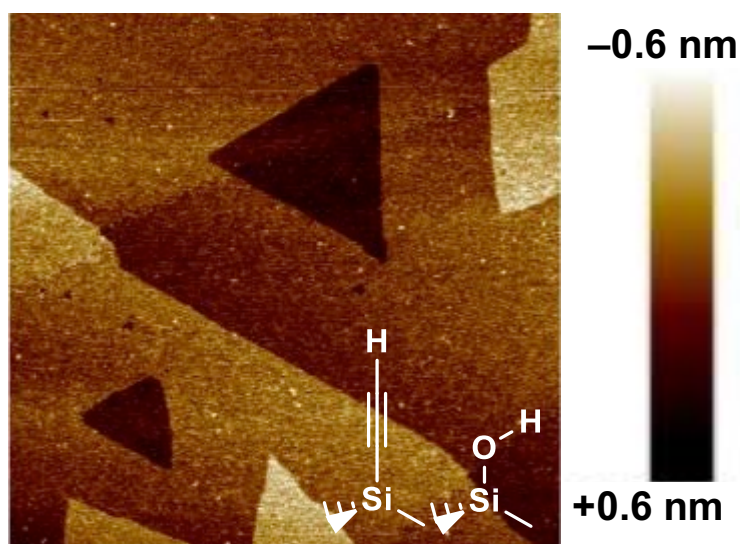


Figure 2.8. Topographical AFM image of the HCC–Si(111) surface. The image is $1 \mu\text{m} \times 1 \mu\text{m}$ with a z-scale of 1.2 nm (-0.6 to $+0.6$ nm).

Figure 2.9 shows a representative EC-STM image of the HCC–Si(111) surface. The HCC–Si(111) surface showed localized areas where species of similar height were observed (representative areas indicated by white circles), consistent with the proposed mixed composition of HCC–Si(111) surfaces, in which a fraction of the surface sites are terminated by Si–OH. The distance between the centers of the areas with similar height was 0.38 nm, which is the same as the distance between Si(111) atop sites.³⁶ The majority of the HCC–Si(111) surface did not exhibit ordering on an atomic scale as observed by room temperature EC-STM.

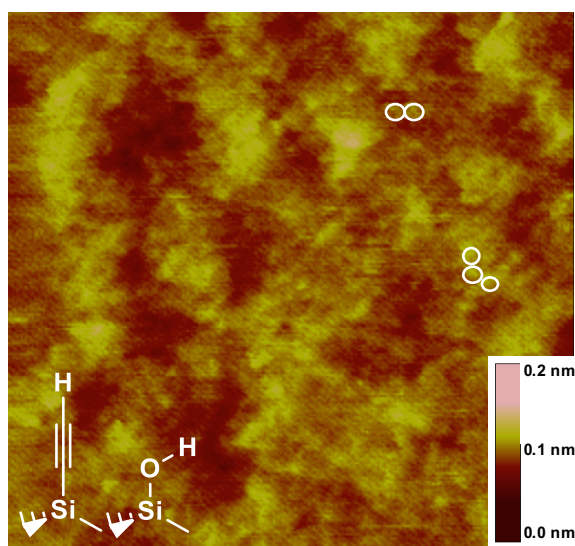


Figure 2.9. EC-STM image of the HCC–Si(111) surface (10 nm ×10 nm) collected at –0.4 V versus Ag/AgCl with a bias voltage of –300 mV and tunneling current of 5 nA. The z-scale is indicated in the figure. The white circles in the figure highlight areas where species of similar height were observed. The distance between the centers of the white circles was 0.38 nm, the same as the distance between Si(111) atop sites. Image courtesy of Y.-G. Kim and M. P. Soriaga.

LEED patterns were collected for HCC–Si(111) surfaces (Figure 2.10) to qualitatively determine the ordering of the top surface layers of the substrate. LEED patterns that exhibit 3-fold symmetry, with diffraction spots forming a hexagon, are indicative of a (1×1) surface unit cell. Generally, LEED has limited sensitivity on the monolayer scale, and disordered Si surfaces that exhibit high crystallinity of the Si immediately below the surface will still display clear diffraction spots. The qualitative intensity of the background relative to the diffraction spots can provide some degree of information about the ordering of the surface layer. HCC–Si(111) exhibited similar 3-fold symmetry with the presence of a hexagonal diffraction pattern appearing at 40 eV beam energy. The background appeared slightly more intense than for CH₃–Si(111) control samples, suggesting a lower level of ordering at the sample surface than for CH₃–Si(111). This behavior was consistent with the observed mixed composition of HCC–Si(111) surfaces, which showed vibrational signatures of Si–CCH and Si–OH groups.

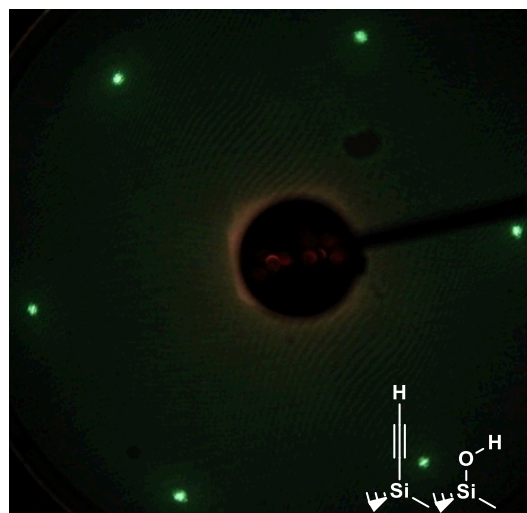


Figure 2.10. Representative LEED pattern for the HCC–Si(111) surface collected at 40 eV incident beam energy.

The HCC–Si(111) and CH₃–Si(111) surfaces exhibited comparably bright and sharp diffraction spots, and the only evidence of lower surface ordering for H–Si(111) samples was in the intensity of the background.

2.3.5 Surface Recombination Velocity Measurements

Figure 2.11 shows the behavior of S determined by use of eq 2.3⁴ for CH₃–Si(111) and HCC–Si(111) surfaces as a function of time in air. Immediately after preparation and cleaning, CH₃–Si(111) and HCC–Si(111) surfaces exhibited S values of $(4 \pm 2) \times 10^1$ and $(2.5 \pm 0.3) \times 10^3 \text{ cm s}^{-1}$, respectively. After being exposed to air for 24 h, the S value for CH₃–Si(111) surfaces decreased to $(1.5 \pm 0.5) \times 10^1 \text{ cm s}^{-1}$, while HCC–Si(111) surfaces exhibited an increase in S to $(3.30 \pm 0.09) \times 10^3 \text{ cm s}^{-1}$. Over extended exposure to air, S for HCC–Si(111) surfaces remained relatively constant at $(3.5 \pm 0.1) \times 10^3 \text{ cm s}^{-1}$.

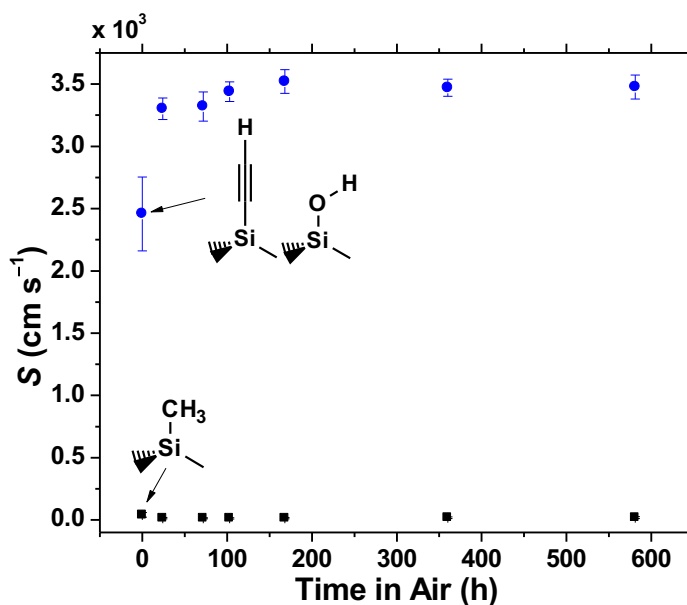


Figure 2.11. S measured as a function of exposure to air for CH₃–Si(111) (black squares) and HCC–Si(111) (blue circles) surfaces. The error bars represent 1 standard deviation about the mean.

The effective trap-state density, N_t , was calculated for $\text{CH}_3\text{-Si(111)}$ and HCC-Si(111) surfaces by use of eq 2.4.⁵ Immediately after preparation, $\text{CH}_3\text{-Si(111)}$ and HCC-Si(111) surfaces were found to have trap-state densities of 4×10^9 and $3 \times 10^{11} \text{ cm}^{-2}$, which is equivalent to 1 trap for every 2×10^5 and 3×10^3 surface sites, respectively. After 581 h of exposure to air, the trap-state densities of $\text{CH}_3\text{-Si(111)}$ and HCC-Si(111) surfaces had adjusted to yield 2×10^9 and $3 \times 10^{11} \text{ cm}^{-2}$, or 1 trap for every 4×10^5 and 2×10^3 surface sites, respectively. The estimated trap-state density for the studied surfaces was below the detection limit for most spectroscopies, hindering the identification of the chemical structures that form the surface trap states.

2.3.6 Reactivity of HCC-Si(111) Surfaces

The reactivity of the terminal alkyne moiety on HCC-Si(111) surfaces was explored by deprotonating the ethynyl group with a strong base. HCC-Si(111) surfaces were soaked in a *t*-BuLi solution to generate putative surface-bound $\text{Si-C}\equiv\text{C-Li}$ groups. Such putative deprotonated surfaces were then soaked in CD_3OD to yield DCC-Si(111) surfaces. Figure 2.12 presents TIRS data for HCC-Si(111) surfaces before and after treatment with *t*-BuLi followed by CD_3OD . This treatment resulted in a reduction in the intensity of the ethynyl $\equiv\text{C-H}$ stretching (3307 and 3296 cm^{-1}) and $\text{C}\equiv\text{C}$ stretching (2019 cm^{-1}) signals as well as in the appearance of new absorption peaks at 2574 , 2559 , and 1897 cm^{-1} . Figure 2.13 shows that the peaks were absent for samples collected at 30° incidence angle, indicating that the groups were oriented perpendicular to the surface. Similar results were obtained using other strong bases, such as *n*-BuLi, LiTMP, LiHMDS, and LDA, as shown in Figure 2.14, indicating that the surface-bound organolithium

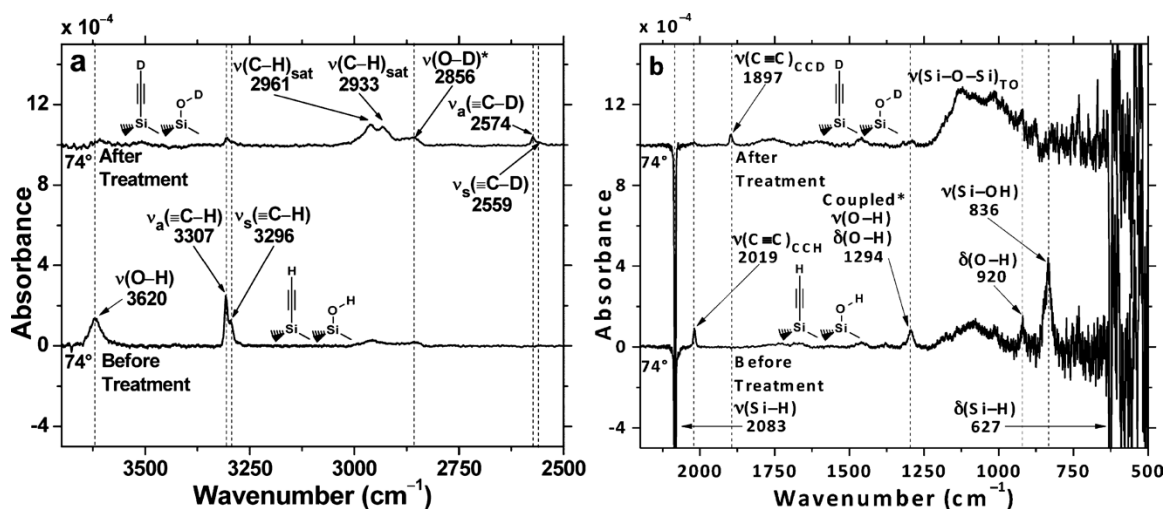


Figure 2.12. TIRS data for HCC-Si(111) surfaces referenced to the H-Si(111) surface before (bottom) and after (top) treatment with *t*-BuLi followed by CD₃OD. Panel a shows the high-energy region, and panel b shows the low-energy region. The peak positions and assignments (* denotes tentative) are indicated in the figure. The subscript “sat” is used to denote C-H stretching signals arising from saturated hydrocarbons and the subscripts CCH and CCD indicate vibrational modes arising from HCC-Si(111) and DCC-Si(111) moieties, respectively. The spectrum shown after treatment was offset vertically for clarity.

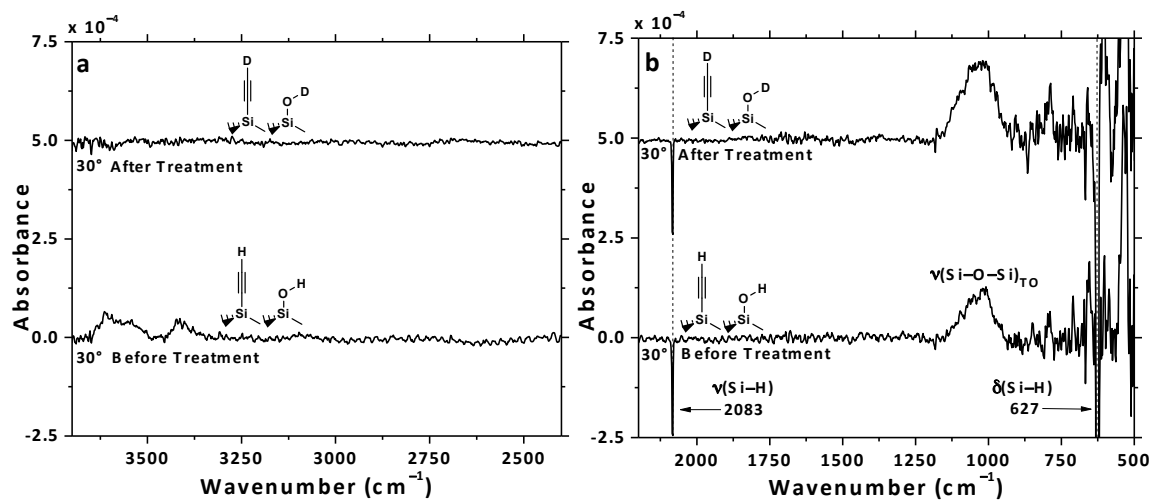


Figure 2.13. TIRS data for HCC-Si(111) surfaces referenced to the H-Si(111) surface collected at 30° incidence angle before (bottom) and after (top) treatment with *t*-BuLi followed by CD₃OD. Panel (a) shows the high-energy region, and panel (b) shows the low-energy region. The negative peaks in panel (b) resulted from the H-Si(111) background. The absence of any signals attributable to -CCD groups after treatment indicates that the modes observed at 74° are perpendicular to the surface. The spectrum collected after treatment is offset vertically for clarity.

species can be generated by reaction routes that are analogous to those displayed by small-molecule terminal alkynes. The shape and spacing of the peaks at 2574 and 2559 cm^{-1} were similar to the signals at 3307 and 3296 cm^{-1} , suggesting that these new peaks arose from $\equiv\text{C}-\text{D}$ asymmetric and symmetric stretching, respectively. The new signal at 1897 cm^{-1} was symmetric and positioned at slightly lower energy than the original $\text{C}=\text{C}$ stretching signal at 2019 cm^{-1} . The signal at 1897 cm^{-1} arose from $\text{C}=\text{C}$ stretching and was shifted to lower energy relative to the $\text{C}=\text{C}$ stretching signal for the $\text{HCC}-\text{Si}(111)$ surface by introduction of the D atom to the ethynyl group. Integration of the area under

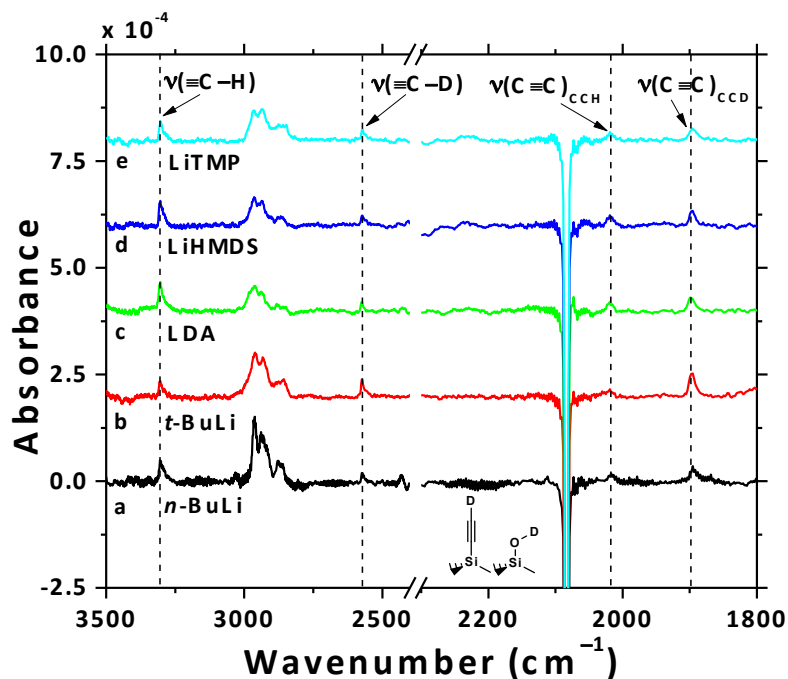


Figure 2.14. TIRS data collected at 74° incidence angle for $\text{HCC}-\text{Si}(111)$ surfaces after treatment with (a) $n\text{-BuLi}$, (b) $t\text{-BuLi}$, (c) LDA, (d), LiHMDS, or (e) LiTMP followed by reaction with CD_3OD . The characteristic peaks corresponding to the $-\text{CCH}$ and $-\text{CCD}$ surface species are indicated by the dotted lines. The negative peak at 2083 cm^{-1} resulted from the $\text{H}-\text{Si}(111)$ background. Spectra collected for all bases yielded comparable peaks ascribable to the surface $-\text{CCD}$ species. The spectra were offset vertically for clarity.

the ethynyl $\equiv\text{C-H}$ stretching peaks at 3307 and 3296 cm^{-1} and under the $\text{C}\equiv\text{C}$ stretching peak at 2019 cm^{-1} in the TIR spectra before and after deuteration showed that the peak area was reduced to roughly 22% of the original area. These data suggested that an estimated 78% of surface-bound ethynyl groups had been converted to $\text{Si-C}\equiv\text{C-D}$ groups by this process.

Treatment of HCC-Si(111) surfaces with $t\text{-BuLi}$ also deprotonated the surface-bound -OH groups, as evidenced by the disappearance of the peak at 3620 cm^{-1} (Figure 2.12). Several new peaks appeared at 2961 , 2933 , and 2856 cm^{-1} in the typical C-H stretching region for adventitious C species, but also resulted from O-D stretching in Si-OD groups. Figure 2.15 shows that this treatment also produced a peak at 2075 cm^{-1} observed in spectra that were referenced to the SiO_x surface, and this signal can be

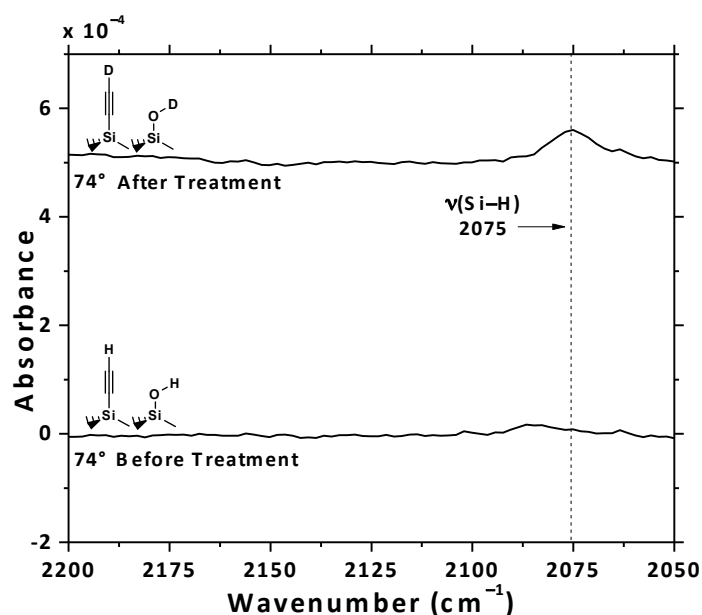


Figure 2.15. TIRS data collected at 74° incidence angle for HCC-Si(111) surfaces referenced to the SiO_x surface before (bottom) and after (top) treatment with $t\text{-BuLi}$ followed by CD_3OD . The center of the Si-H stretching peak is indicated by the dotted line, and the broad peak in the top spectrum at 2075 cm^{-1} is ascribed to Si-H stretching.

ascribed to Si–H stretching. The total area under the Si–H stretching signal was ~8% of the area of the signal on the fully terminated H–Si(111) surface. The vibrational data for the deprotonated DCC–Si(111) surface is summarized in Table 2.3.

Table 2.3. Summary of the Positions and Assigned Modes for the Vibrational Signatures Observed for the DCC–Si(111) Surface

TIRS Frequency (cm⁻¹)	Assigned Mode^a	Orientation to Surface^c
3307	$\nu_a(\equiv\text{C-H})$	\perp
3296	$\nu_s(\equiv\text{C-H})$	\perp
2961	$\nu(\text{C-H})_{\text{sat}}$	
2933	$\nu(\text{C-H})_{\text{sat}}$	
2856	$\nu(\text{O-D})^*$	
2574	$\nu_a(\equiv\text{C-D})$	\perp
2559	$\nu_s(\equiv\text{C-D})$	\perp
2019	$\nu(\text{C}\equiv\text{C})_{\text{CCH}}$	\perp
1897	$\nu(\text{C}\equiv\text{C})_{\text{CCD}}$	\perp
~1050	$\nu(\text{Si-O-Si})_{\text{TO}}$	not \perp

^aThe symbols ν and δ signify stretching and bending motions, respectively, with subscripts a and s indicating whether the mode is asymmetric or symmetric, respectively. The subscript “TO” indicates a transverse optical Si–O–Si motion. The subscript “sat” indicates a C–H stretching signal arising from unidentified saturated hydrocarbons. The subscripts “CCH” and “CCD” indicate C≡C stretching peaks arising from –CCH and –CCD groups, respectively. The assignments marked with * are tentative. ^cThe orientation of the vibrational mode with respect to the plane of the sample surface determined by TIRS is given.

To further demonstrate the reactivity of the lithiated surface, surface-bound Si–C≡C–Li groups were also reacted with neat 4-fluorobenzyl chloride. For comparison, the same reaction was also performed on CH₃–Si(111) surfaces and propynyl-terminated Si(111) (CH₃CC–Si(111)) surfaces (see Chapter 3). Figure 2.16 shows the F 1s XP

spectra for $\text{CH}_3\text{-Si}(111)$, $\text{HCC-Si}(111)$, $\text{CH}_3\text{CC-Si}(111)$, and SiO_x surfaces after sequential reaction with *t*-BuLi followed by 4-fluorobenzyl chloride. $\text{HCC-Si}(111)$ surfaces exhibited a F 1s signal at 687.8 eV after reaction with *t*-BuLi followed by 4-fluorobenzyl chloride. XPS was used to provide a rough estimate of the surface coverage of fluorobenzyl groups by use of eq 2.2⁵⁵ to yield $\Phi_{\text{fluorobenzyl}} = 0.08 \pm 0.03$ ML, and no residual Cl was observed in the Cl 2s region. The absence of Cl indicated that the 4-fluorobenzyl groups were covalently attached to the surface by nucleophilic substitution, and the LiCl product was removed from the surface. Control experiments showed the absence of detectable F by XPS on $\text{CH}_3\text{-Si}(111)$ and $\text{CH}_3\text{CC-Si}(111)$ surfaces that had been reacted sequentially with *t*-BuLi and 4-fluorobenzyl chloride. However, wafers that had been oxidized with a piranha solution and then treated with *t*-BuLi followed by 4-fluorobenzyl chloride produced a F 1s signal centered at 687.0 eV with $\Phi_{\text{fluorobenzyl}} = 0.09$ ML of 4-fluorobenzyl groups bound to the surface. Thus, the 4-fluorobenzyl groups were likely attached at both Si-CCLi and Si-OLi surface sites.

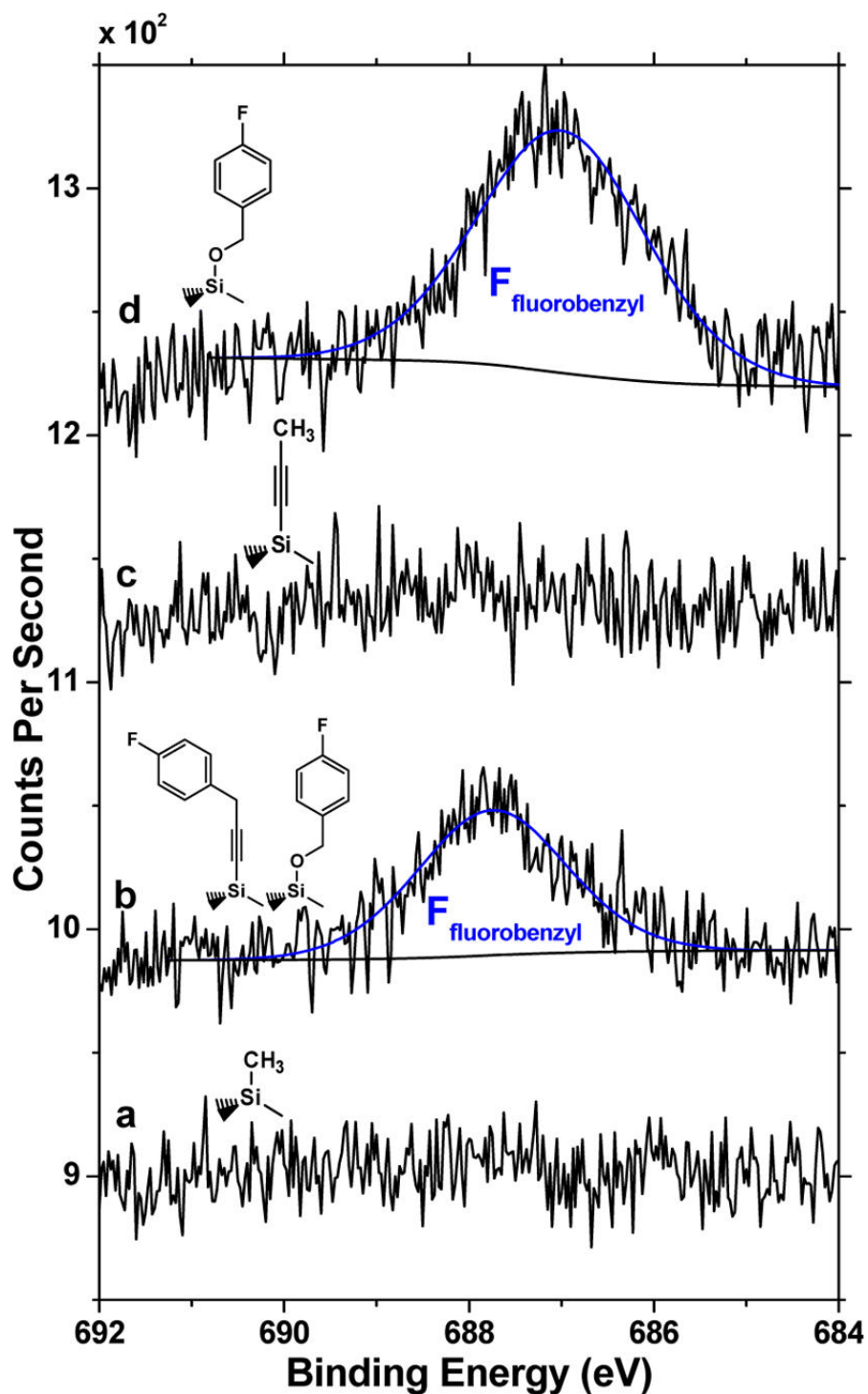


Figure 2.16. High-resolution F 1s XP spectra of (a) $\text{CH}_3\text{-Si}(111)$, (b) $\text{HCC-Si}(111)$, (c) $\text{CH}_3\text{CC-Si}(111)$, and (d) SiO_x surfaces after reaction with *t*-BuLi followed by 4-fluorobenzyl chloride. Only $\text{HCC-Si}(111)$ and SiO_x surfaces showed the presence of detectable F at 687.8 and 687.0 eV, respectively. The proposed structure of the resulting surface is depicted above each spectrum.

2.4 DISCUSSION

2.4.1 Vibrational Spectroscopy of HCC–Si(111) Surfaces

TIRS (Figure 2.1) and HREELS (Figure 2.4) of HCC–Si(111) surfaces prepared using DMSO showed the presence of $\equiv\text{C-H}$, $\text{C}\equiv\text{C}$, and Si-C stretching vibrations, providing strong support for the attachment of ethynyl groups perpendicular to the Si(111) surface. Theoretical calculations have predicted the appearance of a $\equiv\text{C-H}$ stretching mode in the range of 3410 cm^{-1} , with a $\text{C}\equiv\text{C}$ stretching mode expected at $\sim 2075\text{ cm}^{-1}$.⁶⁵ The calculations were performed using uncorrected theoretical harmonic frequencies, however, which tend to yield predicted signals that are higher in energy than experimental results for high-frequency modes. Thus, the experimentally observed modes are in agreement with the theoretical calculations for the HCC–Si(111) surface. The presence of a peak at 648 cm^{-1} in the HREEL spectrum is in close agreement with the theoretical prediction of a Si-C stretching signal at approximately 645 cm^{-1} ,⁶⁵ indicating that the ethynyl groups are covalently bound to the Si(111) surface. Theoretical calculations also predict the presence of a $\equiv\text{C-H}$ bending signal between 568 and 579 cm^{-1} , in addition to a signal between 484 and 492 cm^{-1} resulting from bending of the $\text{Si-C}\equiv\text{C-H}$ unit coupled with phonons in the crystal.⁶⁵ A small peak in the HREEL spectrum at 477 cm^{-1} and a shoulder on the elastic peak at 346 cm^{-1} could possibly result from the $\equiv\text{C-H}$ bending and phonon-coupling vibrations, respectively, but may also arise from Si-O bending or other phonon-coupling modes. However, the limited coverage of the Si(111) surface with ethynyl groups hinders the clear detection of these vibrations by current surface-sensitive vibrational spectroscopy techniques.

TIR spectra (Figure 2.1) exhibited peaks ascribable to Si–OH vibrational modes, with the Si–O bond oriented perpendicular to the surface.^{57-60, 66} The O–H stretching signal exhibited a reduced intensity at 30° incidence, suggesting that the transition was polarized perpendicular to the surface. However, the proposed geometry of a surface-bound Si–O–H group would be expected to have a significant component of the O–H stretch oriented parallel to the surface. One possible explanation for this could involve hydrogen bonding of the hydroxyl groups to adsorbed water, which could affect the orientation of the O–H bond with respect to the surface. Variation of the amount of adsorbed water may have resulted in the observed reduction in the intensity of the O–H stretching peak at 30° incidence. These vibrational signatures are indicative of HO–Si(111) surface sites, indicating that the HCC–Si(111) surfaces are mixed-composition surfaces in which a fraction of the surface sites are alkylated and a fraction are hydroxylated. Few routes are known to the hydroxylation of crystalline Si surfaces without insertion of O into the Si lattice,⁵⁹ and this method has been shown to terminate an estimated 35% of the surface Si(111) sites with –OH groups. The formation of –OH groups on Si surfaces with minimal formation of high-order SiO_x allows for chemical reactions to be performed using versatile hydroxyl group chemistry without introduction of an insulating oxide barrier that is usually intrinsic to oxidized semiconductor surfaces.

The DMSO solvent clearly plays an important role in the formation of Si–OH sites concomitant with Si–CCH sites. Though the DMSO was purchased anhydrous and was dried over molecular sieves prior to use, complete removal of water from DMSO is known to be very difficult, and the surficial –OH groups thus likely arise from trace water

in the solvent. The addition of NaCCH to DMSO with trace water will result in deprotonation of the water to yield NaOH, which can undergo nucleophilic reaction with halogenated surface sites. Reaction of NaCCH with Br-Si(111) surfaces with DMA as the solvent also resulted in the observation of $\equiv\text{C-H}$ and $\text{C}\equiv\text{C}$ stretching vibrational signals, though significant SiO_x and hydrocarbon impurities were also present (Figure 2.2). Thus, the solvent controlled the type of surface oxidation that occurred, and surfaces prepared using DMSO were the most well-defined chemically.

2.4.2 Surface Ordering, Stability, and Defects of HCC-Si(111) Surfaces

Although AFM data showed broad atomic terraces functionalized with uniform overlayers, and LEED patterns were consistent with a (1×1) surface unit cell, room temperature EC-STM images of HCC-Si(111) surfaces showed that these surfaces did not exhibit the same long-range ordering characteristic of $\text{CH}_3\text{-Si}(111)$ surfaces. Instead, HCC-Si(111) surfaces showed localized regions of ordering and exhibited small variations in height that were not consistent with the height of a Si(111) step edge. Assuming that the bright regions in Figure 2.9 indicate areas functionalized with $-\text{CCH}$ groups, while the dark regions are areas functionalized with $-\text{OH}$ groups yielded an estimated coverage of ~ 0.6 ML $-\text{CCH}$ and ~ 0.4 ML $-\text{OH}$, in good agreement with the surface coverage estimates obtained using XPS. The small difference in height observed between regions was indicative of a difference in the density of states, which could result from a difference in orientation of the $-\text{CCH}$ or $-\text{OH}$ groups on the surface. The height difference on the same terrace was small (< 0.1 nm), and the surfaces exhibited localized regions in which ordering was evident, but significant long-range ordering was not

observed for the HCC–Si(111) surface. Given the irreversible nature of the Si–C bond, and the resulting lack of surface mobility of the attached organic groups, steric considerations may in general preclude facile formation of a fully ordered alkylated monolayer over large areas, and the ordering observed for methyl-terminated Si(111) and Ge(111) surfaces⁶⁷ are thus remarkable in this respect.

S measurements of HCC–Si(111) (Figure 2.11) surfaces as a function of time exposed to air suggest that this surface is not well-passivated and exhibited behavior similar to H–Si(111) surfaces. The proposed surface structure contains a partial coverage of –OH groups, and the binding of O to oxide-free Si surfaces generally results in the formation of surface trap states that contribute to the degradation of the electronic properties of the surface. While the trap-state density of HCC–Si(111) surfaces was high compared with CH₃–Si(111) surfaces, the trap-state density was well below the detection limit of most surface-sensitive spectroscopies. The high trap-state density for HCC–Si(111) surfaces most likely resulted from oxidation of the surface, which was already partially oxidized as Si–OH and not well protected at Si–C sites by partial coverage with –CCH groups.

The HCC–Si(111) surface exhibited a lower thermal stability than CH₃–Si(111) surfaces, which are known to be stable up to 450 °C in vacuum.^{28, 31} The ethynyl groups underwent saturation as they reacted with adventitious C species on the sample or in the vacuum chamber, and annealing from 600–700 °C resulted in larger amounts of C on the sample surface. HCC–Si(111) surfaces showed the largest intensity SiC peak upon annealing to 700 °C, and an overall increase in C 1s peak area was observed, suggesting

hydrocarbons in the atmosphere reacted with and were bound to the surface upon heating above 500 °C. These results suggest that the –CCH groups readily undergo reaction with other species adsorbed on the surface and in the vacuum chamber. The results indicate that the chemical reactivity of the surface is increased for HCC–Si(111) surfaces compared with CH₃–Si(111) surfaces.

2.4.3 Reactivity of HCC–Si(111) Surfaces

Terminal alkynes can be deprotonated readily by reaction with a strong base, such as *t*-BuLi. Consistently, HCC–Si(111) surfaces were shown to undergo reaction with *t*-BuLi to form a surface-bound lithium acetylide. Many surface functionalization techniques rely on nucleophilic attack of the surface by a molecular species, whereas generation of a surface-bound nucleophile expands the surface chemistry toolkit for functionalization of Si surfaces. The presence of the surface-bound organolithium was demonstrated by reaction with CD₃OD to yield deuterated ethynyl groups on the surface. TIRS (Figure 2.12) showed the appearance of a pair of $\nu(\equiv\text{C}-\text{D})$ peaks along with a $(\text{C}\equiv\text{C})_{\text{CCD}}$ peak. The difference between the $\nu(\equiv\text{C}-\text{H})$ and $\nu(\equiv\text{C}-\text{D})$ peak positions was $\sim 730\text{ cm}^{-1}$, which is consistent with previous work that has shown the difference in peak position from C–H to C–D stretching to be $\sim 750\text{ cm}^{-1}$ on C₂H₅–Si(111) surfaces.²⁴ The shift from $(\text{C}\equiv\text{C})_{\text{CCH}}$ to $(\text{C}\equiv\text{C})_{\text{CCD}}$ was considerably smaller (122 cm^{-1}) because the D atom interacts indirectly with the C≡C stretching mode.

Attachment of 4-fluorobenzyl groups to the surface of HCC–Si(111) surfaces functionalized $8 \pm 3\%$ of surface sites with 4-fluorobenzyl groups (Figure 2.16). The

absence of Cl observed in Cl 2s spectra suggests that the 4-fluorobenzyl groups were bound to the surface by nucleophilic substitution. Additionally, since no F 1s signal was observed for CH₃-Si(111) and CH₃CC-Si(111) surfaces subjected to the same treatment, the HCC-Si(111) surface appears to possess unique chemistry that allows for the generation of surface-bound nucleophiles. However, SiO_x samples subjected to deprotonation in *t*-BuLi and reaction with 4-fluorobenzyl chloride similarly yielded a surface with ~9% of a ML of 4-fluorobenzyl groups, indicating that surface-bound -OLi groups can also react with 4-fluorobenzyl chloride in a nucleophilic substitution reaction. Thus, deprotonation of HCC-Si(111) surfaces to yield both -CCLi and -OLi groups on the surface allowed both nucleophile species to react with the 4-fluorobenzyl chloride electrophile.

2.4.4 Comparison with Previously Reported Syntheses and Surface Spectroscopy

The synthesis of HCC-Si(111) surfaces has been reported previously, albeit with minimal spectroscopic characterization of the resulting surfaces.⁴⁴⁻⁴⁸ Table 2.4 summarizes the synthetic methods, surface characterization techniques employed, and results of the prior studies. For putative HCC-Si(111) surfaces prepared from Cl-Si(111) surfaces reacted with NaCCH in THF,⁴⁴ the position of the C≡C stretch was reported as 2179 cm⁻¹,⁴⁴ which is 160 cm⁻¹ higher than the signal observed in this work (2019 cm⁻¹) and ~100 cm⁻¹ higher than the upper estimate predicted by theoretical calculations (2075 cm⁻¹).⁶⁵ We attempted to reproduce the results of those reports, but our attempts were unsuccessful except in certain respects on unpredictable occasions. Anodic deposition of HCCMgCl and HCCMgBr on H-Si(111) surfaces has also been reported for the

preparation of HCC–Si(111) and yields a C≡C stretch at $\sim 2040\text{ cm}^{-1}$.⁴⁶⁻⁴⁷ The C≡C stretch at 2019 cm^{-1} observed herein agrees more closely with the behavior of surfaces prepared by anodic deposition, and is in better agreement with theoretical calculations than the signal reported at 2179 cm^{-1} .⁶⁵ HCC–Si(111) surfaces prepared from the reaction of Cl–Si(111) surfaces with NaCCH in xylenes reported no observable C≡C stretch.⁴⁵ Observation of ethynyl ≡C–H stretching at $\sim 3300\text{ cm}^{-1}$ has been reported for samples prepared by anodic deposition that yielded a polymeric layer⁴⁷ as well as for samples prepared by reaction of H/D–Si(111) surfaces with HCCMgBr in THF.⁴⁸ The presence of a Si–C stretching peak at 660 cm^{-1} has only been previously observed for samples prepared by reaction of HCCMgBr with H/D–Si(111) surfaces, which showed incomplete reactivity and contamination from saturated hydrocarbons.⁴⁸ The observation of ethynyl ≡C–H stretching signals at 3307 and 3296 cm^{-1} , in addition to the C≡C stretch at 2019 cm^{-1} and Si–C stretch at 648 cm^{-1} , provides strong evidence for the formation of HCC–Si(111) surfaces using the reaction chemistry described herein.

Table 2.4. Summary of Prior Reports of Synthesis and Characterization of Ethynyl-Terminated Si Surfaces

Publication	Reaction Conditions	Characterization and Evidence for Structure
ref ⁴⁴	Cl-Si(111) reacted with NaCCH in THF to give Si-CCH surfaces, respectively.	XPS: C 1s XP peak at 284.0 eV used to suggest C bound to Si. Coverage estimated to be 0.9 ± 0.1 ML for Si-CCH relative to Si-CH ₃ . No evidence for SiO _x in Si 2p. IR: Si-CCH exhibits C≡C stretch at 2179 cm ⁻¹ polarized perpendicular to the surface. Electrochemical measurements show no Si-H oxidation peak in aqueous electrolyte. Si-CCH surfaces were reacted with <i>n</i> -BuLi, then 4-bromobenzotrifluoride to show C bound to F by XPS.
ref ⁴⁵	Cl-Si(111) reacted with NaCCH in xylenes/mineral oil at 130 °C for 5 h to give Si-CCH surfaces.	XPS: C 1s XP peak at 283.8 eV used to suggest C bound to Si. Coverage with -CCH groups estimated to be 0.97 ± 0.05 ML relative to Si-CH ₃ . Si 2p showed minimal oxidation after preparation, with 0.25 ML of SiO _x present after 6 days in air. IR: Disappearance of Si-H stretching after functionalization was used to show complete termination. Contact-angle measurements with water were $77 \pm 2^\circ$ for the Si-CCH surface. Click chemistry was performed via Cu(I)-catalyzed reaction of Si-CCH surfaces with an azide-functionalized benzoquinone. The surface coverage was estimated to be ~0.07 ML of benzoquinone, which was then removed and ferrocene was attached with a coverage of 0.005 ML.
ref ⁴⁶	Anodic grafting of HCCMgBr in THF to H-Si(111) surfaces. Current density was 100 μA cm ⁻² with a pulse length of 0.1 s for 100 pulses.	IR: The reaction was monitored by IR. As anodic pulses were applied, the Si-H stretching peak at ~2080 cm ⁻¹ was lost and the C≡C stretch at ~2040 cm ⁻¹ peak grew in, though quantitative analysis was precluded by significant overlap of the two signals. The position of the C≡C stretch is in best agreement with the results reported in this work.
ref ⁴⁷	Anodic grafting of HCCMgCl or HCCMgBr in THF to H-Si(111) surfaces. The current density was 0.5 or 0.02 mA cm ⁻² applied over 15–20 min.	SEM indicated the presence of a polymeric layer for all samples prepared. IR: All samples showed disappearance of Si-H after anodic deposition. Samples prepared from HCCMgCl showed acetylenic ≡C-H stretching at ~3300 cm ⁻¹ as well as C≡C stretching at ~2046 cm ⁻¹ . Also present were modes ascribed to the presence of saturated alkyl chains, indicating that the C≡C bond became saturated during grafting and polymerization. Residual Cl was observed on the surface, and the authors postulate it was inserted into the polymer. SXPS: A C 1s XP peak at 283.7 eV was used to qualitatively suggest C bound to Si. Si 2p XP spectra showed shift in surface Si to higher binding energy, further suggesting that the surface Si is bound to C. The observed polymer layer is inconsistent with results reported by Teyssot et al., who concluded the HCCMgBr does not polymerize on H-Si(111) surfaces upon application of anodic current.
ref ⁴⁸	H-Si(111) and D-Si(111) reacted with HCCMgBr in THF at 60–65 °C for 4.25–5 h to yield HCC-Si(111) surfaces	Multiple internal infrared reflection absorption spectroscopy (MI-IRAS) and HREELS used to show vibrational structure. Ethynyl ≡C-H stretch observed at ~3300 cm ⁻¹ and C≡C stretch observed at 2020 cm ⁻¹ , in agreement with the results reported in this work. A peak at 660 cm ⁻¹ was attributed to Si-C stretching. A significant fraction of Si-H and Si-D surface sites remained unreacted. Surfaces were contaminated with saturated hydrocarbons and a small amount of SiO _x was observed.

2.5 CONCLUSIONS

HCC–Si(111) surfaces have been synthesized and characterized by a variety of spectroscopic methods. TIRS and HREELS data show the characteristic vibrational modes for Si–C≡C–H groups covalently bound perpendicular to the surface. HCC–Si(111) surfaces also exhibited the presence of Si–OH vibrational modes when prepared in DMSO. XPS of HCC–Si(111) surfaces exhibited $\Phi_{\text{Si-CCH}} = 0.63 \pm 0.08$ ML and $\Phi_{\text{Si-OH}} = 0.35 \pm 0.03$ ML. The prepared surfaces exhibited no detectable unreacted Si–H or Si–Br sites. Annealing of HCC–Si(111) surfaces in vacuum resulted in the appearance of different C species at elevated temperature, including SiC that formed on the surface. AFM and LEED data showed that the surfaces exhibited terraced structures and ordering comparable to that of CH₃–Si(111) surfaces, though EC-STM data showed that the surfaces did not exhibit the long-range ordering of CH₃–Si(111) surfaces. HCC–Si(111) surfaces were deprotonated using *t*-BuLi to form a surface-bound lithium acetylide, which was shown to undergo a reaction with electrophiles.

The complete vibrational spectra for the HCC–Si(111) surfaces presented in this work definitively establish the covalent attachment of ethynyl and propynyl groups to the Si(111) surface. Vibrational spectroscopy, which is perhaps the most powerful tool for surface structural analysis, used in tandem with XPS, LEED, AFM, EC-STM, and *S* measurements provide a clear picture of the surface structure, allowing for the development of structure-function relationships, new chemistries, and, by extension, new technologies.

2.6 REFERENCES

1. Bansal, A.; Lewis, N. S. Stabilization of Si Photoanodes in Aqueous Electrolytes through Surface Alkylation. *J. Phys. Chem. B* **1998**, *102*, 4058-4060.
2. Bansal, A.; Lewis, N. S. Electrochemical Properties of (111)-Oriented n-Si Surfaces Derivatized with Covalently-Attached Alkyl Chains. *J. Phys. Chem. B* **1998**, *102*, 1067-1070.
3. Webb, L. J.; Lewis, N. S. Comparison of the Electrical Properties and Chemical Stability of Crystalline Silicon(111) Surfaces Alkylated Using Grignard Reagents or Olefins with Lewis Acid Catalysts. *J. Phys. Chem. B* **2003**, *107*, 5404-5412.
4. Royea, W. J.; Juang, A.; Lewis, N. S. Preparation of Air-Stable, Low Recombination Velocity Si(111) Surfaces through Alkyl Termination. *Appl. Phys. Lett.* **2000**, *77*, 1988-1990.
5. Yablonovitch, E.; Allara, D. L.; Chang, C. C.; Gmitter, T.; Bright, T. B. Unusually Low Surface-Recombination Velocity on Silicon and Germanium Surfaces. *Phys. Rev. Lett.* **1986**, *57*, 249-252.
6. Johansson, E.; Boettcher, S. W.; O'Leary, L. E.; Poletayev, A. D.; Maldonado, S.; Brunshwig, B. S.; Lewis, N. S. Control of the pH-Dependence of the Band Edges of Si(111) Surfaces Using Mixed Methyl/Allyl Monolayers. *J. Phys. Chem. C* **2011**, *115*, 8594-8601.
7. Li, Y.; O'Leary, L. E.; Lewis, N. S.; Galli, G. Combined Theoretical and Experimental Study of Band-Edge Control of Si through Surface Functionalization. *J. Phys. Chem. C* **2013**, *117*, 5188-5194.

8. Wong, K. T.; Lewis, N. S. What a Difference a Bond Makes: The Structural, Chemical, and Physical Properties of Methyl-Terminated Si(111) Surfaces. *Acc. Chem. Res.* **2014**, *47*, 3037-3044.
9. Walter, M. G.; Warren, E. L.; McKone, J. R.; Boettcher, S. W.; Mi, Q.; Santori, E. A.; Lewis, N. S. Solar Water Splitting Cells. *Chem. Rev.* **2010**, *110*, 6446-6473.
10. Neergaard Waltenburg, H.; Yates, J. T. Surface Chemistry of Silicon. *Chem. Rev.* **1995**, *95*, 1589-1673.
11. Shen, X.; Sun, B.; Yan, F.; Zhao, J.; Zhang, F.; Wang, S.; Zhu, X.; Lee, S. High-Performance Photoelectrochemical Cells from Ionic Liquid Electrolyte in Methyl-Terminated Silicon Nanowire Arrays. *ACS Nano* **2010**, *4*, 5869-5876.
12. Zhang, F.; Liu, D.; Zhang, Y.; Wei, H.; Song, T.; Sun, B. Methyl/Allyl Monolayer on Silicon: Efficient Surface Passivation for Silicon-Conjugated Polymer Hybrid Solar Cell. *ACS Appl. Mater. Inter.* **2013**, *5*, 4678-4684.
13. Hu, S.; Shaner, M. R.; Beardslee, J. A.; Lichterman, M.; Brunschwig, B. S.; Lewis, N. S. Amorphous TiO₂ coatings stabilize Si, GaAs, and GaP photoanodes for efficient water oxidation. *Science* **2014**, *344*, 1005-1009.
14. Guisinger, N. P.; Greene, M. E.; Basu, R.; Baluch, A. S.; Hersam, M. C. Room Temperature Negative Differential Resistance through Individual Organic Molecules on Silicon Surfaces. *Nano Lett.* **2004**, *4*, 55-59.
15. Yates, J. T. A New Opportunity in Silicon-Based Microelectronics. *Science* **1998**, *279*, 335-336.

16. Haick, H.; Hurley, P. T.; Hochbaum, A. I.; Yang, P.; Lewis, N. S. Electrical Characteristics and Chemical Stability of Non-Oxidized, Methyl-Terminated Silicon Nanowires. *J. Am. Chem. Soc.* **2006**, *128*, 8990-8991.
17. O'Leary, L. E.; Strandwitz, N. C.; Roske, C. W.; Pyo, S.; Brunshwig, B. S.; Lewis, N. S. Use of Mixed CH₃-/HC(O)CH₂CH₂-Si(111) Functionality to Control Interfacial Chemical and Electronic Properties During the Atomic-Layer Deposition of Ultrathin Oxides on Si(111). *J. Phys. Chem. Lett.* **2015**, *6*, 722-726.
18. Maldonado, S.; Knapp, D.; Lewis, N. S. Near-Ideal Photodiodes from Sintered Gold Nanoparticle Films on Methyl-Terminated Si(111) Surfaces. *J. Am. Chem. Soc.* **2008**, *130*, 3300-3301.
19. Lattimer, J. R. C.; Blakemore, J. D.; Sattler, W.; Gul, S.; Chatterjee, R.; Yachandra, V. K.; Yano, J.; Brunshwig, B. S.; Lewis, N. S.; Gray, H. B. Assembly, Characterization, and Electrochemical Properties of Immobilized Metal Bipyridyl Complexes on Silicon(111) Surfaces. *Dalton Trans.* **2014**, *43*, 15004-15012.
20. Lattimer, J. R. C.; Brunshwig, B. S.; Lewis, N. S.; Gray, H. B. Redox Properties of Mixed Methyl/Vinylferrocenyl Monolayers on Si(111) Surfaces. *J. Phys. Chem. C* **2013**, *117*, 27012-27022.
21. O'Leary, L. E.; Johansson, E.; Brunshwig, B. S.; Lewis, N. S. Synthesis and Characterization of Mixed Methyl/Allyl Monolayers on Si(111). *J. Phys. Chem. B* **2010**, *114*, 14298-14302.
22. O'Leary, L. E.; Rose, M. J.; Ding, T. X.; Johansson, E.; Brunshwig, B. S.; Lewis, N. S. Heck Coupling of Olefins to Mixed Methyl/Thienyl Monolayers on Si(111) Surfaces. *J. Am. Chem. Soc.* **2013**, *135*, 10081-10090.

23. Webb, L. J.; Rivillon, S.; Michalak, D. J.; Chabal, Y. J.; Lewis, N. S. Transmission Infrared Spectroscopy of Methyl- and Ethyl-Terminated Silicon(111) Surfaces. *J. Phys. Chem. B* **2006**, *110*, 7349-7356.
24. Johansson, E.; Hurley, P. T.; Brunshwig, B. S.; Lewis, N. S. Infrared Vibrational Spectroscopy of Isotopically Labeled Ethyl-Terminated Si(111) Surfaces Prepared Using a Two-Step Chlorination/Alkylation Procedure. *J. Phys. Chem. C* **2009**, *113*, 15239-15245.
25. Rivillon, S.; Chabal, Y. J. Alkylation of Silicon(111) Surfaces. *J. Phys. IV* **2006**, *132*, 195-198.
26. Rivillon Amy, S.; Michalak, D. J.; Chabal, Y. J.; Wielunski, L.; Hurley, P. T.; Lewis, N. S. Investigation of the Reactions during Alkylation of Chlorine-Terminated Silicon (111) Surfaces. *J. Phys. Chem. C* **2007**, *111*, 13053-13061.
27. Yamada, T.; Kawai, M.; Wawro, A.; Suto, S.; Kasuya, A. HREELS, STM, and STS study of CH₃-Terminated Si(111)-(1 x 1) Surface. *J. Chem. Phys.* **2004**, *121*, 10660-10667.
28. Hunger, R.; Fritsche, R.; Jaeckel, B.; Jaegermann, W.; Webb, L. J.; Lewis, N. S. Chemical and Electronic Characterization of Methyl-Terminated Si(111) Surfaces by High-Resolution Synchrotron Photoelectron Spectroscopy. *Phys. Rev. B* **2005**, *72*, 045317.
29. Webb, L. J.; Michalak, D. J.; Biteen, J. S.; Brunshwig, B. S.; Chan, A. S. Y.; Knapp, D. W.; Meyer, H. M.; Nemanick, E. J.; Traub, M. C.; Lewis, N. S. High-Resolution Soft X-ray Photoelectron Spectroscopic Studies and Scanning Auger Microscopy

- Studies of the Air Oxidation of Alkylated Silicon(111) Surfaces. *J. Phys. Chem. B* **2006**, *110*, 23450-23459.
30. Webb, L. J.; Nemanick, E. J.; Biteen, J. S.; Knapp, D. W.; Michalak, D. J.; Traub, M. C.; Chan, A. S. Y.; Brunschwig, B. S.; Lewis, N. S. High-Resolution X-ray Photoelectron Spectroscopic Studies of Alkylated Silicon(111) Surfaces. *J. Phys. Chem. B* **2005**, *109*, 3930-3937.
31. Jaeckel, B.; Hunger, R.; Webb, L. J.; Jaegermann, W.; Lewis, N. S. High-Resolution Synchrotron Photoemission Studies of the Electronic Structure and Thermal Stability of CH₃- and C₂H₅-Functionalized Si(111) Surfaces. *J. Phys. Chem. C* **2007**, *111*, 18204-18213.
32. Becker, J. S.; Brown, R. D.; Johansson, E.; Lewis, N. S.; Sibener, S. J. Helium Atom Diffraction Measurements of the Surface Structure and Vibrational Dynamics of CH₃--Si(111) and CD₃--Si(111) Surfaces. *J. Chem. Phys.* **2010**, *133*, 104705.
33. Brown, R. D.; Hund, Z. M.; Campi, D.; O'Leary, L. E.; Lewis, N. S.; Bernasconi, M.; Benedek, G.; Sibener, S. J. Hybridization of Surface Waves with Organic Adlayer Librations: A Helium Atom Scattering and Density Functional Perturbation Theory Study of Methyl-Si(111). *Phys. Rev. Lett.* **2013**, *110*, 156102.
34. Brown, R. D.; Hund, Z. M.; Campi, D.; O'Leary, L. E.; Lewis, N. S.; Bernasconi, M.; Benedek, G.; Sibener, S. J. The Interaction of Organic Adsorbate Vibrations with Substrate Lattice Waves in Methyl-Si(111)-(1 × 1). *J. Chem. Phys.* **2014**, *141*, 024702.
35. Malyk, S.; Shalhout, F. Y.; O'Leary, L. E.; Lewis, N. S.; Benderskii, A. V. Vibrational Sum Frequency Spectroscopic Investigation of the Azimuthal Anisotropy and

- Rotational Dynamics of Methyl-Terminated Silicon(111) Surfaces. *J. Phys. Chem. C* **2012**, *117*, 935-944.
36. Yu, H.; Webb, L. J.; Ries, R. S.; Solares, S. D.; Goddard, W. A.; Heath, J. R.; Lewis, N. S. Low-Temperature STM Images of Methyl-Terminated Si(111) Surfaces. *J. Phys. Chem. B* **2004**, *109*, 671-674.
37. Nemanick, E. J.; Solares, S. D.; Goddard, W. A.; Lewis, N. S. Quantum Mechanics Calculations of the Thermodynamically Controlled Coverage and Structure of Alkyl Monolayers on Si(111) Surfaces. *J. Phys. Chem. B* **2006**, *110*, 14842-14848.
38. Nemanick, E. J.; Hurley, P. T.; Brunshwig, B. S.; Lewis, N. S. Chemical and Electrical Passivation of Silicon (111) Surfaces through Functionalization with Sterically Hindered Alkyl Groups. *J. Phys. Chem. B* **2006**, *110*, 14800-14808.
39. Plass, K. E.; Liu, X.; Brunshwig, B. S.; Lewis, N. S. Passivation and Secondary Functionalization of Allyl-Terminated Si(111) Surfaces. *Chem. Mater.* **2008**, *20*, 2228-2233.
40. Miller, T.; Teplyakov, A. V. Attachment Chemistry of PCBM to a Primary-Amine-Terminated Organic Monolayer on a Si(111) Surface. *Langmuir* **2014**, *30*, 5105-5114.
41. Li, M.; Dai, M.; Chabal, Y. J. Atomic Layer Deposition of Aluminum Oxide on Carboxylic Acid-Terminated Self-Assembled Monolayers. *Langmuir* **2009**, *25*, 1911-1914.
42. Strother, T.; Hamers, R. J.; Smith, L. M. Covalent Attachment of Oligodeoxyribonucleotides to Amine-Modified Si (001) Surfaces. *Nucleic Acids Res.* **2000**, *28*, 3535-3541.

43. Strother, T.; Cai, W.; Zhao, X.; Hamers, R. J.; Smith, L. M. Synthesis and Characterization of DNA-Modified Silicon (111) Surfaces. *J. Am. Chem. Soc.* **2000**, *122*, 1205-1209.
44. Hurley, P. T.; Nemanick, E. J.; Brunshwig, B. S.; Lewis, N. S. Covalent Attachment of Acetylene and Methylacetylene Functionality to Si(111) Surfaces: Scaffolds for Organic Surface Functionalization while Retaining Si-C Passivation of Si(111) Surface Sites. *J. Am. Chem. Soc.* **2006**, *128*, 9990-9991.
45. Rohde, R. D.; Agnew, H. D.; Yeo, W.-S.; Bailey, R. C.; Heath, J. R. A Non-Oxidative Approach toward Chemically and Electrochemically Functionalizing Si(111). *J. Am. Chem. Soc.* **2006**, *128*, 9518-9525.
46. Teysot, A.; Fidélis, A.; Fellah, S.; Ozanam, F.; Chazalviel, J. N. Anodic Grafting of Organic Groups on the Silicon Surface. *Electrochim. Acta* **2002**, *47*, 2565-2571.
47. Yang, F.; Hunger, R.; Roodenko, K.; Hinrichs, K.; Rademann, K.; Rappich, J. Vibrational and Electronic Characterization of Ethynyl Derivatives Grafted onto Hydrogenated Si(111) Surfaces. *Langmuir* **2009**, *25*, 9313-9318.
48. Yamada, T.; Shirasaka, K.; Noto, M.; Kato, H. S.; Kawai, M. Adsorption of Unsaturated Hydrocarbon Moieties on H:Si(111) by Grignard Reaction. *J. Phys. Chem. B* **2006**, *110*, 7357-7366.
49. Gleason-Rohrer, D. C.; Brunshwig, B. S.; Lewis, N. S. Measurement of the Band Bending and Surface Dipole at Chemically Functionalized Si(111)/Vacuum Interfaces. *J. Phys. Chem. C* **2013**, *117*, 18031-18042.

50. Rivillon, S.; Chabal, Y. J.; Webb, L. J.; Michalak, D. J.; Lewis, N. S.; Halls, M. D.; Raghavachari, K. Chlorination of Hydrogen-Terminated Silicon (111) Surfaces. *J. Vac. Sci. Technol. A* **2005**, *23*, 1100-1106.
51. Briggs, D.; Seah, M. P. *Practical Surface Analysis: Auger and X-ray Photoelectron Spectroscopy*, 2nd ed.; John Wiley & Sons, Inc.: New York, 1990; Vol. 1.
52. Haber, J. A.; Lewis, N. S. Infrared and X-ray Photoelectron Spectroscopic Studies of the Reactions of Hydrogen-Terminated Crystalline Si(111) and Si(100) Surfaces with Br₂, I₂, and Ferrocenium in Alcohol Solvents. *J. Phys. Chem. B* **2002**, *106*, 3639-3656.
53. van der Marel, C.; Yildirim, M.; Stapert, H. R. Multilayer Approach to the Quantitative Analysis of X-ray Photoelectron Spectroscopy Results: Applications to Ultrathin SiO₂ on Si and to Self-Assembled Monolayers on Gold. *J. Vac. Sci. Technol. A* **2005**, *23*, 1456-1470.
54. Seah, M. P.; Spencer, S. J. Ultrathin SiO₂ on Si II. Issues in Quantification of the Oxide Thickness. *Surf. Interface Anal.* **2002**, *33*, 640-652.
55. Brown, E. S.; Peczonczyk, S. L.; Maldonado, S. Wet Chemical Functionalization of GaP(111)B through a Williamson Ether-Type Reaction. *J. Phys. Chem. C* **2015**, *119*, 1338-1345.
56. Asami, K.; Hashimoto, K.; Shimodaira, S. XPS Determination of Compositions of Alloy Surfaces and Surface Oxides on Mechanically Polished Iron-Chromium Alloys. *Corros. Sci.* **1977**, *17*, 713-723.
57. Weldon, M. K.; Stefanov, B. B.; Raghavachari, K.; Chabal, Y. J. Initial H₂O-Induced Oxidation of Si(100)-(2 x 1). *Phys. Rev. Lett.* **1997**, *79*, 2851-2854.

58. Struck, L. M.; Eng Jr, J.; Bent, B. E.; Flynn, G. W.; Chabal, Y. J.; Christman, S. B.; Chaban, E. E.; Raghavachari, K.; Williams, G. P.; Radermacher, K.; Mantl, S. Vibrational Study of Silicon Oxidation: H₂O on Si(100). *Surf. Sci.* **1997**, *380*, 444-454.
59. Michalak, D. J.; Amy, S. R.; Aureau, D.; Dai, M.; Esteve, A.; Chabal, Y. J. Nanopatterning Si(111) Surfaces as a Selective Surface-Chemistry Route. *Nat. Mater.* **2010**, *9*, 266-271.
60. Rao, G. R. Infrared Reflection Absorption Study of Water Interaction with H-Terminated Si(100) Surfaces. *Bull. Mater. Sci.* **2004**, *27*, 497-500.
61. Michalak, D. J.; Rivillon, S.; Chabal, Y. J.; Estève, A.; Lewis, N. S. Infrared Spectroscopic Investigation of the Reaction of Hydrogen-Terminated, (111)-Oriented, Silicon Surfaces with Liquid Methanol. *J. Phys. Chem. B* **2006**, *110*, 20426-20434.
62. Contarini, S.; Howlett, S. P.; Rizzo, C.; De Angelis, B. A. XPS Study on the Dispersion of Carbon Additives in Silicon Carbide Powders. *Appl. Surf. Sci.* **1991**, *51*, 177-183.
63. Muehlhoff, L.; Choyke, W. J.; Bozack, M. J.; Yates, J. T. Comparative Electron Spectroscopic Studies of Surface Segregation on SiC(0001) and SiC(000 $\bar{1}$). *J. Appl. Phys.* **1986**, *60*, 2842-2853.
64. Becker, R. S.; Golovchenko, J. A.; McRae, E. G.; Swartzentruber, B. S. Tunneling Images of Atomic Steps on the Si(111)7x7 Surface. *Phys. Rev. Lett.* **1985**, *55*, 2028-2031.
65. Ferguson, G. A.; Raghavachari, K. Collective Vibrations in Cluster Models for Semiconductor Surfaces: Vibrational Spectra of Acetylenyl and Methylacetylenyl Functionalized Si(111). *J. Chem. Phys.* **2007**, *127*, 194706.

66. Kato, H. S.; Kawai, M.; Akagi, K.; Tsuneyuki, S. Interaction of Condensed Water Molecules with Hydroxyl and Hydrogen Groups on Si(001). *Surf. Sci.* **2005**, *587*, 34-40.
67. Wong, K. T.; Kim, Y.-G.; Soriaga, M. P.; Brunshwig, B. S.; Lewis, N. S. Synthesis and Characterization of Atomically Flat Methyl-Terminated Ge(111) Surfaces. *J. Am. Chem. Soc.* **2015**.

Chapter 3

SYNTHESIS AND CHARACTERIZATION OF PROPYNYL-TERMINATED Si(111) SURFACES

Plymale, N. T.; Kim, Y.-G.; Soriaga, M. P.; Brunschwig, B. S.; Lewis, N. S. Synthesis, Characterization, and Reactivity of Ethynyl- and Propynyl-Terminated Si(111) Surfaces. *J. Phys. Chem. C* **2015**, *119*, 19847–19862. DOI: 10.1021/acs.jpcc.5b05028

3.1 INTRODUCTION

The chemical composition of semiconductor surfaces can have a substantial impact on the properties of the semiconductor in the context of device architecture.¹⁻² The surface composition can drastically influence the rate of charge carrier recombination at the interface,³⁻⁵ the band-edge positions and resulting maximum achievable output potential at the interface,⁶⁻⁷ the chemical reactivity⁸⁻¹² and physical robustness of the interface,¹³⁻¹⁴ and the electrical properties of the interface.¹⁵⁻¹⁷ Because the surface composition has such a strong influence over the behavior of semiconductor interfaces, a substantial amount of effort has been put towards achieving molecular-level control over the semiconductor surfaces in order to achieve improved and predictable semiconductor interfaces.

One of the best examples of a well-defined semiconductor surface is methyl-terminated Si(111) (CH₃-Si(111)). As discussed in Chapter 1, CH₃-Si(111) surfaces have been extensively characterized and are believed to be fully-terminated with -CH₃ groups

such that each atop Si(111) site is terminated by a Si–C bond.¹⁸⁻³³ This property affords CH₃–Si(111) surfaces exceptional chemical stability. This high degree of stability, however, also makes CH₃–Si(111) surfaces chemically inert towards many potential methods of secondary functionalization. Such limitations have precluded CH₃–Si(111) surfaces alone from providing favorable interfaces with functional device components, such as metals, metal oxides, catalysts, and polymers.

Propynyl-terminated Si(111) (CH₃CC–Si(111)) surfaces, which are terminated by the propynyl (–CCCH₃) group, could potentially exhibit many properties similar to CH₃–Si(111) surfaces. The –CCCH₃ group is sterically similar to –CH₃ groups when considering the radial geometry of the substituent, potentially allowing for near complete termination of the Si(111) atop sites with Si–C bonds. The geometry of the –CCCH₃ group is intriguing from a fundamental perspective because it is essentially a –CH₃ group separated from the Si lattice by a C≡C spacer, which presents unique opportunities to improve understanding of organic/Si interactions. Additionally, the propynyl substituent contains a C≡C group, which is synthetically versatile and could allow for facile secondary functionalization of CH₃CC–Si(111) surfaces. In this way, CH₃CC–Si(111) surfaces could also act as an alternative to mixed monolayer chemistry,^{10-11, 34} which was developed to allow high Si–C termination on Si surfaces functionalized with bulky, but synthetically useful, alkyl groups by passivating residual halogenated surface sites with –CH₃ groups.

The synthesis of CH₃CC–Si(111) surfaces has been reported previously and extensively cited.^{17, 35-39} However, structural characterization of CH₃CC–Si(111) surfaces

is severely lacking in the literature, and notable inconsistencies exist between the reported literature preparations and the resulting spectroscopic and physical properties of the surfaces. Further characterization of these surfaces is therefore needed to fully define the functionalization chemistry and to describe the properties of the modified Si(111) surfaces. We describe herein the synthesis of the CH₃CC–Si(111) surfaces and provide extensive characterization of the modified surfaces by transmission infrared spectroscopy (TIRS), high-resolution electron energy-loss spectroscopy (HREELS), X-ray photoelectron spectroscopy (XPS), atomic-force microscopy (AFM), electrochemical scanning-tunneling microscopy (EC-STM), low-energy electron diffraction (LEED), and surface recombination velocity (*S*) measurements. Additionally, we have compared the results of the surface analysis presented herein with previously reported data for propynyl-terminated Si surfaces.

3.2 EXPERIMENTAL SECTION

3.2.1 Materials and Methods

Water (≥ 18.2 M Ω cm resistivity) was obtained from a Barnstead E-Pure system. Ammonium fluoride (NH₄F(aq), 40%, semiconductor grade, Transene Co., Inc., Danvers, MA) was purged with Ar(g) (99.999%, Air Liquide) for 1 h prior to use.

Czochralski-grown n-Si wafers (Virginia Semiconductor, Fredericksburg, VA) used for the collection of XPS, AFM, EC-STM, LEED, and HREELS data were double-side polished, doped with phosphorus to a resistivity of 1 Ω cm, 381 ± 25 μ m thick, and oriented to within 0.1° of the (111) crystal plane. Collection of TIRS data was performed

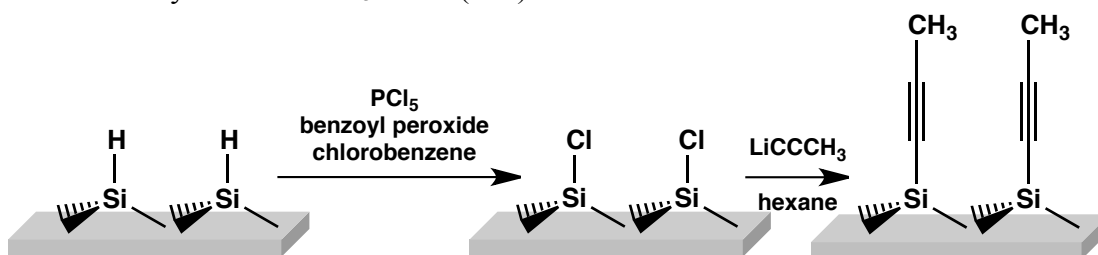
using wafers with one of the following specifications: float-zone-grown n-Si wafers (Silicon Quest International, Santa Clara, CA), double-side polished, doped with phosphorus to a resistivity of 63–77 Ω cm, 435 ± 10 μ m thick, and oriented to within 0.5° of the (111) crystal plane; or float-zone-grown Si wafers (Addison Engineering Inc., San Jose, CA), double-side polished, undoped with a resistivity of >20 k Ω cm, 500 ± 20 μ m thick, and oriented to within 0.5° of the (111) crystal plane. Undoped, float-zone-grown Si wafers (FZWafers.com, Ridgefield Park, NJ) with a resistivity of 20–40 k Ω cm used for S measurements were double-side polished, 300 ± 25 μ m thick, and oriented to within 0.5° of the (111) crystal plane. The wafer thickness was determined using calipers prior to performing S measurements.

1. Preparation of CH₃CC–Si(111) Surfaces. CH₃CC–Si(111) surfaces were prepared from H–Si(111) surfaces using the Cl–Si(111) surface intermediate. Section 2.2.1 of this thesis details the cleaning and etching techniques that were used for the preparation of H–Si(111) surfaces. Cl–Si(111) surfaces were prepared inside a glovebox with <10 ppm O₂(g) by reaction of H–Si(111) surfaces with PCl₅ saturated in chlorobenzene at 90 °C for 45 min using benzoyl peroxide as a radical initiator. A detailed account of the preparation of Cl–Si(111) surfaces can also be found in section 2.2.1.

CH₃CC–Si(111) surfaces were prepared by the reaction of Cl–Si(111) surfaces with CH₃CCLi (1.0 M in hexane, BOC Sciences, Shirley, NY) at 45 ± 2 °C for 3–24 h. The reaction of Cl–Si(111) surfaces with CH₃CCLi was performed in foil-covered test tubes to limit exposure of the CH₃CCLi to ambient light. Upon completion of the reaction,

CH₃CC–Si(111) samples were rinsed with hexanes, then rinsed with and submerged in methanol ($\geq 99.8\%$, anhydrous, Sigma-Aldrich), removed from the glovebox, sonicated for 10 min in methanol, and rinsed with water. Samples were dried under a stream of Ar(g) or N₂(g). Scheme 3.1 summarizes the preparation methods for CH₃CC–Si(111) surfaces.

Scheme 3.1. Synthesis of CH₃CC–Si(111) Surfaces



3.2.2 Instrumentation

Detailed descriptions of the instrumentation used in the collection of TIRS, XPS, AFM, EC-STM, LEED, and HREELS data is presented in section 2.2.1.

3.2.3 Data Analysis

1. Fitting and Quantification of XPS Data. High-resolution XP spectra were analyzed using CasaXPS software v. 2.3.16. The fitting parameters were the same as those described in section 2.2.2.

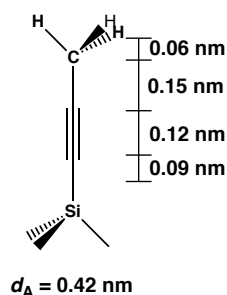
The thickness (d_A) of the overlayer species A was estimated by XPS for CH₃CC–Si(111) surfaces using the substrate-overlayer model⁴⁰⁻⁴¹

$$\left(\frac{I_A}{I_{Si}}\right)\left(\frac{SF_{Si}}{SF_A}\right)\left(\frac{\rho_{Si}}{\rho_A}\right) = \left(\frac{1 - e^{-\frac{d_A}{\lambda_A \sin\theta}}}{e^{-\frac{d_A}{\lambda_{Si} \sin\theta}}}\right) \quad (3.1)$$

where I_A is the area under the photoemission peak arising from the overlayer species A, I_{Si} is the area under the Si 2p photoemission signal, SF_{Si} is the instrument sensitivity factor for Si 2p (0.328), and SF_A is the instrument sensitivity factor for the overlayer species A, which is 0.278 for C 1s photoelectrons in hydrocarbon overlayers. For the hydrocarbon overlayers, I_A is the total area under the C 1s photoemission signal corresponding to all C atoms in the overlayer, which is composed of the signals at 284.3 and 285.3 eV for CH₃CC–Si(111) surfaces. The density of Si (ρ_{Si}) is 2.3 g cm⁻³, and the density of the overlayer species A (ρ_A) is 3.0 g cm⁻³ for hydrocarbon overlayers.²⁹ The attenuation length for the overlayer species (λ_A) has been estimated to be 3.6 nm for C 1s photoelectrons moving through hydrocarbon overlayers.⁴²⁻⁴³ The attenuation length for Si 2p photoelectrons (λ_{Si}) moving through hydrocarbon overlayers has been estimated to be 4.0 nm.⁴²⁻⁴³ The angle between the surface plane and the photoelectron ejection vector (θ) is 90°. The thickness of the overlayer species A was calculated using an iterative process.

The fractional monolayer coverage for the overlayer species A (Φ_A) was estimated by dividing the measured thickness, d_A , by the calculated thickness of 1 ML of overlayer species A, depicted in Scheme 3.2. The thickness of 1 ML of each hydrocarbon overlayer was estimated by summing the bond lengths for the species containing C, but excluding Si and H. Assuming uniform overlayers, the value of Φ_A represents the fraction of surface Si(111) sites that were modified with the overlayer species of interest.

Scheme 3.2. Monolayer Thickness of Surface-Bound $-\text{CCCH}_3$ Groups



2. Calculation of Surface Recombination Velocity and Surface Trap-State Density.

Details on the analysis of surface recombination velocity data for the calculation of S is presented in section 2.2.3. S was calculated for $\text{CH}_3\text{CC}-\text{Si}(111)$ surfaces using eq 2.3.⁴ S was converted to a trap state density, N_t , using eq 2.4.⁴⁴ N_t was used to estimate the absolute number of electrically active defects per surface $\text{Si}(111)$ sites by use of the number density of atop Si sites for an unreconstructed $\text{Si}(111)$ surface, $\Gamma_{\text{Si}(111)}$, which is $7.83 \times 10^{14} \text{ atoms cm}^{-2}$. Thus, a wafer with surface recombination velocity S has 1 electrically active defect for every $\Gamma_{\text{Si}(111)}/N_t$ surface sites.

3.3 RESULTS

3.3.1 Transmission Infrared Spectroscopy

Figure 3.1 shows TIRS data of $\text{CH}_3\text{CC}-\text{Si}(111)$ surfaces. The spectra exhibited three distinct C–H stretching peaks at 2958, 2934, and 2872 cm^{-1} . The absorbance features at 2934 and 2872 cm^{-1} were observed only at the 74° incidence angle, which indicated that those features arose from modes perpendicular to the surface, whereas the absorbance at 2957 cm^{-1} was observed at both angles and was therefore not perpendicular to the surface. A sharp absorbance at 1380 cm^{-1} attributed to the symmetric C–H bending

(δ_s), or “umbrella,” mode was present at 74° incidence but was absent at 30° incidence, which indicated that this mode and the propynyl groups were oriented perpendicular to the surface. A broad and asymmetric absorbance with local maxima at 1061, 1033, and 966 cm^{-1} was also observed at both 74° and 30° , and likely arose from the expected CH_3 rocking motion and subsurface $(\text{Si-O-Si})_{\text{TO}}$ motion. The C-C stretching absorption was also expected in this region, but likely contributed minimally to this absorption band due to the symmetric nature of the C-C single bond. The presence of an absorbance in the $\sim 1000\text{ cm}^{-1}$ region at both angles of incidence suggested that the absorption arose primarily from the CH_3 rocking and $(\text{Si-O-Si})_{\text{TO}}$ modes because the C-C stretching mode is expected to be oriented perpendicular to the surface.

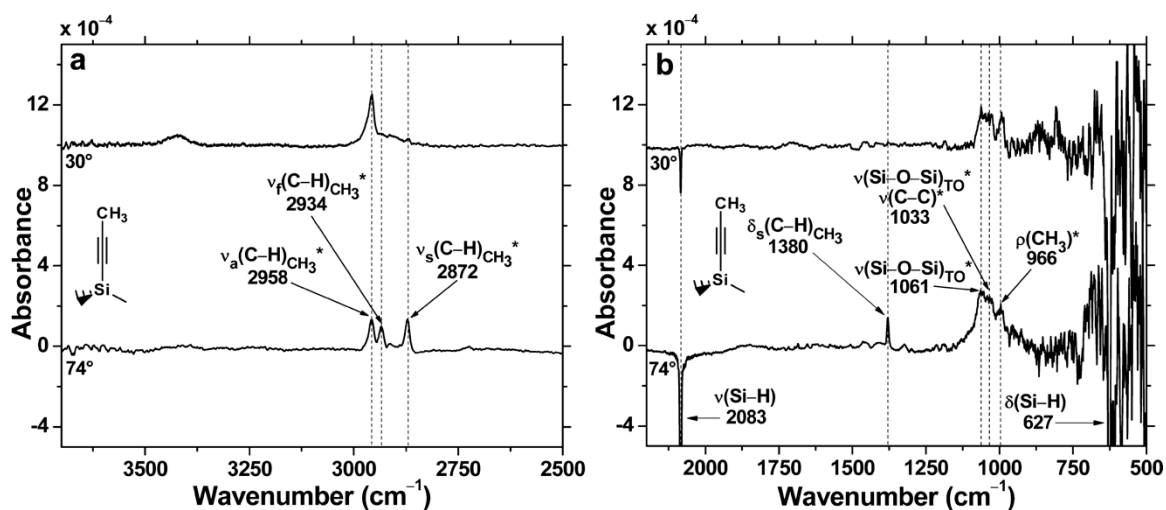


Figure 3.1. TIRS data for $\text{CH}_3\text{CC-Si}(111)$ surfaces referenced to the $\text{H-Si}(111)$ surface collected at 74° (bottom) and 30° (top) from the surface normal. Panel a shows the high-energy region, and panel b shows the low-energy region. The negative peaks in panel b resulted from the $\text{H-Si}(111)$ background. The peak positions and assignments (* denotes tentative) are indicated in the figure. The 30° spectrum is offset vertically for clarity.

Figure 3.2 shows the absence of detectable Si–H stretching for the CH₃CC–Si(111) surfaces prepared in this work.

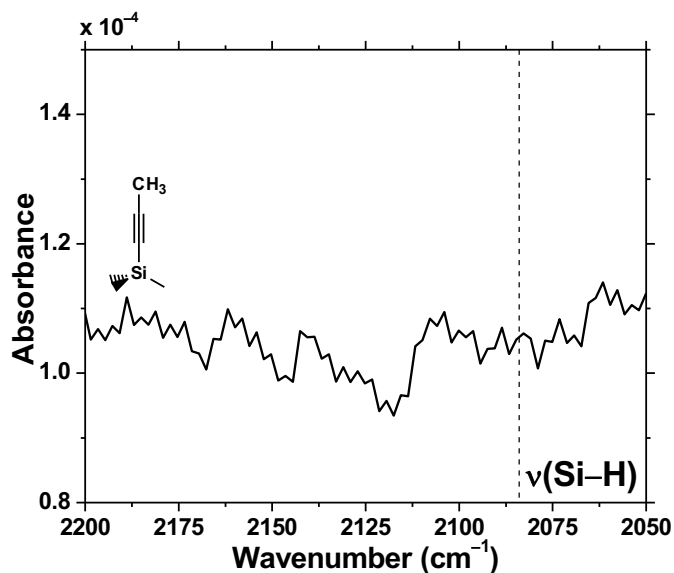


Figure 3.2. TIRS data for the CH₃CC–Si(111) surface referenced to the SiO_x surface. The position of the Si–H stretching peak is indicated by the dotted line.

3.3.2 High-Resolution Electron Energy-Loss Spectroscopy

HREELS data were obtained for CH₃CC–Si(111) surfaces to detect vibrational signals that could not be readily observed by TIRS. The HREELS data for CH₃CC–Si(111) surfaces (Figure 3.3) exhibited a single (C–H)_{CH₃} stretching signal centered at 3004 cm⁻¹, in addition to a broad peak centered at 1435 cm⁻¹, which corresponded to the closely spaced symmetric and asymmetric C–H bending motions, the latter of which was not observed by TIRS. A peak centered at 2216 cm⁻¹ was indicative of C≡C stretching, and supported the proposed structure of the CH₃CC–Si(111) surface. A signal at 670 cm⁻¹ was consistent with Si–C stretching, and provided evidence for the covalent attachment

of propynyl groups to the Si(111) surface. The signal centered at 1048 cm^{-1} arose from the convolution of CH_3 rocking, C–C single-bond stretching, and $(\text{Si–O–Si})_{\text{TO}}$ modes.

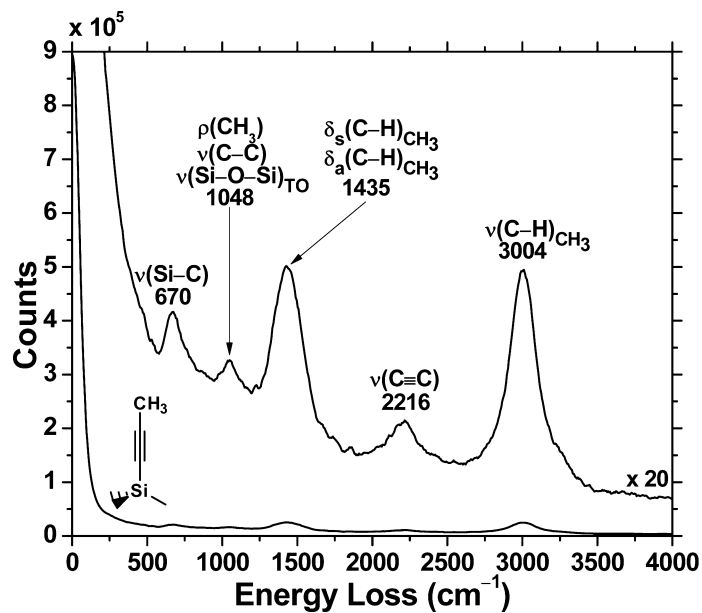


Figure 3.3. HREELS data for $\text{CH}_3\text{CC-Si}(111)$ surfaces. Data were collected in the specular geometry using an incident beam energy of 2.8 eV, and the fwhm of the elastic peak was 15.0 meV. The raw spectrum (bottom) is shown with the magnified spectrum (top) superimposed for clarity. The peak positions and assignments are indicated in the figure.

Table 3.1 summarizes the vibrational modes observed by TIRS and HREELS for CH₃CC–Si(111) surfaces.

Table 3.1. Summary of the Positions and Assigned Modes for the Vibrational Signatures Observed for CH₃CC–Si(111) Surfaces.

TIRS Frequency (cm ⁻¹)	HREELS Frequency (cm ⁻¹) ^a	Assigned Mode ^b	Orientation to Surface ^c
2958	3004	$\nu_a(\text{C-H})_{\text{CH}_3^*}$	not \perp
2934	3004	$\nu_f(\text{C-H})_{\text{CH}_3^*}$	\perp
2872	3004	$\nu_s(\text{C-H})_{\text{CH}_3^*}$	\perp
–	2216	$\nu(\text{C}\equiv\text{C})$	
–	1435	$\delta_a(\text{C-H})_{\text{CH}_3}$	
1380	1435	$\delta_s(\text{C-H})_{\text{CH}_3}$	\perp
1061	1048	$\nu(\text{Si-O-Si})_{\text{TO}^*}$	not \perp
1033	1048	$\nu(\text{Si-O-Si})_{\text{TO}^*}$	not \perp
		$\nu(\text{C-C})^*$	
966	1048	$\rho(\text{CH}_3)^*$	not \perp
–	670	$\nu(\text{Si-C})$	

^aIn some cases, HREELS signals do not resolve multiple vibrational modes that are observed by TIRS. The HREELS signal with the closest energy to the resolved TIRS signal is paired in the table. ^bThe symbols ν , δ , and ρ signify stretching, bending, and rocking motions, respectively, with subscripts a, s, and f indicating whether the mode is asymmetric, symmetric, or resulting from Fermi resonance, respectively. The subscript “CH₃” indicates C–H stretching signals arising from the –CH₃ substituent of the propynyl group. The subscript “TO” indicates a transverse optical Si–O–Si motion. The assignments marked with * are tentative. ^cThe orientation of the vibrational mode with respect to the plane of the sample surface determined by TIRS is given.

3.3.3 X-ray Photoelectron Spectroscopy

XPS data were collected to provide quantitative information about the species present on $\text{CH}_3\text{CC-Si}(111)$ surfaces. Only signals ascribable to Si, C and O were observed, and high-resolution spectra were acquired for the C 1s and Si 2p core levels. Figure 3.4 shows the C 1s high-resolution XP spectrum for $\text{CH}_3\text{CC-Si}(111)$ surfaces. The C 1s spectra exhibited two distinct photoemission signals centered at 284.3 and 285.3 eV along with a small shoulder centered at 286.6 eV. The low binding-energy peak at 284.3 eV was consistent with C bound to Si, and the prominent photoemission signal at 285.3 eV arose from C bound to C, consistent with the proposed structure of the $\text{CH}_3\text{CC-Si}(111)$ surface. The signal at 285.3 eV exhibited a broad fwhm relative to the peak at

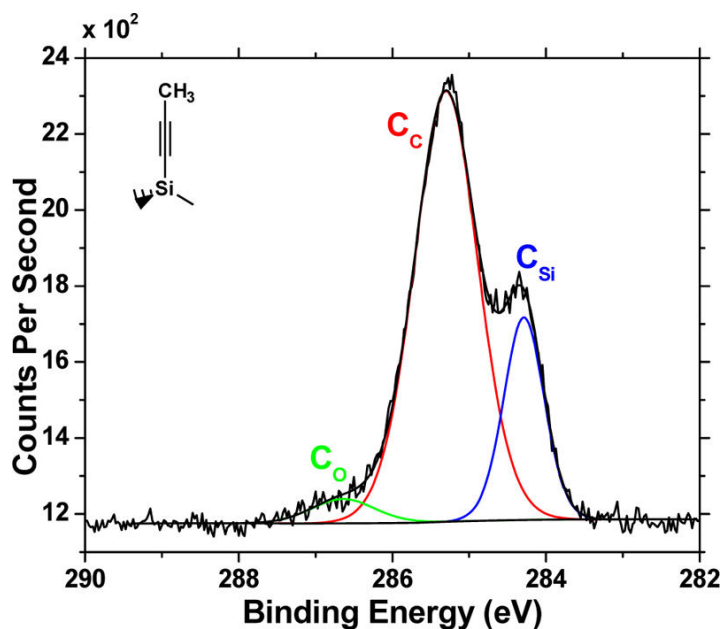


Figure 3.4. High-resolution XP spectrum of the C 1s region for $\text{CH}_3\text{CC-Si}(111)$ surfaces. The low binding energy C photoemission signal at 284.3 eV arises from C bound to Si (blue, C_Si), while the peaks at 285.3 and 286.8 eV arise from C bound to C (red, C_C) and C bound to O (green, C_O), respectively. The peak at 285.3 eV is a convolution of the two C atoms in the propynyl group not bound directly to Si and adventitious C species, while the signal at 286.8 eV arises from adventitious species only.

284.3 eV because the signal at 285.3 eV arose from two chemically different C species in the $\equiv\text{C}-\text{CH}_3$ substituent of the propynyl moiety as well as adventitious C, while the peak at 284.3 eV arose only from the C bound to Si. The signal centered at 286.6 eV was consistent with adventitious C on alkyl-terminated Si surfaces. The ratio of the peak at 285.3 eV to the peak at 284.3 eV was 3.6 ± 0.4 , while, assuming negligible attenuation, the expected ratio for a $-\text{CCCH}_3$ group would be 2.0. Figure 3.5 shows the Si 2p high-resolution XP spectrum for $\text{CH}_3\text{CC}-\text{Si}(111)$ surfaces. The spectra showed no detectable SiO_x .

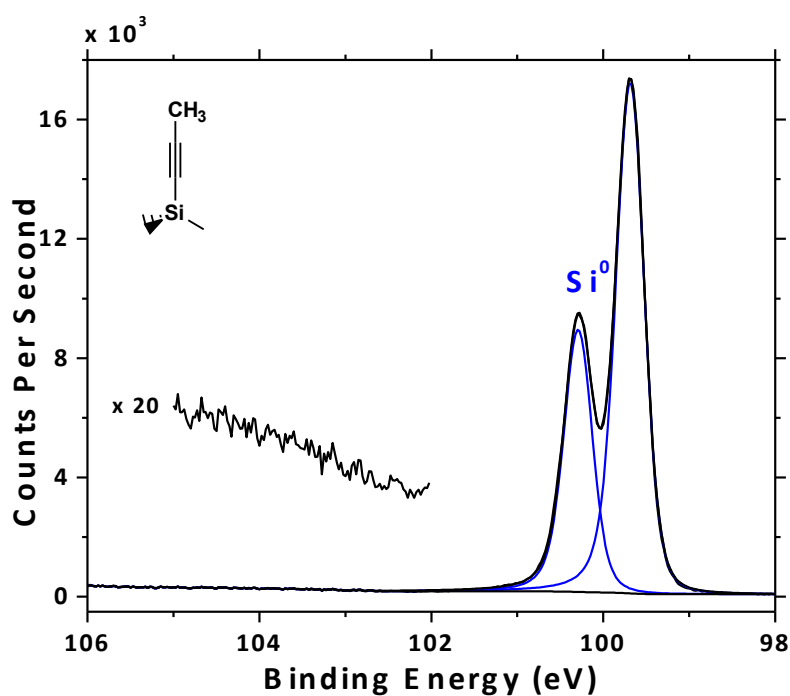


Figure 3.5. High-resolution XP spectrum of the Si 2p region for $\text{CH}_3\text{CC}-\text{Si}(111)$ surfaces. The Si 2p spectrum showed only a contribution from the bulk Si (blue, Si^0). The region from 102–105 eV in the Si 2p spectrum is magnified to show the absence of detectable high-order SiO_x .

The fractional monolayer coverage was estimated for CH₃CC–Si(111) surfaces by XPS by use of eq 1.1⁴⁰⁻⁴¹ to yield $\Phi_{\text{Si-CCCH}_3} = 1.05 \pm 0.06$ ML. The C 1s photoemission signals at 284.3 and 285.3 eV were summed to quantify $\Phi_{\text{Si-CCCH}_3}$ because these signals arise directly from the propynyl group. No detectable signals ascribed to Cl, Li, or SiO_x were observed by XPS on CH₃CC–Si(111) surfaces, and XP survey spectra showed very low amounts of O overall.

The thermal stability of CH₃CC–Si(111) surfaces was investigated in vacuum. Figure 3.6 shows the behavior of CH₃CC–Si(111) surfaces as a function of annealing temperature. CH₃CC–Si(111) surfaces exhibited minimal changes in C 1s signal intensity and shape after annealing to 100 °C, with a small reduction in C 1s signal intensity observed upon heating to 200 °C. Annealing to 300 °C produced a significant reduction in the C 1s signal intensity and concomitant reduction in the coverage of Si(111) surface sites by propynyl groups (Table 3.2). Heating to 400 and 500 °C, respectively, further reduced the intensity of the C 1s signal and increased the intensity of the Si 2p signal, indicating that propynyl groups had been desorbed from the Si(111) surface. Annealing the CH₃CC–Si(111) surface up to 500 °C did not change the ratio of the C 1s peak at 285.3 eV to the peak at 284.3 eV within the statistical error, suggesting that very little adventitious C was on the surface. Annealing to 600 °C resulted in increased intensity and broadening of the C 1s signal with the appearance of a new peak centered at ~283.7 eV, which increased in intensity upon further heating to 700 °C and indicated the formation of silicon carbide (SiC).⁴⁵⁻⁴⁷ An overall increase in the area of the C 1s peak accompanied the formation of SiC and resulted in attenuation of the underlying Si 2p

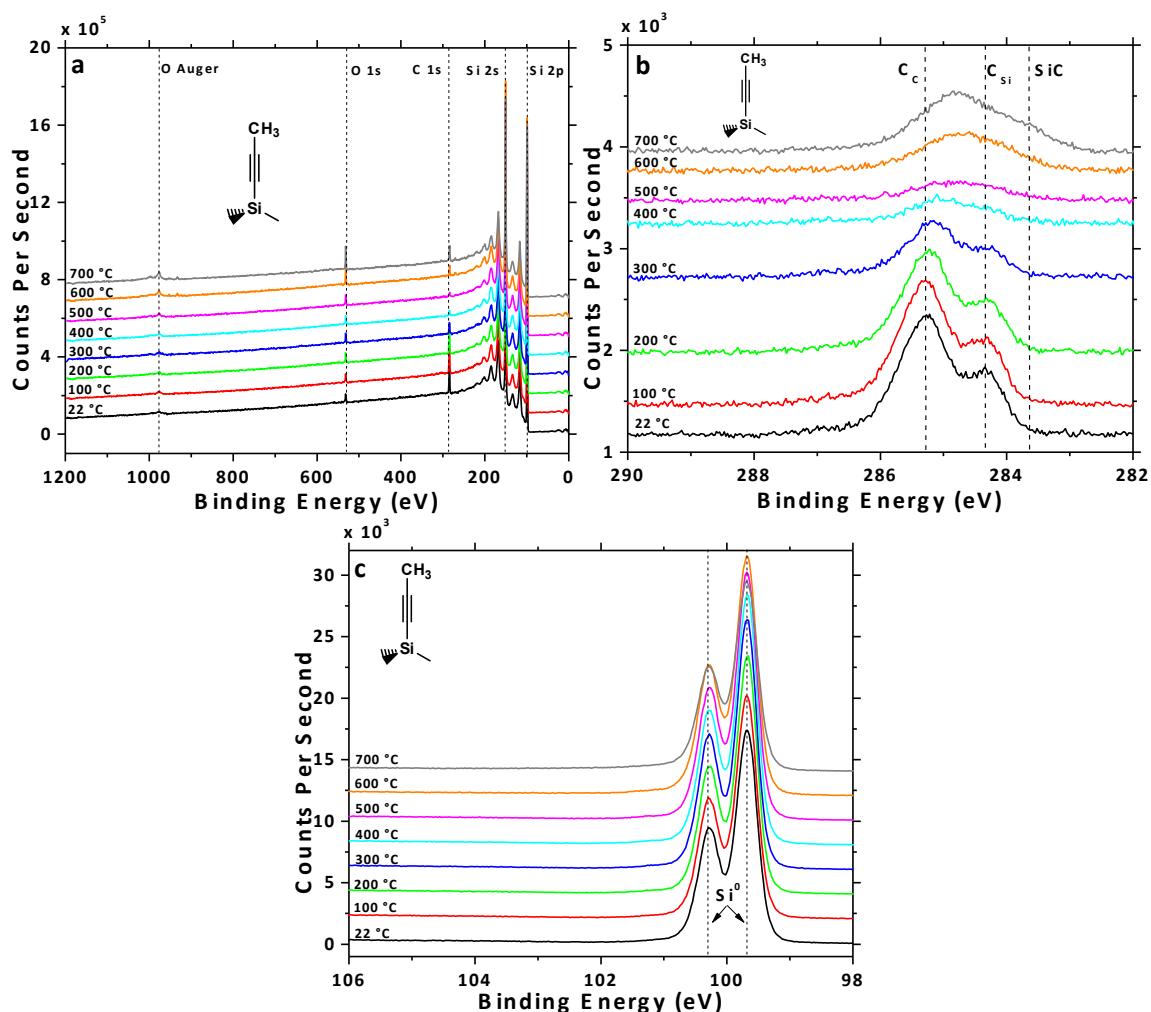


Figure 3.6. Thermal stability in vacuum of CH₃CC-Si(111) surfaces. The annealing temperature is indicated above each spectrum, and the spectra are offset vertically for clarity. The survey spectra (a) show the presence of only the Si 2p, Si 2s, C 1s, and O 1s core level peaks along with the O Auger signal and Si plasmon-loss features. Annealing to 600 and 700 °C resulted in the observation of a small amount of Cu and Cl, which was likely transferred from the sample holder to the sample surface during annealing. The high-resolution C 1s spectra (b) showed the behavior of the C bound to Si (C_{Si}) and C bound to C (C_C) peaks with temperature. Upon annealing to 200–500 °C, the overall amount of C decreased. Heating to 600–700 °C resulted in the appearance of a new C 1s peak at ~283.7 eV (SiC). Si 2p spectra (c) showed increased intensity as C was removed from the surface upon annealing to 500 °C, and decreased intensity upon annealing to 600–700 °C.

photoemission intensity. The chemical structure of the other C species formed on the surface was not readily determined by the XPS measurements performed. Annealing to 600 and 700 °C, respectively, also produced an increase in the O 1s intensity observed in the survey scan, since oxygen-containing hydrocarbon species from the chamber were bound to the surface at elevated temperature.

Table 3.2. The Estimated Fractional ML Coverage, Φ , of a CH₃CC–Si(111) Surface as a Function of Annealing Temperature.

Annealing Temperature (°C)	$\Phi_{\text{Si-CCCH}_3}^a$
22	0.97
100	0.99
200	0.76
300	0.40
400	0.20
500	0.15

^aThe values of Φ were determined using eq 3.1.⁴⁰⁻⁴¹ The appearance of SiC on both surfaces upon annealing to 600 °C precluded accurate determination of Φ beyond 500 °C.

3.3.4 Atomic-Force Microscopy, Electrochemical Scanning-Tunneling Microscopy, and Low-Energy Electron Diffraction

Figure 3.7 presents a topographical AFM image of a CH₃CC–Si(111) surface. CH₃CC–Si(111) surfaces exhibited broad atomic terraces with step edges ~0.3 nm in height, consistent with terraces observed on reconstructed Si(111) surfaces in vacuum.⁴⁸ Some small particulates were observed on the surfaces, and the amount and size of the particles varied between samples. Since no residual metal or halogen contaminants were detected by XPS on these samples, the particulates were likely organic contaminants. The

observation of atomic terraces after alkylation was consistent with the grafting of an overlayer with uniform thickness onto the surface of the Si(111) substrate.

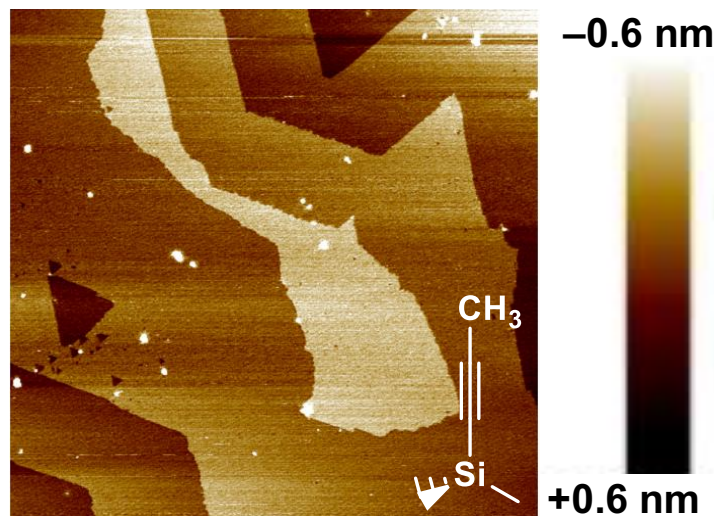


Figure 3.7. Topographical AFM image of a $\text{CH}_3\text{CC-Si}(111)$ surface. The image is $1\ \mu\text{m} \times 1\ \mu\text{m}$ with a z-scale of 1.2 nm (-0.6 to $+0.6$ nm).

Figure 3.8 shows a representative EC-STM image of a $\text{CH}_3\text{CC-Si}(111)$ surface. $\text{CH}_3\text{CC-Si}(111)$ surfaces showed localized areas in which some ordering was detectable by room temperature EC-STM. Representative areas in which species of similar height were observed are indicated by white circles, and the distance between the centers of these areas was 0.38 nm, consistent with the distance between Si(111) atop sites.³³ The height variation from the dark to light regions on a single terrace in was 0.08 ± 0.01 nm, which is smaller than the 0.3 nm Si(111) terrace height. The small height variation suggested that the Si substrate was disordered during the grafting process or that species other than $\text{CH}_3\text{CC-Si}(111)$ groups were present on the surface.

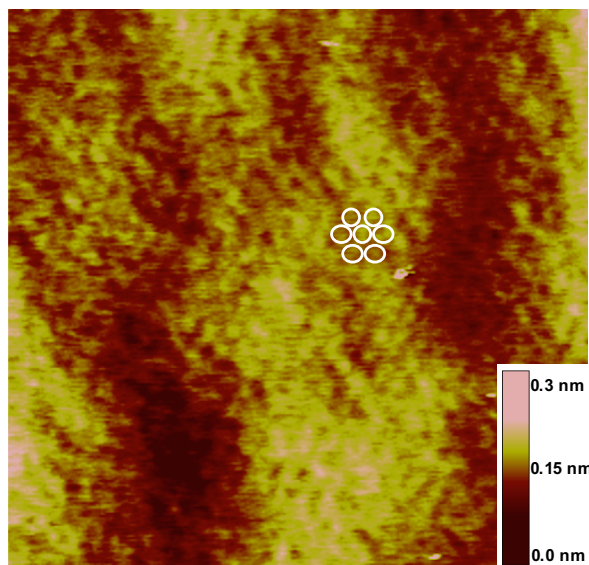


Figure 3.8. Representative EC-STM image a CH₃CC-Si(111) surface (10 nm × 10 nm) collected at -0.4 V versus Ag/AgCl with a bias voltage of -350 mV and tunneling current of 5 nA. The z-scale is indicated in the figure. The white circles in the figures highlight areas where species of similar height were observed, and localized areas of the CH₃CC-Si(111) surface exhibited a (1 × 1) surface unit cell. The distance between the centers of the white circles was 0.38 nm, the same as the distance between Si(111) atop sites.

LEED patterns were collected for CH₃CC-Si(111) surfaces (Figure 3.9) to qualitatively determine the ordering of the top surface layers of the substrate. LEED patterns that exhibit 3-fold symmetry indicate a (1 × 1) surface unit cell. However, while LEED is significantly more surface-sensitive than X-ray diffraction, sharp LEED patterns are often observed for crystalline samples terminated by a disordered monolayer. The intensity of the background relative to the diffraction spots can qualitatively assist in determining the level of ordering on the surface. LEED patterns of CH₃CC-Si(111) surfaces exhibited 3-fold symmetry with the presence of a hexagonal diffraction pattern at 40 eV beam energy, consistent with a (1 × 1) surface unit cell. The intensity of the background was on the same order as that observed for HCC-Si(111) surfaces (see

Chapter 2), which indicated a similar level of ordering at the surface. While both $\text{CH}_3\text{CC-Si(111)}$ and HCC-Si(111) surfaces exhibited comparably bright and sharp diffraction spots, and the only evidence of lower ordering was in the intensity of the background. Both $\text{CH}_3\text{CC-Si(111)}$ and HCC-Si(111) surfaces exhibited brighter backgrounds relative to the diffraction spots compared with $\text{CH}_3\text{-Si(111)}$ surfaces, indicating that the level of surface ordering present on $\text{CH}_3\text{CC-Si(111)}$ and HCC-Si(111) surfaces was not as long-range as has been found for $\text{CH}_3\text{-Si(111)}$ surfaces.

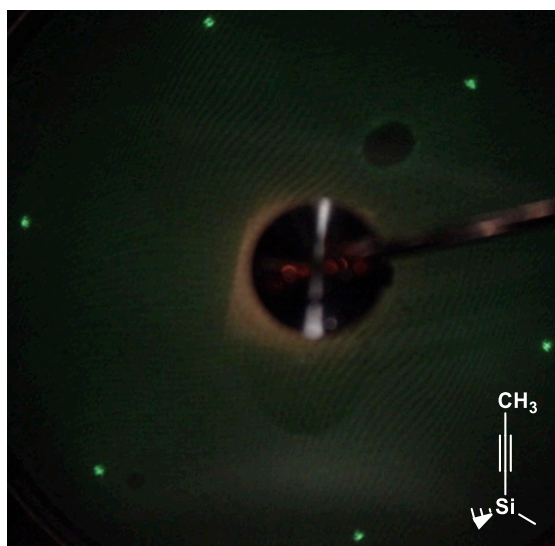


Figure 3.9. Representative LEED pattern for a $\text{CH}_3\text{CC-Si(111)}$ surface collected at 40 eV incident beam energies.

3.3.5 Surface Recombination Velocity Measurements

Figure 3.10 shows the behavior of S determined by use of eq 2.3⁴ for $\text{CH}_3\text{-Si(111)}$ and $\text{CH}_3\text{CC-Si(111)}$ surfaces as a function of time in air. Immediately after preparation and cleaning, $\text{CH}_3\text{-Si(111)}$ and $\text{CH}_3\text{CC-Si(111)}$ surfaces exhibited S values of $(4 \pm 2) \times 10^1$ and $(2.0 \pm 0.2) \times 10^3 \text{ cm s}^{-1}$ respectively. After being exposed to air for 24 h, the S

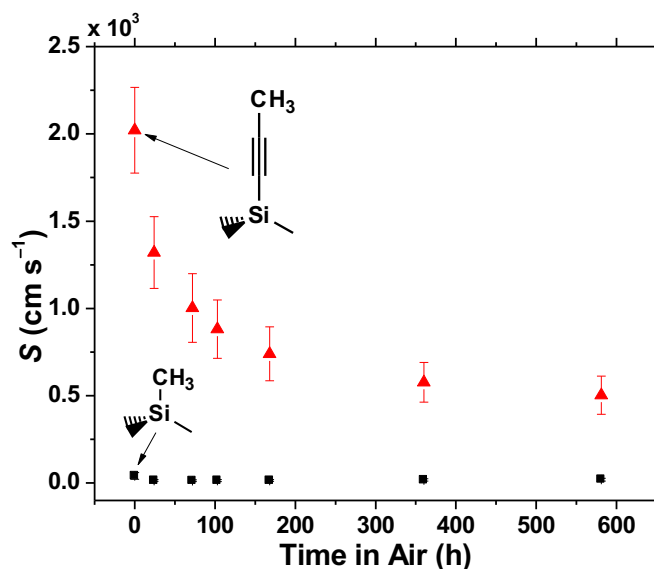


Figure 3.10. S measured as a function of exposure to air for CH₃-Si(111) (black squares) and CH₃CC-Si(111) (red triangles) surfaces. The error bars represent 1 standard deviation about the mean.

value for CH₃-Si(111) and CH₃CC-Si(111) surfaces decreased to $(1.5 \pm 0.5) \times 10^1$ and $(1.3 \pm 0.2) \times 10^3 \text{ cm s}^{-1}$, respectively. Over extended exposure to air, the S value of CH₃CC-Si(111) surfaces continued to decrease, reaching $(5 \pm 1) \times 10^2 \text{ cm s}^{-1}$ after 581 h of air exposure.

The effective trap-state density, N_t , was calculated for CH₃-Si(111) and CH₃CC-Si(111) surfaces by use of eq 2.4.⁴⁴ Immediately after preparation, CH₃-Si(111) and CH₃CC-Si(111) surfaces were found to have trap-state densities of 4×10^9 and $2 \times 10^{11} \text{ cm}^{-2}$, which is equivalent to 1 trap for every 2×10^5 and 4×10^3 surface sites, respectively. After 581 h of exposure to air, the trap-state densities of CH₃-Si(111) and CH₃CC-Si(111) surfaces had adjusted to yield 2×10^9 and $5 \times 10^{10} \text{ cm}^{-2}$, or 1 trap for every 4×10^5 and 2×10^4 surface sites, respectively. The estimated trap-state density for

the studied surfaces was below the detection limit for most spectroscopies, hindering the identification of the chemical structures that form the surface trap states. However, among $\text{CH}_3\text{-Si}(111)$, $\text{HCC-Si}(111)$ (see Chapter 2), and $\text{CH}_3\text{CC-Si}(111)$ surfaces, an increased calculated surface coverage of Si-C correlated with decreased S after 581 h of air exposure.

3.4 DISCUSSION

3.4.1 Vibrational Spectroscopy of $\text{CH}_3\text{CC-Si}(111)$ Surfaces

TIRS (Figure 3.1) and HREELS (Figure 3.3) of $\text{CH}_3\text{CC-Si}(111)$ surfaces showed vibrational signatures characteristic of the proposed $\text{Si-C}\equiv\text{C-CH}_3$ structure. The polarized “umbrella” mode at 1380 cm^{-1} is significantly higher in energy than the “umbrella” signature that is observed on $\text{CH}_3\text{-Si}(111)$ surfaces at 1257 cm^{-1} , and this observation is supported by theoretical calculations, which place the $\text{CH}_3\text{CC-Si}(111)$ “umbrella” mode at $\sim 1392\text{ cm}^{-1}$.⁴⁹ The significant shift in energy is thought to result from the change in bonding environment around the $-\text{CH}_3$ group, which is bonded to either Si or C for $\text{CH}_3\text{-Si}(111)$ or $\text{CH}_3\text{CC-Si}(111)$ surfaces, respectively.

Additionally, the CH_3 rocking mode for $\text{CH}_3\text{CC-Si}(111)$ surfaces at 966 cm^{-1} exhibited a significant shift to higher energy compared with the CH_3 rocking mode for $\text{CH}_3\text{-Si}(111)$ surfaces at 753 cm^{-1} . The $-\text{CH}_3$ group on the $\text{CH}_3\text{CC-Si}(111)$ surface is positioned farther from the Si lattice than in the case of $\text{CH}_3\text{-Si}(111)$ surfaces, resulting in reduced strain and increased energy of the CH_3 rocking motion. This observation is supported by theoretical calculations, which have predicted the appearance of the CH_3

rocking mode at 1018 cm^{-1} .⁴⁹ Theory also predicts a C–C stretching mode at approximately 1030 cm^{-1} , but the symmetry of this bond precludes its observation by TIRS. The proximity of this mode to the $(\text{Si–O–Si})_{\text{TO}}$ mode as well as to the CH_3 rocking mode yielded a single peak at 1048 cm^{-1} in the HREEL spectrum, preventing the clear observation of the C–C bond by vibrational spectroscopy.

Unlike $\text{CH}_3\text{–Si}(111)$ surfaces, which exhibit two C–H stretching modes, $\text{CH}_3\text{CC–Si}(111)$ surfaces show three distinct C–H stretching peaks. Group theory considerations require that a –CH_3 group has both a_1 symmetric and e asymmetric C–H stretching modes. However, gas-phase propyne is known to exhibit an absorbance that arises from Fermi resonance between the asymmetric C–H bending (IR inactive) and symmetric C–H stretching modes.⁵⁰⁻⁵¹ The a_1 symmetric C–H stretch is expected to have a transition dipole along the axis perpendicular to the surface plane, while the e asymmetric C–H stretch is expected to have a transition dipole parallel to the surface plane. The peak resulting from Fermi resonance is predicted to be centered near twice the energy of the asymmetric C–H bend, which theoretical investigations have estimated to be at 1449 cm^{-1} .⁴⁹ A tentative assignment of the C–H stretching peaks from high to low wavenumber is the asymmetric C–H stretch at 2957 cm^{-1} , the Fermi resonance overtone at 2933 cm^{-1} , and the symmetric C–H stretch at 2872 cm^{-1} .

3.4.2 Surface Ordering, Stability, and Defects of $\text{CH}_3\text{CC–Si}(111)$ Surfaces

$\text{CH}_3\text{CC–Si}(111)$ surfaces exhibited AFM images that indicated atomically smooth surfaces, and LEED patterns were consistent with a (1×1) surface unit cell. However,

room temperature EC-STM images of $\text{CH}_3\text{CC-Si(111)}$ surfaces showed that these surfaces did not exhibit the same long-range ordering characteristic of $\text{CH}_3\text{-Si(111)}$ surfaces. Instead, localized regions of ordering were observed on $\text{CH}_3\text{CC-Si(111)}$ surfaces. $\text{CH}_3\text{CC-Si(111)}$ surfaces exhibited larger regions of uniform coverage compared to HCC-Si(111) surfaces (see Chapter 2), but both surfaces exhibited small variations in height that were not consistent with the height of a Si(111) step edge. For $\text{CH}_3\text{CC-Si(111)}$ surfaces, the bright and dark regions in Figure 3.8 correspond to ~ 0.7 ML and ~ 0.3 ML, respectively. The small difference in height observed between regions was indicative of a difference in the density of states, which could result from a difference in orientation of the $-\text{CCCH}_3$ groups or a difference in chemical species bound to the surface. XPS surface coverage estimates predict near complete termination of $\text{CH}_3\text{CC-Si(111)}$ surfaces with Si-C bonds. Thus, the EC-STM images for $\text{CH}_3\text{CC-Si(111)}$ surfaces show either regions in which the atop Si atoms were disordered by the functionalization method to yield regions in which the $-\text{CCCH}_3$ groups were not normal to the surface, or hydrocarbon impurities were present in the alkylating solution and attached along with the propynyl groups. The height difference on the same terrace was small (< 0.1 nm), and the surfaces exhibited localized regions in which ordering was evident, but significant long-range ordering was not observed for $\text{CH}_3\text{CC-Si(111)}$ surfaces. Given the irreversible nature of the Si-C bond, and the resulting lack of mobility of the surface-bound organic groups, steric considerations could preclude facile formation of a fully ordered alkylated monolayer over large areas, and the ordering observed for $\text{CH}_3\text{-Si(111)}$ and $\text{CH}_3\text{-Ge(111)}$ surfaces⁵² are thus unique in this respect.

The behavior of the trap-state density as a function of time for $\text{CH}_3\text{CC-Si(111)}$ surfaces correlates with that observed for $\text{CH}_3\text{-Si(111)}$ surfaces (see Chapter 1). $\text{CH}_3\text{-Si(111)}$ surfaces exhibit unusually low trap-state densities that has been attributed to near 1 ML monolayer $\Phi_{\text{Si-C}}$ and long-range ordering of the surface made possible by the small size of the $-\text{CH}_3$ group. The $\text{CH}_3\text{CC-Si(111)}$ surface has a thicker carbon overlayer and higher $\Phi_{\text{Si-C}}$ compared with the HCC-Si(111) surface (see Chapter 2). These characteristics better protect the $\text{CH}_3\text{CC-Si(111)}$ surface from oxidation and ultimately afford it a lower overall trap-state density. The decrease in trap-state density with time exposed to air observed for $\text{CH}_3\text{-Si(111)}$ and $\text{CH}_3\text{CC-Si(111)}$ surfaces could result from reaction of the existing trap states with water and oxygen in the air without breaking the Si-Si backbonds.

The thermal stability behavior of $\text{CH}_3\text{CC-Si(111)}$ surfaces indicates that $\text{CH}_3\text{CC-Si(111)}$ surfaces have a lower thermal stability than $\text{CH}_3\text{-Si(111)}$ surfaces, which are known to be stable up to 450 °C in vacuum.^{45, 53} $\text{CH}_3\text{CC-Si(111)}$ surfaces appeared to show a loss of the propynyl groups as the sample was annealed to 300–500 °C because the overall intensity of the C 1s peak decreased. The desorption of $-\text{CCCH}_3$ groups from the sample surface is comparable to the behavior observed for $\text{H}_5\text{C}_2\text{-Si(111)}$ surfaces, which exhibit ~40% reduction in C bound to Si upon annealing to 300 °C.⁴⁵ Formation of SiC on $\text{CH}_3\text{CC-Si(111)}$ surfaces annealed to 600 and 700 °C, respectively, was limited by the reduced amount of C on the surface after annealing. These results suggest that the $-\text{CCCH}_3$ surfaces are hindered from reacting with hydrocarbons in the vacuum chamber by the $-\text{CH}_3$ group, and the Si-C bond breaks before the $\text{C}\equiv\text{C}$ bond can react. The results

indicate that the Si–C bond is destabilized for organic species containing Si–C≡C–R functionality compared with CH₃–Si(111) surfaces.

3.4.3 Comparison with Previously Reported Syntheses and Surface Spectroscopy

Preparation of CH₃CC–Si(111) surfaces has been reported by reaction of Cl–Si(111) surfaces with CH₃CCNa in THF³⁵ or CH₃CCMgBr in THF.^{17, 36-38} Table 3.3 summarizes the synthetic methods, surface characterization techniques employed, and results of the prior studies. Anodic deposition of CH₃CCMgBr on H–Si(111) surfaces has also been reported, but a polymeric layer was formed on the surface.³⁹ Our attempts to prepare CH₃CC–Si(111) surfaces by the published halogenation/alkylation procedures yielded widely varying results that were not in general agreement with the detailed spectroscopic signatures and results reported herein. Vibrational spectra reported for anodic deposition of CH₃CCMgBr on H–Si(111) surfaces showed the presence of a peak at ~1100 cm⁻¹, which was assigned to a C≡C–C stretching mode³⁹ and is very near the peaks reported in this work at 1061, 1033, and 966 cm⁻¹. However, due to the polymeric nature of the grafted layer, the modes associated with the CH₃ group of the propynyl moiety were not observed. Using the synthetic routes presented herein, the observation of the vibrational signatures, particularly the C≡C stretch at 2216 cm⁻¹, C–H “umbrella” at 1380 cm⁻¹, and Si–C stretch at 670 cm⁻¹, strongly support the attachment of propynyl groups to the Si(111) surface.

Table 3.3. Summary of Prior Reports of Synthesis and Characterization of Propynyl-Terminated Si Surfaces

Publication	Reaction Conditions	Characterization and Evidence for Structure
ref ³⁵	Cl-Si(111) reacted with NaCCCH ₃ in THF to give Si-CCCH ₃ surfaces.	XPS: C 1s XP peak at 284.0 eV used to suggest C bound to Si. Coverage estimated to be 1.05 ± 0.1 ML for Si-CCCH ₃ relative to Si-CH ₃ . No evidence for SiO _x in Si 2p. Electrochemical measurements show no Si-H oxidation peak in aqueous electrolyte.
ref ¹⁷	Cl-Si(111) reacted with CH ₃ CCMgBr in THF at 120–130 °C for 24 h to give Si-CCCH ₃ surfaces.	No structural characterization reported. Electrochemical measurements for Si-CCCH ₃ surfaces in contact with Hg were shown to exhibit behavior similar to Si-CH ₃ surfaces.
ref ³⁸	Cl-Si(111) reacted with CH ₃ CCMgBr in THF at 120–130 °C for 27 h to yield Si-CCCH ₃ surfaces.	XPS: C1s XP peak at 284.0 eV used to suggest C bound to Si. Coverage with -CCCH ₃ groups was estimated to be 1.05 ± 0.1 ML relative to Si-CH ₃ . No SiO _x observed after preparation. SiO _x was ~0.5 ML after 24 h in water and ~0.15 ML after 65 days in air. ToF-SIMS showed SiCH ₃ ⁺ and SiC ₃ H ₃ ⁺ fragment peak intensities were in a ratio of ~3:2 for Si-CCCH ₃ surfaces.
ref ³⁶	Cl-Si(111) reacted with CH ₃ CCMgBr in THF at 120–130 °C for 27 h to yield Si-CCCH ₃ surfaces.	XPS results are similar to those reported in the previous citation. ToF-SIMS raw data is presented, and shows that Si-CCCH ₃ surfaces gave SiCH ₃ ⁺ and SiC ₃ H ₃ ⁺ (peak ratio 1.9:1) for positive ToF-SIMS. C ₃ H ₃ ⁻ and SiO ₂ (peak ratio 2.7:1) were the primary peaks for negative ToF-SIMS. Spectroscopic ellipsometry gave a thickness of 5.8 Å for Si-CCCH ₃ surfaces, in agreement with theory.
ref ³⁷	Cl-Si(111) and Si-Cl nanowires reacted with CH ₃ CCMgBr in THF at 120–130 °C for 12–27 h to yield Si-CCCH ₃ planar or nanowire surfaces, respectively.	XPS: Si nanowires functionalized with -CCCH ₃ groups exhibit SiO _x /Si bulk 2p area ratio of 0.15 after 720 h of air exposure, which is faster than nanowires functionalized with -CH ₃ or -CH=CH-CH ₃ groups. However, comparative studies performed on Si(111) surfaces show much slower oxidation for CH ₃ CC-Si(111) (SiO _x /Si bulk 2p area ratio ~0.07 after 720 h air exposure) surfaces compared with CH ₃ -Si(111) surfaces.
ref ³⁹	Anodic grafting of HCCMgCl and HCCMgBr in THF to H-Si(111) surfaces. The current density was 0.5 or 0.02 mA cm ⁻² applied over 15–20 min.	SEM indicated the presence of a polymeric layer for all samples prepared. IR: All samples showed disappearance of Si-H after anodic deposition. Samples prepared from CH ₃ CCMgBr showed a C≡C-C stretching vibration at ~1100 cm ⁻¹ , and no C-H stretching peaks were observed. SXPS: A C 1s XP peak at 283.7 eV was used to qualitatively suggest C bound to Si. Si 2p XP spectra showed shift in surface Si to higher binding energy, further suggesting that the surface Si is bound to C.

3.5 CONCLUSIONS

CH₃CC–Si(111) surfaces have been synthesized and characterized by a variety of spectroscopic methods. TIRS and HREELS data show the characteristic vibrational modes for Si–C≡C–CH₃ groups covalently bound perpendicular to the surface. Quantification of XPS data for CH₃CC–Si(111) surfaces exhibited $\Phi_{\text{Si-CCCH}_3} = 1.05 \pm 0.06$ ML. The prepared surfaces exhibited no detectable unreacted Si–H or Si–Cl sites. Annealing of CH₃CC–Si(111) surfaces in vacuum resulted in desorption of the –CCCH₃ groups. AFM and LEED data showed that the surfaces exhibited terraced structures and ordering comparable to that of CH₃–Si(111) surfaces, though EC-STM data showed that the surfaces did not exhibit the long-range ordering of CH₃–Si(111) surfaces.

The complete vibrational spectra for the CH₃CC–Si(111) surfaces presented in this work definitively establish the covalent attachment of ethynyl and propynyl groups to the Si(111) surface. The use of a wide range of surface-sensitive spectroscopic and microscopic techniques provides a clear picture of the surface structure, allowing for the development of structure–function relationships and new chemistries. The development of a comprehensive understanding of the chemical and physical properties of synthesized surfaces is of extraordinary importance in order to further the use of monolayer chemistry in the development of novel new semiconductor devices.

3.6 REFERENCES

1. Bent, S. F. Organic Functionalization of Group IV Semiconductor Surfaces: Principles, Examples, Applications, and Prospects. *Surf. Sci.* **2002**, *500*, 879-903.
2. Buriak, J. M. Organometallic Chemistry on Silicon and Germanium Surfaces. *Chem. Rev.* **2002**, *102*, 1271-1308.
3. Gstrein, F.; Michalak, D. J.; Royea, W. J.; Lewis, N. S. Effects of Interfacial Energetics on the Effective Surface Recombination Velocity of Si/Liquid Contacts. *J. Phys. Chem. B* **2002**, *106*, 2950-2961.
4. Royea, W. J.; Juang, A.; Lewis, N. S. Preparation of Air-Stable, Low Recombination Velocity Si(111) Surfaces through Alkyl Termination. *Appl. Phys. Lett.* **2000**, *77*, 1988-1990.
5. Royea, W. J.; Michalak, D. J.; Lewis, N. S. Role of Inversion Layer Formation in Producing Low Effective Surface Recombination Velocities at Si/Liquid Contacts. *Appl. Phys. Lett.* **2000**, *77*, 2566-2568.
6. Li, Y.; O'Leary, L. E.; Lewis, N. S.; Galli, G. Combined Theoretical and Experimental Study of Band-Edge Control of Si through Surface Functionalization. *J. Phys. Chem. C* **2013**, *117*, 5188-5194.
7. Plymale, N. T.; Kim, Y.-G.; Soriaga, M. P.; Brunshwig, B. S.; Lewis, N. S. Synthesis, Characterization, and Reactivity of Ethynyl- and Propynyl-Terminated Si(111) Surfaces. *J. Phys. Chem. C* **2015**, *119*, 19847-19862.
8. Lattimer, J. R. C.; Blakemore, J. D.; Sattler, W.; Gul, S.; Chatterjee, R.; Yachandra, V. K.; Yano, J.; Brunshwig, B. S.; Lewis, N. S.; Gray, H. B. Assembly, Characterization,

- and Electrochemical Properties of Immobilized Metal Bipyridyl Complexes on Silicon(111) Surfaces. *Dalton Trans.* **2014**, *43*, 15004-15012.
9. Lattimer, J. R. C.; Brunshwig, B. S.; Lewis, N. S.; Gray, H. B. Redox Properties of Mixed Methyl/Vinylferrocenyl Monolayers on Si(111) Surfaces. *J. Phys. Chem. C* **2013**, *117*, 27012-27022.
10. O'Leary, L. E.; Rose, M. J.; Ding, T. X.; Johansson, E.; Brunshwig, B. S.; Lewis, N. S. Heck Coupling of Olefins to Mixed Methyl/Thienyl Monolayers on Si(111) Surfaces. *J. Am. Chem. Soc.* **2013**, *135*, 10081-10090.
11. O'Leary, L. E.; Strandwitz, N. C.; Roske, C. W.; Pyo, S.; Brunshwig, B. S.; Lewis, N. S. Use of Mixed CH₃-/HC(O)CH₂CH₂-Si(111) Functionality to Control Interfacial Chemical and Electronic Properties During the Atomic-Layer Deposition of Ultrathin Oxides on Si(111). *J. Phys. Chem. Lett.* **2015**, *6*, 722-726.
12. Plass, K. E.; Liu, X.; Brunshwig, B. S.; Lewis, N. S. Passivation and Secondary Functionalization of Allyl-Terminated Si(111) Surfaces. *Chem. Mater.* **2008**, *20*, 2228-2233.
13. Cho, C. J.; O'Leary, L.; Lewis, N. S.; Greer, J. R. In Situ Nanomechanical Measurements of Interfacial Strength in Membrane-Embedded Chemically Functionalized Si Microwires for Flexible Solar Cells. *Nano Lett.* **2012**, *12*, 3296-3301.
14. Gallant, B. M.; Gu, X. W.; Chen, D. Z.; Greer, J. R.; Lewis, N. S. Tailoring of Interfacial Mechanical Shear Strength by Surface Chemical Modification of Silicon Microwires Embedded in Nafion Membranes. *ACS Nano* **2015**, *9*, 5143-5153.

15. Maldonado, S.; Knapp, D.; Lewis, N. S. Near-Ideal Photodiodes from Sintered Gold Nanoparticle Films on Methyl-Terminated Si(111) Surfaces. *J. Am. Chem. Soc.* **2008**, *130*, 3300-3301.
16. Maldonado, S.; Lewis, N. S. Behavior of Electrodeposited Cd and Pb Schottky Junctions on CH₃-Terminated n-Si(111) Surfaces. *J. Electrochem. Soc.* **2009**, *156*, H123-H128.
17. Maldonado, S.; Plass, K. E.; Knapp, D.; Lewis, N. S. Electrical Properties of Junctions between Hg and Si(111) Surfaces Functionalized with Short-Chain Alkyls. *J. Phys. Chem. C* **2007**, *111*, 17690-17699.
18. Bansal, A.; Lewis, N. S. Stabilization of Si Photoanodes in Aqueous Electrolytes through Surface Alkylation. *J. Phys. Chem. B* **1998**, *102*, 4058-4060.
19. Bansal, A.; Lewis, N. S. Electrochemical Properties of (111)-Oriented n-Si Surfaces Derivatized with Covalently-Attached Alkyl Chains. *J. Phys. Chem. B* **1998**, *102*, 1067-1070.
20. Bansal, A.; Li, X.; Lauermann, I.; Lewis, N. S.; Yi, S. I.; Weinberg, W. H. Alkylation of Si Surfaces Using a Two-Step Halogenation/Grignard Route. *J. Am. Chem. Soc.* **1996**, *118*, 7225-7226.
21. Bansal, A.; Li, X.; Yi, S. I.; Weinberg, W. H.; Lewis, N. S. Spectroscopic Studies of the Modification of Crystalline Si(111) Surfaces with Covalently-Attached Alkyl Chains Using a Chlorination/Alkylation Method. *J. Phys. Chem. B* **2001**, *105*, 10266-10277.

22. Becker, J. S.; Brown, R. D.; Johansson, E.; Lewis, N. S.; Sibener, S. J. Helium Atom Diffraction Measurements of the Surface Structure and Vibrational Dynamics of CH₃--Si(111) and CD₃--Si(111) Surfaces. *J. Chem. Phys.* **2010**, *133*, 104705.
23. Brown, R. D.; Hund, Z. M.; Campi, D.; O'Leary, L. E.; Lewis, N. S.; Bernasconi, M.; Benedek, G.; Sibener, S. J. Hybridization of Surface Waves with Organic Adlayer Librations: A Helium Atom Scattering and Density Functional Perturbation Theory Study of Methyl-Si(111). *Phys. Rev. Lett.* **2013**, *110*, 156102.
24. Brown, R. D.; Hund, Z. M.; Campi, D.; O'Leary, L. E.; Lewis, N. S.; Bernasconi, M.; Benedek, G.; Sibener, S. J. The Interaction of Organic Adsorbate Vibrations with Substrate Lattice Waves in Methyl-Si(111)-(1 × 1). *J. Chem. Phys.* **2014**, *141*, 024702.
25. Grimm, R. L.; Bierman, M. J.; O'Leary, L. E.; Strandwitz, N. C.; Brunschwig, B. S.; Lewis, N. S. Comparison of the Photoelectrochemical Behavior of H-Terminated and Methyl-Terminated Si(111) Surfaces in Contact with a Series of One-Electron, Outer-Sphere Redox Couples in CH₃CN. *J. Phys. Chem. C* **2012**, *116*, 23569-23576.
26. Nihill, K. J.; Hund, Z. M.; Muzas, A.; Díaz, C.; del Cueto, M.; Frankcombe, T.; Plymale, N. T.; Lewis, N. S.; Martín, F.; Sibener, S. J. Experimental and Theoretical Study of Rotationally Inelastic Diffraction of H₂(D₂) from Methyl-Terminated Si(111). *J. Chem. Phys.* **2016**, *145*, 084705.
27. Webb, L. J.; Lewis, N. S. Comparison of the Electrical Properties and Chemical Stability of Crystalline Silicon(111) Surfaces Alkylated Using Grignard Reagents or Olefins with Lewis Acid Catalysts. *J. Phys. Chem. B* **2003**, *107*, 5404-5412.
28. Webb, L. J.; Michalak, D. J.; Biteen, J. S.; Brunschwig, B. S.; Chan, A. S. Y.; Knapp, D. W.; Meyer, H. M.; Nemanick, E. J.; Traub, M. C.; Lewis, N. S. High-Resolution

- Soft X-ray Photoelectron Spectroscopic Studies and Scanning Auger Microscopy Studies of the Air Oxidation of Alkylated Silicon(111) Surfaces. *J. Phys. Chem. B* **2006**, *110*, 23450-23459.
29. Webb, L. J.; Nemanick, E. J.; Biteen, J. S.; Knapp, D. W.; Michalak, D. J.; Traub, M. C.; Chan, A. S. Y.; Brunschwig, B. S.; Lewis, N. S. High-Resolution X-ray Photoelectron Spectroscopic Studies of Alkylated Silicon(111) Surfaces. *J. Phys. Chem. B* **2005**, *109*, 3930-3937.
30. Webb, L. J.; Rivillon, S.; Michalak, D. J.; Chabal, Y. J.; Lewis, N. S. Transmission Infrared Spectroscopy of Methyl- and Ethyl-Terminated Silicon(111) Surfaces. *J. Phys. Chem. B* **2006**, *110*, 7349-7356.
31. Wong, K. T.; Lewis, N. S. What a Difference a Bond Makes: The Structural, Chemical, and Physical Properties of Methyl-Terminated Si(111) Surfaces. *Acc. Chem. Res.* **2014**, *47*, 3037-3044.
32. Yamada, T.; Kawai, M.; Wawro, A.; Suto, S.; Kasuya, A. HREELS, STM, and STS study of CH₃-Terminated Si(111)-(1 x 1) Surface. *J. Chem. Phys.* **2004**, *121*, 10660-10667.
33. Yu, H.; Webb, L. J.; Ries, R. S.; Solares, S. D.; Goddard, W. A.; Heath, J. R.; Lewis, N. S. Low-Temperature STM Images of Methyl-Terminated Si(111) Surfaces. *J. Phys. Chem. B* **2004**, *109*, 671-674.
34. O'Leary, L. E.; Johansson, E.; Brunschwig, B. S.; Lewis, N. S. Synthesis and Characterization of Mixed Methyl/Allyl Monolayers on Si(111). *J. Phys. Chem. B* **2010**, *114*, 14298-14302.

35. Hurley, P. T.; Nemanick, E. J.; Brunschwig, B. S.; Lewis, N. S. Covalent Attachment of Acetylene and Methylacetylene Functionality to Si(111) Surfaces: Scaffolds for Organic Surface Functionalization while Retaining Si–C Passivation of Si(111) Surface Sites. *J. Am. Chem. Soc.* **2006**, *128*, 9990-9991.
36. Puniredd, S. R.; Assad, O.; Haick, H. Highly Stable Organic Monolayers for Reacting Silicon with Further Functionalities: The Effect of the C–C Bond nearest the Silicon Surface. *J. Am. Chem. Soc.* **2008**, *130*, 13727-13734.
37. Assad, O.; Puniredd, S. R.; Stelzner, T.; Christiansen, S.; Haick, H. Stable Scaffolds for Reacting Si Nanowires with Further Organic Functionalities while Preserving Si–C Passivation of Surface Sites. *J. Am. Chem. Soc.* **2008**, *130*, 17670-17671.
38. Puniredd, S. R.; Assad, O.; Haick, H. Highly Stable Organic Modification of Si(111) Surfaces: Towards Reacting Si with Further Functionalities while Preserving the Desirable Chemical Properties of Full Si–C Atop Site Terminations. *J. Am. Chem. Soc.* **2008**, *130*, 9184-9185.
39. Yang, F.; Hunger, R.; Roodenko, K.; Hinrichs, K.; Rademann, K.; Rappich, J. Vibrational and Electronic Characterization of Ethynyl Derivatives Grafted onto Hydrogenated Si(111) Surfaces. *Langmuir* **2009**, *25*, 9313-9318.
40. Briggs, D.; Seah, M. P. *Practical Surface Analysis: Auger and X-ray Photoelectron Spectroscopy*, 2nd ed.; John Wiley & Sons, Inc.: New York, 1990; Vol. 1.
41. Haber, J. A.; Lewis, N. S. Infrared and X-ray Photoelectron Spectroscopic Studies of the Reactions of Hydrogen-Terminated Crystalline Si(111) and Si(100) Surfaces with Br₂, I₂, and Ferrocenium in Alcohol Solvents. *J. Phys. Chem. B* **2002**, *106*, 3639-3656.

42. van der Marel, C.; Yildirim, M.; Stapert, H. R. Multilayer Approach to the Quantitative Analysis of X-ray Photoelectron Spectroscopy Results: Applications to Ultrathin SiO₂ on Si and to Self-Assembled Monolayers on Gold. *J. Vac. Sci. Technol. A* **2005**, *23*, 1456-1470.
43. Seah, M. P.; Spencer, S. J. Ultrathin SiO₂ on Si II. Issues in Quantification of the Oxide Thickness. *Surf. Interface Anal.* **2002**, *33*, 640-652.
44. Yablonovitch, E.; Allara, D. L.; Chang, C. C.; Gmitter, T.; Bright, T. B. Unusually Low Surface-Recombination Velocity on Silicon and Germanium Surfaces. *Phys. Rev. Lett.* **1986**, *57*, 249-252.
45. Jaeckel, B.; Hunger, R.; Webb, L. J.; Jaegermann, W.; Lewis, N. S. High-Resolution Synchrotron Photoemission Studies of the Electronic Structure and Thermal Stability of CH₃- and C₂H₅-Functionalized Si(111) Surfaces. *J. Phys. Chem. C* **2007**, *111*, 18204-18213.
46. Contarini, S.; Howlett, S. P.; Rizzo, C.; De Angelis, B. A. XPS Study on the Dispersion of Carbon Additives in Silicon Carbide Powders. *Appl. Surf. Sci.* **1991**, *51*, 177-183.
47. Muehlhoff, L.; Choyke, W. J.; Bozack, M. J.; Yates, J. T. Comparative Electron Spectroscopic Studies of Surface Segregation on SiC(0001) and SiC(000 $\bar{1}$). *J. Appl. Phys.* **1986**, *60*, 2842-2853.
48. Becker, R. S.; Golovchenko, J. A.; McRae, E. G.; Swartzentruber, B. S. Tunneling Images of Atomic Steps on the Si(111)7x7 Surface. *Phys. Rev. Lett.* **1985**, *55*, 2028-2031.

49. Ferguson, G. A.; Raghavachari, K. Collective Vibrations in Cluster Models for Semiconductor Surfaces: Vibrational Spectra of Acetylenyl and Methylacetylenyl Functionalized Si(111). *J. Chem. Phys.* **2007**, *127*, 194706.
50. Boyd, D. R. J.; Thompson, H. W. The Infra-Red Spectrum of Methyl Acetylene. *T. Faraday Soc.* **1952**, *48*, 493-501.
51. Kondo, S.; Koga, Y. Infrared Absorption Intensities of Methyl Acetylene. *J. Chem. Phys.* **1978**, *69*, 4022-4031.
52. Wong, K. T.; Kim, Y.-G.; Soriaga, M. P.; Brunswig, B. S.; Lewis, N. S. Synthesis and Characterization of Atomically Flat Methyl-Terminated Ge(111) Surfaces. *J. Am. Chem. Soc.* **2015**.
53. Hunger, R.; Fritsche, R.; Jaeckel, B.; Jaegermann, W.; Webb, L. J.; Lewis, N. S. Chemical and Electronic Characterization of Methyl-Terminated Si(111) Surfaces by High-Resolution Synchrotron Photoelectron Spectroscopy. *Phys. Rev. B* **2005**, *72*, 045317.

*Chapter 4***CONTROL OF THE BAND-EDGE POSITIONS OF CRYSTALLINE Si(111) BY SURFACE FUNCTIONALIZATION WITH 3,4,5-TRIFLUOROPHENYLACETYLENYL MOIETIES**

Plymale, N. T.; Ramachandran, A. R.; Lim, A. N.; Brunshwig, B. S.; Lewis, N. S. Control of the Band-Edge Positions of Crystalline Si(111) Surfaces by Functionalization with 3,4,5-Trifluorophenylacetylenyl Moieties. *J. Phys. Chem. C* **2016**, *120*, 14157–14169. DOI: 10.1021/acs.jpcc.6b03824

4.1 INTRODUCTION

The photovoltage produced by a semiconductor device is defined by the energetics of the junction.¹ Modern semiconductor devices rely heavily on p-n homojunctions to form a voltage-producing junction that is independent of the energetics of the interfacing phase, which can include metals,²⁻³ metal oxides,⁴⁻⁸ catalysts,⁹⁻¹⁰ conductive polymers,¹¹⁻¹⁴ and electrolytes.¹⁵⁻¹⁷ Many semiconductors cannot, however, be doped to form high-quality p-n homojunctions, and moreover the diffusive doping processes used to fabricate emitter layers are generally not compatible with small-grain-size polycrystalline thin-film semiconducting base layers.¹⁸⁻¹⁹ In these cases it is often necessary to form a voltage-producing junction between the semiconductor and a contacting phase, for example, a semiconductor/liquid junction. Therefore, the development of methods to tune the semiconductor energetics relative to those of the

contacting phase using thin or monolayer films could enable the use of new polycrystalline or thin-film materials in devices as well as lower the processing costs associated with device fabrication.

In the context of this work, the term “surface dipole” is used to refer to the unequal distributions of positive and negative charge at the silicon surface. This surface dipole produces an interfacial electric field that shifts the band-edge positions of the silicon relative to those in the contacting phase. Thus, shifts in band-edge positions produced by the surface dipole are reported in volts or electronvolts.

Control over the direction and magnitude of the dipole at the semiconductor surface, through chemical attachment of a molecular species, allows for manipulation of the semi-conductor’s interfacial electric field to produce effective charge separation at the interface.²⁰ In principle, the barrier height, Φ_b , can be adjusted as a function of the surface dipole moment, allowing the relative band-edge positions to be tuned to drive a desired process (Figure 4.1). Control of the surface dipole for use in photoelectrochemical devices requires that the surface is stable under operational conditions and that a small or negligible fraction of the current is lost to surface recombination. A positive surface dipole has been produced on GaInP₂ and GaAs substrates by chemical functionalization.²¹⁻²³ The band-edge positions of Si(111) surfaces have also been modified to improve the energetics of junctions with metal oxides for use in catalytic applications.²⁴⁻²⁵

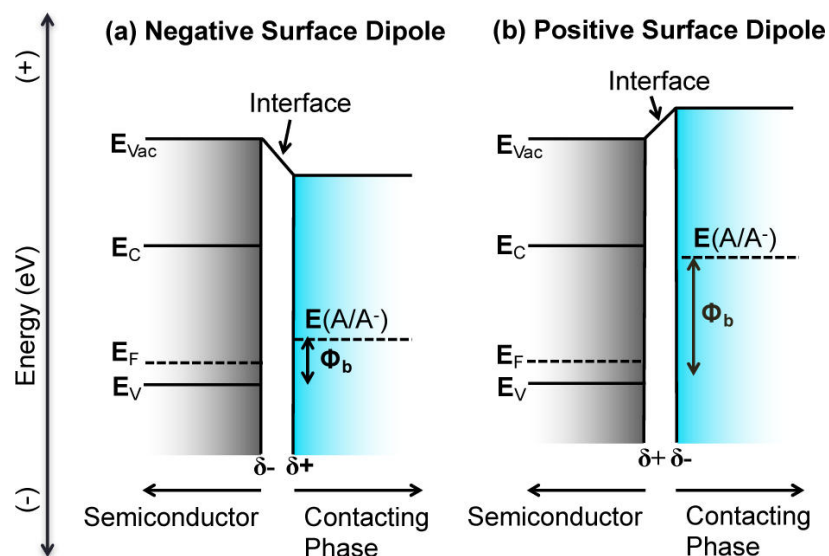


Figure 4.1. Effect of a surface dipole on the band-edge positions and barrier height, Φ_b , for a p-type semiconductor. The partial δ^+ and δ^- charges show the orientation of the dipole moment at the interface necessary to achieve the desired band-edge shift. The relative energy positions of the valence band, E_V , the Fermi level, E_F , the conduction band, E_C , the vacuum level, E_{Vac} , and the average electron energy of the contacting phase, $E(A/A^-)$, are indicated.

Alkyl termination of Si surfaces using wet chemical methods²⁶⁻³⁰ could provide a scalable and versatile method to control the band-edge positions. A two-step halogenation/alkylation process³¹ has been shown to produce methyl-terminated Si(111) surfaces, Si(111)-CH₃, with low surface recombination velocities, S , that are stable for >500 h in air.³²⁻³⁴ Relative to Si(111)-H surfaces, Si(111)-CH₃ surfaces are more stable against oxide formation³⁵⁻³⁷ and are readily interfaced with metals without the formation of metal silicides;³⁸⁻³⁹ however, methyl termination of Si(111) produces a -0.4 V surface dipole,³⁸⁻⁴² which on p-Si surfaces will lower Φ_b at the Si interface and reduce the electric field at the junction that drives the charge separation.

Surface functionalization with groups that contain C–F bonds, such as 3,4,5-trifluorophenylacetylene (TFPA), should in principle produce a dipole moment opposite in sign to the C–H bonds in –CH₃ groups and thus lead to a reversal of the negative dipole at p-type Si(111)–CH₃ surfaces. Mixed monolayer chemistry at Si(111) surfaces allows for functionalization of the surface with bulky groups that contain a desired functionality while maintaining low *S* and high Si–C termination.^{7, 34, 43-45} A mixed methyl/TFPA (MMTFPA) surface could therefore provide desirable passivation of the Si surface while allowing for the dipole to be moved more positive as a function of the fractional monolayer TFPA coverage, θ_{TFPA} . Additionally, the C–F bonds in the TFPA groups are chemically inert and are oriented with a significant portion of the dipole moment normal to the surface. MMTFPA monolayers on Si(111) surfaces could provide a robust method for controlling the semiconductor band-edge positions to impart desirable interfacial energetics without requiring formation of a p-n homojunction. Accordingly, we describe herein the synthesis and characterization of Si(111)–MMTFPA surfaces, the electrochemical properties of these surfaces in contact with Hg, and the photoelectrochemical behavior of Si(111)–MMTFPA surfaces in contact with CH₃CN solutions that contain the 1-electron redox couples decamethylferrocenium/decamethylferrocene (Cp*₂Fe⁺⁰) and methyl viologen (MV^{2+/+}).

4.2 EXPERIMENTAL SECTION

4.2.1 Materials and Methods

Water with a resistivity of $\geq 18.2 \text{ M}\Omega \text{ cm}$ was obtained from a Barnstead E-Pure system. Ammonium fluoride ($\text{NH}_4\text{F}(\text{aq})$, 40%, semiconductor grade, Transene, Danvers, MA) was purged with $\text{Ar}(\text{g})$ (99.999%, Air Liquide) for $\geq 1 \text{ h}$ prior to use. 3,4,5-Trifluorophenylacetylene (TFPA, SynQuest Laboratories, Alachua, FL) was purified by four freeze-pump-thaw cycles, dried over activated 3 Å molecular sieves (Sigma-Aldrich), and stored in a $\text{N}_2(\text{g})$ -purged glovebox ($< 10 \text{ ppm O}_2(\text{g})$) in a foil-wrapped glass Schlenk tube. All other chemicals were used as received.

Si wafers were oriented to within 0.5° of the (111) crystal plane. Float-zone-grown Si wafers (University Wafer, Boston, MA) that were used for transmission infrared spectroscopy (TIRS) were double-side polished, not intentionally doped, had a resistivity of $> 2 \text{ k}\Omega \text{ cm}$, and were $525 \pm 15 \mu\text{m}$ thick. Float-zone-grown Si wafers (FZwafers.com, Ridgefield Park, NJ) used for S measurements were double-side polished, not intentionally doped, had a resistivity of 20–40 $\text{k}\Omega \text{ cm}$, and were $300 \pm 25 \mu\text{m}$ thick. Czochralski-grown n-Si wafers (University Wafer, Boston, MA) used for electrochemical experiments were single-side polished, doped with phosphorus to a resistivity of 1.1 to 1.2 $\Omega \text{ cm}$, and were $380 \mu\text{m}$ thick. Czochralski-grown p-Si wafers (Silicon Quest International, San Jose, CA or Addison Engineering, San Jose, CA) used for electrochemical experiments were single-side polished (Silicon Quest International) or

double-side polished (Addison Engineering), doped with boron to a resistivity of 0.40 to 0.43 Ω cm, and were 300 ± 25 μ m thick.

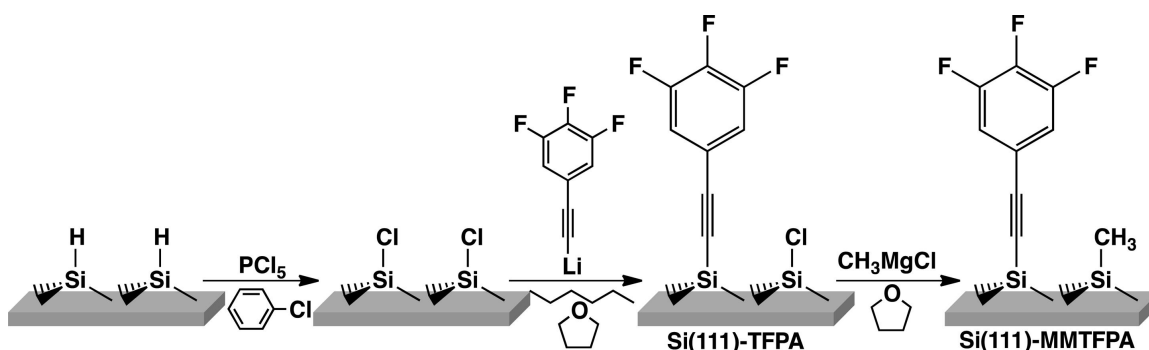
1. Preparation of Lithium 3,4,5-Trifluorophenylacetylide. In a 250 mL round-bottomed flask that was connected to a Schlenk line, degassed and dried 3,4,5-trifluorophenylacetylene (TFPA, 1.95 g, 12.5 mmol) was dissolved in hexanes (100 mL, anhydrous, mixture of isomers, $\geq 99\%$, Sigma-Aldrich). The contents of the flask were cooled to -78 $^{\circ}$ C in a dry ice/acetone bath and were stirred vigorously while *n*-butyllithium (*n*-BuLi, 1.68 M in hexanes, 7.3 mL, 12.3 mmol, Sigma-Aldrich) was added dropwise via a syringe. The reaction was allowed to proceed at -78 $^{\circ}$ C for 30 min, after which the flask was allowed to warm to room temperature while being stirred for an additional 60 min, yielding a white slurry. The slurry was transferred under an inert atmosphere to an amber bottle, which was stored at 8 $^{\circ}$ C. Immediately before use, tetrahydrofuran (THF, anhydrous, $\geq 99.9\%$, Sigma-Aldrich) was added to the lithium 3,4,5-trifluorophenylacetylide (LiTFPA) slurry in 1:4 v/v THF/hexanes to solvate the product, forming a 0.10 M solution.

2. Preparation of Si(111)-H Surfaces. Wafers were cut to the desired size using a diamond-tipped scribe. The samples were washed sequentially with water, methanol ($\geq 99.8\%$, BDH), acetone ($\geq 99.5\%$, BDH), methanol, and water. The wafers were then immersed in a piranha solution (1:3 v/v of 30% H_2O_2 (aq) (EMD)/18 M H_2SO_4 (EMD)) and heated to 95 ± 5 $^{\circ}$ C for 10–15 min. The solution was drained and the wafers were rinsed with copious amounts of water. The oxide was removed by immersing the wafers in aqueous buffered hydrofluoric acid (HF, semiconductor grade, Transene) for 18 s,

followed by a brief rinse with water. Atomically flat Si(111)–H surfaces were formed by anisotropic etching for 5.5 min in an Ar(g)-purged solution of NH₄F(aq).³³ To remove bubbles that formed on the surface, the wafers were agitated at the start of every minute of etching, and the solution was purged throughout the etching process. After etching, the wafers were rinsed with water and dried under Ar(g).

3. Preparation of Si(111)–Cl Surfaces. The Si(111)–H wafers were transferred to a N₂(g)-purged glovebox with <10 ppm O₂(g) and were rinsed with chlorobenzene (anhydrous, ≥99.8%, Sigma-Aldrich). The wafers were placed into a saturated solution of phosphorus pentachloride (PCl₅, ≥99.998% metal basis, Alfa Aesar) in chlorobenzene, and were heated to 90 ± 2 °C for 45 min.³³ The addition of benzoyl peroxide, which has been used as a radical initiator,⁴⁶ was found not to be necessary to yield high-quality Si(111)–Cl surfaces. When the reaction finished, the wafers were removed from the reaction solution and rinsed sequentially with chlorobenzene and anhydrous THF.

4. Alkylation of Si(111)–Cl Surfaces. Si(111)–CH₃ surfaces were prepared by immersing the Si(111)–Cl surfaces in a 3.0 M solution of methylmagnesium chloride (CH₃MgCl, Acros Organics) and heating to 50 ± 2 °C for 12–24 h.³³ Mixed methyl/TFPA (MMTFPA) monolayers (Scheme 4.1) were formed by first reacting Si(111)–Cl surfaces with LiTFPA (0.10 M in 1:4 v/v THF/hexanes) for 1–20 h at 23–65 °C in the absence of light. The wafers were then rinsed with THF and submerged in 3.0 M CH₃MgCl for 12–24 h at 50 °C.^{7, 34, 43} Si(111)–TFPA surfaces were prepared by reacting Si(111)–Cl wafers with LiTFPA (0.10 M) at 65 °C for 10–20 h.

Scheme 4.1. Synthesis of Si(111)-TFPA and Si(111)-MMTFPA Surfaces

After completion of the reactions to yield the target surfaces, the wafers were removed from the reaction solution, rinsed with THF, and submerged in THF. The samples were removed from the glovebox and sonicated for 10 min in each of THF, methanol, and water. Following sonication, the wafers were rinsed with water and dried under $\text{Ar}(\text{g})$. For the fabrication of electrodes, wafers were broken into appropriately sized pieces, rinsed again with water, and dried under $\text{Ar}(\text{g})$.

5. *Formation of Ohmic Contacts to the Back of n- and p-Si(111) Electrodes.* After functionalization, ohmic contacts were formed to the back of n-Si(111) electrodes by application of Ga-In eutectic (78% Ga, 22% In by weight) using a diamond-tipped scribe. Prior to functionalization, ohmic contacts were formed to p-Si(111) samples by electron-beam evaporation (Denton Vacuum) of 100 nm of Al onto the backside of the wafer.⁴⁷ The wafers were then annealed in a Carbolite tube furnace at 450 °C for 30 min under an atmosphere of forming gas (5% $\text{H}_2(\text{g})$ in $\text{N}_2(\text{g})$) flowing at 5 L min^{-1} . The Al layer was isolated from the reaction solution during the functionalization process by use of a custom Teflon reaction vessel (Figure 4.2).

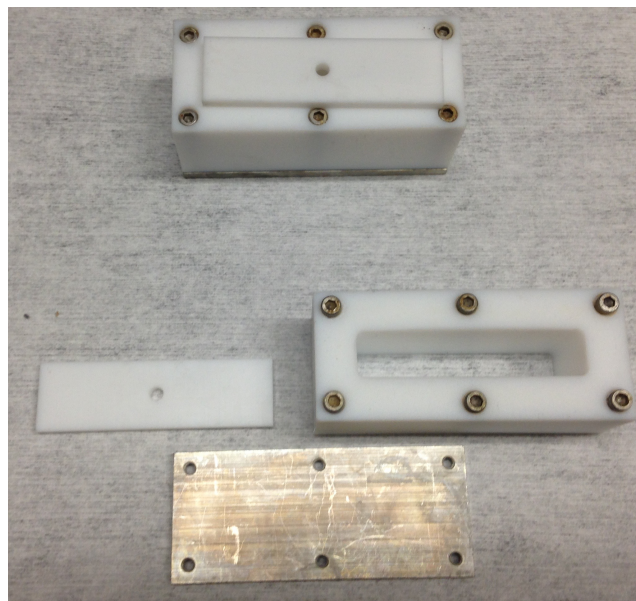


Figure 4.2. The Teflon reaction vessels used to isolate the Al-coated side of p-Si electrodes to allow for reaction on one side of the wafer without etching away the Al layer. The assembled vessel (top) is shown along with the separate aluminum base, Teflon well, and Teflon cap.

6. *Electrochemical Measurements in Contact with Hg.* Electrochemical measurements in contact with Hg⁴⁰ (electronic grade, 99.9999% trace metal basis, Sigma-Aldrich or Alfa Aesar) were performed inside an Ar(g)-filled glovebox (<0.3 ppm O₂(g)) at 23 °C. The wafers were placed on a Cu plate (with the Ga-In eutectic contacting the Cu plate), and a cylindrical Teflon cell was placed on top of the wafer, to produce an electrode area of 0.314 cm². Hg was added to the Teflon cell to cover the exposed area of the wafer, and a Pt wire contacted the top of the Hg. Electrochemical measurements were collected using a two-electrode setup, with the Cu plate connected to the working electrode and the Pt wire connected to the counter electrode. All voltages measured in a two-electrode setup are indicated by V , while potentials measured in a three-electrode setup are indicated by E .

Current density versus voltage (J - V) measurements were performed from -0.5 to $+0.5$ V at a scan rate of 20 mV s^{-1} . The sampling rate was 1 mV per data point using a Solartron 1287 potentiostat operated by CorrWare software (v. 3.2c). Three J - V scans were collected before and after collection of differential capacitance versus voltage (C_{diff} - V) data. C_{diff} - V data were acquired with a 10 mV amplitude sinusoidal signal at an applied DC bias, with the DC bias varied in increments of 0.05 V between 0 and $+0.5 \text{ V}$ for n-Si and between 0 and -0.5 V for p-Si electrodes. The frequency was varied from 10^1 to 10^6 Hz at each DC bias. C_{diff} - V measurements were collected using a Schlumberger SI 1260 frequency response analyzer operated by ZPlot software (v. 3.3e).

7. *Photoelectrochemical Measurements in Acetonitrile.* Si working electrodes were fabricated by using high-purity conductive Ag paint (SPI Supplies, West Chester, PA) to affix a coil of tinned Cu wire to the back side of the Si electrode. The wire was threaded through a $1/4''$ outer diameter Pyrex tube, and the wafer was secured to the tube using Loctite 9460 epoxy (cured under ambient conditions for 12–24 h) such that the wafer surface was perpendicular to the length of the tube. Electrodes used for current density versus potential (J - E) and differential capacitance versus potential (C_{diff} - E) measurements were 0.14 to 0.61 cm^2 in area, as determined by analyzing scanned images of each electrode with ImageJ software. All J - E and C_{diff} - E measurements used a standard three-electrode setup.

Decamethylferrocene (Cp^*_2Fe , bis(pentamethylcyclopentadienyl)iron(II), 99%) was purchased from Strem Chemical and was purified by sublimation. Oxidized decamethylferrocenium (Cp^*_2Fe^+ , bis(pentamethylcyclopentadienyl)iron(III) tetrafluoro-

borate) was synthesized by chemical oxidation of decamethylferrocene and purified by recrystallization from diethyl ether and acetonitrile.⁴⁸ Methyl viologen (MV^{2+} , 1,1'-dimethyl-4,4'-bipyridinium hexafluorophosphate) was prepared according to a literature procedure.⁴⁹ The reduced species $MV^{+\bullet}$ was generated by controlled-potential electrolysis of MV^{2+} at -0.85 V versus $AgNO_3/Ag$ (Bioanalytical Systems) with a Pt mesh working electrode in the main electrochemical cell compartment and a Pt mesh counter electrode located in a compartment that was separated from the main electrochemical cell by a Vycor frit. Subsequent in situ generation of the $MV^{+\bullet}$ species was performed to maintain the cell potential within 25 mV of the initial measured open-circuit potential versus a $AgNO_3/Ag$ reference electrode.

Photoelectrochemical measurements were performed in acetonitrile (CH_3CN , EMD, dried over columns of activated alumina) with 1.0 M $LiClO_4$ (battery grade, Sigma-Aldrich) inside an $Ar(g)$ -filled glovebox that contained <0.5 ppm of $O_2(g)$. The concentrations of the redox-couple species in solution were either 1.2 mM $Cp^*_2Fe^+$ and 0.92 mM Cp^*_2Fe or were 1.5 mM MV^{2+} and 0.035 mM $MV^{+\bullet}$ (calculated based on charge passed during electrolysis). Open-circuit measurements were collected in the dark and also under 100 $mW\ cm^{-2}$ of illumination provided by a 300 W ELH-type tungsten-halogen lamp operated at 110 V. The light intensity was calibrated by use of a Si photodiode (Thor Laboratories). $J-E$ data were collected from -0.5 to $+0.5$ V versus a Pt wire pseudoreference electrode in a three-electrode setup with a Pt mesh counter electrode, using a Gamry Reference 600 potentiostat operated by Gamry Instruments Framework software (v. 5.61). A four- port, cylindrical, flat-bottomed, borosilicate glass

cell was used for the photoelectrochemical measurements. $C_{\text{diff}}-E$ measurements were collected using a Gamry Reference 600 potentiostat with the same specifications used for the measurements performed in contact with Hg.

4.2.2 Instrumentation

1. *Transmission Infrared Spectroscopy.* TIRS data were collected using a Thermo Scientific Nicolet 6700 optical spectrometer³³ equipped with a thermoelectrically cooled deuterated L-alanine-doped triglycine sulfate (DLaTGS) detector, an electronically temperature-controlled (ETC) EverGlo mid-IR source, a $\text{N}_2(\text{g})$ purge, and a KBr beam splitter. A custom attachment allowed the wafers (1.3×3.2 cm) to be mounted with the incident IR beam at 74° (Brewster's Angle for Si) or 30° with respect to the surface normal. Spectra collected at 74° show modes that are either perpendicular or parallel to the surface, while spectra collected at 30° show primarily modes parallel to the surface.⁵⁰ The spectra reported herein are averages of 1500 scans at 4 cm^{-1} resolution. The baseline was flattened and the residual water peaks were subtracted in the reported spectra. Spectra were collected and processed using OMNIC software v. 9.2.41. The background SiO_x and Si(111)-H spectra were recorded separately for each sample.

2. *X-ray Photoelectron Spectroscopy.* X-ray photoelectron spectroscopy (XPS) data were collected using a Kratos AXIS Ultra spectrometer.^{7, 33, 51} The instrument was equipped with a hybrid magnetic and electrostatic electron lens system, a delay-line detector (DLD), and a monochromatic Al $K\alpha$ X-ray source (1486.7 eV). Data were collected at pressures $<9 \times 10^{-9}$ Torr, and the photoelectron ejection vector was 90° with

respect to the sample surface plane. The electron-collection lens aperture was set to sample a $700 \times 300 \mu\text{m}$ spot, and the analyzer pass energy was 80 eV for survey spectra and 10 eV for high-resolution spectra. The instrument energy scale and work function were calibrated using clean Au, Ag, and Cu standards. The instrument was operated by Vision Manager software v. 2.2.10 revision 5.

3. *Surface Recombination Velocity.* Surface recombination velocity (S) measurements were performed using a contactless microwave conductivity apparatus.^{7,33-34,43} A 20 ns laser pulse at 905 nm provided by an OSRAM laser diode and an ETX-10A-93 driver generated electron-hole pairs. The charge-carrier lifetime was determined by monitoring the change in reflected microwave intensity using a PIN diode connected to an oscilloscope. The data were collected using a custom LabView program. All photoconductivity decay curves were averages of 64 consecutive decays. Reported data were collected after the S value had stabilized in the presence of air, usually 24–72 h after preparation of the surface.

4.2.3 Data Analysis

1. *Fitting and Quantification of XPS Data.* High-resolution XPS data were analyzed using CasaXPS software v. 2.3.16. A Shirley background was applied to all C 1s, F 1s, and Si 2p spectra, except when analyzing small amounts of SiO_x in the 102–104 eV range, for which a linear background was used. C 1s and F 1s data were fitted using a Voigt GL(30) function that consisted of 70% Gaussian and 30% Lorentzian character. Cl 2p data were fitted using a Voigt GL(90) function that consisted of 10% Gaussian and 90% Lorentzian

character. Bulk Si 2p spectra were fitted with asymmetric Lorentzian convoluted with Gaussian line shapes of the form $LA(e, f, g)$, where e and f determine the asymmetry of the line shape and g determines the Gaussian width of the function. $LA(1.2, 1.4, 200)$ fit the obtained Si 2p spectra consistently, and the peak widths were set to be equal to each other. The SiO_x contributions from 102–104 eV were fitted using the $GL(30)$ function.

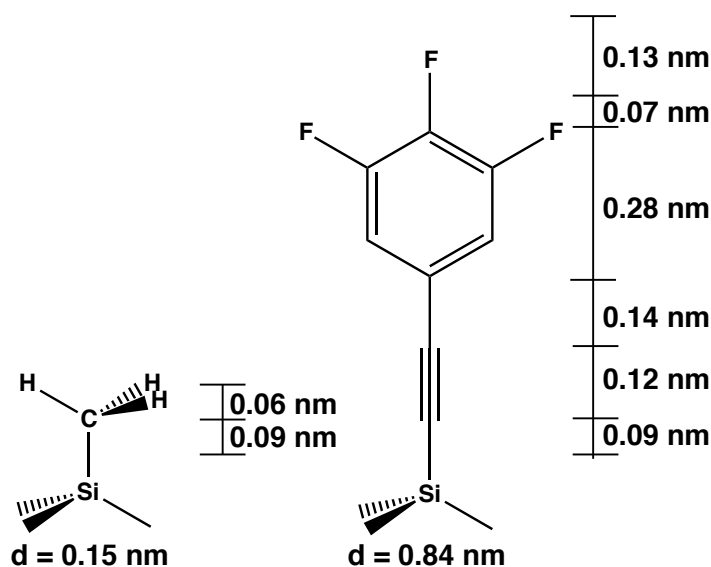
The Si(111)–MMTFPA surfaces were terminated by mixed monolayers that had a large difference in thickness of the two terminating species. As such, a modified two-layer substrate-overlayer model was used to determine the thickness of the desired overlayer species. An initial average overlayer thickness was estimated by assuming that all surface Si sites were terminated by either $-CH_3$ or TFPA groups, and the ratio of the C 1s photoemission signal at 284.2 eV (C_{Si}) was determined relative to the signal at 288.0 eV (C_F). The fractional coverage of TFPA groups was estimated using this method, and the average overlayer thickness was estimated using the calculated fractional coverage of $-CH_3$ and TFPA groups in conjunction with the estimated thickness of each species shown in Scheme 4.2. With an estimated average overlayer thickness, a two-layer substrate-overlayer model was used to determine the thickness of the F monolayer (d_A), as expressed by eq 4.1:

$$\left(\frac{I_A}{I_{Si}}\right)\left(\frac{SF_{Si}}{SF_A}\right)\left(\frac{\rho_{Si}}{\rho_A}\right) = \left(\frac{1 - e^{-\frac{d_A}{\lambda_A \sin \varphi}}}{e^{-\frac{d_A + d_B}{\lambda_{Si} \sin \varphi}}}\right) \quad (4.1)$$

I_A and I_{Si} are the core level peak areas for the overlayer species A and for the Si substrate, respectively, SF_A and SF_{Si} are the sensitivity factors for the overlayer species A ($SF_{F\ 1s} = 1.00$) and for the Si substrate ($SF_{Si\ 2p} = 0.328$), respectively, ρ_A and ρ_{Si} are the densities of the overlayer species A (3.0 g cm^{-3} for hydrocarbon overlayers) and the Si substrate (2.3 g

cm^{-3}), respectively, and λ_A and λ_{Si} are the attenuation lengths for the photoelectrons arising from the overlayer species A ($\lambda_{\text{F } 1s} = 1.6 \text{ nm}$)⁵² and from the Si 2p core level ($\lambda_{\text{Si}} = 4.0 \text{ nm}$), respectively. The angle between the photoelectron ejection vector and the surface plane (φ) was 90° . The quantity $(d_A + d_B)$ is the thickness of the mixed monolayer, which was estimated using the method described above.

Scheme 4.2. Estimated Thickness of $-\text{CH}_3$ and TFPA Groups



Samples with $\theta_{\text{TFPA}} > 0.15 \text{ ML}$ often showed the presence of unreacted Si-Cl sites. The fractional ML coverage of Si-Cl was determined using eq 4.1, with $SF_{\text{Cl } 2s} = 0.493$ and $\lambda_{\text{Cl } 2s} = 2.8 \text{ nm}$.⁵² The overlayer density, ρ_A , was assumed to be the same as for hydrocarbon overlayers, and the average overlayer thickness $(d_A + d_B)$ was estimated as described above. The thickness of 1 ML of Cl atoms was estimated to be the length of the Si-Cl bond (0.20 nm). The Cl 2p photoelectrons were assumed to be unattenuated by neighboring TFPA groups.

Small concentrations of SiO_x were detected on Si(111)–MMTFPA surfaces with $\theta_{\text{TFPA}} > 0.15$ ML and on Si(111)–TFPA surfaces. For estimating the thickness of SiO_x using eq 4.1, the quantity $(SF_{\text{Si}}/SF_{\text{A}})(\rho_{\text{Si}}/\rho_{\text{A}})$ reduces to 1.3, and the quantity $d_{\text{A}} + d_{\text{B}}$ reduces simply to d_{A} . For this estimate, all photoelectrons originate in Si, so $\lambda_{\text{A}} = \lambda_{\text{Si}} = 3.4$ nm for photoelectrons attenuated by a SiO_x overlayer.⁵³⁻⁵⁴ The thickness of 1 ML of SiO_x was assumed to be 0.35 nm.^{33,35,52}

2. Calculation of Surface Recombination Velocity and Surface Trap State Density.

The minority-carrier lifetime, τ , was determined by fitting the photoconductivity decay versus time data to an exponential decay equation.³⁴ The surface recombination velocity (S) was estimated for a given value of τ using:

$$S = \frac{a}{2\tau} \quad (4.2)$$

where a is the thickness of the Si wafer. The effective surface trap-state density, N_{t} , was determined from S using:

$$N_{\text{t}} = \frac{S}{\sigma v_{\text{th}}} \quad (4.3)$$

where σ is the trap-state capture cross section (10^{-15} cm²) and v_{th} is the thermal velocity of the charge carriers (10^7 cm s⁻¹).

3. Determination of the Barrier Height by Current Density Versus Voltage Curve Analysis.

Barrier heights, Φ_{b} , and ideality factors (n) were estimated for 2-electrode measurements performed in contact with Hg by fitting the linear region of the forward-bias portion of a semi-log current density versus voltage (J - V) plot to the thermionic emission model.

$$J = A^{**} T^2 e^{-\frac{q\Phi_b}{k_B T}} \left(e^{\frac{qV}{nk_B T}} - 1 \right) \quad (4.4)$$

A^{**} is the modified Richardson's constant for Si ($112 \text{ A cm}^{-2} \text{ K}^{-2}$ for n-Si and $32 \text{ A cm}^{-2} \text{ K}^{-2}$ for p-Si), k_B is Boltzmann's constant ($1.381 \times 10^{-23} \text{ J K}^{-1}$), and T is the temperature in Kelvin (296 K). By convention, the forward-bias region of the J - V curves was depicted and analyzed in the first quadrant.

4. *Determination of the Barrier Height by Analysis of Differential Capacitance Versus Voltage Data.* Differential capacitance versus voltage ($C_{\text{diff}}-V$) data were collected for Si/Hg junctions using a 2-electrode setup. Nyquist plots were hemispherical, indicating a parallel RC circuit in series with a resistance R_s (Randles Circuit). $C_{\text{diff}}-V$ data were fitted across frequencies for which the measured phase angle was $>80^\circ$ and for which Bode plots were linear. The Mott-Schottky equation was used to determine the flat-band potential, V_{fb} , of the Si

$$C^{-2} = \frac{2}{q\epsilon\epsilon_0 N_D A_S^2} \left(V_{\text{fb}} + \frac{k_B T}{q} - V \right) \quad (4.5)$$

where C is the differential capacitance, q is the absolute value of the elementary charge ($1.602 \times 10^{-19} \text{ C}$), ϵ is the dielectric constant of silicon (11.8), ϵ_0 is the vacuum permittivity ($8.85 \times 10^{-14} \text{ F cm}^{-1}$), N_D is the dopant density determined from the measured resistivity, and A_S is the junction area in cm^2 . By convention, the applied DC bias was negative, and the obtained V_{fb} was positive for n- and p-type Si. The barrier height ($\Phi_{\text{b,n}}$ for n-Si and $\Phi_{\text{b,p}}$ for p-Si) was calculated using:

$$\Phi_{\text{b,n}} = V_{\text{fb}} - \frac{k_B T}{q} \ln \left(\frac{N_D}{N_C} \right) \quad (4.6)$$

$$\Phi_{b,p} = V_{fb} - \frac{k_B T}{q} \ln\left(\frac{N_D}{N_V}\right) \quad (4.7)$$

where N_C is the effective density of states in the Si conduction band ($2.8 \times 10^{19} \text{ cm}^{-3}$), N_V is the effective density of states for the Si valence band ($1.0 \times 10^{19} \text{ cm}^{-3}$), and N_D is the dopant density determined by four-point probe measurement to be $4.4 \times 10^{15} \text{ cm}^{-3}$ for n-Si and $4.0 \times 10^{16} \text{ cm}^{-3}$ for p-Si.

5. *Determination of the Barrier Height by Analysis of Differential Capacitance Versus Potential Data.* Differential capacitance versus potential ($C_{\text{diff}}-E$) data were collected in contact with decamethylferrocenium/decamethylferrocene ($\text{Cp}^*_2\text{Fe}^{+/0}$) or methyl viologen^{2+/+} in CH_3CN using a three-electrode setup. The data were collected versus a platinum wire pseudoreference electrode, and the flat-band potential E_{fb} was determined versus the potential of the solution using eq 4.8 for n-Si and eq 4.9 for p-Si.

$$C^{-2} = \frac{2}{q\epsilon\epsilon_0 N_D A_S^2} \left(E - E_{fb} - \frac{k_B T}{q} \right) \quad (4.8)$$

$$C^{-2} = \frac{2}{q\epsilon\epsilon_0 N_D A_S^2} \left(E_{fb} + \frac{k_B T}{q} - E \right) \quad (4.9)$$

where E is the DC potential applied versus the potential of the solution. The barrier heights, $\Phi_{b,n}$ and $\Phi_{b,p}$, were determined versus the potential of the solution using

$$\Phi_{b,n} = E_{fb} + \frac{k_B T}{q} \ln\left(\frac{N_D}{N_C}\right) \quad (4.10)$$

$$\Phi_{b,p} = E_{fb} - \frac{k_B T}{q} \ln\left(\frac{N_D}{N_V}\right) \quad (4.11)$$

The calculated values for $\Phi_{b,n}$ were negative and the calculated values of $\Phi_{b,p}$ were positive. The reported values of Φ_b are unsigned in order to align with the common conventions for reporting Φ_b and to provide a direct comparison with the magnitudes of Φ_b determined by two-electrode measurements in contact with Hg.

6. *Determination of the Effective Solution Potentials for Photoelectrochemical Cells.* The Nernstian cell potential, $E(\text{Cp}^*\text{Fe}^{+/0})$, for $\text{Cp}^*\text{Fe}^{+/0}$ in CH_3CN with 1.0 M LiClO_4 was measured to be +0.023 V versus the formal potential of the redox couple, which is $E^\circ(\text{Cp}^*\text{Fe}^{+/0}) = -0.468$ V versus ferrocenium/ferrocene.⁴⁷ The reference potential was converted to the saturated calomel electrode (SCE) by use of the experimentally determined value of $E^\circ(\text{Fc}^{+/0}) = +0.311$ versus SCE.⁴⁷ $E(\text{MV}^{2+/+})$ for the $\text{MV}^{2+/+}$ couple in CH_3CN with 1.0 M LiClO_4 was measured as -0.781 V versus AgNO_3/Ag . The cell reference potential was converted to SCE using $E(\text{AgNO}_3/\text{Ag}) = +0.393$ V versus SCE.⁵⁵ The measured cell potentials were converted to effective cell potentials, for which a normalizing 10 mM concentration was used for comparison with previous results. The effective cell potential for n-Si electrodes, $E_{\text{eff},n}(\text{A}/\text{A}^-)$ was determined by⁴⁷

$$E_{\text{eff},n}(\text{A}/\text{A}^-) = E(\text{A}/\text{A}^-) + \frac{k_B T}{q} \ln \frac{[\text{A}^-_{\text{eff}}]}{[\text{A}^-]} \quad (4.12)$$

and the effective cell potential for p-Si electrodes $E_{\text{eff},p}(\text{A}/\text{A}^-)$ was determined by

$$E_{\text{eff},p}(\text{A}/\text{A}^-) = E(\text{A}/\text{A}^-) - \frac{k_B T}{q} \ln \frac{[\text{A}^-_{\text{eff}}]}{[\text{A}]} \quad (4.13)$$

Here, $[A_{\text{eff}}^-]$ and $[A_{\text{eff}}]$ are the effective 10 mM concentrations of the reduced and oxidized species, respectively, and $[A^-]$ and $[A]$ are the solution concentrations of the reduced and oxidized species, respectively. For the $\text{Cp}^*_2\text{Fe}^{+/0}$ cell, $E_{\text{eff,n}}(\text{Cp}^*_2\text{Fe}^{+/0}) = -0.073$ V versus SCE and $E_{\text{eff,p}}(\text{Cp}^*_2\text{Fe}^{+/0}) = -0.188$ V versus SCE. For the $\text{MV}^{2+/+}$ cell, $E_{\text{eff,n}}(\text{MV}^{2+/+}) = -0.244$ V versus SCE and $E_{\text{eff,p}}(\text{MV}^{2+/+}) = -0.436$ V versus SCE.

4.3 RESULTS

4.3.1 Spectroscopic Characterization and Surface Recombination Velocity of Si(111)-TFPA and Si(111)-MMTFPA Surfaces

Figure 4.3 presents TIRS data for a Si(111)-TFPA surface collected at 74° and 30° incidence with respect to the surface normal. The spectrum collected at 74° incidence exhibited an intense peak at 1533 cm^{-1} , which was ascribed to primary skeletal phenyl C-C stretching vibrations.⁵⁶⁻⁵⁷ This peak was reduced in intensity at 30° incidence, indicating that this motion has a significant component that is perpendicular to the surface. At 74° incidence, weak peaks were observed at 1612, 1584, 1432, 1366, and 1351 cm^{-1} and were characteristic of aromatic systems.⁵⁷ At 30° incidence, the signal at 1432 cm^{-1} was readily observed, while the other characteristic aromatic C-C stretching peaks were not present. A sharp signal observed for 74° incidence at 1251 cm^{-1} of C-F stretching,⁵⁷⁻⁵⁹ and this peak was greatly reduced in intensity at 30° incidence. A very weak signal at 2160 cm^{-1} was observed only at 74° incidence, indicating the presence of C≡C triple bond stretching perpendicular to the surface.⁵⁷ Weak C-H stretching signals were observed only for 74° incidence at 2962 and 2853 cm^{-1} , which can be ascribed to

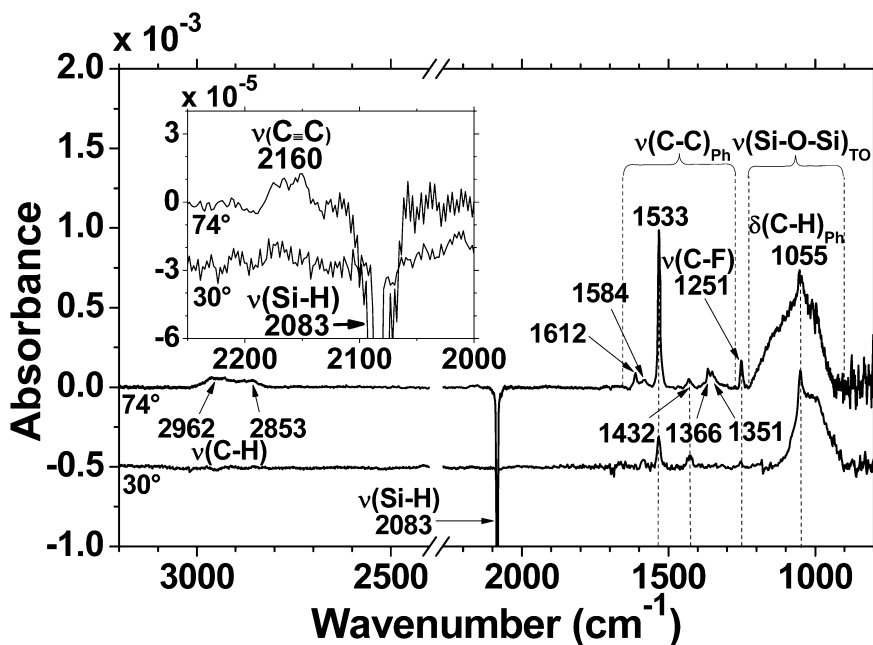


Figure 4.3. TIRS data for a Si(111)–TFPA surface collected at 74° (top) and 30° (bottom) with respect to the surface normal. The symbols ν and δ indicate stretching and bending motions, respectively, and the subscript “Ph” indicates modes associated with the phenyl ring. The spectrum collected at 74° had $\theta_{\text{TFPA}} = 0.16$ ML and $\theta_{\text{SiO}_x} = 0.17$ ML, while the spectrum collected at 30° had $\theta_{\text{TFPA}} = 0.25$ ML and $\theta_{\text{SiO}_x} = 0.03$ ML. The spectra were referenced to the Si(111)–H surface. The peak at 1533 cm^{-1} and the surrounding satellite peaks were attributed to skeletal C–C stretching in the phenyl ring. The C–F stretch was observed at 1251 cm^{-1} , and a weak C \equiv C stretch was observed at 2160 cm^{-1} . The inset shows a magnified portion of the spectrum from 2250 to 2000 cm^{-1} .

adventitious saturated hydrocarbon species.⁵⁰ No distinct aromatic C–H stretching signal (typically near 3050 cm^{-1}) was observed for the surface-bound TFPA group. A broad peak centered near 1050 cm^{-1} was ascribed to transverse optical (TO) Si–O–Si stretching.⁵⁰ The observation of this mode indicated the presence of subsurface SiO_x, consistent with the oxidation of unreacted Si–Cl sites on the functionalized surface. A sharp signal overlapped by the Si–O–Si stretching peak was observed at both angles of incidence centered at 1055 cm^{-1} and was ascribed to in-plane aromatic C–H bending. No

residual Si–H signal was detected when a SiO_x surface was used as a reference, indicating that the surface sites were only terminated by TFPA or Cl moieties.

TIRS data for a Si(111)–MMTFPA sample with $\theta_{\text{TFPA}} = 0.16$ ML are presented in Figure 4.4. The Si(111)–MMTFPA surface showed the modes associated with the phenyl ring and aromatic C–F stretching observed in Figure 4.3 in addition to reduced SiO_x content. The symmetric C–H bending, $\delta_s(\text{C–H})$,⁵⁰ mode overlapped significantly with the C–F stretching peak, resulting in a single peak at 1253 cm⁻¹. Additionally, the –CH₃ rocking mode was observed at 762 cm⁻¹.⁵⁰ The presence of these peaks demonstrates that the Si(111)–MMTFPA exhibits both TFPA and –CH₃ functionality.

Figure 4.5 shows the surface recombination velocity (S) as a function of the composition of the functionalized Si surfaces. The Si(111)–CH₃ surface exhibited $S = 13 \pm 5$ cm s⁻¹, which corresponds to a trap-state density, N_t , of $\sim 1.3 \times 10^9$ cm⁻², that is, one trap for every 6.0×10^5 surface sites. This low trap-state density has been shown to be stable over >500 h of air exposure.³²⁻³³ A substantial increase in S was observed for surfaces with $\theta_{\text{TFPA}} > 0.1$ ML, which is consistent with an increase in S observed for increased fractional coverages of bulky groups in mixed monolayers on Si(111) surfaces.^{34, 43} A Si(111)–MMTFPA surface with $\theta_{\text{TFPA}} = 0.10$ ML exhibited $S = (1.6 \pm 0.5) \times 10^2$ cm⁻¹, corresponding to $N_t = 1.6 \times 10^{10}$ cm⁻². With $\theta_{\text{TFPA}} = 0.22$ ML, a Si(111)–MMTFPA surface had $S = (1.9 \pm 0.1) \times 10^3$ cm s⁻¹, corresponding to $N_t = 1.9 \times 10^{11}$ cm⁻². The Si(111)–TFPA surface, which had higher θ_{TFPA} than the measured Si(111)–MMTFPA samples, exhibited substantially higher S than was observed for the measured Si(111)–MMTFPA samples.

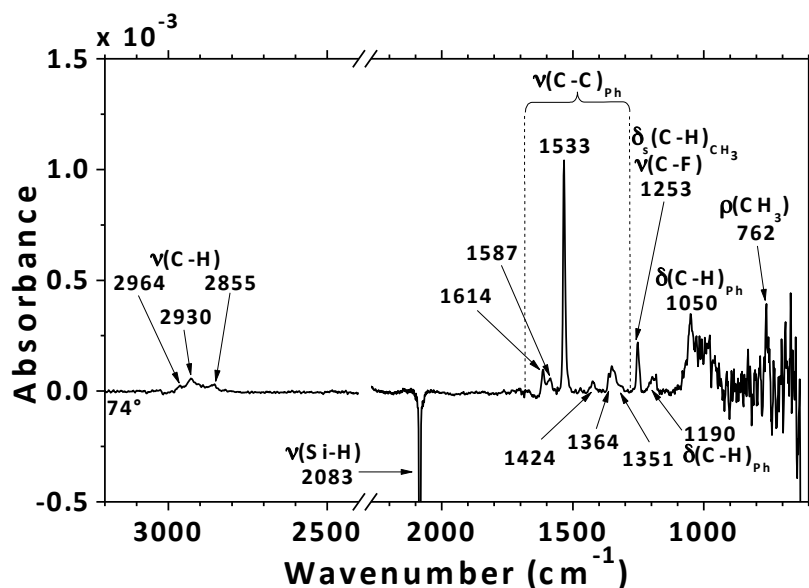


Figure 4.4. TIRS data for a Si(111)–MMTFPA surface with $\theta_{\text{TFPA}} = 0.16$ ML collected at 74° with respect to the surface normal. The symbols ν , δ , and ρ indicate stretching, bending, and rocking motions, respectively, and the subscript “Ph” indicates modes associated with the phenyl ring. The spectrum was referenced to the Si(111)–H surface. The peak at 1533 cm^{-1} and the surrounding satellite peaks were attributed to skeletal C–C stretching in the phenyl ring. The C–F stretching was convoluted with the symmetric C–H bending peak, appearing at 1253 cm^{-1} .

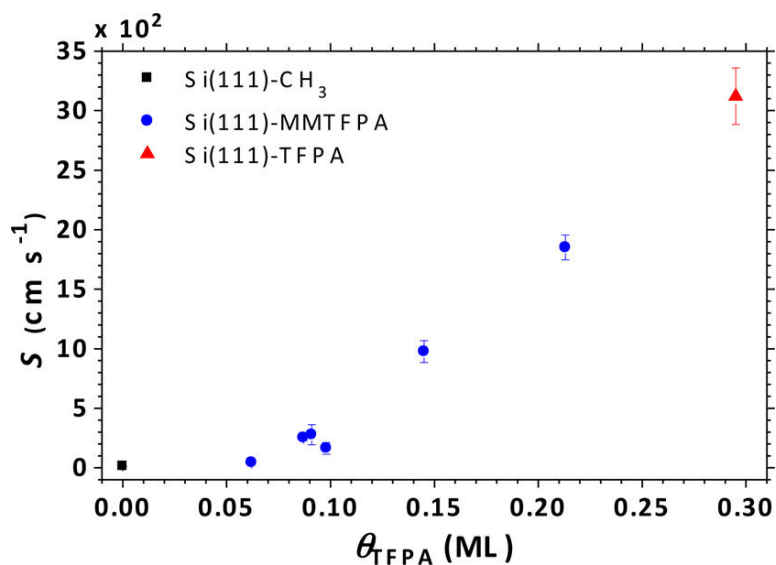


Figure 4.5. S values for Si(111)– CH_3 , Si(111)–MMTFPA, and Si(111)–TFPA surfaces as a function of fractional monolayer coverage with TFPA groups. For $\theta_{\text{TFPA}} > 0.1$ ML, S increased rapidly.

Figure 4.6a presents a representative XP survey spectrum of a Si(111)–MMTFPA surface with $\theta_{\text{TFPA}} = 0.11$ ML. Survey spectra were free of contaminants and only showed the presence of Si, C, O, and F core-level peaks. A high-resolution C 1s spectrum showed the presence of C bound to Si at 284.2 eV,^{33, 41, 60} C bound to C at 285.3 eV, C bound to O at 286.8 eV, and C bound to F at 288.0 eV (Figure 4.6b).^{45, 61-62} Figure 4.6c shows the high-resolution Si 2p XP spectrum, which showed only bulk Si⁰ and no detectable high-order SiO_x in the 102–104 eV region. The F 1s high-resolution spectrum exhibited a single peak at 688.3 eV (Figure 4d), indicative of a single source of F on the surface.⁶² In general, samples with $\theta_{\text{TFPA}} < 0.15$ ML exhibited no detectable SiO_x in the 102–104 eV range, while samples with $\theta_{\text{TFPA}} > 0.15$ ML exhibited $\theta_{\text{SiO}_x} = 0.07 \pm 0.02$ ML. Samples with $\theta_{\text{TFPA}} > 0.2$ ML also often exhibited a small amount of residual Cl, which gave an average Si–Cl coverage, θ_{Cl} , of 0.11 ± 0.01 ML.

Figure 4.7 shows analogous XP spectra for a Si(111)–TFPA surface with $\theta_{\text{TFPA}} = 0.35$ ML. Without subsequent methylation, the Si(111)–TFPA surface exhibited residual Cl, as seen in the survey spectrum (Figure 4.7a) and in the high-resolution Cl 2s spectrum (Figure 4.7e). The C 1s spectrum similarly showed contributions from C bound to Si (284.1 eV), C bound to C (285.0 eV), C bound to O (286.2 eV), and C bound to F (287.6 eV) (Figure 4.7b). The Si 2p spectrum shown did not exhibit detectable levels of SiO_x, while $\theta_{\text{SiO}_x} = 0.11 \pm 0.07$ ML across multiple Si(111)–TFPA sample preparations (Figure 4.7c). The F 1s spectrum exhibited a single signal centered at 687.9 eV (Figure 4.7d).

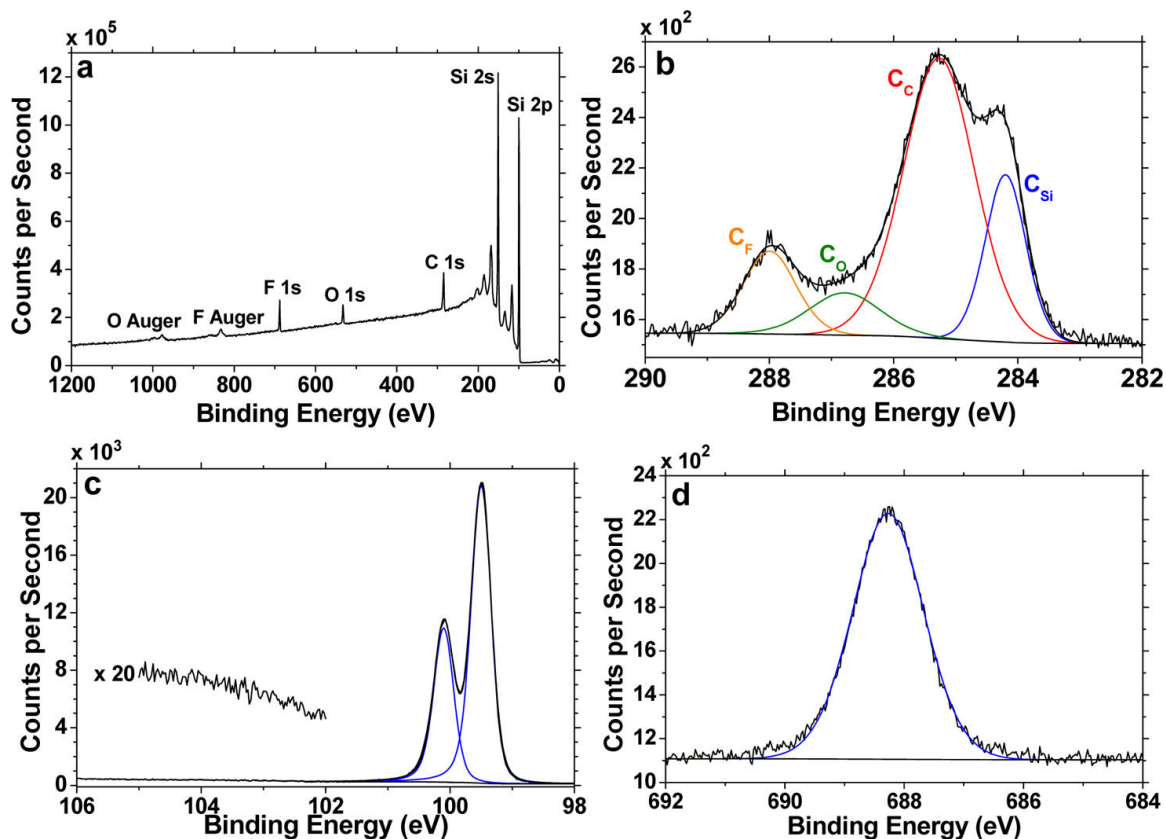


Figure 4.6. XPS data for an n-Si(111)-MMTFPA surface with $\theta_{\text{TFPA}} = 0.11$ ML. The survey spectrum (a) exhibited signals from Si, C, O, and F. The high-resolution C 1s spectrum (b) showed signals ascribed to C bound to Si (C_{Si}), C bound to C (C_{C}), C bound to O (C_{O}), and C bound to F (C_{F}). The Si 2p high-resolution spectrum (c) showed peaks attributed to bulk Si^0 with no detectable high-order SiO_x (magnified region). The F 1s high-resolution spectrum (d) exhibited a single peak ascribed to F bound to C.

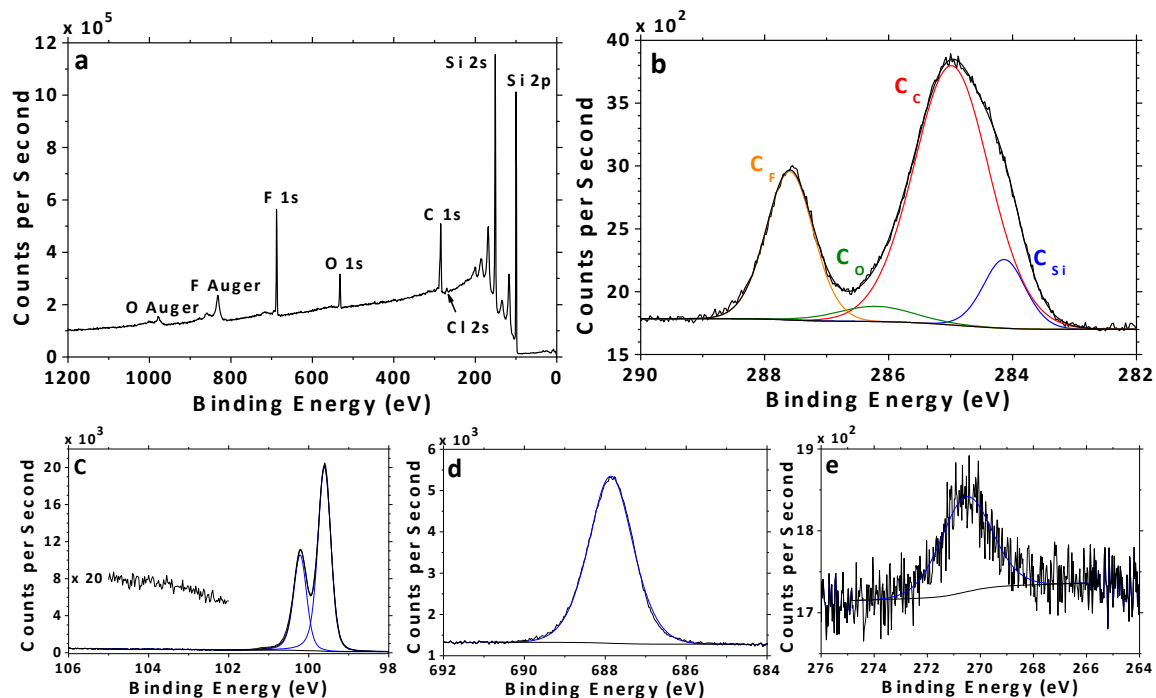


Figure 4.7. XPS data for the Si(111)–TFPA surface with $\theta_{\text{TFPA}} = 0.35$ ML. The survey spectrum (a) exhibited signals from Si, C, O, F, and Cl. The high-resolution C 1s spectrum (b) showed signals ascribable to C bound to Si (C_{Si}), C bound to C (C_{C}), C bound to O (C_{O}), and C bound to F (C_{F}). The Si 2p high-resolution spectrum (c) showed peaks attributed to bulk Si^0 with no detectable high-order SiO_x (magnified region). The F 1s high-resolution spectrum (d) showed a single peak ascribable to F bound to C. The Cl 2s high-resolution spectrum (e) showed a single peak indicative of unreacted Cl bound to Si.

4.3.2 Hg Contacts to Si(111)–MMTFPA Surfaces

Figure 4.8a displays the J - V behavior for n-Si(111)–MMTFPA/Hg contacts having a range of θ_{TFPA} . By convention, measured values of Φ_{b} and of the built-in voltage were unsigned for two-electrode measurements in contact with Hg. The n-Si(111)– CH_3 /Hg contact exhibited strongly rectifying behavior ($\Phi_{\text{b}} = 0.9$ V), evidenced by small, near-constant current at reverse bias.⁴⁰ The n-Si(111)–MMTFPA/Hg contacts exhibited less rectification as θ_{TFPA} increased, suggesting that the molecular dipole induced by the

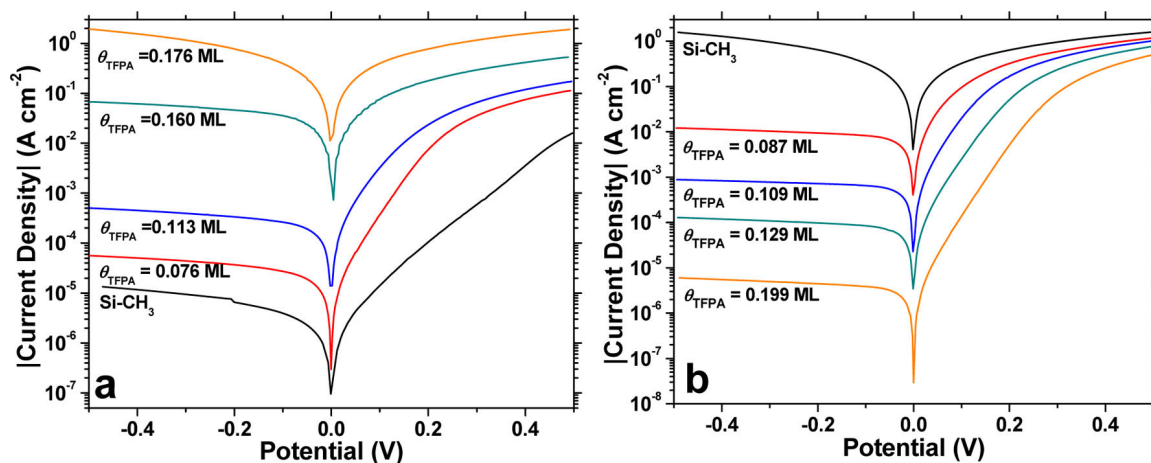


Figure 4.8. Representative two-electrode J - V behavior for (a) n-type and (b) p-type Si(111)-MMTFPA/Hg junctions. The fractional ML coverage of TFPA for a given curve is indicated below each curve. By convention, the forward bias region is depicted in the first quadrant.

C-F bonds in the TFPA group shifted the band-edge positions to produce a smaller built-in voltage at the n-Si(111)-MMTFPA/Hg junction. At high θ_{TFPA} , the n-Si-MMTFPA/Hg contact was ohmic to Hg, indicating $\Phi_b \leq 0.3$ V and corresponding to a shift of ≥ 0.6 V in the Si band-edge positions compared with n-Si(111)-CH₃ surfaces. Samples that exhibited low values for Φ_b generally did not exhibit clear linear regions in the forward-bias portion of the semilog J - V plot, which precluded analysis of the J - V data within a thermionic emission model. The diode-ideality factor, n , for the n-Si(111)-MMTFPA/Hg junctions was estimated as 1.5 ± 0.2 (eq 4.4), which is comparable to previous observations on junctions between alkyl-terminated n-Si and Hg.⁴⁰

Figure 4.8b shows J - V data for p-Si(111)-MMTFPA surfaces in contact with Hg. The p-Si(111)-CH₃ samples exhibited ohmic behavior in contact with Hg, and previous

work has indicated that $\Phi_b < 0.15$ V for this junction.⁴⁰ The addition of TFPA to the alkyl monolayer resulted in increased rectification of the junction, producing measurable values for Φ_b . Similar to n-Si/Hg junctions, p-Si/Hg junctions that exhibited low values for Φ_b gave semilog J - V response curves with no definitive linear portion in the forward-bias region, thereby limiting the determination of Φ_b for these samples. The p-Si(111)–MMTFPA samples showed increased rectification with increasing θ_{TFPA} , which indicated an increase in the built-in voltage for p-Si/Hg junctions as θ_{TFPA} increased. Analysis of the J - V response yielded a maximum measured value for Φ_b of 0.7 V on p-Si(111)–MMTFPA/Hg junctions, which indicated a shift in the band-edge positions of ≥ 0.5 V relative to p-Si(111)–CH₃ surfaces. The value of the diode-ideality factor, n , for p-Si(111)–MMTFPA/Hg junctions was 1.3 ± 0.2 (eq 4.4).

C_{diff} - V data were also collected for the functionalized n-Si/Hg and p-Si/Hg junctions. The flat-band position was calculated from the C_{diff} - V data using eq 4.5, and the flat-band values were used to determine Φ_b (eq 4.6 or 4.7). As with J - V measurements, samples with small Φ_b in contact with Hg generally did not exhibit ideal behavior by C_{diff} - V measurements, precluding determination of Φ_b for samples that did not show strong rectification. The dopant density, N_D , was also calculated from these measurements and was compared with the value of N_D determined by four-point probe measurements. For n-Si, N_D determined by C_{diff} - V analysis was $(2.7 \pm 0.3) \times 10^{15} \text{ cm}^{-3}$, and N_D determined by four-point probe data was $4.4 \times 10^{15} \text{ cm}^{-3}$. For p-Si, N_D determined by C_{diff} - V analysis was $(1.7 \pm 0.4) \times 10^{16} \text{ cm}^{-3}$ and $4.0 \times 10^{16} \text{ cm}^{-3}$ by four-point probe.

For either n-Si and p-Si samples, the values of N_D were thus within a factor of ~ 2 when calculated by the $C_{\text{diff}}-V$ or by four-point probe measurements.

Figure 4.9 presents the values of Φ_b calculated from the $J-V$ response and $C_{\text{diff}}-V$ analysis for Si(111)–MMTFPA/Hg junctions as a function of θ_{TFPA} . The n-Si(111)–MMTFPA/ Hg junctions exhibited values of Φ_b that were in close agreement for both methods. Samples for which the junction appeared ohmic are plotted with a value of $\Phi_b = 0.15 \pm 0.15$ V. The p-Si(111)–MMTFPA/Hg junctions showed values of Φ_b that generally were not in good agreement for the two analytical methods used, and Φ_b determined by $C_{\text{diff}}-V$ measurements exhibited significantly greater spread for a given θ_{TFPA} than Φ_b determined from $J-V$ measurements. For high θ_{TFPA} , the p-Si/Hg junctions

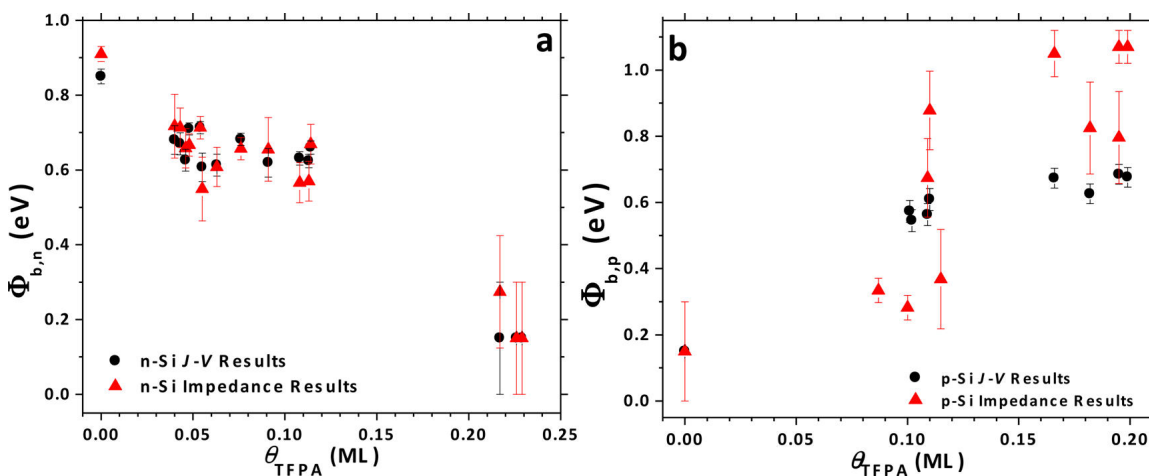


Figure 4.9. Correlation between the calculated barrier height for Si(111)–MMTFPA/Hg junctions and the fractional monolayer coverage of TFPA for (a) n-type and (b) p-type samples. The barrier heights calculated from fitting the forward bias region of the $J-V$ curves using eq 4.4 are shown as black circles, and the barrier heights calculated from fitting the $C_{\text{diff}}-V$ data using eqs 4.5–4.7 are shown as red triangles. Samples that showed low Φ_b values did not exhibit ideal junction behavior, precluding analysis of Φ_b for samples with poor rectification. Error bars represent the statistical variation in Φ_b for samples from the same preparation.

exhibited values of Φ_b determined by Mott-Schottky analysis near the Si band gap, while apparent Φ_b values determined from analysis of the J - V response were considerably lower, at ~ 0.65 V.

4.3.3 Photoelectrochemical Behavior of Si(111)-TFPA and Si(111)-MMTFPA Surfaces in Contact with $\text{CH}_3\text{CN-Cp}^*\text{Fe}^{+/0}$

Figure 4.10 presents representative J - E data for functionalized n- and p-Si(111) samples in contact with $\text{CH}_3\text{CN-Cp}^*\text{Fe}^{+/0}$ (1.2, 0.92 mM) under 100 mW cm^{-2} of simulated solar illumination. The effective cell potential, $E_{\text{eff}}(\text{Cp}^*\text{Fe}^{+/0})$, was determined using eqs 4.12 and 4.13, to give $E_{\text{eff,n}}(\text{Cp}^*\text{Fe}^{+/0}) = -0.073$ V and $E_{\text{eff,p}}(\text{Cp}^*\text{Fe}^{+/0}) = -0.188$ V versus SCE. Data for the Si(111)- CH_3 surface were collected for comparison with Si(111)-MMTFPA and Si(111)-TFPA samples. The photocurrent density was limited by mass transport because the electrode areas were relatively large and the redox couple concentrations were low. Large electrode areas were required to produce reliable $C_{\text{diff}}\text{-}E$ measurements with minimal edge effects. Table 4.1 presents the measured values of the open circuit potential (E_{oc}) for the functionalized electrodes under 100 mW cm^{-2} illumination as well as the values of Φ_b determined from $C_{\text{diff}}\text{-}E$ measurements. Values of Φ_b are reported as unsigned magnitudes.

The E_{oc} , shown in Table 4.1, of n-Si(111)-MMTFPA and n-Si(111)-TFPA samples shifted by +0.27 V and +0.36 V, respectively, compared with the E_{oc} for n-Si(111)- CH_3 samples in contact with $\text{CH}_3\text{CN-Cp}^*\text{Fe}^{+/0}$. The calculated values of Φ_b for

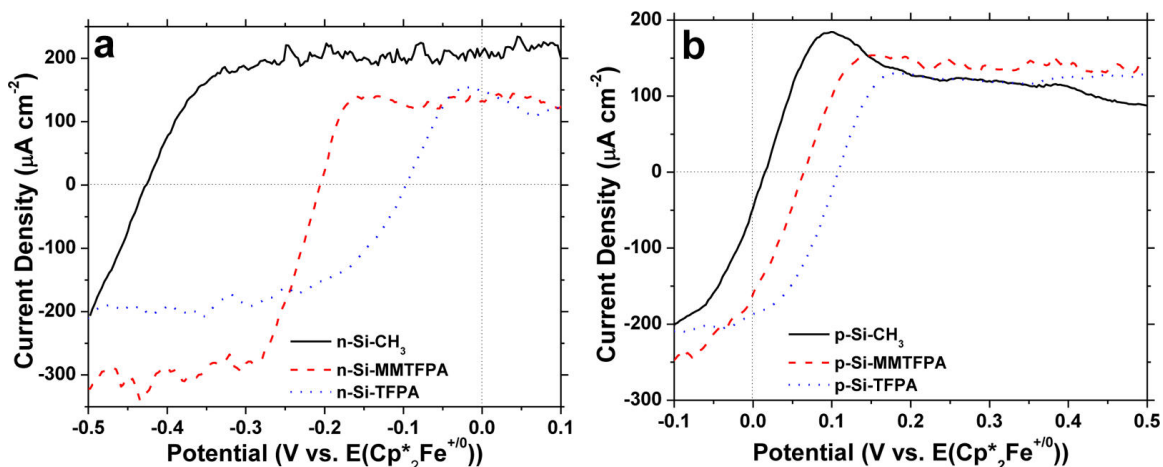


Figure 4.10. Representative J - E data under 100 mW cm^{-2} simulated sunlight illumination for functionalized Si(111) surfaces in contact with $\text{Cp}^*\text{Fe}^{+/0}$ (1.2, 0.92 mM) in dry CH_3CN for (a) n-type and (b) p-type samples. Si(111)- CH_3 samples (solid black) are shown for comparison with Si(111)-MMTFPA (dashed red) and Si(111)-TFPA (blue dotted) samples.

Table 4.1. E_{oc} and Φ_{b} measurements for functionalized Si surfaces in contact with $\text{CH}_3\text{CN-Cp}^*\text{Fe}^{+/0}$.

Surface	E_{oc} in $\text{Cp}^*\text{Fe}^{+/0}$ (V) ^a	Φ_{b} in $\text{Cp}^*\text{Fe}^{+/0}$ (V) ^b	θ_{TFPA} (ML)
n-Si- CH_3	-0.43 ± 0.02	1.07	0
n-Si-MMTFPA	-0.16 ± 0.03	0.56 ± 0.01	0.23 ± 0.01
n-Si-TFPA	-0.072 ± 0.001	0.427 ± 0.001	0.307 ± 0.007
p-Si- CH_3	$+0.03 \pm 0.03$	–	0
p-Si-MMTFPA	$+0.095 \pm 0.004$	0.56 ± 0.07	0.193 ± 0.007
p-Si-TFPA	$+0.12 \pm 0.02$	0.35 ± 0.01	0.27 ± 0.02

^aThe redox couple concentrations were 1.2 mM Cp^*Fe^+ and 0.92 mM Cp^*Fe . The effective cell potentials calculated from eq 4.12 and eq 4.13 were $E_{\text{eff,n}}(\text{Cp}^*\text{Fe}^{+/0}) = -0.073 \text{ V}$ and $E_{\text{eff,p}}(\text{Cp}^*\text{Fe}^{+/0}) = -0.188 \text{ V}$ versus SCE. ^bThe values of Φ_{b} were determined by $C_{\text{diff}}-E$ measurements using eq 4.8 through 4.11 and are reported as unsigned magnitudes. No value for Φ_{b} is reported for samples that formed weakly rectifying junctions with the redox solution.

n-Si(111)–MMTFPA and n-Si(111)–TFPA samples were lowered in magnitude by 0.51 and 0.64 V, respectively, compared with Φ_b for n-Si(111)–CH₃ samples in contact with CH₃CN-Cp*₂Fe⁺⁰. The dopant density, N_D , for functionalized n-Si samples was found to be $(4.6 \pm 0.8) \times 10^{15} \text{ cm}^{-3}$, which agreed well with N_D determined from four-point probe measurements ($4.4 \times 10^{15} \text{ cm}^{-3}$).

For p-Si samples in contact with CH₃CN-Cp*₂Fe⁺⁰, the E_{oc} shifted positively and Φ_b increased in magnitude for surfaces that contained TFPA functionality compared with p-Si(111)–CH₃ surfaces. The p-Si(111)–CH₃ samples exhibited very low photovoltages (Table 4.1), and Φ_b was too small to be accurately determined by C_{diff} - E measurements. The p-Si(111)–MMTFPA samples exhibited a moderate shift in E_{oc} of +0.07 V relative to p-Si(111)–CH₃ samples, and p-Si(111)–TFPA samples showed a slightly greater shift in E_{oc} of +0.09 V. The p-Si(111)–MMTFPA samples yielded $\Phi_b = 0.56 \pm 0.07$ V, while p-Si(111)–TFPA samples yielded an apparent Φ_b of 0.35 ± 0.01 V despite the higher E_{oc} observed for these samples relative to p-Si(111)–MMTFPA samples. The value of N_D determined from C_{diff} - E measurements in contact with CH₃CN-Cp*₂Fe⁺⁰ was $2.0 \pm 0.3 \times 10^{16} \text{ cm}^{-3}$, compared with the value of $N_D = 4.0 \times 10^{16} \text{ cm}^{-3}$ determined from four-point probe measurements.

4.3.4 Photoelectrochemical Behavior of Si(111)-TFPA and Si(111)-MMTFPA Surfaces in Contact with CH₃CN- MV^{2+/+}

Figure 4.11 shows representative J - E data for functionalized n- and p-Si(111) samples in contact with CH₃CN-MV^{2+/+} (1.5, 0.035 mM) under 100 mW⁻² simulated solar illumination. The effective cell potential, $E_{\text{eff}}(\text{MV}^{2+/+})$, was determined using eqs 4.12 and 4.13 to give $E_{\text{eff,n}}(\text{MV}^{2+/+}) = -0.244$ V and $E_{\text{eff,p}}(\text{MV}^{2+/+}) = -0.436$ V versus SCE. Low concentrations (0.035 mM) of the radical MV⁺ species resulted in very low anodic photocurrent densities. Table 4.2 presents the measured values of E_{oc} determined for the functionalized electrodes under 100 mW cm⁻² illumination, in addition to the absolute values of Φ_{b} determined from $C_{\text{diff}}-E$ measurements.

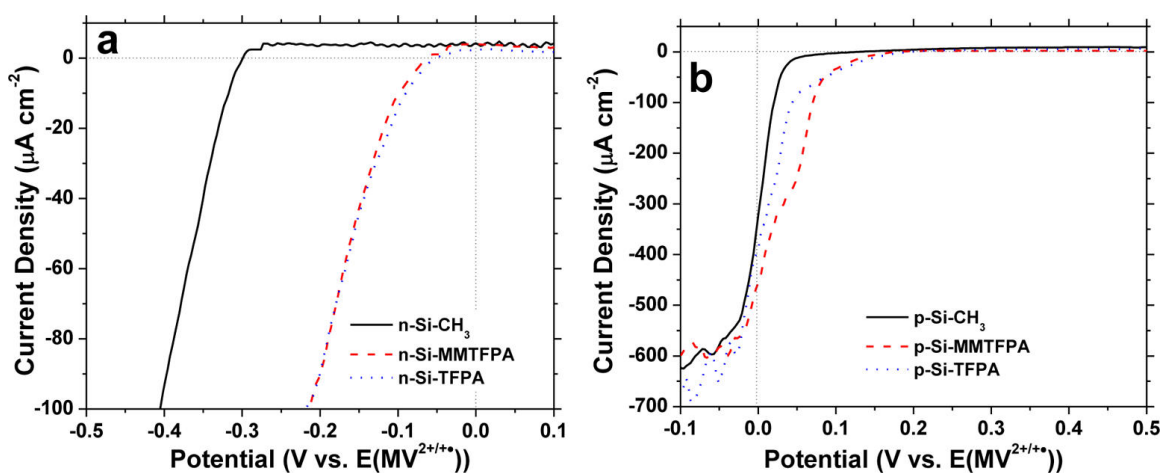


Figure 4.11. Representative J - E data under 100 mW cm⁻² illumination for functionalized Si(111) surfaces in contact with MV^{2+/+} (1.5, 0.035 mM) in dry CH₃CN for (a) n-type and (b) p-type samples. Si(111)-CH₃ samples (solid black) are shown for comparison with Si(111)-MMTFPA (dashed red) and Si(111)-TFPA (blue dotted) samples.

The E_{oc} , shown in Table 4.2, of n-Si(111)-MMTFPA samples in contact with CH₃CN-MV^{2+/+} shifted by +0.24 V relative to the E_{oc} of n-Si(111)-CH₃ samples. This

shift is comparable to the shift observed for the same samples in contact with CH₃CN-Cp*₂Fe⁺⁰. The n-Si(111)-TFPA samples in contact with CH₃CN-MV^{2+/+} exhibited a slightly larger shift in E_{oc} of +0.25 V compared with the E_{oc} for n-Si(111)-CH₃ samples. The value of Φ_b for n-Si(111)-CH₃ samples in contact with CH₃CN-MV^{2+/+} was 0.64 ± 0.06 V, while the low barrier at n-Si(111)-MMTFPA and n-Si(111)-TFPA junctions with CH₃CN-MV^{2+/+} precluded determination of Φ_b by C_{diff} - E measurements. The change in measured E_{oc} and Φ_b for n-Si samples containing TFPA functionality is consistent with an overall positive shift in the composite molecular dipole present at the interface. The dopant density, N_D , for functionalized n-Si samples was found to be $(4.7 \pm 0.2) \times 10^{15} \text{ cm}^{-3}$ in contact with CH₃CN-MV^{2+/+}.

Table 4.2. E_{oc} and Φ_b measurements for functionalized Si surfaces in contact with CH₃CN-MV^{2+/+}.

Surface	E_{oc} in MV ^{2+/+} (V) ^a	Φ_b in MV ^{2+/+} (V) ^b	θ_{TFPA} (ML)
n-Si-CH ₃	-0.26 ± 0.02	0.64 ± 0.06	0
n-Si-MMTFPA	-0.021 ± 0.007	–	0.23 ± 0.01
n-Si-TFPA	-0.01 ± 0.01	–	0.310 ± 0.007
p-Si-CH ₃	$+0.15 \pm 0.01$	0.51 ± 0.08	0
p-Si-MMTFPA	$+0.254 \pm 0.009$	0.99 ± 0.07	0.196 ± 0.002
p-Si-TFPA	$+0.24 \pm 0.02$	0.7 ± 0.1	0.26 ± 0.02

^aThe redox couple concentrations were 1.5 mM MV²⁺ and 0.035 mM MV⁺. The effective cell potentials calculated from eq 4.12 and eq 4.13 were $E_{eff,n}(MV^{2+/+}) = -0.244$ V and $E_{eff,p}(MV^{2+/+}) = -0.436$ V versus SCE. ^bThe values of Φ_b were determined by C_{diff} - E measurements using eq 4.8 through 4.11 and are reported as unsigned magnitudes. No value for Φ_b is reported for samples that formed weakly rectifying junctions with the redox solution.

As observed for p-Si samples in contact with $\text{CH}_3\text{CN-Cp}^*\text{Fe}^{+/0}$, the E_{oc} for p-Si(111)–MMTFPA and p-Si(111)–TFPA samples in contact with $\text{CH}_3\text{CN-MV}^{2+/+}$ shifted positively relative to E_{oc} for p-Si(111)– CH_3 surfaces (Table 4.2). The positive shift in E_{oc} was accompanied by an increase in the magnitude of Φ_{b} . The p-Si(111)–MMTFPA samples exhibited a modest shift in E_{oc} , of +0.10 V in contact with $\text{MV}^{2+/+}$ relative to the E_{oc} of p-Si(111)– CH_3 samples, and p-Si(111)–TFPA samples showed a very similar shift in E_{oc} of +0.09 V relative to p-Si(111)– CH_3 samples. For p-Si(111)– CH_3 samples, Φ_{b} was determined by $C_{\text{diff}}-E$ measurements to be 0.51 ± 0.08 V, while $\Phi_{\text{b}} = 0.99 \pm 0.07$ V for p-Si(111)–MMTFPA surfaces; that is, the barrier height of this junction is close to the Si band gap. As was observed in contact with $\text{Cp}^*\text{Fe}^{+/0}$, p-Si(111)–TFPA samples yielded a lower Φ_{b} of 0.7 ± 0.1 V, despite the nearly identical E_{oc} observed for these samples as compared with p-Si(111)–MMTFPA samples. The value of N_{D} determined from $C_{\text{diff}}-E$ measurements was $(2.4 \pm 0.4) \times 10^{16} \text{ cm}^{-3}$.

4.4 DISCUSSION

4.4.1 Si(111)–TFPA Surface Characterization

The TIRS data for Si(111)–TFPA surfaces yielded modes consistent with the presence of a phenyl ring, aryl C–F bonds, and a $\text{C}\equiv\text{C}$ bond (Figure 4.3). The observation of the $\text{C}\equiv\text{C}$ stretch at 2160 cm^{-1} at 74° incidence but not at 30° incidence indicates that the TFPA groups are predominantly oriented perpendicular to the surface. The large reduction in intensity of the primary aromatic C–C stretching peak at 1533 cm^{-1} for 30° incidence relative to 74° incidence demonstrates that this mode is primarily oriented

perpendicular to the surface. Similarly, the C–F stretching signal at 1251 cm^{-1} was greatly reduced at 30° incidence relative to 74° incidence, indicating that the majority of this mode is oriented perpendicular to the surface. The residual intensity observed for the 1533 and 1251 cm^{-1} modes at 30° incidence indicates that a fraction of each mode is not perpendicular to the surface, in accord with expectations based on the geometry of the TFPA group. The in-plane aromatic C–H bend was observed at both angles of incidence at 1055 cm^{-1} , indicating that this mode is not primarily oriented perpendicular to the surface. The aryl C–H stretching peaks near 3050 cm^{-1} were not observed by TIRS, suggesting that substitution of the phenyl group with C–F bonds weakens the C–H stretching signal for the TFPA group.

TIRS data for the Si(111)–MMTFPA surface, presented in Figure 4.4, showed a single peak at 1253 cm^{-1} that was ascribed to the overlap of the symmetric C–H bending and C–F stretching modes. The energy of this mode falls between the TFPA C–F stretch, observed at 1251 cm^{-1} , and the symmetric C–H bend of the $-\text{CH}_3$ group, observed at 1257 cm^{-1} .⁵⁰ The Si(111)–TFPA sample exhibited a 0.18 height ratio of the peak at 1253 cm^{-1} relative to the peak at 1533 cm^{-1} , while the Si(111)–MMTFPA sample yielded a 0.22 height ratio of the peak at 1251 cm^{-1} relative to the peak at 1533 cm^{-1} . Thus, the peak at 1253 cm^{-1} on the Si(111)–MMTFPA sample results from a convolution of the symmetric C–H bending and C–F stretching modes, indicating that both TFPA and $-\text{CH}_3$ groups are present on the surface.

The shoulder observed in the C 1s XPS signal of the Si(111)–TFPA surface (Figure 4.7b) centered at 284.1 eV provides evidence of the formation of a Si–C bond.

The residual Cl observed on Si(111)–MMTFPA surfaces for samples with $\theta_{\text{Tfpa}} > 0.2$ ML is consistent with steric crowding on the surface that prevented the reaction of a small fraction of residual Si–Cl sites with CH_3MgCl . This behavior suggests considerable steric crowding that limited further passivation of the remaining Si–Cl sites on surfaces with $\theta_{\text{Tfpa}} > 0.2$ ML.

A small amount of SiO_x was observed in the Si 2p spectrum from 102–104 eV on Si(111)–MMTFPA surfaces containing $\theta_{\text{Tfpa}} > 0.15$ ML and on Si(111)–TFPA surfaces. Mixed monolayers with high concentrations of bulky groups can prevent passivation of neighboring Si–Cl sites with $-\text{CH}_3$ groups for steric reasons, leaving the surface sites more susceptible to oxidation.³⁴ Consistently, slightly more SiO_x was observed on Si(111)–TFPA surfaces compared with Si(111)–MMTFPA surfaces with high θ_{Tfpa} .

Si(111)–MMTFPA samples exhibited high S compared with previously reported mixed monolayers.^{7, 34, 43} High concentrations of bulky groups in mixed monolayers can sterically block passivation of Si–Cl sites with $-\text{CH}_3$ groups, leaving the unreacted sites susceptible to oxidation and formation of surface states.^{7, 34, 43} This expectation is consistent with the behavior of Si(111)–MMTFPA surfaces with $\theta_{\text{Tfpa}} > 0.2$ ML, which had unreacted Si–Cl sites that likely contributed to increased surface recombination velocity, S , for surfaces with high θ_{Tfpa} . Mixed methyl/allyl³⁴ and mixed methyl/propionaldehyde⁷ monolayers, which were formed using Grignard reagents only, exhibited $S < 100 \text{ cm s}^{-1}$. Mixed methyl/thienyl monolayers,⁴³ prepared using 2-thienyllithium, exhibited $S < 100 \text{ cm s}^{-1}$ for $\theta_{\text{SC}_4\text{H}_3} < 0.3$ ML. However, the Si(111)–MMTFPA surface exhibited significantly

higher S , even for $\theta_{\text{TFPA}} = 0.15$ ML (Figure 4.5), than has been observed for other mixed monolayers.

Small-molecule silanes have been shown to undergo cleavage of the Si–Si bonds in the presence of organolithium reagents, such as methyllithium.⁶³⁻⁶⁴ Furthermore, addition of organolithium reagents to H-terminated porous Si surfaces has been proposed to proceed by cleavage of Si–Si bonds.⁶⁵⁻⁶⁶ The reaction of 1-propynyllithium with Si(111)–Cl surfaces also yields samples with $S = 1.0 \times 10^3$ cm s⁻¹ (72 h after preparation), despite near complete termination of the Si atop sites with Si–C bonds.³³ However, reaction of CH₃Li with Si(111)–Cl surfaces is known to yield samples with S values comparable to those of samples prepared by reaction with CH₃MgCl.⁴³ Thus, the chemical nature of the organolithium reagent plays an important role in properties of the resulting functionalized surfaces. CH₃Li could form surfaces with low S because the small size of the –CH₃ group kinetically allows for passivation of all Si(111) atop sites without the breaking of Si–Si bonds. Hence, a route that utilizes only Grignard reagents to attach the bulky group to Si(111)–Cl surfaces for the synthesis of mixed methyl monolayers could be required to obtain low S values at functionalized Si(111) surfaces. Grignard reagents formed from terminal acetylides have been observed to undergo undetectable or slow reaction with Si(111)–Cl surfaces,³³ and consistently, reaction of the Grignard reagent 3,4,5-trifluorophenylethynylmagnesium chloride with Si(111)–Cl at 50 °C yielded a maximum $\theta_{\text{TFPA}} < 0.05$ ML. Thus, the organolithium reagent, LiTFPA, used herein for the synthesis of Si(111)–TFPA and Si(111)–MMTFPA surfaces, was necessary to achieve the reported monolayer compositions and shifts in the band-edge positions.

4.4.2 Hg Contacts to Si(111)–MMTFPA Surfaces

The work function of Hg is 4.49 eV,⁶⁷ which lies between the energies of the bottom of the conduction band and the top of the valence band of bulk Si and is very near the estimated energy of the absolute electrochemical potential for the standard hydrogen electrode (SHE), which is 4.44 eV at 25 °C.⁶⁸⁻⁶⁹ Hg can also be readily applied to and removed from the Si surface at room temperature without the formation of metal silicides.⁴⁰

The J - V data presented in Figure 4.8 and the plots of Φ_b versus θ_{TFPA} in Figure 4.9 show a clear trend in the value of Φ_b as a function of θ_{TFPA} for functionalized n- and p-Si(111) surfaces in contact with Hg. The surface composition played an essential role in the electrical behavior of the junction. The composite dipole at the interface between the Si and the Hg results in a net electric field that can be tuned to energetically favor the transfer of electrons from p-Si to Hg or holes from n-Si to Hg, respectively. The n-Si/Hg junction exhibited maximum rectification for surfaces terminated by $-\text{CH}_3$ groups, and addition of TFPA to the monolayer yielded junctions with lower Φ_b . The decrease in Φ_b with increase in θ_{TFPA} resulted from a shift in the band-edge positions of the Si relative to those of the Hg contacting phase. The electrical behavior of n-Si(111)–MMTFPA/Hg junctions that showed ohmic behavior by J - V analysis could have also been influenced by a high surface recombination velocity, which was measured for samples with high θ_{TFPA} .

For p-Si, the Si(111)– CH_3 surface formed an ohmic contact with Hg. The addition of TFPA to the monolayer resulted in an increase in Φ_b as θ_{TFPA} increased. Therefore, as

θ_{TFFPA} increased, the band-edge positions of the Si shifted relative to the band-edge positions of Si(111)–CH₃ surfaces. This behavior is consistent with the formation of a surface dipole in the orientation shown in Figure 4.1b due to the addition of surficial TFFPA. The resulting electric field at the interface is favorable for the flow of electrons from p-Si to the Hg contacting phase.

The values of Φ_b for Hg contacts to n-Si electrodes determined by J - V analysis agreed well with those obtained by C_{diff} - V analysis. In contrast, C_{diff} - V analysis for p-Si/Hg contacts with θ_{TFFPA} near 0.2 ML yielded $\Phi_b = 1.07$ V, that is, close to the Si band gap, while J - V data of the same samples yielded $\Phi_b = 0.68$ V. The C_{diff} - V analysis is performed while the sample is in reverse bias and passes only small amounts of current to measure the real and imaginary impedance as well as the current-voltage phase shift. C_{diff} - V analysis thus minimizes the effects of recombination current on the calculated Φ_b . J - V analysis, in contrast, is performed in forward bias, for which significantly more current passes, and where the effects of high surface recombination are greater. The difference in Φ_b determined for p-Si(111)–MMTFPA/Hg by J - V versus C_{diff} - V methods indicates that high S values yield lower Φ_b when measured by J - V analysis.

Si(111)–H surfaces have been widely used for fabrication of Si-based optoelectronic devices, and comparison of the band-edge positions of Si(111)–H surfaces with the results reported in this work is informative. For n-Si, the electrical behavior of Si(111)–H surfaces in contact with Hg produced a junction with $\Phi_b = 0.3$ V, which appeared ohmic when measured at 296 K.⁴⁰ The n-Si(111)–MMTFPA samples with $\theta_{\text{TFFPA}} > 0.17$ ML in contact with Hg produced behavior similar to the n-Si(111)–H

samples. Previous results for p-Si(111)–H/Hg junctions yielded $\Phi_b = 0.8$ V by both J - V and C_{diff} - V measurements,⁴⁰ while p-Si(111)–MMTFPA samples achieved a maximum Φ_b of 0.68 V when measured by J - V analysis. The near-band gap Φ_b measured by C_{diff} - V analysis for p-Si(111)–MMTFPA samples indicated that the band-edge positions were energetically closer to the vacuum level than the band-edge positions of Si(111)–H surfaces, but high S values for these surfaces limited the Φ_b measured under J - V operation.

4.4.3 Photoelectrochemical Measurements of Si(111)–TFPA and Si(111)–MMTFPA Surfaces in CH₃CN

Photoelectrochemical measurements for n- and p- Si(111)–CH₃ samples in contact with CH₃CN–Cp*₂Fe⁺⁰ were in good agreement with previously reported results;⁴⁷ however, n- and p-Si(111)–CH₃ samples in contact with CH₃CN–MV^{2+/+} exhibited E_{oc} values of -0.26 ± 0.02 and $+0.15 \pm 0.01$ V, respectively, that were not within the error of previously reported results of -0.10 ± 0.03 and $+0.31 \pm 0.02$ V, respectively.⁴⁷ The calculated values of $E_{\text{eff,n}}$ (MV^{2+/+}) and $E_{\text{eff,p}}$ (MV^{2+/+}) were shifted by -0.16 and -0.13 V, respectively, compared with previous work. This difference in effective solution potential likely arose because the previous work used 1,1'-dimethyl-4,4'-bipyridinium dichloride hydrate as the source of MV²⁺, while this work used 1,1'-dimethyl-4,4'-bipyridinium hexafluorophosphate. The reversible potential for the MV^{2+/+} couple has previously been found to be dependent on the nature of the anion in the electrolyte.⁷⁰ For the calculated values of $E_{\text{eff,n}}$ (A/A⁻) and $E_{\text{eff,p}}$ (A/A⁻), extrapolation of

the results previously reported predicts E_{oc} values that are within close agreement with the values measured in this work.

Photoelectrochemical measurements under 100 mW cm^{-2} illumination demonstrated that the E_{oc} exhibited by the semiconductor-liquid junctions was sensitive to the surface composition. Compared with Si(111)-CH₃ samples, E_{oc} for n-Si(111)-MMTFPA samples shifted by +0.27 V in contact with CH₃CN-Cp*₂Fe⁺⁰ and by +0.24 V in contact with CH₃CN-MV^{2+/+}. The n-Si(111)-TFPA samples exhibited a greater shift in E_{oc} , suggesting that the residual Si-Cl sites, with a molecular dipole in the positive direction (Figure 4.1b), and greater θ_{TFPA} contributed to the positive shift in the band-edge positions. Despite higher S observed for Si(111)-TFPA samples (Figure 4.5), Si(111)-TFPA samples showed larger shifts in E_{oc} than those observed for Si(111)-MMTFPA samples. This behavior indicated that the overall greater θ_{TFPA} observed for Si(111)-TFPA samples and inclusion of Si(111)-Cl sites contributed more to the overall E_{oc} than the high S measured for Si(111)-TFPA samples. The observation of different E_{oc} values for n-Si(111)-MMTFPA and n-Si(111)-TFPA samples in contact with different redox species indicates that the Fermi level of the semiconductor is not fully pinned by surface states, evidenced by the high observed S . The observed decrease in the magnitude of Φ_b for n-Si(111)-TFPA and n-Si(111)-MMTFPA samples was indicative of a substantial positive shift in the band-edge positions of these surfaces relative to Si(111)-CH₃ samples. The E_{oc} observed for n-Si(111)-MMTFPA samples in contact with Cp*₂Fe⁺⁰ and MV^{2+/+} was further shifted positively by the high S observed for samples with high θ_{TFPA} .

The p-Si(111)–MMTFPA and p-Si(111)–TFPA samples exhibited a maximum shift in E_{oc} of +0.10 V relative to p-Si(111)–CH₃ samples in contact with Cp*₂Fe⁺⁰ and MV^{2+/+}. The increase in Φ_b observed for p-Si(111)–MMTFPA samples relative to p-Si(111)–CH₃ samples was ~0.5 V, which should produce a larger increase in E_{oc} than was observed. The E_{oc} observed for p-Si(111)–MMTFPA samples in contact with Cp*₂Fe⁺⁰ and MV^{2+/+} was shifted negatively by the high S observed for samples with high θ_{TFPA} . For p-Si samples, the effect on E_{oc} of high S opposes the effect on E_{oc} produced by the surface dipole, so the reduced positive shift in E_{oc} achieved for p-Si samples as compared with n-Si samples is consistent with the presence of significant surface recombination at such interfaces.

Monolayer chemistry on Si(111) surfaces can effectively control the interfacial energetics at Si(111) interfaces. Moreover, alkyl monolayers can be applied to a broad range of crystalline, polycrystalline, and thin-film semiconductors without requiring expensive, specialized processing equipment. The electrochemical measurements presented in this work demonstrate that mixed monolayers on Si(111) can produce measurable shifts in the band-edge positions to yield junctions with tunable energetics. The development of methods to reduce S while maintaining a surface composition comparable to that of the MMTFPA monolayers presented in this work may enable the use of a broad range of materials in semiconductor devices.

4.5 CONCLUSIONS

The electrochemical behavior of n- and p-Si(111)–MMTFPA samples in contact with Hg showed that the addition of TFPA to the monolayer produced shifts in the band-edge positions, relative to Si(111)–CH₃ surfaces, by ≥ 0.6 V for n-Si and ≥ 0.5 V for p-Si samples. Photoelectrochemical measurements in contact with CH₃CN–Cp*₂Fe⁺⁰ and CH₃CN–MV^{2+/+} demonstrated that the composition of the organic monolayer on the surface yielded shifts in E_{oc} consistent with a net positive molecular dipole at the Si surface. The n-Si(111)–MMTFPA samples exhibited E_{oc} values that shifted by as much as +0.27 V compared with n-Si(111)–CH₃ surfaces, and the p-Si(111)–MMTFPA samples showed E_{oc} values that shifted by up to +0.10 V with respect to the p-Si(111)–CH₃ surface. The change in E_{oc} for p-Si was limited by high surface recombination, suggesting that larger changes in E_{oc} could be achieved by maintaining low S while allowing for comparable levels of F coverage on the surface. Si(111)–MMTFPA surfaces provide a versatile and scalable means of tuning the Si band-edge positions, especially for samples with low θ_{TFPA} . Semiconductor surface chemistry therefore holds promise to allow for control of the interface between semiconductors and functional components, such as metals, metal oxides, catalysts, and conductive polymers.

4.6 REFERENCES

1. Walter, M. G.; Warren, E. L.; McKone, J. R.; Boettcher, S. W.; Mi, Q.; Santori, E. A.; Lewis, N. S. Solar Water Splitting Cells. *Chem. Rev.* **2010**, *110*, 6446-6473.
2. Huang, Z.; McKone, J. R.; Xiang, C.; Grimm, R. L.; Warren, E. L.; Spurgeon, J. M.; Lewerenz, H.-J.; Brunschwig, B. S.; Lewis, N. S. Comparison Between the Measured and Modeled Hydrogen-Evolution Activity of Ni- or Pt-Coated Silicon Photocathodes. *Int. J. Hydrogen Energy* **2014**, *39*, 16220-16226.
3. McKone, J. R.; Warren, E. L.; Bierman, M. J.; Boettcher, S. W.; Brunschwig, B. S.; Lewis, N. S.; Gray, H. B. Evaluation of Pt, Ni, and Ni-Mo Electrocatalysts for Hydrogen Evolution on Crystalline Si Electrodes. *Energy Environ. Sci.* **2011**, *4*, 3573-3583.
4. Sun, K.; Saadi, F. H.; Lichterman, M. F.; Hale, W. G.; Wang, H.-P.; Zhou, X.; Plymale, N. T.; Omelchenko, S. T.; He, J.-H.; Papadantonakis, K. M.; Brunschwig, B. S.; Lewis, N. S. Stable Solar-Driven Oxidation of Water by Semiconducting Photoanodes Protected by Transparent Catalytic Nickel Oxide Films. *Proc. Natl. Acad. Sci. U.S.A.* **2015**, *112*, 3612-3617.
5. Sun, K.; McDowell, M. T.; Nielander, A. C.; Hu, S.; Shaner, M. R.; Yang, F.; Brunschwig, B. S.; Lewis, N. S. Stable Solar-Driven Water Oxidation to O₂(g) by Ni-Oxide-Coated Silicon Photoanodes. *J. Phys. Chem. Lett.* **2015**, *6*, 592-598.
6. Hu, S.; Shaner, M. R.; Beardslee, J. A.; Lichterman, M.; Brunschwig, B. S.; Lewis, N. S. Amorphous TiO₂ coatings stabilize Si, GaAs, and GaP photoanodes for efficient water oxidation. *Science* **2014**, *344*, 1005-1009.

7. O'Leary, L. E.; Strandwitz, N. C.; Roske, C. W.; Pyo, S.; Brunchwitz, B. S.; Lewis, N. S. Use of Mixed $\text{CH}_3\text{-}/\text{HC(O)CH}_2\text{CH}_2\text{-Si(111)}$ Functionality to Control Interfacial Chemical and Electronic Properties During the Atomic-Layer Deposition of Ultrathin Oxides on Si(111). *J. Phys. Chem. Lett.* **2015**, *6*, 722-726.
8. Kim, H. J.; Kearney, K. L.; Le, L. H.; Pekarek, R. T.; Rose, M. J. Platinum-Enhanced Electron Transfer and Surface Passivation through Ultrathin Film Aluminum Oxide (Al_2O_3) on Si(111)- CH_3 Photoelectrodes. *ACS Appl. Mater. Inter.* **2015**, *7*, 8572-8584.
9. Roske, C. W.; Popczun, E. J.; Seger, B.; Read, C. G.; Pedersen, T.; Hansen, O.; Vesborg, P. C. K.; Brunchwitz, B. S.; Schaak, R. E.; Chorkendorff, I.; Gray, H. B.; Lewis, N. S. Comparison of the Performance of CoP-Coated and Pt-Coated Radial Junction n^+p -Silicon Microwire-Array Photocathodes for the Sunlight-Driven Reduction of Water to $\text{H}_2(\text{g})$. *J. Phys. Chem. Lett.* **2015**, *6*, 1679-1683.
10. Warren, E. L.; McKone, J. R.; Atwater, H. A.; Gray, H. B.; Lewis, N. S. Hydrogen-Evolution Characteristics of Ni-Mo-Coated, Radial Junction, n^+p -Silicon Microwire Array Photocathodes. *Energy Environ. Sci.* **2012**, *5*, 9653-9661.
11. Juang, A.; Scherman, O. A.; Grubbs, R. H.; Lewis, N. S. Formation of Covalently Attached Polymer Overlayers on Si(111) Surfaces Using Ring-Opening Metathesis Polymerization Methods. *Langmuir* **2001**, *17*, 1321-1323.
12. Sailor, M. J.; Klavetter, F. L.; Grubbs, R. H.; Lewis, N. S. Electronic Properties of Junctions between Silicon and Organic Conducting Polymers. *Nature* **1990**, *346*, 155-157.

13. Giesbrecht, P. K.; Bruce, J. P.; Freund, M. S. Electric and Photoelectric Properties of 3,4-Ethylenedioxythiophene-Functionalized n-Si/PEDOT:PSS Junctions. *ChemSusChem* **2016**, *9*, 109-117.
14. Bruce, J. P.; Oliver, D. R.; Lewis, N. S.; Freund, M. S. Electrical Characteristics of the Junction between PEDOT:PSS and Thiophene-Functionalized Silicon Microwires. *ACS Appl. Mater. Inter.* **2015**, *7*, 27160-27166.
15. Warren, E. L.; Boettcher, S. W.; Walter, M. G.; Atwater, H. A.; Lewis, N. S. pH-Independent, 520 mV Open-Circuit Voltages of Si/Methyl Viologen^{2+/+} Contacts Through Use of Radial n⁺p-Si Junction Microwire Array Photoelectrodes. *J. Phys. Chem. C* **2011**, *115*, 594-598.
16. Johansson, E.; Boettcher, S. W.; O'Leary, L. E.; Poletayev, A. D.; Maldonado, S.; Brunshwig, B. S.; Lewis, N. S. Control of the pH-Dependence of the Band Edges of Si(111) Surfaces Using Mixed Methyl/Allyl Monolayers. *J. Phys. Chem. C* **2011**, *115*, 8594-8601.
17. Boettcher, S. W.; Warren, E. L.; Putnam, M. C.; Santori, E. A.; Turner-Evans, D.; Kelzenberg, M. D.; Walter, M. G.; McKone, J. R.; Brunshwig, B. S.; Atwater, H. A.; Lewis, N. S. Photoelectrochemical Hydrogen Evolution Using Si Microwire Arrays. *J. Am. Chem. Soc.* **2011**, *133*, 1216-1219.
18. Heller, A., Chemical Control of Surface and Grain Boundary Recombination in Semiconductors. In *Photoeffects at Semiconductor-Electrolyte Interfaces*, AMERICAN CHEMICAL SOCIETY: 1981; Vol. 146, pp 57-77.
19. Zhou, X.; Liu, R.; Sun, K.; Friedrich, D.; McDowell, M. T.; Yang, F.; Omelchenko, S. T.; Saadi, F. H.; Nielander, A. C.; Yalamanchili, S.; Papadantonakis, K. M.;

- Brunschwig, B. S.; Lewis, N. S. Interface Engineering of the Photoelectrochemical Performance of Ni-Oxide-Coated n-Si Photoanodes by Atomic-Layer Deposition of Ultrathin Films of Cobalt Oxide. *Energy Environ. Sci.* **2015**, *8*, 2644-2649.
20. Smith, W. A.; Sharp, I. D.; Strandwitz, N. C.; Bisquert, J. Interfacial Band-Edge Energetics for Solar Fuels Production. *Energy Environ. Sci.* **2015**, *8*, 2851-2862.
21. Kocha, S. S.; Turner, J. A. Displacement of the Bandedges of GaInP₂ in Aqueous Electrolytes Induced by Surface Modification. *J. Electrochem. Soc.* **1995**, *142*, 2625-2630.
22. Hilal, H. S.; Turner, J. A. Controlling Charge-Transfer Processes at Semiconductor/Liquid Junctions. *Electrochim. Acta* **2006**, *51*, 6487-6497.
23. MacLeod, B. A.; Steirer, K. X.; Young, J. L.; Koldemir, U.; Sellinger, A.; Turner, J. A.; Deutsch, T. G.; Olson, D. C. Phosphonic Acid Modification of GaInP₂ Photocathodes Toward Unbiased Photoelectrochemical Water Splitting. *ACS Appl. Mater. Inter.* **2015**, *7*, 11346-11350.
24. Kim, H. J.; Seo, J.; Rose, M. J. H₂ Photogeneration Using a Phosphonate-Anchored Ni-PNP Catalyst on a Band-Edge-Modified p-Si(111)|AZO Construct. *ACS Appl. Mater. Inter.* **2016**, *8*, 1061-1066.
25. Seo, J.; Kim, H. J.; Pekarek, R. T.; Rose, M. J. Hybrid Organic/Inorganic Band-Edge Modulation of p-Si(111) Photoelectrodes: Effects of R, Metal Oxide, and Pt on H₂ Generation. *J. Am. Chem. Soc.* **2015**, *137*, 3173-3176.
26. Ciampi, S.; Harper, J. B.; Gooding, J. J. Wet Chemical Routes to the Assembly of Organic Monolayers on Silicon Surfaces via the Formation of Si-C Bonds: Surface Preparation, Passivation and Functionalization. *Chem. Soc. Rev.* **2010**, *39*, 2158-2183.

27. Ciampi, S.; Luais, E.; James, M.; Choudhury, M. H.; Darwish, N. A.; Gooding, J. J. The Rapid Formation of Functional Monolayers on Silicon under Mild Conditions. *Phys. Chem. Chem. Phys.* **2014**, *16*, 8003-8011.
28. Linford, M. R.; Chidsey, C. E. D. Alkyl Monolayers Covalently Bonded to Silicon Surfaces. *J. Am. Chem. Soc.* **1993**, *115*, 12631-12632.
29. Buriak, J. M. Illuminating Silicon Surface Hydrosilylation: An Unexpected Plurality of Mechanisms. *Chem. Mater.* **2014**, *26*, 763-772.
30. Buriak, J. M.; Sikder, M. D. H. From Molecules to Surfaces: Radical-Based Mechanisms of Si-S and Si-Se Bond Formation on Silicon. *J. Am. Chem. Soc.* **2015**, *137*, 9730-9738.
31. Bansal, A.; Li, X.; Lauermann, I.; Lewis, N. S.; Yi, S. I.; Weinberg, W. H. Alkylation of Si Surfaces Using a Two-Step Halogenation/Grignard Route. *J. Am. Chem. Soc.* **1996**, *118*, 7225-7226.
32. Royea, W. J.; Juang, A.; Lewis, N. S. Preparation of Air-Stable, Low Recombination Velocity Si(111) Surfaces through Alkyl Termination. *Appl. Phys. Lett.* **2000**, *77*, 1988-1990.
33. Plymale, N. T.; Kim, Y.-G.; Soriaga, M. P.; Brunshwig, B. S.; Lewis, N. S. Synthesis, Characterization, and Reactivity of Ethynyl- and Propynyl-Terminated Si(111) Surfaces. *J. Phys. Chem. C* **2015**, *119*, 19847-19862.
34. O'Leary, L. E.; Johansson, E.; Brunshwig, B. S.; Lewis, N. S. Synthesis and Characterization of Mixed Methyl/Allyl Monolayers on Si(111). *J. Phys. Chem. B* **2010**, *114*, 14298-14302.

35. Webb, L. J.; Lewis, N. S. Comparison of the Electrical Properties and Chemical Stability of Crystalline Silicon(111) Surfaces Alkylated Using Grignard Reagents or Olefins with Lewis Acid Catalysts. *J. Phys. Chem. B* **2003**, *107*, 5404-5412.
36. Webb, L. J.; Michalak, D. J.; Biteen, J. S.; Brunschwig, B. S.; Chan, A. S. Y.; Knapp, D. W.; Meyer, H. M.; Nemanick, E. J.; Traub, M. C.; Lewis, N. S. High-Resolution Soft X-ray Photoelectron Spectroscopic Studies and Scanning Auger Microscopy Studies of the Air Oxidation of Alkylated Silicon(111) Surfaces. *J. Phys. Chem. B* **2006**, *110*, 23450-23459.
37. Bansal, A.; Lewis, N. S. Stabilization of Si Photoanodes in Aqueous Electrolytes through Surface Alkylation. *J. Phys. Chem. B* **1998**, *102*, 4058-4060.
38. Maldonado, S.; Knapp, D.; Lewis, N. S. Near-Ideal Photodiodes from Sintered Gold Nanoparticle Films on Methyl-Terminated Si(111) Surfaces. *J. Am. Chem. Soc.* **2008**, *130*, 3300-3301.
39. Maldonado, S.; Lewis, N. S. Behavior of Electrodeposited Cd and Pb Schottky Junctions on CH₃-Terminated n-Si(111) Surfaces. *J. Electrochem. Soc.* **2009**, *156*, H123-H128.
40. Maldonado, S.; Plass, K. E.; Knapp, D.; Lewis, N. S. Electrical Properties of Junctions between Hg and Si(111) Surfaces Functionalized with Short-Chain Alkyls. *J. Phys. Chem. C* **2007**, *111*, 17690-17699.
41. Hunger, R.; Fritsche, R.; Jaeckel, B.; Jaegermann, W.; Webb, L. J.; Lewis, N. S. Chemical and Electronic Characterization of Methyl-Terminated Si(111) Surfaces by High-Resolution Synchrotron Photoelectron Spectroscopy. *Phys. Rev. B* **2005**, *72*, 045317.

42. Wong, K. T.; Lewis, N. S. What a Difference a Bond Makes: The Structural, Chemical, and Physical Properties of Methyl-Terminated Si(111) Surfaces. *Acc. Chem. Res.* **2014**, *47*, 3037-3044.
43. O'Leary, L. E.; Rose, M. J.; Ding, T. X.; Johansson, E.; Brunschwig, B. S.; Lewis, N. S. Heck Coupling of Olefins to Mixed Methyl/Thienyl Monolayers on Si(111) Surfaces. *J. Am. Chem. Soc.* **2013**, *135*, 10081-10090.
44. Lattimer, J. R. C.; Blakemore, J. D.; Sattler, W.; Gul, S.; Chatterjee, R.; Yachandra, V. K.; Yano, J.; Brunschwig, B. S.; Lewis, N. S.; Gray, H. B. Assembly, Characterization, and Electrochemical Properties of Immobilized Metal Bipyridyl Complexes on Silicon(111) Surfaces. *Dalton Trans.* **2014**, *43*, 15004-15012.
45. Lattimer, J. R. C.; Brunschwig, B. S.; Lewis, N. S.; Gray, H. B. Redox Properties of Mixed Methyl/Vinylferrocenyl Monolayers on Si(111) Surfaces. *J. Phys. Chem. C* **2013**, *117*, 27012-27022.
46. Rivillon, S.; Chabal, Y. J.; Webb, L. J.; Michalak, D. J.; Lewis, N. S.; Halls, M. D.; Raghavachari, K. Chlorination of Hydrogen-Terminated Silicon (111) Surfaces. *J. Vac. Sci. Technol. A* **2005**, *23*, 1100-1106.
47. Grimm, R. L.; Bierman, M. J.; O'Leary, L. E.; Strandwitz, N. C.; Brunschwig, B. S.; Lewis, N. S. Comparison of the Photoelectrochemical Behavior of H-Terminated and Methyl-Terminated Si(111) Surfaces in Contact with a Series of One-Electron, Outer-Sphere Redox Couples in CH₃CN. *J. Phys. Chem. C* **2012**, *116*, 23569-23576.
48. Hendrickson, D. N.; Sohn, Y. S.; Gray, H. B. Magnetic Susceptibility Study of Various Ferricenium and Iron(III) Dicarbolide Compounds. *Inorg. Chem.* **1971**, *10*, 1559-1563.

49. Megehee, E. G.; Johnson, C. E.; Eisenberg, R. Optical versus Thermal Electron Transfer between Iridium(I) Maleonitriledithiolate Complexes and Methyl Viologen. *Inorg. Chem.* **1989**, *28*, 2423-2431.
50. Webb, L. J.; Rivillon, S.; Michalak, D. J.; Chabal, Y. J.; Lewis, N. S. Transmission Infrared Spectroscopy of Methyl- and Ethyl-Terminated Silicon(111) Surfaces. *J. Phys. Chem. B* **2006**, *110*, 7349-7356.
51. Li, Y.; O'Leary, L. E.; Lewis, N. S.; Galli, G. Combined Theoretical and Experimental Study of Band-Edge Control of Si through Surface Functionalization. *J. Phys. Chem. C* **2013**, *117*, 5188-5194.
52. Haber, J. A.; Lewis, N. S. Infrared and X-ray Photoelectron Spectroscopic Studies of the Reactions of Hydrogen-Terminated Crystalline Si(111) and Si(100) Surfaces with Br₂, I₂, and Ferrocenium in Alcohol Solvents. *J. Phys. Chem. B* **2002**, *106*, 3639-3656.
53. Seah, M. P.; Spencer, S. J. Ultrathin SiO₂ on Si II. Issues in Quantification of the Oxide Thickness. *Surf. Interface Anal.* **2002**, *33*, 640-652.
54. van der Marel, C.; Yildirim, M.; Stapert, H. R. Multilayer Approach to the Quantitative Analysis of X-ray Photoelectron Spectroscopy Results: Applications to Ultrathin SiO₂ on Si and to Self-Assembled Monolayers on Gold. *J. Vac. Sci. Technol. A* **2005**, *23*, 1456-1470.
55. Kratochvil, B.; Lorah, E.; Garber, C. Silver-Silver Nitrate Couple as Reference Electrode in Acetonitrile. *Anal. Chem.* **1969**, *41*, 1793-1796.
56. Kim, N. Y.; Laibinis, P. E. Derivatization of Porous Silicon by Grignard Reagents at Room Temperature. *J. Am. Chem. Soc.* **1998**, *120*, 4516-4517.

57. Socrates, G. *Infrared and Raman Characteristic Group Frequencies: Tables and Charts*, 3rd ed.; John Wiley & Sons Ltd.: Chichester, West Sussex, England, 2001.
58. Larkin, P. J. *IR and Raman Spectroscopy: Principles and Spectral Interpretation*; Elsevier: Waltham, MA, USA, 2011.
59. Stuart, B. H. *Infrared Spectroscopy: Fundamentals and Applications*; John Wiley & Sons Ltd.: Chichester, West Sussex, England, 2004.
60. Jaeckel, B.; Hunger, R.; Webb, L. J.; Jaegermann, W.; Lewis, N. S. High-Resolution Synchrotron Photoemission Studies of the Electronic Structure and Thermal Stability of CH₃- and C₂H₅-Functionalized Si(111) Surfaces. *J. Phys. Chem. C* **2007**, *111*, 18204-18213.
61. Moulder, J. F.; Stickle, W. F.; Sobol, P. E.; Bomen, K. D. *Handbook of X-ray Photoelectron Spectroscopy: A Reference Book of Standard Spectra for Identification and Interpretation of XPS Data*; Physical Electronics USA, Inc.: Chanhassen, Minnesota, 1995.
62. Collins, G.; O'Dwyer, C.; Morris, M.; Holmes, J. D. Palladium-Catalyzed Coupling Reactions for the Functionalization of Si Surfaces: Superior Stability of Alkenyl Monolayers. *Langmuir* **2013**, *29*, 11950-11958.
63. Still, W. C. Conjugate Addition of Trimethylsilyllithium. A Preparation of 3-Silyl Ketones. *J. Org. Chem.* **1976**, *41*, 3063-3064.
64. Hevesi, L.; Dehon, M.; Crutzen, R.; Lazarescu-Grigore, A. Kinetic Control in the Cleavage of Unsymmetrical Disilanes. *J. Org. Chem.* **1997**, *62*, 2011-2017.

65. Song, J. H.; Sailor, M. J. Functionalization of Nanocrystalline Porous Silicon Surfaces with Aryllithium Reagents: Formation of Silicon–Carbon Bonds by Cleavage of Silicon–Silicon Bonds. *J. Am. Chem. Soc.* **1998**, *120*, 2376-2381.
66. Kim, N. Y.; Laibinis, P. E. Improved Polypyrrole/Silicon Junctions by Surface Modification of Hydrogen-Terminated Silicon Using Organolithium Reagents. *J. Am. Chem. Soc.* **1999**, *121*, 7162-7163.
67. *Handbook of Chemistry and Physics*, 75th ed.; CRC Press, Inc.: Boca Raton, Florida, 1994.
68. Trasatti, S. The Absolute Electrode Potential: An Explanatory Note. *Pure Appl. Chem.* **1986**, *58*, 955-966.
69. Dekker, M. *Standard Potentials in Aqueous Solution*; CRC Press, Inc.: New York, 1985.
70. Bird, C. L.; Kuhn, A. T. Electrochemistry of the Viologens. *Chem. Soc. Rev.* **1981**, *10*, 49-82.

*Chapter 5***A MECHANISTIC STUDY OF THE OXIDATIVE REACTION OF HYDROGEN-TERMINATED Si(111) SURFACES WITH LIQUID METHANOL**

Plymale, N. T.; Dasog, M.; Brunschwig, B. S.; Lewis, N. S. A Mechanistic Study of the Oxidative Reaction of Hydrogen-Terminated Si(111) Surfaces with Liquid Methanol, *in preparation*.

5.1 INTRODUCTION

The device properties of Si can be manipulated through control over the structure and chemical composition of crystalline Si surfaces.¹⁻² The reactivity of hydrogen-terminated Si(111) (H-Si(111)) surfaces toward organic nucleophiles, including alkenes,³⁻⁴ alkynes,⁵⁻⁶ amines,⁷⁻¹¹ thiols and disulfides,¹²⁻¹³ Grignards,¹⁴⁻¹⁵ and alcohols,¹⁶⁻²⁵ has been widely exploited to impart desirable functionality to the Si interface. These surface reactions have been used to control the interface between Si and metals,²⁶⁻³¹ metal oxides,³²⁻³⁵ polymers,³⁶⁻⁴¹ and redox assemblies.⁴²⁻⁴⁹

Many nucleophiles react with H-Si(111) surfaces under mild conditions⁵⁰⁻⁵¹ compared to analogous reactions with molecular silanes. For example, the reaction of H-Si(111) surfaces with alcohols has no analogous molecular counterpart.^{52,18} The unique reactivity of H-Si(111) surfaces with alcohols, including CH₃OH, has been exploited as a versatile method to impart a desired functionality to the surface via the robust Si-O bond,

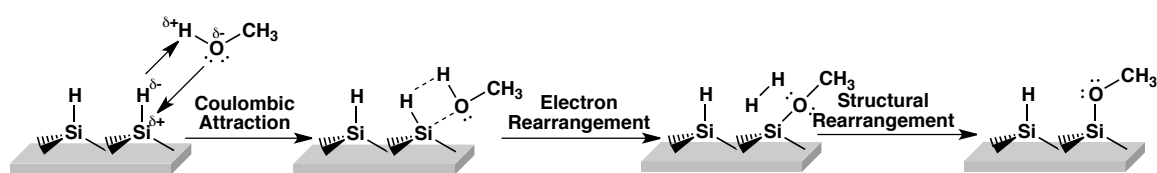
without the formation of thick insulating silicon oxide layers on the surface. For example, n-Si/CH₃OH junctions have yielded high open-circuit voltages (632–640 mV) and high device efficiencies (12–14%)⁵³⁻⁵⁴ in regenerative photoelectrochemical cells, with the device performance correlated with low surface recombination velocities⁵⁵⁻⁵⁷ as well as the favorable band-edge positions⁵⁸ of the methoxylated Si surface. The methoxy termination can moreover be converted to F-termination or OH-termination,^{19, 24} both of which are synthetically difficult to achieve otherwise on Si(111) surfaces.

Small molecule silanes that model the H–Si(111) surface, such as tris(trimethylsilyl)silane (TTMSS), are generally good models for radical reactions at H–Si(111) surfaces because the Si–H bond strength is comparable for both systems.⁵⁹ In the presence of CH₃OH, however, TTMSS decomposes by Si–Si bond cleavage.^{52, 60} Similarly, the Si–Si bonds on H-terminated nanoporous Si surfaces cleave by thermal reaction with alcohols.^{52, 61} In contrast, the H–Si(111) surface primarily undergoes a substitution reaction with alcohols, resulting in ≡Si–OR functionality on the surface. Scanning-tunneling microscopy (STM) data have demonstrated that the H–Si(111) surface undergoes microscopic etching after 30 min in warm (65 °C) CH₃OH, but methoxylated H–Si(111) sites are effectively passivated toward etching.⁶²

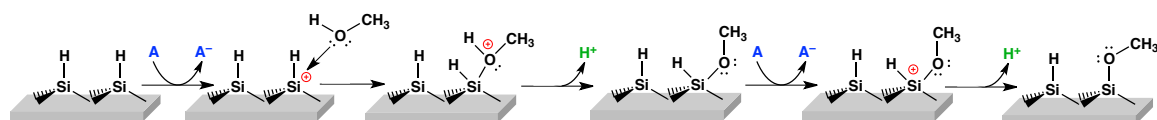
The electronic structure of crystalline Si, which differs significantly from that of model silanes, is often invoked to understand reactions that take place exclusively on H–Si(111) surfaces. Reactions that involve electron transfer at the H–Si(111) surface, such as the reaction of H–Si(111) surfaces with alcohols, are good candidate reactions to elucidate the role of the Si electronic structure in surface reactions. The general

understanding of the alkoxylation mechanism has been focused primarily on a qualitative discussion that implicates the narrow band gap of bulk Si in supporting more electronic states than can be supported by analogous molecular silanes. These mechanisms shown in Schemes 5.1,²¹ 5.2,¹⁸ provide a description of the chemical transformations that take place during surface alkoxylation, but the electronic rearrangements during these reactions are not yet clearly elaborated. Elucidating the mechanism of the reaction of H–Si(111) surfaces with CH₃OH in the presence of a series of oxidants offers a unique opportunity to determine the role of the Si electronic structure in the surface reaction.

Scheme 5.1. Methoxylation of H–Si(111) Surfaces in the Absence of an Oxidant²¹



Scheme 5.2. Oxidant-Activated Methoxylation of H–Si(111)¹⁷⁻¹⁸



Herein we characterize the reaction of H–Si(111) surfaces with CH₃OH in the absence or presence of an oxidant species and in the absence or presence of illumination. We have elucidated the dependence of the methoxylation reaction on the formal potential of the oxidant. Additionally, we have delineated the roles of the electronic surface states and bulk Si band structure in the electron transfer processes that are involved in the methoxylation reaction. A general mechanism by which the reaction of H–Si(111) surfaces with CH₃OH takes place under the conditions studied is proposed in the context of conventional charge transfer kinetics at the semiconductor interface.

5.2 EXPERIMENTAL SECTION

5.2.1 Materials and Methods

Water (≥ 18.2 M Ω cm resistivity) was obtained from a Barnstead E-Pure system. Aqueous ammonium fluoride (NH₄F(aq), 40% semiconductor grade, Transene Co. Inc., Danvers MA) was deaerated by bubbling with Ar(g) (99.999%, Air Liquide) for ≥ 1 h prior to use. Methanol (CH₃OH, anhydrous, $\geq 99.8\%$, Sigma-Aldrich) was used as received. Float-zone-grown, phosphorus-doped n-Si(111) “intrinsic” wafers (University Wafer, Boston, MA) were double-side polished, 525 ± 15 μm thick, oriented within 0.5° of the (111) crystal plane, and had a resistivity of 2.0 k Ω cm. Czochralski-grown, phosphorus-doped n-Si(111) wafers (Virginia Semiconductor, Fredericksburg, VA) were double-side polished, 381 ± 25 μm thick, oriented within 0.1° of the (111) crystal plane, and had a resistivity of 1.0 Ω cm. Czochralski-grown, boron-doped p-Si(111) wafers

(Addison Engineering, San Jose, CA) were double-side polished, $300 \pm 25 \mu\text{m}$ thick, oriented within 0.5° of the (111) crystal plane, and had a resistivity of $0.40 \Omega \text{ cm}$.

The dopant densities (N_d) were determined from the resistivities for each Si substrate. For intrinsic Si(111), $N_d = 2.2 \times 10^{12} \text{ cm}^{-3}$; for n-type Si(111), $N_d = 4.9 \times 10^{15} \text{ cm}^{-3}$; and for p-type Si(111), $N_d = 4.2 \times 10^{16} \text{ cm}^{-3}$. The positions of the n-type and p-type Si(111) bulk Fermi levels ($E_{F,n,b}$ and $E_{F,p,b}$, respectively) were determined using eq 5.1 and eq 5.2 for each of the dopant concentrations used.

$$E_{F,n,b} = E_{cb} + k_B T \ln\left(\frac{N_d}{N_C}\right) \quad (5.1)$$

$$E_{F,p,b} = E_{vb} - k_B T \ln\left(\frac{N_d}{N_C}\right) \quad (5.2)$$

E_{cb} and E_{vb} are the energy positions of the Si conduction band minimum (-4.05 eV vs E_{Vac}) and Si valence band maximum (-5.17 eV vs E_{Vac}),⁶³ respectively, k_B is the Boltzmann constant, T is the temperature in Kelvin (296 K), q is the absolute value of the elementary charge, N_C is the effective density of states of the Si conduction band ($2.8 \times 10^{19} \text{ cm}^{-3}$), and N_V is the effective density of states of the Si valence band ($1.0 \times 10^{19} \text{ cm}^{-3}$). The bulk Fermi level of intrinsic Si(111) ($E_{F,i,b}$), which was lightly n-type, was determined using eq 5.1.

1. Preparation and Purification of the Oxidants. 1,1'-dimethylferrocenium ($\text{Me}_2\text{Cp}_2\text{Fe}^+\text{BF}_4^-$, bis(methylcyclopentadienyl)iron(III) tetrafluoroborate), octamethylferrocenium ($\text{Me}_8\text{Cp}_2\text{Fe}^+\text{BF}_4^-$, bis(tetramethylcyclopentadienyl)iron(III) tetrafluoroborate), and decamethylferrocenium ($\text{Cp}^*\text{Fe}^+\text{BF}_4^-$, bis(pentamethylcyclopentadienyl)iron(III) tetrafluoroborate) were prepared by chemical oxidation of the neutral

metallocenes⁶⁴⁻⁶⁵ 1,1'-dimethylferrocene ($\text{Me}_2\text{Cp}_2\text{Fe}$, bis(methylcyclopentadienyl)iron(II), 95%, Sigma-Aldrich), octamethylferrocene ($\text{Me}_8\text{Cp}_2\text{Fe}$, bis(tetramethylcyclopentadienyl)iron(II), 98%, Strem Chemical), and decamethylferrocene (Cp^*_2Fe , bis(pentamethylcyclopentadienyl)iron(II), 99%, Strem Chemical), respectively. Ferrocenium ($\text{Cp}_2\text{Fe}^+\text{BF}_4^-$, bis(cyclopentadienyl)iron(III) tetrafluoroborate, technical grade, Sigma-Aldrich) $\text{Me}_2\text{Cp}_2\text{Fe}^+\text{BF}_4^-$, $\text{Me}_8\text{Cp}_2\text{Fe}^+\text{BF}_4^-$, and $\text{Cp}^*_2\text{Fe}^+\text{BF}_4^-$ were purified by recrystallization from diethyl ether (inhibitor-free, $\geq 99.9\%$ Sigma-Aldrich) and CH_3CN (anhydrous, $\geq 99.8\%$ Sigma-Aldrich). Methyl viologen ($\text{MV}^{2+}(\text{Cl}^-)_2$, 1,1'-dimethyl-4,4'-bipyridinium dichloride hydrate, 98%, Sigma-Aldrich) and cobaltocenium ($\text{Cp}_2\text{Co}^+\text{PF}_6^-$, bis(cyclopentadienyl)cobalt(III) hexafluorophosphate, 98%, Sigma-Aldrich) were recrystallized from ethanol (anhydrous, $\geq 99.5\%$ Sigma-Aldrich) prior to use. Acetylferrocenium ($(\text{CpCOCH}_3)\text{CpFe}^+$, (acetylcyclopentadienyl)cyclopentadienyl-iron(III)) was generated in CH_3OH containing 1.0 M LiClO_4 (battery grade, Sigma-Aldrich) from acetylferrocene ($(\text{CpCOCH}_3)\text{CpFe}$, acetylcyclopentadienyl)cyclopentadienyliron(II), Sigma-Aldrich, purified by sublimation) by controlled-potential electrolysis at a Pt mesh working electrode with a Pt mesh counter electrode located in a compartment separated from the working electrode by a Vycor frit.⁶⁵ The electrolysis was performed at +0.5 V vs a Pt pseudo-reference electrode, and sufficient current was passed to generate 1.0 mM $(\text{CpCOCH}_3)\text{CpFe}^+$ from 10 mM $(\text{CpCOCH}_3)\text{CpFe}$. The $(\text{CpCOCH}_3)\text{CpFe}^+$ was used within 1 min of its generation.

2. *Preparation of H-Si(111) Surfaces.* Si wafers were scored and broken to the desired size using a diamond- or carbide-tipped scribe. The Si surfaces were rinsed

sequentially with water, methanol ($\geq 99.8\%$, BDH), acetone ($\geq 99.5\%$, BDH), methanol, and water. The samples were oxidized in a piranha solution (1:3 v/v of 30% $\text{H}_2\text{O}_2(\text{aq})$ (EMD): 18 M $\text{H}_2\text{SO}_4(\text{aq})$ (EMD)) for 10–15 min at 95 ± 5 °C. The wafers were removed, rinsed with copious amounts of water, and immersed in buffered hydrofluoric acid(aq) (BHF, semiconductor grade, Transene Co. Inc.) for 18 s. The BHF solution was drained and the wafers were rinsed with H_2O . Anisotropic etching was then performed in an Ar(g)-purged solution of 40% $\text{NH}_4\text{F}(\text{aq})$ for 5.5 min for wafers having a 0.5° miscut angle, and for 9.0 min for wafers having a 0.1° miscut angle.⁶⁶ The wafers were removed, rinsed with H_2O , and dried under a stream of Ar(g).

3. Methoxylation of H-Si(111) Surfaces. The H-Si(111) wafers were transferred to a $\text{N}_2(\text{g})$ -purged glovebox (< 10 ppm $\text{O}_2(\text{g})$) and immersed in either neat CH_3OH or in a solution of CH_3OH that contained 1.0 mM of $(\text{CpCOCH}_3)\text{CpFe}^+$, $\text{Cp}_2\text{Fe}^+\text{BF}_4^-$, $\text{Me}_2\text{Cp}_2\text{Fe}^+\text{BF}_4^-$, $\text{Me}_8\text{Cp}_2\text{Fe}^+\text{BF}_4^-$, $\text{Cp}^*\text{Fe}^+\text{BF}_4^-$, $\text{MV}^{2+}2\text{Cl}^-$, or $\text{Cp}_2\text{Co}^+\text{PF}_6^-$. Reactions in the dark were performed in test tubes wrapped in black vinyl electrical tape with the top covered in Al foil, whereas reactions in the light were performed under ambient illumination. Upon completion of the reaction, the wafers were removed from the CH_3OH solution and rinsed sequentially with CH_3OH and tetrahydrofuran (THF, anhydrous, $\geq 99.9\%$, Sigma-Aldrich). The THF was allowed to evaporate and the samples were removed from the glovebox. Prior to analysis, the wafers were rinsed briefly with H_2O and dried under a stream of Ar(g).

4. Potentiostatic Methoxylation of H-Si(111). Si samples were cleaned using a piranha solution for 10 min at 95 ± 5 °C and etched in BHF for 18 s prior to electrode

fabrication. Ohmic contacts to the back of n-Si(111) ($1.0 \Omega \text{ cm}$) electrodes were made by using a diamond-tipped scribe to apply Ga-In eutectic (78% Ga, 22% In by weight). Ohmic contacts to the back of p-Si(111) ($0.40 \Omega \text{ cm}$) electrodes were made by electron-beam evaporation (Denton Vacuum) of 100 nm of Al to the rear face of the electrode, followed by a 30 min anneal under forming gas (5% $\text{H}_2(\text{g})$ in $\text{N}_2(\text{g})$) at $450 \text{ }^\circ\text{C}$.⁶⁷ Using high-purity conductive Ag paint (SPI supplies, West Chester, PA), the Si working electrodes were adhered to a coil of tinned Cu wire that had been threaded through 1/4" outer diameter Pyrex tubing. Loctite 9460 epoxy was used to insulate the rear face of the electrode from the electrolyte as well as to immobilize the Si wafer such that the electrode face was perpendicular to the length of the tubing.⁶⁷ The electrode areas ($0.2\text{--}0.4 \text{ cm}^2$) were measured by analysis of scanned images of the electrodes using ImageJ software.

Immediately prior to performing the electrochemical experiments, the electrodes were immersed in BHF for 18 s, rinsed with water, and dried thoroughly. The electrodes were then immersed in 40% $\text{NH}_4\text{F}(\text{aq})$, with wafers having a 0.5° miscut angle immersed for 5.5 min whereas wafers that had a 0.1° miscut angle were immersed for 9.0 min. The electrodes were rinsed with water and dried thoroughly prior to performing electrochemical measurements.

Electrochemical measurements were performed in a four-port, cylindrical, flat-bottomed, borosilicate glass cell that contained CH_3OH with 1.0 M LiClO_4 . Electrochemical measurements were collected using a Solartron 1286 model potentiostat operated by CorrWare software v. 3.2c. Current density vs potential (J - E) measurements

were collected using a 3-electrode setup with a Si working electrode, a saturated calomel reference electrode (SCE, CH instruments, Inc., Austin TX), and a Pt mesh counter electrode. *J-E* data were collected by sweeping the potential from negative to positive using a scan rate of 50 mV s^{-1} and a sampling rate of 1 mV per data point, with active stirring of the electrolyte. Measurements were performed in the dark as well as under 10 mW cm^{-2} of illumination intensity provided by a 300 W ELH-type W-halogen lamp. The illumination intensity was determined by use of a calibrated Si photodiode (Thor Laboratories, Newton, NJ).

5. *Determination of the Oxidant Formal Potentials.* The formal potentials of the oxidant species (1.0 mM in CH_3OH) were determined by cyclic voltammetry vs a $\text{Cp}_2\text{Fe}^{+/0}$ internal reference using Pt wire working and reference electrodes and a Pt mesh counter electrode. The formal potential of the $\text{Cp}_2\text{Fe}^{+/0}$ couple was measured vs a SCE reference ($E^\circ(\text{Cp}_2\text{Fe}^{+/0}) = 0.325 \text{ V vs SCE}$), and all of the oxidant formal potentials was converted to SCE using this value for the shift in reference potentials.. The supporting electrolyte was 1.0 M LiClO_4 for $(\text{CpCOCH}_3)\text{CpFe}^{+/0}$, $\text{Cp}_2\text{Fe}^{+/0}$, $\text{Me}_2\text{Cp}_2\text{Fe}^{+/0}$, $\text{Me}_8\text{Cp}_2\text{Fe}^{+/0}$, $\text{Cp}^*_2\text{Fe}^{+/0}$, and $\text{Cp}_2\text{Co}^{+/0}$ and was 0.1 M tetrabutylammonium hexafluorophosphate (TBAPF_6 , Sigma-Aldrich) for $\text{MV}^{2+/+}$.

5.2.2 Instrumentation

1. *Transmission Infrared Spectroscopy.* Transmission infrared spectroscopy (TIRS) was performed using a Thermo Scientific Nicolet 6700 optical spectrometer equipped with an electronically temperature-controlled EverGlo mid-IR source, a KBr beamsplitter, a deuterated L-alanine-doped triglycine sulfate (DLATGS) detector, and a

$\text{N}_2(\text{g})$ purge.⁶⁶⁻⁶⁷ The samples, cut to $\sim 1.3 \times 3.2$ cm, were mounted using a custom attachment such that the angle between the path of the beam and the surface normal was 74° (Brewster's angle for Si). The reported spectra are averages of 1500 consecutive scans collected at 4 cm^{-1} resolution. Spectra were referenced to spectrum of either the silicon oxide (SiO_x) or H-Si(111) surface, which were collected separately for each sample. Data were collected and processed using OMNIC software v. 9.2.41. The baseline was flattened and residual water peaks were subtracted to produce the reported spectral data.

2. *X-ray Photoelectron Spectroscopy.* X-ray photoelectron spectroscopic (XPS) data were collected using a Kratos AXIS Ultra spectrometer equipped with a monochromatic Al K α X-ray source at 1486.7 eV, a hybrid electrostatic and magnetic lens system, and a delay-line detector.⁶⁶⁻⁶⁷ Photoelectrons from a $700 \mu\text{m} \times 300 \mu\text{m}$ area were ejected at 90° with respect to the sample surface. Survey and high-resolution spectra were collected with an analyzer pass energy of 80 eV and 10 eV, respectively. The chamber base pressure was $\sim 8 \times 10^{-10}$ Torr. Calibration of the energy scale and work function was performed using clean Au, Ag, and Cu samples. The data were collected using Vision Manager software v. 2.2.10 revision 5.

5.2.3 Analysis of TIRS and XPS Data

1. *Calculation of the Methoxy Fractional Monolayer Coverage from TIRS Data.*

The fractional monolayer (ML) coverage of H-Si(111) sites remaining after reaction in CH_3OH ($\theta_{\text{Si-H}}$) was determined using eq 5.3:

$$\theta_{\text{Si-H}} = \frac{A_{\text{V}(\text{Si-H}),f}}{A_{\text{V}(\text{Si-H}),i}} \quad (5.3)$$

$A_{\text{V}(\text{Si-H}),f}$ and $A_{\text{V}(\text{Si-H}),i}$ are the final and initial area, respectively, under the Si–H stretching peak. Assuming that all atop sites are terminated by Si–H or Si–OCH₃ groups, the fractional ML coverage of CH₃O–Si(111) sites ($\theta_{\text{Si-OCH}_3}$) was determined using eq 5.4:

$$\theta_{\text{Si-OCH}_3} = 1 - \theta_{\text{Si-H}} \quad (5.4)$$

2. Calculation of the Methoxy Fractional Monolayer Coverage from XPS Data.

High-resolution C 1s and Si 2p XPS data were analyzed using CasaXPS v. 2.3.16. C 1s spectra were fitted using a Voigt GL(30) line function, which consisted of 70% Gaussian and 30% Lorentzian character. Bulk Si 2p data were fitted using a line function of the form LA(a, b, n), where a and b define the asymmetry of the line shape and n defines the Gaussian width. LA(1.2, 1.4, 200) was used in this work. Contributions from SiO_x were fitted using the GL(30) line shape. Spectra were analyzed using a linear background.

A substrate-overlayer model was used to determine the thickness of the methoxy overlayer, $d_{\text{Si-OCH}_3}$, by XPS:

$$\left(\frac{I_{\text{C-O}}}{I_{\text{Si}}} \right) \left(\frac{SF_{\text{Si}}}{SF_{\text{C-O}}} \right) \left(\frac{\rho_{\text{Si}}}{\rho_{\text{C-O}}} \right) = \left(\frac{1 - e^{-\frac{d_{\text{Si-OCH}_3}}{\lambda_{\text{C-O}} \sin \varphi}}}{e^{-\frac{d_{\text{Si-OCH}_3}}{\lambda_{\text{Si}} \sin \varphi}}} \right) \quad (5.5)$$

$I_{\text{C-O}}$ and I_{Si} are the areas under the photoemission peaks arising from C bound to O and from bulk Si, respectively, $SF_{\text{C-O}}$ and SF_{Si} are the sensitivity factors for the C 1s (0.278) and Si 2p (0.328) photoemission signals, respectively, $\rho_{\text{C-O}}$ and ρ_{Si} are the density of the hydrocarbon overlayer (3.0 g cm⁻³) and Si (2.3 g cm⁻³), respectively, $\lambda_{\text{C-O}}$ and λ_{Si} are the attenuation lengths of C 1s photoelectrons (3.6 nm) and Si 2p photoelectrons (4.0 nm),

respectively, moving through a hydrocarbon overlayer, and φ is the angle between the photoelectron ejection vector and the instrument analyzer (90° for this work). The thickness $d_{\text{Si-OCH}_3}$ was determined using an iterative process, and $\theta_{\text{Si-OCH}_3}$ was calculated by dividing by the estimated thickness of 1 ML of methoxy groups (0.20 nm).

Some samples exhibited the presence of F by XPS. The fractional monolayer coverage of F^- was calculated from high-resolution XPS data using eq 5.6.

$$\left(\frac{I_{\text{F } 1s}}{I_{\text{Si}}}\right)\left(\frac{SF_{\text{Si}}}{SF_{\text{F } 1s}}\right)\left(\frac{\rho_{\text{Si}}}{\rho_{\text{O}}}\right) = \left(\frac{1 - e^{-\frac{d_{\text{F}}}{\lambda_{\text{F}} \sin \varphi}}}{e^{-\frac{d_{\text{F}}}{\lambda_{\text{Si}} \sin \varphi}}}\right) \quad (5.6)$$

$I_{\text{F } 1s}$ is the area under the F 1s photoemission peak (both peaks present in Figure 5.9), $SF_{\text{F } 1s}$ is the sensitivity factor for the F 1s photoemission signal (1.00), ρ_{O} is the density of the terminating overlayer (assumed to be primarily hydrocarbon, giving $\rho_{\text{S}} = 3.0 \text{ g cm}^{-3}$), and λ_{F} is the attenuation length of F 1s photoelectrons moving through a halogen overlayer (1.6 nm).¹⁸ The remaining terms in eq 5.6 are defined for eq 5.5. The thickness of the F layer d_{F} was determined using an iterative process, and the fractional monolayer coverage of F, θ_{F} , was calculated by dividing by the estimated thickness of 1 ML of F^- ion (0.13 nm).⁶⁷

5.3 RESULTS

5.3.1 Reaction of H-Si(111) with CH_3OH Solutions in the Dark

Figure 5.1 presents time dependence for the dark reaction of H-Si(111) surfaces with CH_3OH in the absence or presence of Cp_2Fe^+ . The reaction of H-Si(111) with

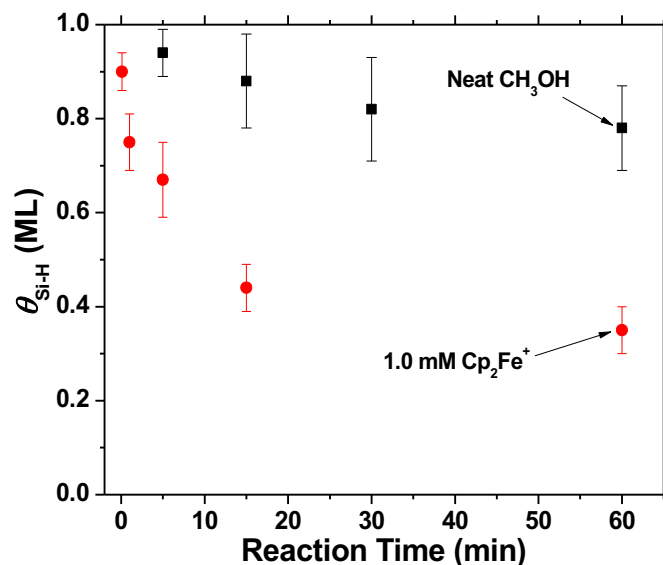


Figure 5.1. Time dependence of the reaction of H-Si(111) with neat CH₃OH and CH₃OH containing 1.0 mM Cp₂Fe⁺ in the dark. $\theta_{\text{Si-H}}$ was determined from TIRS measurements using eq 5.3. Figure courtesy of M. Dasog.

CH₃OH proceeded slowly in the absence of electron acceptors in solution, but increased substantially upon addition of Cp₂Fe⁺. This observation agrees with previous results that describe increased reaction rates for the methoxylation of H-Si(111) in CH₃OH solutions that contained Cp₂Fe⁺ or Me₂Cp₂Fe⁺.^{18, 21, 68-69}

A substantial difference in the peak area of the Si-H stretching, $\nu(\text{Si-H})$, signal was observable between the two reaction conditions after a 5 min reaction time. A greater difference was observed for a 15 min reaction time, but measurable subsurface silicon oxide (SiO_x) was consistently observed after 15 min in the presence of Cp₂Fe⁺. Therefore, a 5 min reaction time was chosen as a standard point of comparison in this work.

The reaction of H-Si(111) surfaces with liquid CH₃OH was performed for 5 min in solutions that contained 1.0 mM of the oxidants indicated in Figure 5.2 as well as in

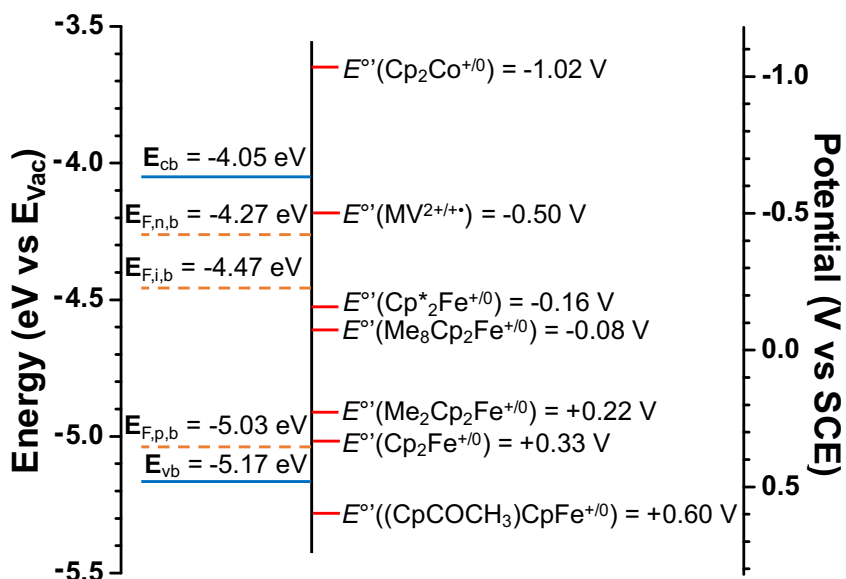


Figure 5.2. Energy diagram showing the relative energy positions vs the vacuum level (E_{Vac}) of the Si valence band maximum (E_{vb}), Si conduction band minimum (E_{cb}), and the calculated bulk Fermi levels (eq 5.1 and eq 5.2) of the intrinsic Si(111) ($E_{\text{F,i,b}}$), n-type Si(111) ($E_{\text{F,n,b}}$), and p-type Si(111) ($E_{\text{F,p,b}}$) used in this work. The measured formal potentials ($E^{\circ'}$) vs SCE of each oxidant are indicated relative to the Si band positions ($\text{SCE} = -(E_{\text{Vac}} + 4.68)$).

neat CH₃OH. The experimentally determined formal potentials, $E^{\circ'}(A/A^-)$, for each oxidant are indicated relative to the energy positions of the Si valence band, the Si conduction band, and the Fermi levels of the planar Si samples used in this work.⁶³ The formal potentials of the oxidants spanned the range from below the valence-band maximum to above the conduction-band minimum, allowing for determination of the reactivity of H-Si(111) with CH₃OH over a wide range of oxidizing conditions. Note that only the oxidized species were added to CH₃OH solutions, except in the case of (CpCOCH₃)CpFe⁺, and the Nernstian solution potentials were thus shifted positive of the measured formal potentials.

Figure 5.3 shows TIRS data for H-Si(111) surfaces after 5 min of exposure to CH₃OH in the presence or absence of the indicated oxidants. The peak positions, shifts, and assignments have been described previously.²¹ The highest reactivity, for which the $\nu(\text{Si-H})$ peak area (Figure 5.3a) substantially broadened and reduced in intensity compared with the initial peak area, was observed for reactions performed using $(\text{CpCOCH}_3)\text{CpFe}^+$, Cp_2Fe^+ , and $\text{Me}_2\text{Cp}_2\text{Fe}^+$ as oxidants. The activity of these three oxidants is also indicated by the presence of three substantial C-H stretching, $\nu(\text{C-H})_{\text{CH}_3}$, peaks (Figure 5.3b) and two broad peaks shown in Figure 5.3c that correspond to C-H symmetric bending, $\delta_s(\text{C-H})_{\text{CH}_3}$, and to a complex mode that consists of O-C stretching, $\nu(\text{O-C})$, coupled with -CH₃ rocking, $\rho(\text{CH}_3)$. A broad and low-intensity shoulder on the low energy side of the complex $\nu(\text{O-C}) + \rho(\text{CH}_3)$ was occasionally observed, and corresponds to transverse optical Si-O-Si stretching, $\nu(\text{Si-O-Si})_{\text{TO}}$.

The transition from the broad, low-intensity peak observed for reactions performed with $\text{Me}_2\text{Cp}_2\text{Fe}^+$ to the sharp peak observed for reactions performed with $\text{Me}_8\text{Cp}_2\text{Fe}^+$ represents the most evident shift in reaction behavior. The $\nu(\text{Si-H})$ peak generally sharpened gradually as $E^{\circ'}(\text{A/A}^-)$ decreased beyond $E^{\circ'}(\text{Me}_8\text{Cp}_2\text{Fe}^{+/0})$. The overall peak shape for reactions performed with Cp_2Co^+ was comparable to reactions performed in the absence of oxidant.

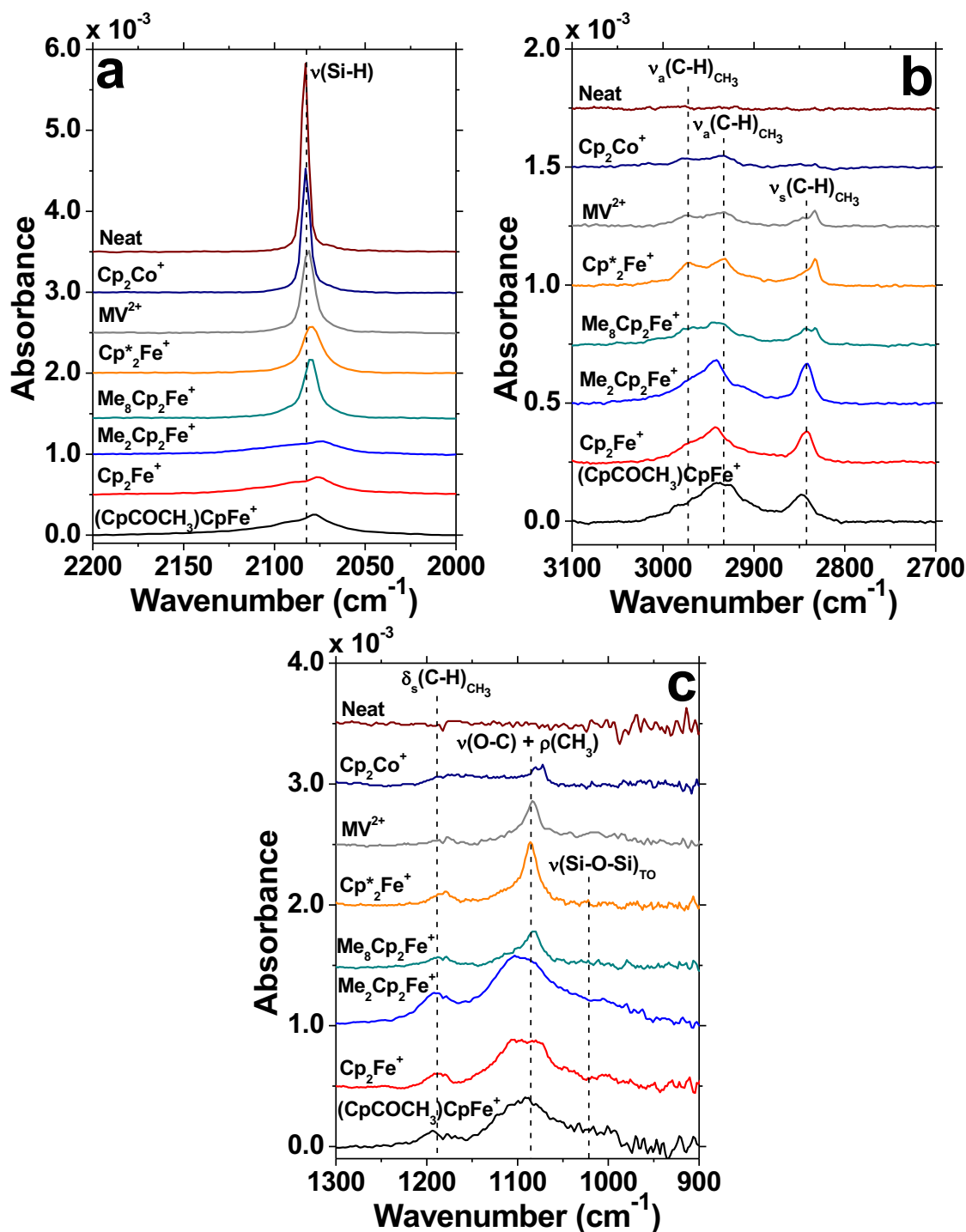


Figure 5.3. TIRS data for intrinsic H-Si(111) surfaces after treatment in neat CH_3OH or CH_3OH containing 1.0 mM of oxidant in the dark for 5 min. The Si-H stretching peak (a), the C-H stretching peaks (b), and the C-H bending and O-C stretching coupled with the CH_3 rocking peaks (c) are shown with the oxidant indicated above each spectrum. The spectra are offset vertically for clarity. The symbols ν , δ , and ρ denote stretching, bending, and rocking motions, respectively.

The intensity and width of the modes associated with the grafting of $-\text{OCH}_3$ groups to the H-Si(111) surface presented in Figure 5.3b and Figure 5.3c were greatly reduced for $\text{Me}_8\text{Cp}_2\text{Fe}^+$ and Cp^*Fe^+ compared with the peak areas observed for more oxidizing species. These spectral features were further weakened for reactions performed in solutions that contained MV^{2+} , and reactions performed in neat CH_3OH or in CH_3OH that contained Cp_2Co^+ yielded nearly undetectable $\nu(\text{C-H})_{\text{CH}_3}$, $\delta_s(\text{C-H})_{\text{CH}_3}$, or $\nu(\text{O-C}) + \rho(\text{CH}_3)$ modes. These results indicate that the thermodynamic formal potential of oxidants with $E^{\circ'}(\text{A}/\text{A}^-) \leq E^{\circ'}(\text{Me}_8\text{Cp}_2\text{Fe}^{+/0})$ is not sufficient to efficiently promote oxidative addition of CH_3OH to H-Si(111).

Figure 5.4a presents values of $\theta_{\text{Si-OCH}_3}$ determined from TIRS measurements as a function of the oxidizing conditions used for the reaction of H-Si(111) with CH_3OH for intrinsic, n-type, and p-type H-Si(111) samples. The data presented in Figure 5.4a show a relatively constant $\theta_{\text{Si-OCH}_3}$ for $(\text{CpCOCH}_3)\text{CpFe}^+$, Cp_2Fe^+ , and $\text{Me}_2\text{Cp}_2\text{Fe}^+$ as the oxidant. A substantial decrease in $\theta_{\text{Si-OCH}_3}$ was observed for reactions performed in CH_3OH solutions that contained oxidants having $E^{\circ'}(\text{A}/\text{A}^-) \leq E^{\circ'}(\text{Me}_8\text{Cp}_2\text{Fe}^{+/0})$. This transition, which occurred for $E^{\circ'}(\text{A}/\text{A}^-)$ between 0.22 V and -0.08 V vs SCE, is marked in Figure 5.4 by a vertical black dotted line. The general trend indicated that $(\text{CpCOCH}_3)\text{CpFe}^+$, Cp_2Fe^+ , and $\text{Me}_2\text{Cp}_2\text{Fe}^+$ were capable of serving as electron acceptors in the reaction of H-Si(111) with CH_3OH , while $\text{Me}_8\text{Cp}_2\text{Fe}^+$, Cp^*Fe^+ , MV^{2+} , and Cp_2Co^+ were not effective oxidants in driving this reaction.

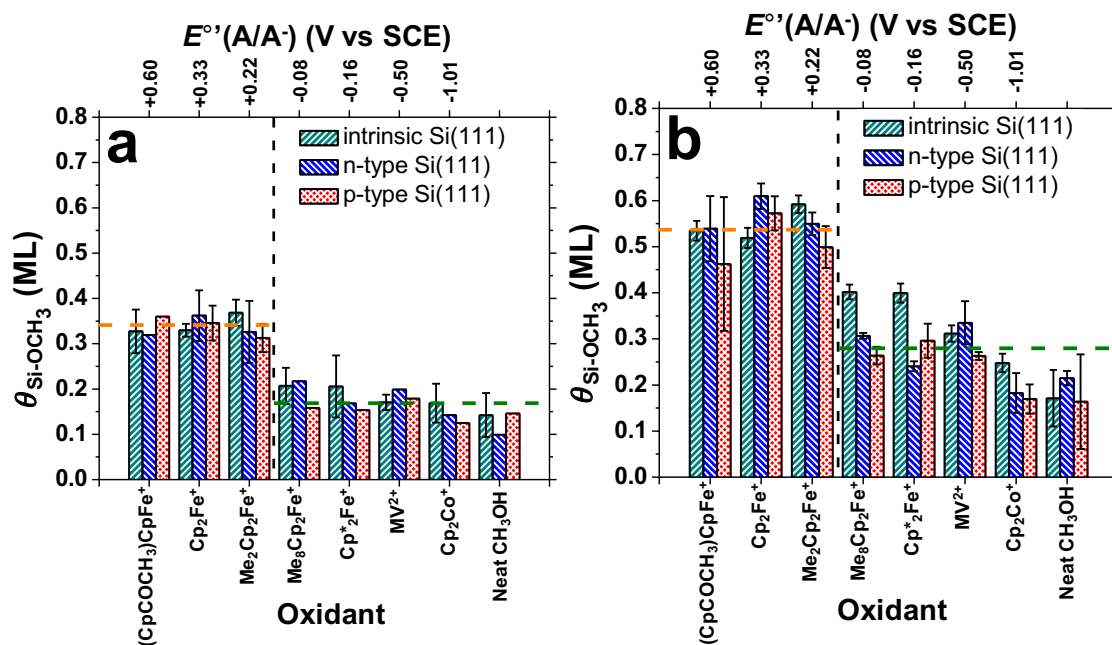


Figure 5.4. Correlation between $\theta_{\text{Si-OCH}_3}$ and the oxidizing conditions used in the reaction of H-Si(111) surfaces with CH_3OH in the dark. Reactions were performed for 5 min in neat CH_3OH or CH_3OH containing 1.0 mM of the oxidant species indicated. The experimentally determined formal potentials, $E^{\circ'}(\text{A/A}^-)$, for each oxidant are given above each plot. Panel a gives $\theta_{\text{Si-OCH}_3}$ determined by TIRS measurements using eqs 5.1 and 5.2, and panel b gives $\theta_{\text{Si-OCH}_3}$ determined by XPS measurements using eq 5.5. The orange and green dotted lines are averages of $\theta_{\text{Si-OCH}_3}$ for all samples left and right of the black dotted line, respectively. Error bars represent statistical variation across multiple samples, and data points with no error bars represent single measurements.

Figure 5.4b presents values of $\theta_{\text{Si-OCH}_3}$ determined from XPS measurements as a function of the oxidizing conditions used. For all sample types, the values of $\theta_{\text{Si-OCH}_3}$ determined by XPS were substantially larger than those determined using TIRS measurements. For reference, the C 1s core level XP spectra for representative H-Si(111) samples after 5 min exposure to CH_3OH solutions is shown in Figure 5.5. Adventitious hydrocarbon species, the majority of which are likely unbound CH_3OH or THF, contributed to the XPS signal ascribable to C bound to O, artificially increasing the value

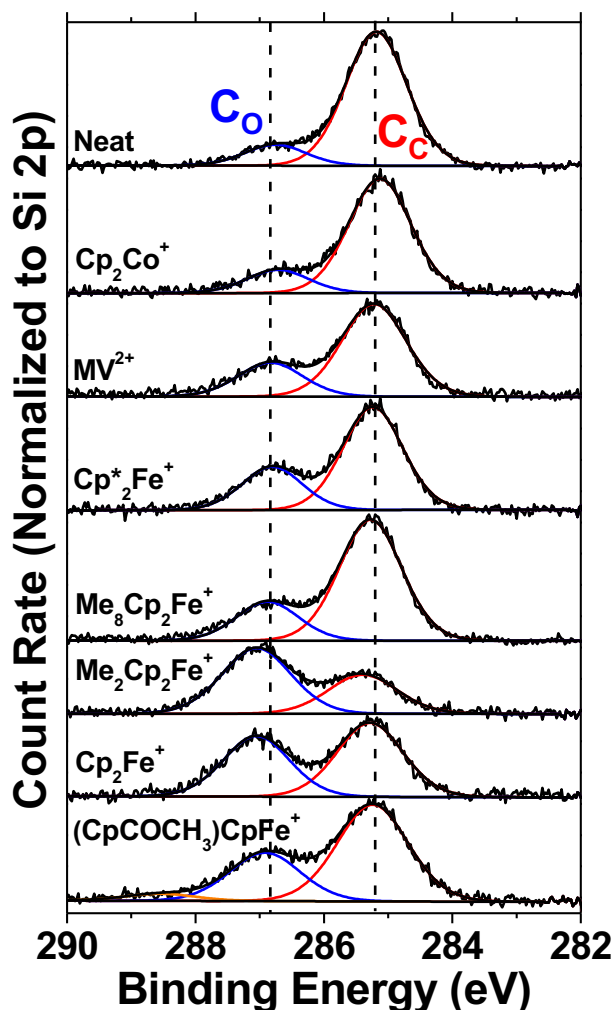


Figure 5.5. XPS data for the C 1s core level of H-Si(111) surfaces after 5 min exposure to neat CH₃OH or CH₃OH solutions containing 1.0 mM of the oxidant indicated above each spectrum. The approximate positions of the C bound to O (C_O) and C bound to C (C_C) peaks are indicated. The C_C peak arises from adventitious hydrocarbon species. The intensity of each spectrum was normalized to the Si 2p core level intensity, and the spectra are offset vertically for clarity.

of $\theta_{\text{Si-OCH}_3}$ determined by XPS. The results in Figure 5.4b nevertheless show a large and relatively stable $\theta_{\text{Si-OCH}_3}$ for reactions performed in CH₃OH solutions that contained (CpCOCH₃)CpFe⁺, Cp₂Fe⁺, or Me₂Cp₂Fe⁺ as oxidants, with a marked decrease in $\theta_{\text{Si-OCH}_3}$ for reactions performed in CH₃OH solutions that contained Me₈Cp₂Fe⁺.

Compared with results for TIRS measurements, for oxidants with $E^{\circ'}(A/A^-) \leq -0.08$ V vs SCE, the overall trend showed that $\theta_{\text{Si-OCH}_3}$ decreased more gradually as the formal potential of the oxidant in solution became less oxidizing.

Figure 5.6 presents the area under the $\nu(\text{C-H})_{\text{CH}_3}$ peaks ($3050\text{--}2800\text{ cm}^{-1}$) as a function of the oxidizing conditions used. These data closely parallel the XPS data

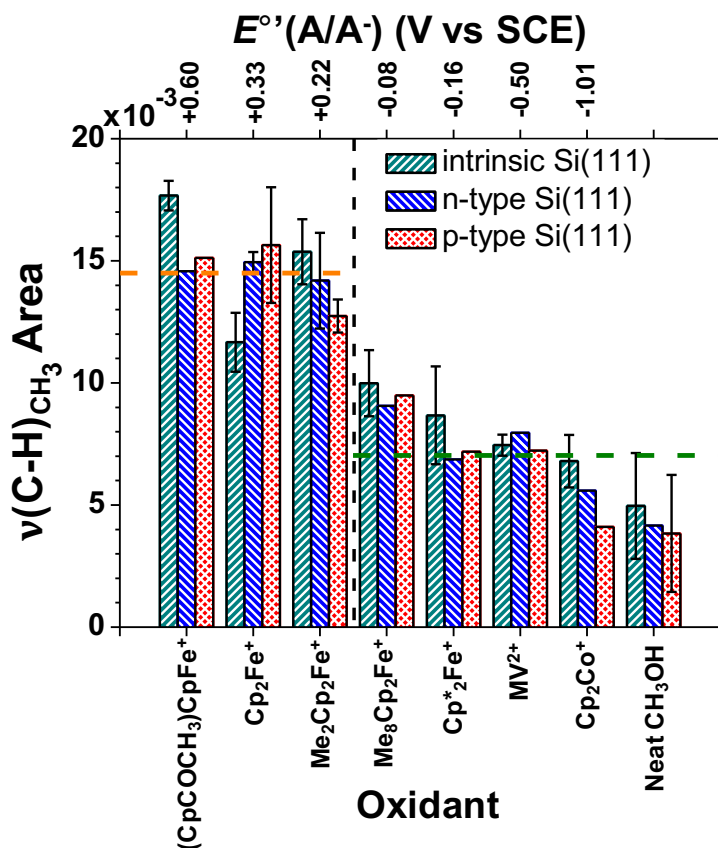


Figure 5.6. Correlation showing the area under the region containing the three $\nu(\text{C-H})_{\text{CH}_3}$ peaks ($3050\text{--}2800\text{ cm}^{-1}$) as a function of the oxidizing conditions used in the reaction of H-Si(111) surfaces with CH_3OH in the absence of light. Reactions were performed for 5 min in neat CH_3OH or CH_3OH containing 1.0 mM of an oxidant. The experimentally determined formal potentials, $E^{\circ'}(A/A^-)$, for each oxidant are given above the plot. The orange and green dotted lines are averages of the area under the $\nu(\text{C-H})_{\text{CH}_3}$ peaks for all samples left and right of the black dotted line, respectively. Error bars represent statistical variation across multiple samples, and data points with no error bars represent single measurements.

presented in Figure 5.4b, with the largest peak areas observed for reactions performed in CH₃OH solutions that contained (CpCOCH₃)CpFe⁺, Cp₂Fe⁺, and Me₂Cp₂Fe⁺ as oxidants. Oxidants with $E^{\circ}(A/A^-) \leq -0.08$ V vs SCE yielded a decreased $\nu(\text{C-H})_{\text{CH}_3}$ peak area compared with the three most oxidizing species. The $\nu(\text{C-H})_{\text{CH}_3}$ peak area, like the C 1s photoemission signal, is sensitive to adventitious hydrocarbons, thereby introducing a potentially confounding variable in interpreting the XPS data. Nonetheless, the data indicate a trend showing a gradual decrease in the $\nu(\text{C-H})_{\text{CH}_3}$ peak area as $E^{\circ}(A/A^-)$ decreased, in agreement with the data presented in Figure 4.

Figure 5.7 presents the area under the $\delta_s(\text{C-H})_{\text{CH}_3}$ and complex $\nu(\text{C-O}) + \rho(\text{CH}_3)$ peaks (1250–950 cm⁻¹) as a function of the oxidizing conditions used. The results show a clear difference between oxidants having $E^{\circ}(A/A^-) \geq 0.22$ V vs SCE and oxidants with $E^{\circ}(A/A^-) \leq -0.08$ V vs SCE. Specifically, a substantial decrease in peak area was apparent between reactions performed in CH₃OH solutions that contained Me₂Cp₂Fe⁺ relative to reactions in CH₃OH solutions that contained Me₈Cp₂Fe⁺. The data in Figure 5.7 closely parallel the observed trend in Figure 5.4a.

The TIRS peak area analysis data presented in Figure 5.4a and Figure 5.6 clearly indicate that the oxidant-activated reaction of H–Si(111) surfaces with CH₃OH is not effectively achieved by oxidants having $E^{\circ}(A/A^-) \leq E^{\circ}(\text{Me}_8\text{Cp}_2\text{Fe}^{+/0})$. Additionally, the data indicate that, in the dark, the reaction of H–Si(111) samples with CH₃OH under the specified conditions is independent of the dopant type and dopant density of the Si(111) substrate.

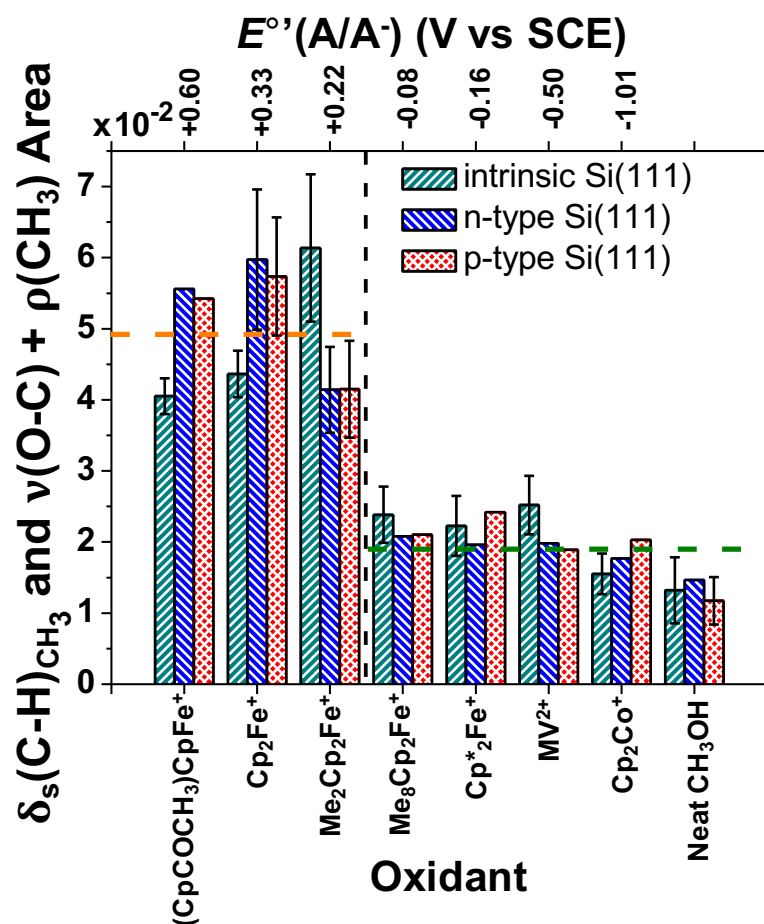


Figure 5.7. Correlation showing the area under the region containing the $\delta_s(\text{C-H})_{\text{CH}_3}$ and $\nu(\text{C-O}) + \rho(\text{CH}_3)$ peaks ($1250\text{--}950 \text{ cm}^{-1}$) as a function of the oxidizing conditions used in the reaction of H-Si(111) surfaces with CH_3OH in the absence of light. Reactions were performed for 5 min in neat CH_3OH or CH_3OH containing 1.0 mM of an oxidant. The experimentally determined formal potentials, $E^{\circ'} (A/A^-)$, for each oxidant are given above the plot. The orange and green dotted lines are averages of the area under the $\delta_s(\text{C-H})_{\text{CH}_3}$ and $\nu(\text{C-O}) + \rho(\text{CH}_3)$ peaks for all samples left and right of the black dotted line, respectively. Error bars represent statistical variation across multiple samples, and data points with no error bars represent single measurements.

5.3.2 Reaction of H-Si(111) with CH_3OH Solutions in the Presence of Light

Figure 5.8 shows $\theta_{\text{Si-OCH}_3}$ as a function of the oxidizing conditions used for the reaction of H-Si(111) with CH_3OH in the dark or under ambient light. For intrinsic or n-

type H–Si(111) samples in CH₃OH solutions that contained Cp₂Fe⁺ or Me₂Cp₂Fe⁺, $\theta_{\text{Si-OCH}_3}$ determined by TIRS measurements after a 5 min reaction in the presence of ambient light increased relative to $\theta_{\text{Si-OCH}_3}$ for the same reaction in the dark. For intrinsic or n-type H–Si(111) samples in CH₃OH solutions that contained Me₈Cp₂Fe⁺, the reaction in ambient light exhibited significantly higher $\theta_{\text{Si-OCH}_3}$ compared with the same reaction in the dark, but the level of reactivity was not the same as that observed for CH₃OH solutions that contained Cp₂Fe⁺ or Me₂Cp₂Fe⁺. For solutions that contained Cp^{*}₂Fe⁺, MV²⁺, or Cp₂Co⁺, intrinsic or n-type H–Si(111) samples exhibited $\theta_{\text{Si-OCH}_3}$ that was comparable to $\theta_{\text{Si-OCH}_3}$ observed in the dark. The results observed for p-type H–Si(111) surfaces in the light were not statistically different from the results observed in the dark.

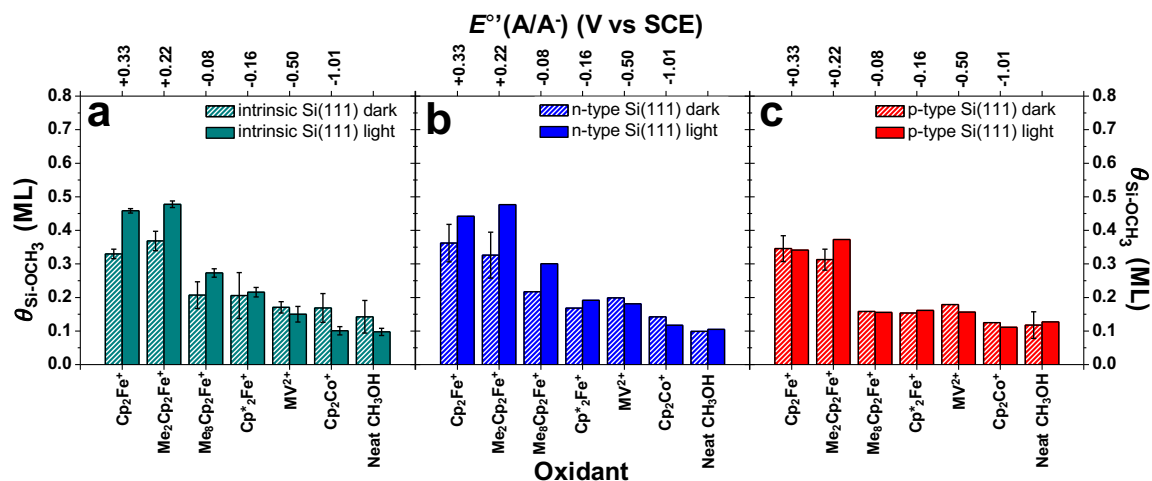


Figure 5.8. Correlation between $\theta_{\text{Si-OCH}_3}$ and the oxidizing conditions used in the reaction of (a) intrinsic, (b) n-type, and (c) p-type H–Si(111) surfaces with CH₃OH in the absence (striped) and presence (solid) of ambient light. Reactions were performed for 5 min in neat CH₃OH or CH₃OH containing 1.0 mM of an oxidant. Experimentally determined formal potentials, $E^\circ(\text{A/A}^-)$, for each oxidant are given above each plot. The values for $\theta_{\text{Si-OCH}_3}$ were determined by TIRS measurements using eqs 5.1 and 5.2. Error bars represent statistical variation across multiple samples, and data points with no error bars represent single measurements.

The intrinsic samples, so called because of their low dopant density, were very lightly n-doped (Figure 5.2), implying that the valence band states are fully occupied in the absence of illumination. The reactivity observed herein indicates that samples having Fermi levels situated positive of (above) the middle of the band gap, that is, intrinsic or n-type samples, were capable of exhibiting an increased rate of methoxylation of H-Si(111) surfaces in the presence of illumination relative to the rate of methoxylation in the dark.

5.3.3 Analysis of F Content on H-Si(111) Surfaces Reacted in CH₃OH Solutions

XPS detected the presence of F on a number of H-Si(111) samples after reaction with CH₃OH in the presence of an oxidant having a F-based counter ion (BF₄⁻). Figure 5.9 presents representative high-resolution XPS data for the F 1s region of an intrinsic H-Si(111) sample exposed to CH₃OH containing Me₂Cp₂Fe⁺BF₄⁻. A photoemission signal at 686.2 eV was ascribed to free F⁻ and a photoemission signal at 687.4 eV was ascribed to BF₄⁻.⁷⁰ The data indicate that a significant fraction of BF₄⁻ counter ion decomposed to yield F⁻ and BF₃, the latter being removed from the surface during rinsing. No residual Fe was detected from the oxidant on the surface, indicating that the observed F⁻ and BF₄⁻ was adsorbed to the surface upon reduction of the Me₂Cp₂Fe⁺ species by the H-Si(111) surface to give neutral Me₂Cp₂Fe.

The results from analysis of the F 1s photoemission data from eq 5.6 are presented in Figure 5.10. F was observed primarily on samples that were reacted with CH₃OH containing Cp₂Fe⁺ or Me₂Cp₂Fe⁺. XPS did not detect F on surfaces reacted with CH₃OH containing (CpCOCH₃)CpFe⁺, which was generated in situ prior to use, or

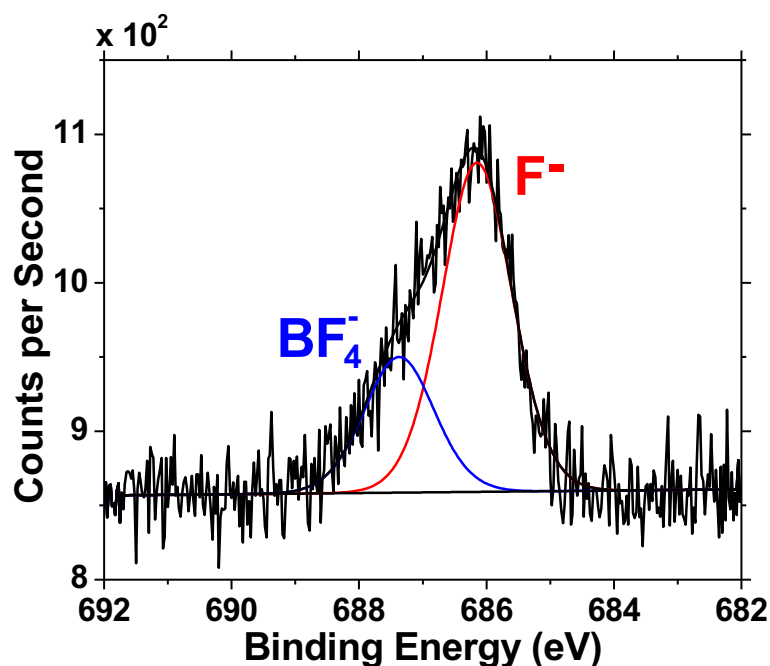


Figure 5.9. High-resolution XPS data for the F 1s region of an intrinsic H-Si(111) sample reacted with CH₃OH containing 1.0 mM Me₂Cp₂Fe⁺BF₄⁻ for 5 min in ambient light. The BF₄⁻ counter ion provided the source of the F detected.

Cp₂Co⁺PF₆⁻. Samples reacted with CH₃OH solutions containing MV²⁺2Cl⁻ did not exhibit detectable Cl by XPS. F was only observed in trace amounts on samples reacted with CH₃OH containing Me₈Cp₂Fe⁺ or Cp*₂Fe⁺, and F was detected more often for these oxidants when the reactions were performed with illumination present. This data indicate that only samples reacted with CH₃OH under conditions that allow for oxidant-mediated methoxylation of the H-Si(111) surface exhibited detectable levels of F on the surface. This provides evidence for the transfer of electrons to Cp₂Fe⁺ or Me₂Cp₂Fe⁺, leaving the BF₄⁻ counter ion associated with a H⁺ from the methoxylation reaction adsorbed to the surface.

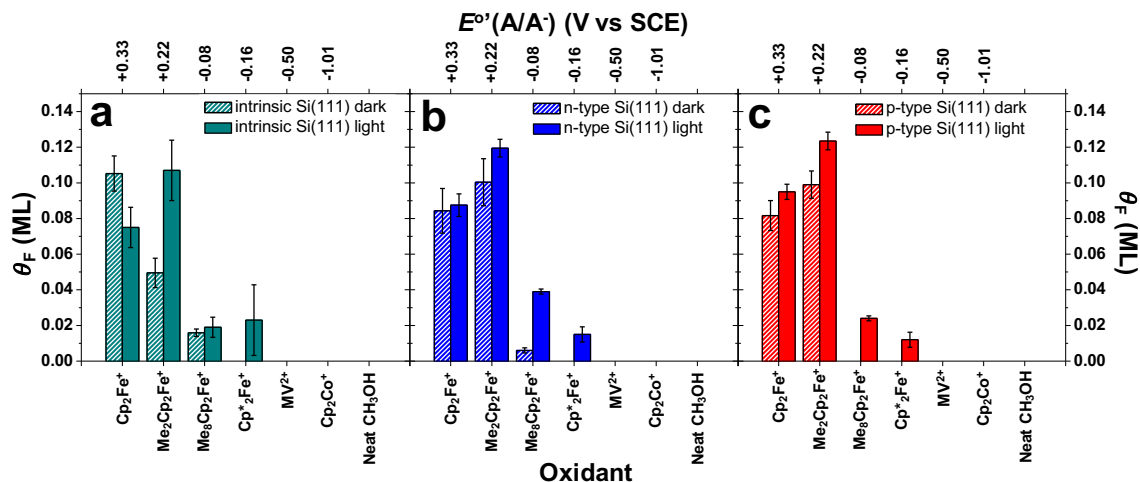


Figure 5.10. Correlation between θ_F and the oxidizing conditions used in the reaction of (a) intrinsic, (b) n-type, and (c) p-type H-Si(111) surfaces with CH₃OH in the absence (striped) and presence (solid) of ambient light. Reactions were performed for 5 min in neat CH₃OH or CH₃OH containing 1.0 mM of an oxidant. Experimentally determined formal potentials, $E^0(A/A)$, for each oxidant are given above each plot. The values for θ_F were determined by XPS measurements using eq 5.6.

5.3.4 Potentiostatic Reaction of H-Si(111) with CH₃OH

The reaction of H-Si(111) with CH₃OH was investigated under applied external bias in the dark as well as under illumination. Figure 5.11 presents J - E data for n-type and p-type H-Si(111) surfaces in contact with CH₃OH solutions that contained 1.0 M LiClO₄ as the supporting electrolyte. In the dark, the methoxylation of n-type H-Si(111) was observed as a gradual increase in current starting near -0.4 V vs SCE, with a peak observed at -0.08 V vs SCE. A gradual decline in current was observed past the peak current, suggesting that the initial rise in current arose from methoxylation of H-Si(111) surfaces. Under illumination, n-type H-Si(111) surfaces showed much higher current density, in addition to a sharp peak centered at -0.17 V vs SCE that is consistently assigned to the methoxylation of H-Si(111) surfaces. At more positive potentials, a rapid

rise in current density was observed beginning at 0 V vs SCE, and was indicative of subsurface oxidation of the Si(111) substrate.

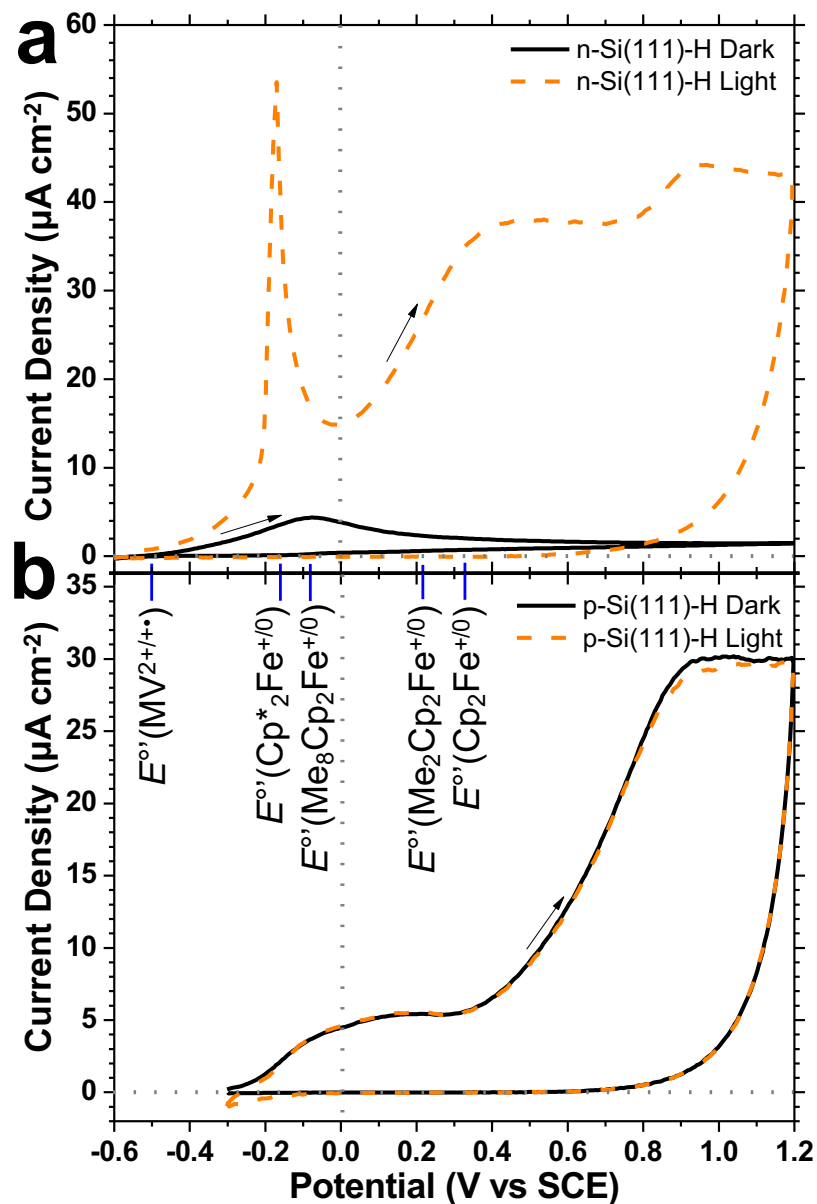


Figure 5.11. J - E behavior of (a) n-type and (b) p-type H-Si(111) samples in contact with CH_3OH solutions containing 1.0 M LiClO_4 as supporting electrolyte. Data collected in the dark (solid black) and under 10 mW cm^{-2} of simulated solar illumination (dashed orange) are shown. The formal potentials of the oxidants used in this work are indicated by the vertical blue lines at the top of panel b.

For p-type H-Si(111), a gradual increase in current density that is consistently assigned to methoxylation was observed near -0.2 V vs SCE. A distinct peak current due to the methoxylation reaction was not observed directly, as the onset of the subsurface oxidation of the H-Si(111) substrate was observed near $+0.4$ V vs SCE. The results indicate that the methoxylation of p-type H-Si(111) samples was not sensitive to illumination, as the dark and light curves in Figure 5.11b overlapped substantially. A second sweep of the n-type and p-type electrodes in Figure 5.11 (not shown) was flat through the region ascribed to potentiostatic methoxylation.

Table 5.1 summarizes the quantification of the current passed for the region assigned to the methoxylation of H-Si(111) surfaces. The quantification of $\theta_{\text{Si-OCH}_3}$ assumed that 2 electrons were passed for the reaction of each surface site with CH_3OH . The $\theta_{\text{Si-OCH}_3}$ resulting from potentiostatic methoxylation of n-type H-Si(111) surfaces in the dark was comparable to $\theta_{\text{Si-OCH}_3}$ obtained from potentiostatic methoxylation of p-type H-Si(111) surfaces in the dark as well as under illumination. In contrast, illuminated n-type H-Si(111) surfaces showed significantly greater anodic current that resulted in higher $\theta_{\text{Si-OCH}_3}$ compared with samples that were methoxylated in the dark.

Table 5.1. Summary of the Quantification for the Potentiostatic Methoxylation of H–Si(111) Surfaces

Dopant Type	Illumination	Potential Range Quantified (V) ^a	$\theta_{\text{Si-OCH}_3}$ (ML) ^b	Potential at Half $\theta_{\text{Si-OCH}_3}$ (V) ^c
n-type	Dark	–0.4 to +0.6	0.22 ± 0.05	0.00 ± 0.07
n-type	10 mW cm ^{–2}	–0.3 to 0	0.39 ± 0.07	$–0.17 \pm 0.05$
p-type	Dark	–0.2 to +0.3	0.23 ± 0.06	$+0.02 \pm 0.04$
p-type	10 mW cm ^{–2}	–0.2 to +0.3	0.20 ± 0.01	$+0.02 \pm 0.06$

^aPotential vs SCE. ^bQuantified based on anodic current passed assuming 2 electrons per surface site that reacts with CH₃OH. ^cPotential vs SCE at which half the charge attributed to the methoxylation of the surface was passed.

The potential at which half of the current ascribed to the methoxylation reaction had been passed ($E_{1/2}$) was determined and is given in Table 5.1. The $E_{1/2}$ observed for multiple samples was observed to be the same within error for n-type samples in the dark and p-type samples in the dark or under illumination. For n-type samples under illumination, $E_{1/2}$ was shifted by $–0.17 \pm 0.05$ V compared with n-type samples in the dark, indicating the presence of a photovoltage at the n-Si interface that produced higher anodic current densities and shifted $E_{1/2}$ to more negative potentials.

5.4. DISCUSSION

5.4.1. Kinetic Description and Mechanism of Oxidant-Activated Methoxylation of H–Si(111) Surfaces

The data reported herein indicate that there are potentially two mechanisms by which the methoxylation of H–Si(111) surfaces can occur. Methoxylation in the absence of an oxidant has been previously postulated to occur by an electron rearrangement that yields H₂ and the methoxylated surface site.²¹ This mechanism (Scheme 5.1) could

conceivably occur by a mechanism in which two electrons undergo transfer from the Si surface to form a H–H bond, which has an ionization energy (15.4 eV)⁷¹ that places the H–H bond state well below the Si valence band maximum. The oxidant-activated methoxylation process has been proposed (Scheme 5.2) to proceed by two consecutive 1-electron transfers¹⁷⁻¹⁸ that could conceivably result in an increased rate of reaction by allowing for a lower activation energy. The two reaction mechanisms occur simultaneously and are not readily isolated. Because the behavior of the oxidant-activated mechanism was found to be dependent on the strength of the oxidants in solution, this discussion aims to develop a kinetic model that describes the behavior of the oxidant-activated methoxylation mechanism that is consistent with the data reported.

An understanding of the surface electronic states native to the H–Si(111) surface provides a foundation for the oxidant-activated methoxylation mechanism. Ultraviolet photoelectron spectroscopy (UPS) indicates that the electrons in the Si–H σ bond on the H–Si(111) surface lie in an occupied electronic surface state having an energy of ~ 5 eV below the Si valence-band maximum.⁷² The electrons in the Si–H σ bond are therefore not directly accessible to the oxidant species or applied external potentials used in this work. Two-photon photoemission (2PPE) spectroscopy has revealed the presence of an occupied surface resonance on H–Si(111) surfaces in vacuum that is centered ~ 0.1 eV below the valence-band maximum.⁷³ Theoretical calculations of the local density of states for H–Si(111) surfaces have additionally identified an occupied electronic state at the $\bar{\Gamma}$ point (center) of the surface Brillouin zone immediately below the valence band maximum.⁷⁴⁻⁷⁵ Upon contact with CH₃OH, hydrogen bonding between the H–Si(111)

surface and the CH₃OH could conceivably increase the electron density at the Si surface and shift the energy of the surface resonance positive into the band gap. Oxidation of this surface resonance by an oxidant in solution or by an applied external potential could initiate the methoxylation reaction by activating the surface Si towards nucleophilic attack by CH₃OH.

Figure 5.12 presents a schematic of n-type and p-type Si interfaced with solutions containing redox species having a Nernstian solution potential of $E(A/A^-)$ with a corresponding energy of $E(A/A^-) = -qE(A/A^-)$. The proposed energy position of the surface resonance, corresponding to the formal oxidation potential of the surface Si, when the Si is in contact with CH₃OH is indicated by $E^{\circ'}(Si^{+/0})$. The placement of $E^{\circ'}(Si^{+/0})$ in the Si band gap is justified by the potentiostatic methoxylation experiments that showed $E_{1/2}$ near 0 V vs SCE. The rate constants for cathodic and anodic charge transfer to and from the valence band are represented as $k_{vb,C}$ and $k_{vb,A}$, respectively, and the rate constants for cathodic and anodic charge transfer from and to the conduction band are represented as $k_{cb,C}$ and $k_{cb,A}$, respectively. Note that, for oxidant-activated methoxylation to occur, cathodic current (loss of an electron from the Si surface to the solution) must dominate the anodic current.

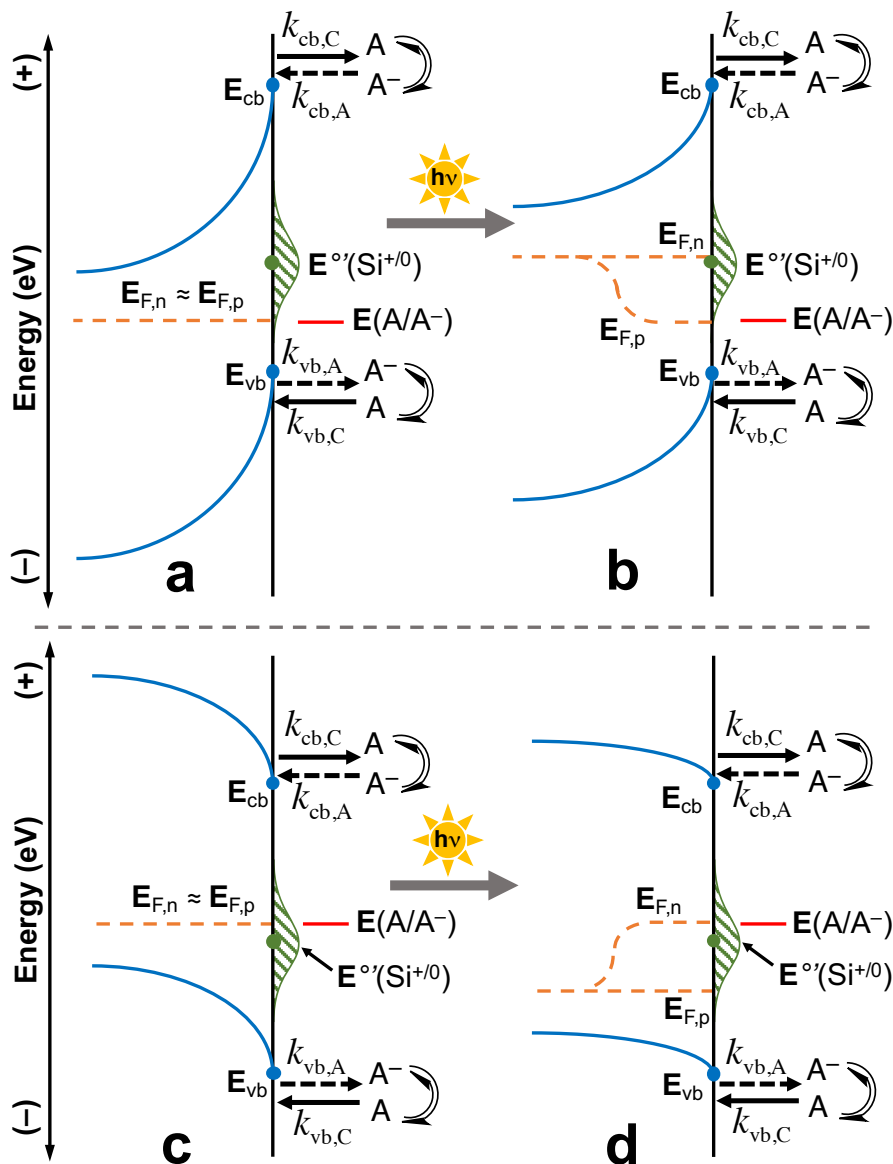


Figure 5.12. Schematic representation of charge transfer across a semiconductor/liquid interface for oxidant-activated methoxylation. The energy positions for the semiconductor valence band (E_{vb}), conduction band (E_{cb}), electron quasi-Fermi level ($E_{F,n}$), hole quasi-Fermi level ($E_{F,p}$), the proposed oxidation energy of the surface Si ($E^{\circ'}(\text{Si}^{+/0})$), and solution energy ($E(\text{A}/\text{A}^-)$) are indicated. The rate constants for cathodic and anodic charge transfer to and from the valence band are $k_{vb,C}$ and $k_{vb,A}$, respectively, and the rate constants for cathodic and anodic charge transfer from and to the conduction band are $k_{cb,C}$ and $k_{cb,A}$, respectively. Solid and dashed arrows indicate cathodic and anodic charge transfer, respectively. Panel a gives the band structure for an n-type contact in the dark, and panel b shows the same contact under illumination. Panel c gives the band structure for a p-type contact in the dark, and panel c shows the same contact under illumination.

The kinetic behavior of the oxidant-activated methoxylation of H-Si(111) surfaces is consistent with the standard kinetic model for charge transfer from a semiconductor to a molecular redox species dissolved in solution. The valence band cathodic current density ($J_{vb,C}$) and anodic current density ($J_{vb,A}$) are described by eqs 5.7 and 5.8, respectively.⁷⁶⁻⁷⁷

$$J_{vb,C} = -qk_{vb,C}[A] \quad (5.7)$$

$$J_{vb,A} = qk_{vb,A}p_s[A^-] \quad (5.8)$$

Here, q is the unsigned elementary charge of an electron, $[A]$ and $[A^-]$ are the concentrations of the molecular oxidant and reductant, respectively, in solution, and p_s is the concentration of holes in the valence band at the surface. Similarly, the conduction band cathodic current density ($J_{cb,C}$) and anodic current density ($J_{cb,A}$) are described by eqs 5.9 and 5.10, respectively.⁷⁶⁻⁷⁷

$$J_{cb,C} = -qk_{cb,C}n_s[A] \quad (5.9)$$

$$J_{cb,A} = qN_A k_{cb,A}[A^-] \quad (5.10)$$

Here, n_s is the concentration of electrons in the conduction band at the surface. The ratios $|J_{vb,C}/J_{vb,A}|$ and $|J_{cb,C}/J_{cb,A}|$ are derived in terms of the quasi-Fermi levels below.

The Nernst equation can be rearranged to yield the relationship given in eq 5.11.

$$\frac{[A]}{[A^-]} = e^{\left(\frac{E^{\circ}(A/A^-) - E(A/A^-)}{k_B T}\right)} \quad (5.11)$$

The formal solution energy is represented as $\mathbf{E}^{\circ\prime}(A/A^-) = -qE^{\circ\prime}(A/A^-)$, the Nernstian solution energy is represented as $\mathbf{E}(A/A^-) = -qE(A/A^-)$, and k_B is the Boltzmann constant, and T is the absolute temperature. The ratio of the cathodic to anodic charge transfer rate constants for the valence band and the conduction band are given in eqs 5.12 and 5.13, respectively.⁷⁸

$$\frac{k_{\text{vb,C}}}{k_{\text{vb,A}}} = N_V e^{\left(\frac{\mathbf{E}_{\text{vb}} - \mathbf{E}^{\circ\prime}(A/A^-)}{k_B T}\right)} \quad (5.12)$$

$$\frac{k_{\text{cb,C}}}{k_{\text{cb,A}}} = \frac{1}{N_C} e^{\left(\frac{\mathbf{E}_{\text{cb}} - \mathbf{E}^{\circ\prime}(A/A^-)}{k_B T}\right)} \quad (5.13)$$

Here, N_V and N_C are the effective densities of states of the valence and conduction bands, respectively, \mathbf{E}_{vb} is the valence band energy, and \mathbf{E}_{cb} is the conduction band energy. Using eqs 5.11–5.13, the general forms for the ratios $|J_{\text{vb,C}}/J_{\text{vb,A}}| = R_{\text{vb}}$ and $|J_{\text{cb,C}}/J_{\text{cb,A}}| = R_{\text{cb}}$ are given in eqs 5.14 and 5.15, respectively.

$$R_{\text{vb}} = \left| \frac{J_{\text{vb,C}}}{J_{\text{vb,A}}} \right| = \frac{N_V}{p_s} e^{\left(\frac{\mathbf{E}_{\text{vb}} - \mathbf{E}^{\circ\prime}(A/A^-)}{k_B T}\right)} \quad (5.14)$$

$$R_{\text{cb}} = \left| \frac{J_{\text{cb,C}}}{J_{\text{cb,A}}} \right| = \frac{n_s}{N_C} e^{\left(\frac{\mathbf{E}_{\text{cb}} - \mathbf{E}^{\circ\prime}(A/A^-)}{k_B T}\right)} \quad (5.15)$$

An increase in R_{vb} or R_{cb} indicates an increase in the cathodic current relative to the anodic current, and $R_{\text{vb}} = R_{\text{cb}} = 1$ occurs at equilibrium.

The hole and electron concentrations at the semiconductor surface are related to the quasi-Fermi level positions according to eqs 5.16 and 5.17, respectively.

$$p_s = N_v e^{\left(\frac{E_{vb} - E_{F,p}}{k_B T}\right)} \quad (5.16)$$

$$n_s = N_C e^{\left(\frac{E_{F,n} - E_{cb}}{k_B T}\right)} \quad (5.17)$$

Substituting eq 5.16 for p_s in eq 5.14 gives R_{vb} in terms of the hole quasi-Fermi level position.

$$R_{vb} = e^{\left(\frac{E_{F,p} - E(A/A^-)}{k_B T}\right)} \quad (5.18)$$

Similarly, substituting eq 5.17 for n_s in eq 5.15 gives R_{cb} in terms of the electron quasi-Fermi level position.

$$R_{cb} = e^{\left(\frac{E_{F,n} - E(A/A^-)}{k_B T}\right)} \quad (5.19)$$

For eqs 5.18 and 5.19, equilibrium is reached when $E_{F,n} = E_{F,p} = E(A/A^-)$. The oxidant-activated methoxylation reaction is proposed to initiate when two conditions are met: (1) the net cathodic current (transfer of electrons from the semiconductor to the solution) dominates the anodic current, and (2) the holes in the valence band are sufficiently oxidizing that the valence band can oxidize the surface resonance (i.e. $E_{F,p} < E^{\circ}(\text{Si}^{+/0})$). Eq 5.18 shows that the valence band cathodic current dominates the anodic current ($R_{vb} > 1$) when $E_{F,p} > E(A/A^-)$, and eq 5.19 shows that the conduction band cathodic current outweighs the anodic current ($R_{cb} > 1$) when $E_{F,n} > E(A/A^-)$.

Figure 5.12a and 5.12c depict an n-type and p-type Si samples, respectively, in the dark in contact with a redox species providing a solution energy in the Si band gap. In both cases, the system is at equilibrium, with no net charge passing in either direction. As

$E(A/A^-)$ moves more oxidizing and approaches E_{vb} , the capacity of the dopant atoms in the solid to equilibrate the surface Fermi levels with the solution is diminished and $E_{F,n}$ and $E_{F,p}$ fall out of equilibrium with $E(A/A^-)$. With $E_{F,n}$ and $E_{F,p} > E(A/A^-)$, R_{vb} and R_{cb} increase exponentially, and cathodic current dominates the anodic current at the interface. Additionally, with $E_{F,p}$ falling below $E^{\circ}(\text{Si}^{+/0})$, the holes in the valence band are able to oxidize the Si surface and initiate the methoxylation reaction.

In the case of $(\text{CpCOCH}_3)\text{CpFe}^{+/0}$, the oxidized/reduced ratio was 1:9, yielding a Nernstian solution potential $E((\text{CpCOCH}_3)\text{CpFe}^{+/0}) = +0.54 \text{ V vs SCE}$, placing the solution potential positive of (below) the E_{vb} . All other oxidants were present without deliberately added reductant, and the corresponding Nernstian solution potentials were shifted positive of the formal potentials in Figure 5.2. Assuming that the reduced species were present as contaminants with an oxidized/reduced ratio near 1000:1, the Nernstian solution potentials were shifted positive by $\sim 0.2 \text{ V}$. This places $-qE(\text{Me}_2\text{Cp}_2\text{Fe}^{+/0})$, $-qE(\text{Cp}_2\text{Fe}^{+/0})$, and $-qE((\text{CpCOCH}_3)\text{CpFe}^{+/0})$ at or below E_{vb} , for which $E_{F,n}$ and $E_{F,p} > E(A/A^-)$, with the less oxidizing species having $E(A/A^-)$ positive of (above) E_{vb} . As the differences $E_{F,n} - E(A/A^-)$ and $E_{F,p} - E(A/A^-)$ grow more positive, R_{vb} and R_{cb} increase exponentially, which is consistent with the abrupt change in behavior observed in Figure 5.4. The exponential increase in cathodic current could quickly become limited by diffusion in solution, resulting in the similar rates observed for $\text{Me}_2\text{Cp}_2\text{Fe}^{+/0}$, $\text{Cp}_2\text{Fe}^{+/0}$, and $(\text{CpCOCH}_3)\text{CpFe}^{+/0}$. The experimental results in the dark presented in Figure 5.4 are consistent with the charge transfer model in Figure 5.12a and 5.12c, where charge transfer equilibrium is maintained for n-type and p-type samples until $E(A/A^-) \leq E_{vb}$.

Under illumination, n-type samples exhibit a photovoltage that results from quasi-Fermi level splitting at the interface, as depicted in Figure 5.12b. For a sample with substantial band bending at the interface, n_s is substantially depleted such that illumination pushes the electron quasi-Fermi level positive of $\mathbf{E}(A/A^-)$, while the hole quasi-Fermi level remains equilibrated with $\mathbf{E}(A/A^-)$. For n-type samples, R_{vb} remains at equilibrium, while R_{cb} increases exponentially with the difference $\mathbf{E}_{F,n} - \mathbf{E}(A/A^-)$, allowing cathodic charge transfer to occur from the conduction band to solution. With $R_{cb} > 1$ at illuminated n-type interfaces, oxidant-activated methoxylation can occur at more positive $\mathbf{E}(A/A^-)$ than was observed in the dark, given that $\mathbf{E}_{F,p} < \mathbf{E}^{\circ}(\text{Si}^{+/0})$, as shown in Figure 5.12b. The increase in the reactivity of illuminated intrinsic and n-type H-Si(111) surfaces toward CH_3OH solutions containing $\text{Me}_8\text{Cp}_2\text{Fe}^+$ compared with the reactivity in the dark (Figure 5.8a and 5.8b) is in agreement with the charge transfer model developed here.

Illuminated p-type samples, which have depleted p_s at the interface, exhibit an a decrease in $\mathbf{E}_{F,p}$ relative to $\mathbf{E}(A/A^-)$, which remains equilibrated with $\mathbf{E}_{F,p}$, as shown in Figure 5.12d. The decrease in $\mathbf{E}_{F,p}$ results in $R_{vb} < 1$, and anodic current dominates in the valence band. This increase in anodic current could yield a reduction in the rate of oxidant-activated methoxylation, though this effect would be masked by the baseline rate of methoxylation that occurs in the absence of any oxidant species. The current in the conduction band remains at equilibrium ($R_{cb} = 1$), indicating that illumination of p-type samples does not result in an increase in the cathodic current necessary to drive the oxidant-activated methoxylation reaction. The data presented in Figure 5.8c are in

agreement with the conclusions of the charge transfer model for p-type samples under illumination because the rate of methoxylation of p-type samples was found to be independent of illumination.

5.4.2. Kinetic Description and Mechanism of the Potentiostatic Methoxylation of H-Si(111) Surfaces

The potentiostatic methoxylation reaction performed in this work was performed in the absence of a well-defined 1-electron acceptor species in solution. The anodic current passed (Figure 5.11) during the methoxylation process is assumed to result in oxidation of the Si lattice. Therefore, all current passed resulted from oxidation or reduction of either the surface of the Si electrode or the CH₃OH in solution. Figure 5.13 depicts the energetics at n-type and p-type surfaces electrically connected to a potentiostat in the dark and under illumination.

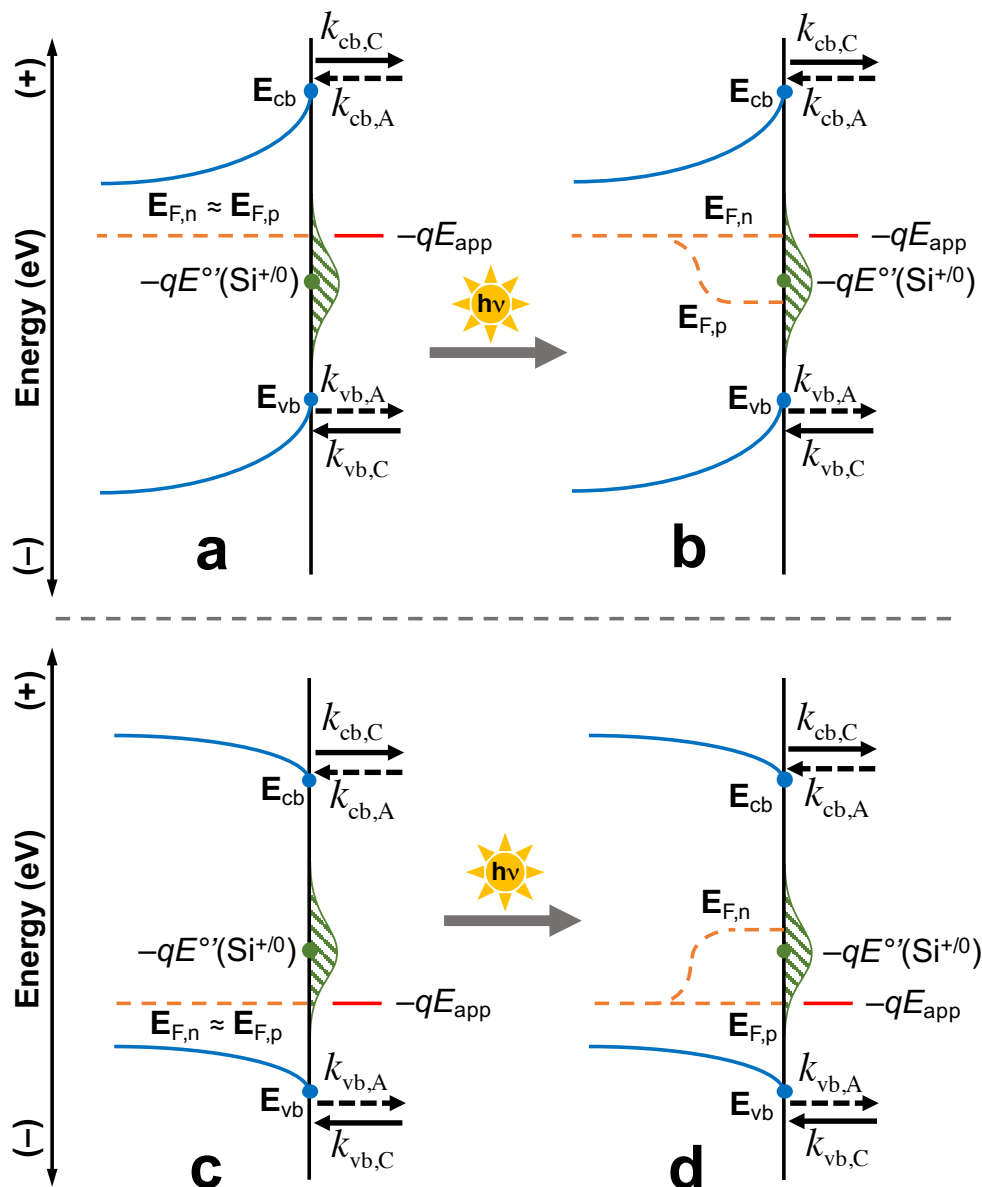


Figure 5.13. Schematic representation of charge transfer across a semiconductor/liquid interface for potentiostatic methoxylation. The energy positions for the semiconductor valence band (E_{vb}), conduction band (E_{cb}), electron quasi-Fermi level ($E_{F,n}$), hole quasi-Fermi level ($E_{F,p}$), the proposed oxidation energy of the surface Si ($-qE^{\circ}(\text{Si}^{+/0})$), and solution energy ($-qE(A/A^-)$) are indicated. The rate constants for cathodic and anodic charge transfer to and from the valence band are $k_{vb,C}$ and $k_{vb,A}$, respectively, and the rate constants for cathodic and anodic charge transfer from and to the conduction band are $k_{cb,C}$ and $k_{cb,A}$, respectively. Solid and dashed arrows indicate cathodic and anodic charge transfer, respectively. Panel a gives the band structure for an n-type contact in the dark, and panel b shows the same contact under illumination. Panel c gives the band structure for a p-type contact in the dark, and panel c shows the same contact under illumination.

For potentiostatic methoxylation, the electronic states that can accept anodic charge are assumed to be in the Si lattice, and the positions of the quasi-Fermi levels relative to $-qE(\text{Si}^{+/0})$ determines the rate of oxidation at the interface. The surface can be oxidized and activated towards reaction with CH_3OH when $\mathbf{E}_{\text{F,n}}$ or $\mathbf{E}_{\text{F,p}}$ fall at more negative energy than $-qE(\text{Si}^{+/0})$. For the potentiostatic reaction, $[\text{A}]$ and $[\text{A}^-]$ from eqs 5.7–5.10 are fixed at equal concentrations, and so do not factor into the charge transfer equilibrium. Following a derivation similar to that used to arrive at eqs 5.18 and 5.19, the charge transfer equilibrium for potentiostatic methoxylation can be expressed as

$$R_{\text{vb}} = e^{\left(\frac{\mathbf{E}_{\text{F,p}} - (-qE(\text{Si}^{+/0}))}{k_{\text{B}}T} \right)} \quad (5.20)$$

$$R_{\text{cb}} = e^{\left(\frac{\mathbf{E}_{\text{F,n}} - (-qE(\text{Si}^{+/0}))}{k_{\text{B}}T} \right)} \quad (5.21)$$

where $-qE(\text{Si}^{+/0})$ is the formal oxidation energy for the Si surface, equivalent to $\mathbf{E}(\text{Si}^{+/0})$.

The data presented in Figure 5.11 for the dark potentiostatic methoxylation of H–Si(111) surfaces shows that, while the onset potential for potentiostatic methoxylation was more negative for n-type samples than for p-type samples, the potential at which half of the current ascribed to methoxylation had passed ($E_{1/2}$) was near 0 V vs SCE for both dopant densities. Assuming that each surface site can be treated separately, this potential represents the formal oxidation potential of the surface. In order to oxidize the surface, $\mathbf{E}_{\text{F,p}}$ or $\mathbf{E}_{\text{F,n}}$ must lie lower in energy than $\mathbf{E}(\text{Si}^{+/0})$, such that anodic current at the interface dominates the cathodic current.

For n-type and p-type samples in the dark (Figure 5.13a and 5.13c), the band bending at the interface is controlled by the potential applied at the back of the electrode, and the quasi-Fermi levels are assumed to be equilibrated. For $-qE_{\text{app}} > \mathbf{E}(\text{Si}^{+/0})$, the quasi-Fermi levels are positioned higher in energy than the energy required to oxidize a surface state, and, by eqs 5.20 and 5.21, cathodic current dominates the anodic current from both bands. Here, cathodic current does not affect the rate of methoxylation because the methoxylation reaction is only activated by anodic current. As $-qE_{\text{app}}$ decreases, the quasi-Fermi levels at the surface fall low enough in energy that $R_{\text{vb}} < 1$ and $R_{\text{cb}} < 1$, and the anodic current dominates the cathodic current. Thus, for the conditions $\mathbf{E}_{\text{F,n}} < \mathbf{E}(\text{Si}^{+/0})$ and $\mathbf{E}_{\text{F,p}} < \mathbf{E}(\text{Si}^{+/0})$, the methoxylation reaction proceeds at the surface. This model agrees with the data presented in Figure 5.11 because the J - E behavior showed an increase in anodic current as $-qE_{\text{app}}$ approached $\mathbf{E}(\text{Si}^{+/0})$ and both n-type and p-type samples exhibited similar $E_{1/2}$ in the dark.

Illuminated n-type samples (Figure 5.13b) exhibit quasi-Fermi level splitting. Here, $-qE_{\text{app}}$ controls the band bending at the interface, and, therefore, is aligned with the majority carrier quasi-Fermi level. Illumination of n-type samples generally results in an increase in p_{s} , which is dependent on the barrier height, that lowers $\mathbf{E}_{\text{F,p}}$ at the interface. Because the methoxylation reaction is activated by anodic current flow at the interface, the decrease in $\mathbf{E}_{\text{F,p}}$ upon illumination of n-type interfaces allows the methoxylation reaction to occur at more negative E_{app} . This was observed for illuminated n-type samples as a negative shift in $E_{1/2}$ relative to samples methoxylated in the dark (Table 5.1). Illuminated n-type samples also exhibited nearly double the $\theta_{\text{Si-OCH}_3}$ and a significantly

sharper anodic peak ascribed to the methoxylation reaction than samples reacted in dark. These results support the charge transfer model outlined herein, which predicts an increase in anodic current that drives the methoxylation reaction by eq 5.20 ($R_{vb} < 1$) at illuminated n-type interfaces.

The schematic representation of the energetics at the interface of p-type samples is given in Figure 5.13d. Under illumination, n_s increases and pushes $E_{F,n}$ positive of $E_{F,p}$, which remains aligned with $-qE_{app}$, resulting in an increase in cathodic current at the interface (R_{cb} increases). The anodic current from the valence band, however, remains the same for a given $-qE_{app}$, resulting in oxidative addition of CH_3OH to the Si surface. The experimental results showed no significant dependence of the potentiostatic methoxylation of p-type H-Si(111) surfaces on the presence of illumination. This suggests that the position of $E_{F,p}$ relative to $E(Si^{+/0})$ determines $E_{1/2}$ for the potentiostatic methoxylation reaction. This additionally suggests that an increase in R_{cb} by a more positive $E_{F,n}$ at illuminated p-type interfaces does not effect the rate of methoxylation, possibly because the electronic states on the surface that are oxidized by $E_{F,p}$ cannot be further reduced by a more positive $E_{F,n}$.

5.5. CONCLUSIONS

The reaction of H-Si(111) surfaces with CH_3OH was investigated in the absence or presence of a molecular oxidant and in the absence or presence of illumination. The oxidant-activated methoxylation of H-Si(111) surfaces in the dark proceeded in the presence of oxidants that provided a solution energy, $E(A/A^-)$, at or below the valence band maximum, E_{vb} . Under ambient illumination, the oxidant-activated methoxylation of

intrinsic and n-type H–Si(111) surfaces exhibited increased reactivity and allowed for oxidants that did not perform oxidant-activated methoxylation in the dark to impart an increased rate of methoxylation in the light. A conventional kinetic framework that predicts an exponential increase in the methoxylation rate as $E(A/A^-)$ moves negative of E_{vb} and the observed behavior under illumination was consistent with the results reported herein. Potentiostatic methoxylation in the dark revealed that the formal oxidation potential of the Si surface, $E^{\circ'}(Si^{+/0})$ was approximately 0 V vs SCE, falling near the middle of the band gap. Illumination of n-type H–Si(111) surfaces exposed to CH_3OH under applied external bias resulted in an increase in the anodic current density and a negative shift in $E_{1/2}$, while p-type H–Si(111) surfaces exposed to CH_3OH under applied external bias were unaffected by the presence of illumination.

The unique reactivity of H–Si(111) surfaces toward CH_3OH not observed for small molecules appears to arise from the narrow band gap of crystalline Si and the capacity of the crystal lattice to form an electric field at the interface that can favor charge transfer in the desired direction. Molecular systems do not have the necessary density of electronic states to perform the oxidant-activated methoxylation reaction for the oxidants used herein. The results presented herein provide a basis for a general mechanistic framework to understand the process by which nucleophiles can undergo reaction with H–Si(111) surfaces in the presence or absence of an oxidant and/or an illumination source.

5.6 REFERENCES

1. Peng, W.; Rupich, S. M.; Shafiq, N.; Gartstein, Y. N.; Malko, A. V.; Chabal, Y. J. Silicon Surface Modification and Characterization for Emergent Photovoltaic Applications Based on Energy Transfer. *Chem. Rev.* **2015**, *115*, 12764-12796.
2. Smith, W. A.; Sharp, I. D.; Strandwitz, N. C.; Bisquert, J. Interfacial Band-Edge Energetics for Solar Fuels Production. *Energy Environ. Sci.* **2015**, *8*, 2851-2862.
3. Buriak, J. M. Illuminating Silicon Surface Hydrosilylation: An Unexpected Plurality of Mechanisms. *Chem. Mater.* **2014**, *26*, 763-772.
4. Huck, L. A.; Buriak, J. M. UV-Initiated Hydrosilylation on Hydrogen-Terminated Silicon (111): Rate Coefficient Increase of Two Orders of Magnitude in the Presence of Aromatic Electron Acceptors. *Langmuir* **2012**, *28*, 16285-16293.
5. G. Robins, E.; P. Stewart, M.; M. Buriak, J. Anodic and Cathodic Electrografting of Alkynes on Porous Silicon. *Chem. Commun.* **1999**, 2479-2480.
6. Ciampi, S.; Böcking, T.; Kilian, K. A.; James, M.; Harper, J. B.; Gooding, J. J. Functionalization of Acetylene-Terminated Monolayers on Si(100) Surfaces: A Click Chemistry Approach. *Langmuir* **2007**, *23*, 9320-9329.
7. Dai, M.; Wang, Y.; Kwon, J.; Halls, M. D.; Chabal, Y. J. Nitrogen Interaction with Hydrogen-Terminated Silicon Surfaces at the Atomic Scale. *Nat. Mater.* **2009**, *8*, 825-830.
8. Tian, F.; Teplyakov, A. V. Silicon Surface Functionalization Targeting Si-N Linkages. *Langmuir* **2013**, *29*, 13-28.
9. Tian, F.; Taber, D. F.; Teplyakov, A. V. -NH- Termination of the Si(111) Surface by Wet Chemistry. *J. Am. Chem. Soc.* **2011**, *133*, 20769-20777.

10. Chopra, T. P.; Longo, R. C.; Cho, K.; Chabal, Y. J. Ammonia Modification of Oxide-Free Si(111) Surfaces. *Surf. Sci.* **2016**, *650*, 285-294.
11. Chopra, T. P.; Longo, R. C.; Cho, K.; Halls, M. D.; Thissen, P.; Chabal, Y. J. Ethylenediamine Grafting on Oxide-Free H-, 1/3 ML F-, and Cl-Terminated Si(111) Surfaces. *Chem. Mater.* **2015**, *27*, 6268-6281.
12. Buriak, J. M.; Sikder, M. D. H. From Molecules to Surfaces: Radical-Based Mechanisms of Si-S and Si-Se Bond Formation on Silicon. *J. Am. Chem. Soc.* **2015**, *137*, 9730-9738.
13. Hu, M.; Liu, F.; Buriak, J. M. Expanding the Repertoire of Molecular Linkages to Silicon: Si-S, Si-Se, and Si-Te Bonds. *ACS Appl. Mater. Inter.* **2016**, *8*, 11091-11099.
14. Yamada, T.; Shirasaka, K.; Noto, M.; Kato, H. S.; Kawai, M. Adsorption of Unsaturated Hydrocarbon Moieties on H:Si(111) by Grignard Reaction. *J. Phys. Chem. B* **2006**, *110*, 7357-7366.
15. Boukherroub, R.; Morin, S.; Bensebaa, F.; Wayner, D. D. M. New Synthetic Routes to Alkyl Monolayers on the Si(111) Surface. *Langmuir* **1999**, *15*, 3831-3835.
16. Cleland, G.; Horrocks, B. R.; Houlton, A. Direct Functionalization of Silicon via the Self-Assembly of Alcohols. *J. Chem. Soc., Faraday Trans.* **1995**, *91*, 4001-4003.
17. Haber, J. A.; Lauermann, I.; Michalak, D.; Vaid, T. P.; Lewis, N. S. Electrochemical and Electrical Behavior of (111)-Oriented Si Surfaces Alkoxylated through Oxidative Activation of Si-H Bonds. *J. Phys. Chem. B* **2000**, *104*, 9947-9950.
18. Haber, J. A.; Lewis, N. S. Infrared and X-ray Photoelectron Spectroscopic Studies of the Reactions of Hydrogen-Terminated Crystalline Si(111) and Si(100) Surfaces with Br₂, I₂, and Ferrocenium in Alcohol Solvents. *J. Phys. Chem. B* **2002**, *106*, 3639-3656.

19. Michalak, D. J.; Amy, S. R.; Aureau, D.; Dai, M.; Esteve, A.; Chabal, Y. J. Nanopatterning Si(111) Surfaces as a Selective Surface-Chemistry Route. *Nat. Mater.* **2010**, *9*, 266-271.
20. Michalak, D. J.; Amy, S. R.; Estève, A.; Chabal, Y. J. Investigation of the Chemical Purity of Silicon Surfaces Reacted with Liquid Methanol. *J. Phys. Chem. C* **2008**, *112*, 11907-11919.
21. Michalak, D. J.; Rivillon, S.; Chabal, Y. J.; Estève, A.; Lewis, N. S. Infrared Spectroscopic Investigation of the Reaction of Hydrogen-Terminated, (111)-Oriented, Silicon Surfaces with Liquid Methanol. *J. Phys. Chem. B* **2006**, *110*, 20426-20434.
22. Dusciac, D.; Chazalviel, J.-N.; Ozanam, F.; Allongue, P.; de Villeneuve, C. H. Thermal Stability of Alkoxy Monolayers Grafted on Si(111). *Surf. Sci.* **2007**, *601*, 3961-3964.
23. Boukherroub, R.; Morin, S.; Sharpe, P.; Wayner, D. D. M.; Allongue, P. Insights into the Formation Mechanisms of Si-OR Monolayers from the Thermal Reactions of Alcohols and Aldehydes with Si(111)-H. *Langmuir* **2000**, *16*, 7429-7434.
24. Thissen, P.; Fuchs, E.; Roodenko, K.; Peixoto, T.; Batchelor, B.; Smith, D.; Schmidt, W. G.; Chabal, Y. Nanopatterning on H-Terminated Si(111) Explained as Dynamic Equilibrium of the Chemical Reaction with Methanol. *J. Phys. Chem. C* **2015**, *119*, 16947-16953.
25. Khung, Y. L.; Ngali, S. H.; Meda, L.; Narducci, D. Preferential Formation of Si-O-C over Si-C Linkage upon Thermal Grafting on Hydrogen-Terminated Silicon (111). *Chemistry – A European Journal* **2014**, *20*, 15151-15158.

26. Perrine, K. A.; Lin, J.-M.; Teplyakov, A. V. Controlling the Formation of Metallic Nanoparticles on Functionalized Silicon Surfaces. *J. Phys. Chem. C* **2012**, *116*, 14431-14444.
27. Aureau, D.; Varin, Y.; Roodenko, K.; Seitz, O.; Pluchery, O.; Chabal, Y. J. Controlled Deposition of Gold Nanoparticles on Well-Defined Organic Monolayer Grafted on Silicon Surfaces. *J. Phys. Chem. C* **2010**, *114*, 14180-14186.
28. Maldonado, S.; Knapp, D.; Lewis, N. S. Near-Ideal Photodiodes from Sintered Gold Nanoparticle Films on Methyl-Terminated Si(111) Surfaces. *J. Am. Chem. Soc.* **2008**, *130*, 3300-3301.
29. Nguyen, H. M.; Seitz, O.; Aureau, D.; Sra, A.; Nijem, N.; Gartstein, Y. N.; Chabal, Y. J.; Malko, A. V. Spectroscopic Evidence for Nonradiative Energy Transfer between Colloidal CdSe/ZnS Nanocrystals and Functionalized Silicon Substrates. *Appl. Phys. Lett.* **2011**, *98*, 161904.
30. Khatri, O. P.; Ichii, T.; Murase, K.; Sugimura, H. UV Induced Covalent Assembly of Gold Nanoparticles in Linear Patterns on Oxide Free Silicon Surface. *J. Mater. Chem.* **2012**, *22*, 16546-16551.
31. Caillard, L.; Seitz, O.; Campbell, P. M.; Doherty, R. P.; Lamic-Humblot, A.-F.; Lacaze, E.; Chabal, Y. J.; Pluchery, O. Gold Nanoparticles on Oxide-Free Silicon–Molecule Interface for Single Electron Transport. *Langmuir* **2013**, *29*, 5066-5073.
32. O’Leary, L. E.; Strandwitz, N. C.; Roske, C. W.; Pyo, S.; Brunshwig, B. S.; Lewis, N. S. Use of Mixed CH₃–/HC(O)CH₂CH₂–Si(111) Functionality to Control Interfacial Chemical and Electronic Properties During the Atomic-Layer Deposition of Ultrathin Oxides on Si(111). *J. Phys. Chem. Lett.* **2015**, *6*, 722-726.

33. Li, M.; Dai, M.; Chabal, Y. J. Atomic Layer Deposition of Aluminum Oxide on Carboxylic Acid-Terminated Self-Assembled Monolayers. *Langmuir* **2009**, *25*, 1911-1914.
34. Peng, W.; Seitz, O.; Chapman, R. A.; Vogel, E. M.; Chabal, Y. J. Probing the Intrinsic Electrical Properties of Thin Organic Layers/Semiconductor Interfaces using an Atomic-Layer-Deposited Al₂O₃ Protective Layer. *Appl. Phys. Lett.* **2012**, *101*, 051605.
35. Peng, W.; DeBenedetti, W. J. I.; Kim, S.; Hines, M. A.; Chabal, Y. J. Lowering the Density of Electronic Defects on Organic-Functionalized Si(100) Surfaces. *Appl. Phys. Lett.* **2014**, *104*, 241601.
36. Bruce, J. P.; Oliver, D. R.; Lewis, N. S.; Freund, M. S. Electrical Characteristics of the Junction between PEDOT:PSS and Thiophene-Functionalized Silicon Microwires. *ACS Appl. Mater. Inter.* **2015**, *7*, 27160-27166.
37. Giesbrecht, P. K.; Bruce, J. P.; Freund, M. S. Electric and Photoelectric Properties of 3,4-Ethylenedioxythiophene-Functionalized n-Si/PEDOT:PSS Junctions. *ChemSusChem* **2016**, *9*, 109-117.
38. Sailor, M. J.; Klavetter, F. L.; Grubbs, R. H.; Lewis, N. S. Electronic Properties of Junctions between Silicon and Organic Conducting Polymers. *Nature* **1990**, *346*, 155-157.
39. Gallant, B. M.; Gu, X. W.; Chen, D. Z.; Greer, J. R.; Lewis, N. S. Tailoring of Interfacial Mechanical Shear Strength by Surface Chemical Modification of Silicon Microwires Embedded in Nafion Membranes. *ACS Nano* **2015**, *9*, 5143-5153.

40. Zhang, F.; Liu, D.; Zhang, Y.; Wei, H.; Song, T.; Sun, B. Methyl/Allyl Monolayer on Silicon: Efficient Surface Passivation for Silicon-Conjugated Polymer Hybrid Solar Cell. *ACS Appl. Mater. Inter.* **2013**, *5*, 4678-4684.
41. Cho, C. J.; O'Leary, L.; Lewis, N. S.; Greer, J. R. In Situ Nanomechanical Measurements of Interfacial Strength in Membrane-Embedded Chemically Functionalized Si Microwires for Flexible Solar Cells. *Nano Lett.* **2012**, *12*, 3296-3301.
42. Fabre, B. Functionalization of Oxide-Free Silicon Surfaces with Redox-Active Assemblies. *Chem. Rev.* **2016**, *116*, 4808-4849.
43. Lattimer, J. R. C.; Blakemore, J. D.; Sattler, W.; Gul, S.; Chatterjee, R.; Yachandra, V. K.; Yano, J.; Brunshwig, B. S.; Lewis, N. S.; Gray, H. B. Assembly, Characterization, and Electrochemical Properties of Immobilized Metal Bipyridyl Complexes on Silicon(111) Surfaces. *Dalton Trans.* **2014**, *43*, 15004-15012.
44. Lattimer, J. R. C.; Brunshwig, B. S.; Lewis, N. S.; Gray, H. B. Redox Properties of Mixed Methyl/Vinylferrocenyl Monolayers on Si(111) Surfaces. *J. Phys. Chem. C* **2013**, *117*, 27012-27022.
45. Kang, O. S.; Bruce, J. P.; Herbert, D. E.; Freund, M. S. Covalent Attachment of Ferrocene to Silicon Microwire Arrays. *ACS Appl. Mater. Inter.* **2015**, *7*, 26959-26967.
46. O'Leary, L. E.; Rose, M. J.; Ding, T. X.; Johansson, E.; Brunshwig, B. S.; Lewis, N. S. Heck Coupling of Olefins to Mixed Methyl/Thienyl Monolayers on Si(111) Surfaces. *J. Am. Chem. Soc.* **2013**, *135*, 10081-10090.
47. Yzambart, G.; Fabre, B.; Roisnel, T.; Dorcet, V.; Ababou-Girard, S.; Meriadec, C.; Lorcy, D. Assembly of Platinum Diimine Dithiolate Complexes onto Hydrogen-Terminated Silicon Surfaces. *Organometallics* **2014**, *33*, 4766-4776.

48. Seo, J.; Pekarek, R. T.; Rose, M. J. Photoelectrochemical Operation of a Surface-Bound, Nickel-Phosphine H₂ Evolution Catalyst on p-Si(111): A Molecular Semiconductor|Catalyst Construct. *Chem. Commun.* **2015**, *51*, 13264-13267.
49. Fabre, B.; Cordier, S.; Molard, Y.; Perrin, C.; Ababou-Girard, S.; Godet, C. Electrochemical and Charge Transport Behavior of Molybdenum-Based Metallic Cluster Layers Immobilized on Modified n- and p-Type Si(111) Surfaces. *J. Phys. Chem. C* **2009**, *113*, 17437-17446.
50. Ciampi, S.; Luais, E.; James, M.; Choudhury, M. H.; Darwish, N. A.; Gooding, J. J. The Rapid Formation of Functional Monolayers on Silicon under Mild Conditions. *Phys. Chem. Chem. Phys.* **2014**, *16*, 8003-8011.
51. Sun, Q.-Y.; de Smet, L. C. P. M.; van Lagen, B.; Giesbers, M.; Thüne, P. C.; van Engelenburg, J.; de Wolf, F. A.; Zuilhof, H.; Sudhölter, E. J. R. Covalently Attached Monolayers on Crystalline Hydrogen-Terminated Silicon: Extremely Mild Attachment by Visible Light. *J. Am. Chem. Soc.* **2005**, *127*, 2514-2523.
52. Wayner, D. D. M.; Wolkow, R. A. Organic Modification of Hydrogen Terminated Silicon Surfaces. *Journal of the Chemical Society, Perkin Transactions 2* **2002**, 23-34.
53. Rosenbluth, M. L.; Lieber, C. M.; Lewis, N. S. 630-mV Open Circuit Voltage, 12% Efficient n-Si Liquid Junction. *Appl. Phys. Lett.* **1984**, *45*, 423-425.
54. Gibbons, J. F.; Cogan, G. W.; Gronet, C. M.; Lewis, N. S. A 14% efficient nonaqueous semiconductor/liquid junction solar cell. *Appl. Phys. Lett.* **1984**, *45*, 1095-1097.
55. Michalak, D. J.; Lewis, N. S. Use of Near-Surface Channel Conductance and Differential Capacitance versus Potential Measurements to Correlate Inversion Layer

- Formation with Low Effective Surface Recombination Velocities at n-Si/Liquid Contacts. *Appl. Phys. Lett.* **2002**, *80*, 4458-4460.
56. Gstrein, F.; Michalak, D. J.; Royea, W. J.; Lewis, N. S. Effects of Interfacial Energetics on the Effective Surface Recombination Velocity of Si/Liquid Contacts. *J. Phys. Chem. B* **2002**, *106*, 2950-2961.
57. Royea, W. J.; Michalak, D. J.; Lewis, N. S. Role of Inversion Layer Formation in Producing Low Effective Surface Recombination Velocities at Si/Liquid Contacts. *Appl. Phys. Lett.* **2000**, *77*, 2566-2568.
58. Chazalviel, J. N. Surface Methoxylation as the Key Factor for the Good Performance of n-Si/Methanol Photoelectrochemical Cells. *Journal of Electroanalytical Chemistry and Interfacial Electrochemistry* **1987**, *233*, 37-48.
59. Rijksen, B.; van Lagen, B.; Zuilhof, H. Mimicking the Silicon Surface: Reactivity of Silyl Radical Cations toward Nucleophiles. *J. Am. Chem. Soc.* **2011**, *133*, 4998-5008.
60. Giese, B.; Dickhaut, J.; Chatgililoglu, C., Tris(trimethylsilyl)silane. In *Encyclopedia of Reagents for Organic Synthesis*, John Wiley & Sons, Ltd: 2001.
61. Kim, N. Y.; Laibinis, P. E. Thermal Derivatization of Porous Silicon with Alcohols. *J. Am. Chem. Soc.* **1997**, *119*, 2297-2298.
62. Skibinski, E. S.; DeBenedetti, W. J. I.; Rupich, S. M.; Chabal, Y. J.; Hines, M. A. Frustrated Etching during H/Si(111) Methoxylation Produces Fissured Fluorinated Surfaces, Whereas Direct Fluorination Preserves the Atomically Flat Morphology. *J. Phys. Chem. C* **2015**, *119*, 26029-26037.
63. Hunger, R.; Fritsche, R.; Jaeckel, B.; Jaegermann, W.; Webb, L. J.; Lewis, N. S. Chemical and Electronic Characterization of Methyl-Terminated Si(111) Surfaces by

- High-Resolution Synchrotron Photoelectron Spectroscopy. *Phys. Rev. B* **2005**, *72*, 045317.
64. Hendrickson, D. N.; Sohn, Y. S.; Gray, H. B. Magnetic Susceptibility Study of Various Ferricenium and Iron(III) Dicarbolide Compounds. *Inorg. Chem.* **1971**, *10*, 1559-1563.
65. Grimm, R. L.; Bierman, M. J.; O'Leary, L. E.; Strandwitz, N. C.; Brunshwig, B. S.; Lewis, N. S. Comparison of the Photoelectrochemical Behavior of H-Terminated and Methyl-Terminated Si(111) Surfaces in Contact with a Series of One-Electron, Outer-Sphere Redox Couples in CH₃CN. *J. Phys. Chem. C* **2012**, *116*, 23569-23576.
66. Plymale, N. T.; Kim, Y.-G.; Soriaga, M. P.; Brunshwig, B. S.; Lewis, N. S. Synthesis, Characterization, and Reactivity of Ethynyl- and Propynyl-Terminated Si(111) Surfaces. *J. Phys. Chem. C* **2015**, *119*, 19847-19862.
67. Plymale, N. T.; Ramachandran, A. A.; Lim, A.; Brunshwig, B. S.; Lewis, N. S. Control of the Band-Edge Positions of Crystalline Si(111) by Surface Functionalization with 3,4,5-Trifluorophenylacetylenyl Moieties. *J. Phys. Chem. C* **2016**, *120*, 14157-14169.
68. Pomykal, K. E.; Fajardo, A. M.; Lewis, N. S. Stability of n-Si/CH₃OH Contacts as a Function of the Reorganization Energy of the Electron Donor. *J. Phys. Chem.* **1995**, *99*, 8302-8310.
69. Shreve, G. A.; Karp, C. D.; Pomykal, K. E.; Lewis, N. S. Limits on the Corrosion Rate of Si Surfaces in Contact with CH₃OH-Ferrocene⁺⁰ and CH₃OH-1,1'-Dimethylferrocene⁺⁰ Solutions. *J. Phys. Chem.* **1995**, *99*, 5575-5580.
70. Moulder, J. F.; Stickle, W. F.; Sobol, P. E.; Bomen, K. D. *Handbook of X-ray Photoelectron Spectroscopy: A Reference Book of Standard Spectra for Identification*

- and Interpretation of XPS Data*; Physical Electronics USA, Inc.: Chanhassen, Minnesota, 1995.
71. Price, W. C.; Harris, P. V.; Passmore, T. R. The Ionization and Dissociation Energies of Molecules and Radicals. *J. Quant. Spectrosc. Radiat. Transfer* **1962**, *2*, 327-333.
72. Hideyuki, Y.; Kazuyuki, M.; Shin-ichiro, A.; Hiroyuki, S.; Satoshi, K.; Yasushi, A.; Koji, K. O.; Shinji, H.; Yoshiya, H.; Nobuo, U. Surface States of Hydrogen-Terminated Si(111) by Metastable Atom Electron Spectroscopy and Angle-Resolved Ultraviolet Photoelectron Spectroscopy. *Japanese Journal of Applied Physics* **2000**, *39*, 1706.
73. Nakamura, T.; Miyajima, K.; Hirata, N.; Matsumoto, T.; Morikawa, Y.; Tada, H.; Nakajima, A. Electronic Structure of Hydrogen-Terminated Silicon Surfaces [H-Si(111)] Studied by Two-Photon Photoemission. *Appl. Phys. A* **2010**, *98*, 735-743.
74. Blase, X.; Zhu, X.; Louie, S. G. Self-Energy Effects on the Surface-State Energies of H-Si(111)1x1. *Phys. Rev. B* **1994**, *49*, 4973-4980.
75. Li, Y.; Galli, G. Electronic and Spectroscopic Properties of the Hydrogen-Terminated Si(111) Surface from *ab initio* Calculations. *Phys. Rev. B* **2010**, *82*, 045321.
76. Kumar, A.; Santangelo, P. G.; Lewis, N. S. Electrolysis of Water at Strontium Titanate (SrTiO₃) Photoelectrodes: Distinguishing between the Statistical and Stochastic Formalisms for Electron-Transfer Processes in Fuel-Forming Photoelectrochemical Systems. *J. Phys. Chem.* **1992**, *96*, 834-842.
77. Lewis, N. S. An Analysis of Charge Transfer Rate Constants for Semiconductor/Liquid Interfaces. *Annu. Rev. Phys. Chem.* **1991**, *42*, 543-580.

78. Shreve, G. A.; Lewis, N. S. An Analytical Description of the Consequences of Abandoning the Principles of Detailed Balance and Microscopic Reversibility in Semiconductor Photoelectrochemistry. *J. Electrochem. Soc.* **1995**, *142*, 112-119.